Tune Measurement at GSI SIS-18: Methods and Applications

Zur Erlangung des akademischen Grades Doktor-Ingenieur (Dr.-Ing.)
genehmigte Dissertation von Dipl.-Ing. Rahul Singh aus Jalesar
Mai 2014 — Darmstadt — D 17

TECHNISCHE
UNIVERSITÄT
DARMSTADT

T E M F

Tune Measurement at GSI SIS-18: Methods and Applications

Genehmigte Dissertation von Dipl.-Ing. Rahul Singh aus Jalesar

1. Gutachten: Prof. Dr. Ing. Thomas Weiland
2. Gutachten: Prof. Dr. Ing. Harald Klingbeil

Tag der Einreichung: 09.07.2013
Tag der Prüfung: 05.03.2014

Darmstadt — D 17

Bitte zitieren Sie dieses Dokument als:
URN: urn:nbn:de:tuda-tuprints-
URL: http://tuprints.ulb.tu-darmstadt.de/

Erklärung zur Dissertation

Hiermit versichere ich, die vorliegende Dissertation ohne Hilfe Dritter nur mit den angegebenen Quellen und Hilfsmitteln angefertigt zu haben. Alle Stellen, die aus Quellen entnommen wurden, sind als solche kenntlich gemacht. Diese Arbeit hat in gleicher oder ähnlicher Form noch keiner Prüfungsbehörde vorgelegen.

Darmstadt, den May 12, 2014

(Rahul Singh)

Contents

List of Figures

List of Tables

Abstract

Two parallel tune measurement systems are installed at GSI SIS-18 based on different principles. The first is called the Tune, Orbit and POSition measurement system TOPOS. Its working principle involves direct digitization of BPM signals at 125 MSa/s, which is used for online bunch-by-bunch position calculation in FPGAs. In the course of this work, position calculation algorithms were developed and studied for real time implementation in the TOPOS FPGAs. The regression fit algorithm is found to be more efficient and robust in comparision to previously used weighted mean algorithm with the baseline restoration procedure. The second system is the Baseband Tune measurement system referred to as BBQ system. The operational principle of this system was concieved at the CERN Beam Instrumentation group and is based on direct diode detection. In the framework of this work, this system was optimized and brought into operation at GSI SIS-18. Front-end data from both systems are used to calculate the tune spectrum every $250 - 5000$ beam revolutions or turns within SIS-18 based on the resolution requirement and the mode of operation. Advanced non-parametric spectrum estimation method like amplitude Capon estimator is compared to the conventional DFT based methods in terms of resolving power and computational requirements for the calculated spectrum. Further the TOPOS and BBQ systems are compared and characterized in terms of sensitivity, reliability and operational usage. The results from both systems are found to be consistent with each other and have their favoured regimes of operation. The effects on tune spectra obtained from both systems were studied with different types of excitations with excitation power levels up to 6 mW/Hz.

These systems in association with other beam diagnostic devices at SIS-18 were used to conduct extensive experiments to understand the effect of high intensity beams on the tune spectrum. These careful measurements recorded all the relevant beam parameters, thus leaving out no “free parameters”. Several important results were established in course of these experiments. Coherent tune shifts in dependence of intensity gave direct measurements of transverse machine impedances. The high resolution tune spectrum allowed identification of higher order head-tail modes. The relative spectral positions of these head-tail modes when compared with the analytical theory based on the “square well airbag model” gave a direct measurement of the incoherent tune spread in bunched beams. The measurements agreed well with the perturbative treatment applied in the theory only for space charge parameter in the range $q_{sc} \lesssim 4$ after which significant deviations from the theoretical predictions occur. These deviations were understood by using self-consistent simulations and are attributed to the unaccounted role of the pipe impedances in Landau damping of head-tail modes. A novel chromaticity measurement method is demonstrated using temporal separation of each head-tail mode using chirp excitation. Other applications of the parallel tune measurement systems such as linear betatron coupling measurements or tune measurements during acceleration ramps are demonstrated. This work forms a basis for understanding beam dynamics at GSI SIS-18 for high beam currents.

Zusammenfassung

Am Synchrotron SIS18 der GSI werden zurzeit zwei Messysteme zur Tune Bestimmung betrieben, denen unterschiedliche Prinzipien zu Grunde liegen. Eines der Messysteme hat den Namen “Tune, Orbit und POSition TOPOS”. Es basiert auf der direkten Digitalisierung der BPM Signale mit einem 125 MSa/s ADC und der Berechnung der Position eines Bunches mit Hilfe eines FPGAs. Im Rahmen dieser Arbeit wurden Algorithmen zur Positionsbestimmung entwickelt und für die FPGA Implementierung bei TOPOS vorbereitet. Es zeigt sich, dass die Regressions-Anpassungen numerisch effizienter und robuster sind, als die bisher benutzten Algorithmen mit gewichtetem Mittelwert und Basislinien-Rekonstruktion. Das zweite Messsystem hat den Namen “BaseBand Tune (Q)” und wird im Weiteren als BBQ System bezeichnet. Die auf “Direkter Dioden Detektion” basierende Hardware wurde von der Beam-Instrumentation-Gruppe am CERN entwickelt. Im Rahmen dieser Arbeit wurde das BBQ System für die Erfordernisse der GSI modifiziert und in Betrieb genommen. Aus den Roh-daten beider Systeme wurden Tune-Spektren für typisch 250 bis 5000 Strahlumläufe im SIS18 berechnet. Zur Berechnung der Tune-Spektren wurden nicht-parametrische Methoden wie der “Amplituden-Capton-Schätzer” benutzt und mit den üblichen DFT-basierten Methoden hinsichtlich ihrer jeweiligen Auflösung und den numerischen Anforderungen verglichen. Weiterhin wurden die beiden Systeme TOPOS und BBQ hinsichtlich ihrer Nachweisempfindlichkeit, Zuverlässigkeit und der praktischen Benutzbarkeit verglichen. Es zeigte sich, dass beide Systeme jeweils einen vorteilhaften Anwendungsbereich haben. Es konnte gezeigt werden, dass die Beschleuniger-physikalischen Ergebnisse zur Tune Messung beider Systemen gleich sind. Die gewonnenen Tune-Spektren wurden für verschiedene Anregungsmethoden und Anregungsleistungen bis 6 mW/Hz untersucht.

Beide Messsysteme TOPOS und BBQ wurden bei detaillierten Untersuchungen am SIS18 benutzt, um den Einfluss hoher Strahlintensitäten auf die Tune-Spektren detailliert zu untersuchen. Bei diesen Messungen wurden alle relevanten Strahlparameter gemessen, so dass keine freien, an die Theorie anzupassenden Parameter auftreten. Wichtige Resultate wurden durch diese Experimente verifiziert: Die kohärente Tune-Verschiebung in Abhängigkeit von der Strahlintensität stellt eine direkte Messung der Maschinenimpedanz dar. Durch die gute Auflösung der Spektren konnten “Head-Tail Moden” klar identifiziert werden. Die Schwerpunkte dieser Moden im Frequenzspektrum wurden mit einer analytischen, auf einem “airbag-Model” basierenden Theorie verglichen und liefern damit eine Messung der inkohärenten Tune-Verschiebung. Eine gute Übereinstimmung zwischen dem störungstheoretischen Ansatz des Modells und der Messung konnte für kleine Raumladungsparameter $q_{sc} \lesssim 4$ demonstriert werden. Für höhere Raumladungsparameter treten aber wie erwartet signifikante Abweichungen auf. Derartige Abweichungen wurden durch numerische Simulationen bestätigt und konnten auf den Einfluss von Srahlimpedanzen und die dadurch bedingte Landau-Dämpfung der “Head-Tail-Moden” zurückgeführt werden. Eine Methode zur genauen Messung der Chromatizität wird im Rahmen dieser Arbeit beschrieben, sie basiert auf der selektiven Anregung und zeitaufgelösten Messung der “Head-Tail-Schwingungen” sowie der numerischen Anpassung der Chromatizitäts-abhängigen Phasenentwicklung an die Daten. Weitere Anwendungen der beiden Messsysteme wie etwa die Bestimmung der Betatron-Kopplungsstärke sowie die Tune-Variation während der Ionenbeschleunigung wurden demonstriert. Die vorliegende Doktorarbeit stellt eine Basis zum Verständnis der transversalen Strahldynamik bei hohen Strahlintensitäten am SIS18 dar.

1 Introduction

This chapter presents an overview of the GSI facility where the work has been performed. Then the motivation of this work is discussed and the chapter ends with the description of the structure of this thesis.

1.1 GSI facility

The GSI Helmholtzzentrum für Schwerionenforschung (Helmholtz center for heavy ion research) is a facility for fundamental research with ion beams. It was set-up in 1969 and is jointly funded by the Federal Republic of Germany and the state of Hessen. The first section, the Universal Linear Accelerator UNILAC was built to provide ion beams for experiments in nuclear physics and it came under operation in 1975. Its versatility to accelerate ions over a wide range of masses and charges spanning from protons to Uranium leads to it being termed as "universal". The SIS-18 heavy ion synchrotron was built to raise the beam energy and came into operation in 1990. In SIS-18, the ions are accelerated to an adjustable energy whose peak value depends on their mass-to-charge ratio, the maximum magnetic rigidity of the synchrotron is 18 Tm, indicated in the name. The maximum energy lies between 1 GeV/u for U^{73+} ions, where u is the unit for atomic mass and 4.5 GeV for protons. The tune measurement systems and the associated results presented in this work are all in respect to the SIS-18 where they are commissioned as operating tools. Experimental storage ring (ESR) is the third major infrastructure which is used for experiments for beam cooling and storage over long times primarily for studying complex nuclei. In order to accommodate the demand for higher beam energy and intensity for more advanced physics experiments, the international Facility for Antiproton and Ion Research (FAIR) [1] is currently being constructed at GSI and is presently expected to come under operation by 2019 [2, 3]. This section describes very briefly the basic operational infrastructure of the GSI facility and upcoming FAIR. The relation of this work to the current and future facility is highlighted at appropriate places. Some important beam and machine parameters of the SIS-18 and FAIR facilities will also be mentioned.

1.1.1 UNILAC

Well known to accelerate "everything", UNILAC provides particle species and their charge states over a wide range. The final energies can be different based on the charge state and ion species. We will refer to the design particle species U^{28+} when discussing the final energies of each stage. Ions are generated at various sources, namely CHORDIS/MUCIS/MEVVA, each with a distinct principle of operation. The generated ions are accelerated to $\approx$ 1.4 MeV/ u by the high current injector (HSI) which consists of an RFQ and two IH-Structures at a frequency of 36 MHz. Subsequently, a gas stripper is used to increase the charge state of the ions. At this point, another high charge state injector (HLI) is connected in parallel to the UNILAC for supplying alternative particles from an ECR Source with its own RFQ and IH-structure. Following the gas stripper is the four tank Alvarez section operating at 108 MHz which increases the beam energy to 11.4 MeV/u. After acceleration by the Alvarez structure, the beam energy can be varied by a series of 15 single gap resonators (ERs) before being fed to the experimental hall (EH), where experiments are directly performed using these final energies. Otherwise, the beam is routed through the transfer channel (TK) and injected into the SIS-18. The injection energy at SIS-18 is $\approx$ 11.4 MeV/u. An important feature of the UNILAC control system and devices is that they are designed to have 16 so called virtual accelerators which can run in parallel with any complex combination of any 3 ion species and various target locations.

1.1.2 SIS-18

SIS-18 consists of 12 identical lattice sections and a circumference of $\approx$ 216.72 m. The layout of machine optics is shown in Fig. 1.2. Each cell has two dipoles, three quadrupoles and one sextupole magnets. The maximal field

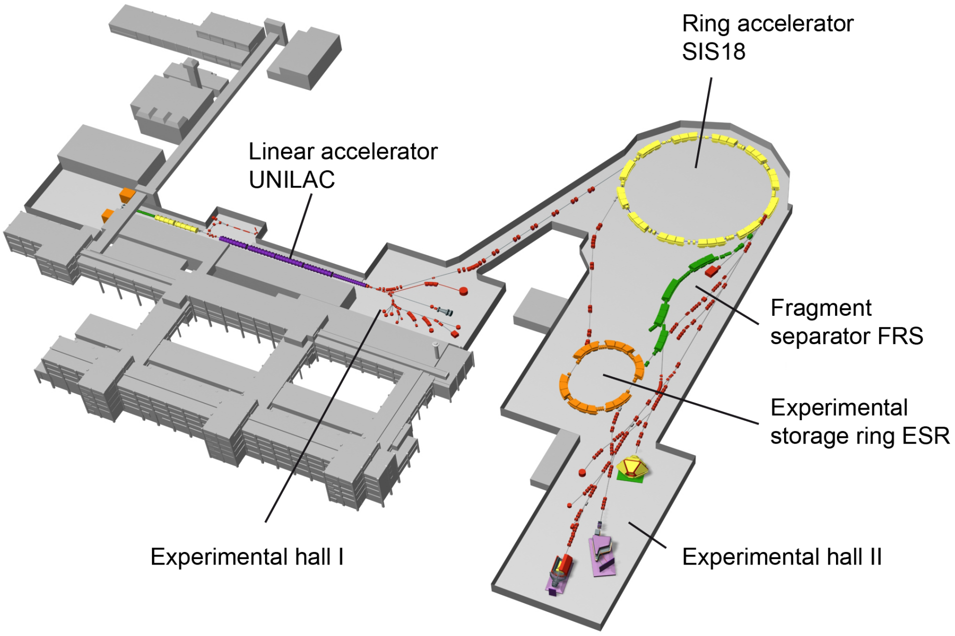

Figure 1.1: A schematic view of GSI facility. All the major components are marked.

strength of the normal conducting dipoles is 1.8 T. Two radio frequency cavities are used for the acceleration. The spacing between the magnets is occupied by different devices in various sections. The technical parameters of SIS-18 can be found in [4].

The basic parameters for SIS-18 are:

- Machine circumference: $C = 216.720$ m
- Magnet bending radius: $R_b = 10.000$ m
- Maximum magnetic field: $B = 1.8$ T
- Maximum bending power: $BR_b = 18$ Tm (magnetic rigidity)
- Magnet ramping rate: $dB/dt = 4$ T/s (10 T/s)
- Harmonic number: $h = 4$
- rf frequency: $f_{rf} = 0.8 - 5.4$ MHz
- Vacuum: $1.3 \cdot 10^{-8}$ Pa
- Kinetic energy at injection: $W_{kin} \approx 11.4$ MeV/u
- Ferrite loaded cavity for particle acceleration

The beam diagnostics instruments are also spaced between the magnets. A list of major beam diagnostics devices installed in SIS-18 can be found in Fig. 1.2. The tune is a property of the synchrotron, and this thesis is primarily based on the 12 beam position monitors and their signal processing. However, the experimental part also uses few other diagnostic instruments mentioned in Fig. 1.2.

A typical acceleration cycle in SIS-18 is comprised of the following steps. The beam is injected from the UNILAC via the transfer channel into the SIS-18 with no longitudinal rf voltage (no bucket-bucket transfer) over ~ 20 turns (multi-turn injection). Injection is a crucial step in the acceleration cycle in terms of beam quality and requires neat

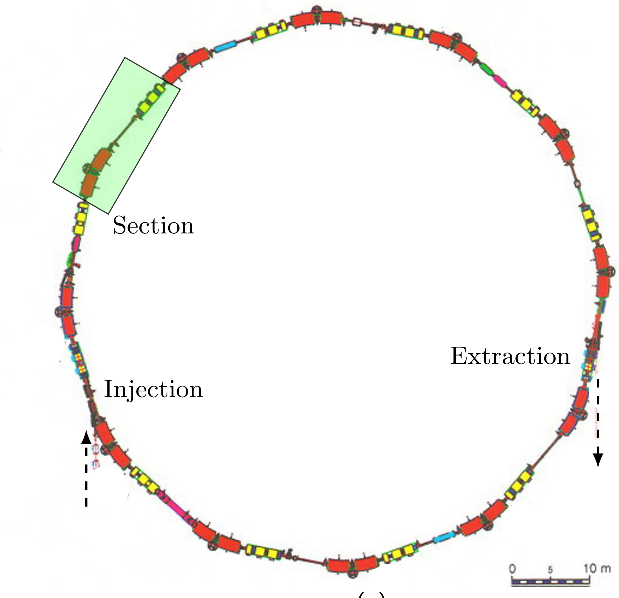

(a)

Device	Purpose
12 BPMs	Position, tune
3 Phase pick-up	Longitudinal structure
Quad pick-up	Tune, Quadrupole oscillations
Schottky pick-up	Schottky diagnostics
2 DC-CTs	Current
1 FCT	Bunch structure
1 ACT	Injected current
1 IPM	Transverse profile
1 Wire grid	Transverse profile
1 Scint. screen	Transverse profile
2 Beam exciters	Excitation
15 BLMs	Beam losses

(b)

Figure 1.2: Layout of SIS-18 synchrotron (a). List of beam diagnostic devices installed at SIS-18 (b).

optimization. The coasting beam thus injected is captured in four radio frequency buckets using adiabatic bunching and then accelerated. Following that, the beam acceleration starts, when the ramp for the cavity frequency and the dipole magnetic field increase in snychronism. In principle, all the timing parameters in the acceleration cycle can be tuned as per the requirements of machine experiments, taking machine safety and any resulting radiation damage or activation into account. There are standard modes defined for users during normal operations. Most of the experiments performed in the scope of this thesis were on the bunched injection plateau i.e. between **(b)** and **(c)** in Fig. 5.7. The state of the synchrotron after acceleration ramp is called flat-top **(e)** and is followed by the extraction of the beam **(f)**. There are two ways to extract the beam. The slow extraction is initialized by shifting the beam on a resonance with the sextupoles. The ions then drift off the closed orbit until they can be pushed out by an electrostatic field. This is also referred as Knock Out (KO) extraction. For the fast extraction the beam is kicked off the closed orbit by fast-switching magnets, the extraction kickers, within one turn. An electron cooler is also installed to decrease the beam emittance (size) and thus to increase the beam intensity [5].

1.1.3 ESR and other experiments

After the extraction, the beam is used for experiments in plasma physics, atomic physics, astrophysics, nuclear physics, material sciences, biophysics and cancer therapy [6]. The goals of the experiments are the investigation of atoms, nuclei, nucleons, elementary particles and the forces acting between them, matter under extreme heat and pressure, and the synthesis of the elements in stars. Numerous articles published in scientific journals witness the productivity of the research at GSI (see e.g. [7]). An overview of the current research activities by both users and accelerator departments is given in the annual GSI scientific reports [8].

1.1.4 FAIR

FAIR will host two ion synchrotrons, SIS-100 and SIS-300, and several storage rings as well as beam targets [2]. The full layout of FAIR is described in [1]. The synchrotrons SIS-100 and SIS-300 will be built for FAIR to accumulate and accelerate the beams from SIS-18. Their circumference is 1083 m and the rigidity in Tm is indicated in their names. From SIS-100 the U^{28+} beams can be delivered with a maximal energy of 2715 MeV/u to the experiments or

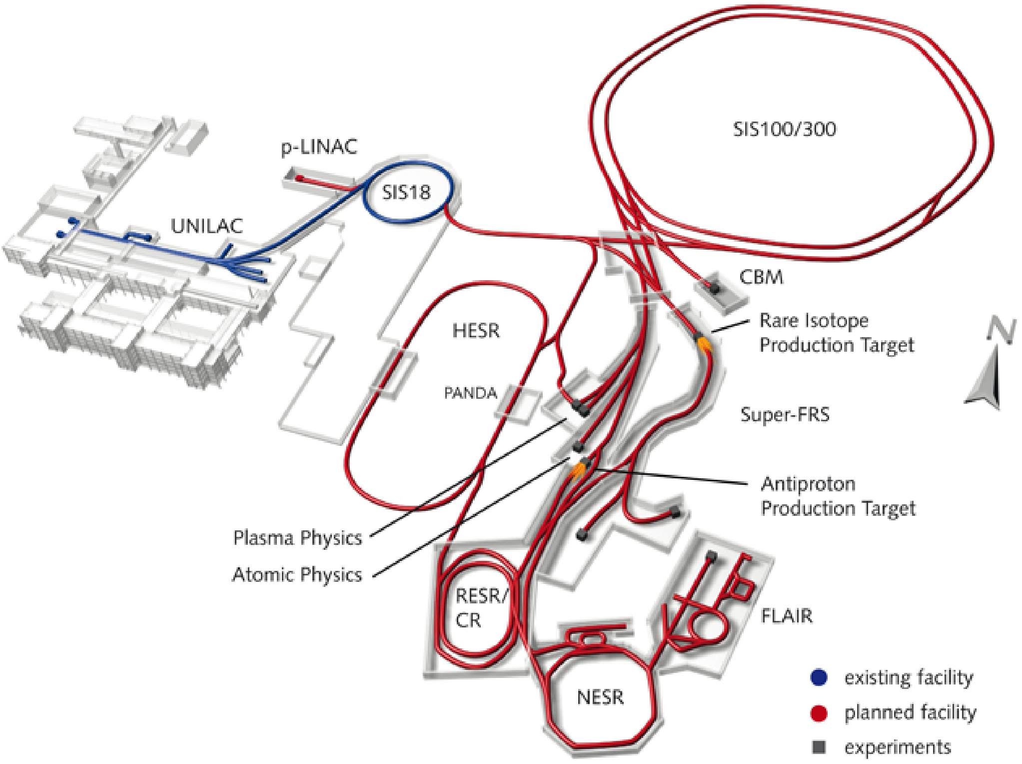

Figure 1.3: Schematic of the proposed FAIR facility.

transferred to SIS-300 for further acceleration up to 34 GeV/u after increasing the charge state to 92+ [9]. The energy density of the beams in FAIR gives access to nuclear reactions and extreme matter states that cannot be achieved with SIS-18. The increased particle density furthermore allows the observation of rare events. The possibility to experiment with antiproton beams is completely new. Further advances in the scientific fields addressed by GSI will follow with benefits for quantum chromodynamics, astrophysics and other disciplines [10, 11, 12]. The radioactive secondary ions will be generated by the bombardment of a fixed production target with heavy ions. The fragments of exotic nuclei thus formed will be subsequently sent to super-fragment separator (Super-FRS [13]) and the selected isotopes will be transferred for further investigations in the storage rings CR (Cooler Ring), HESR or NESR (New Experimental Storage Ring) where the deceleration and cooling the beams will be done or fixed-target experiments will be performed.

SIS-18 is planned to serve as booster and injector for SIS-100 for most cases. The targeted beam intensities go considerably beyond the values achieved in the past. Therefore FAIR demands an upgrade of SIS-18 and UNILAC to ensure that current facility can provide beams with the quality and intensity required by FAIR. Hence the upgrade of SIS-18 is an essential part of the FAIR project. The highest beam intensities in SIS-18 accomplished so far and the design intensity for FAIR are discussed in [1]. This work focusses on designing the position and tune measurement system for the undergoing SIS-18 upgrade and further testing it as a prototype for the FAIR accelerator rings. As mentioned earlier, other experimental storage rings are planned to have acceleration or deceleration of beams and stochastic cooling which would require the services of a high precision and a high resolution tune measurement system. As the FAIR machine construction and development is approaching, constant efforts for better, optimal diagnostics are required and this work is one of them.

Betatron tune measurement systems form an essential part of any beam diagnostic systems in most synchrotrons. However, there are many “tune” definitions used in the literature and it is a pre-requisite to define betatron tune in a synchrotron. The concept of tune is rooted in the fact, that any charged particle source emits particles with a finite transverse momentum distribution and finite beam size, and the charged particles repel each other. This property of beam particles is often described with the concept of beam emittance, explained in section 2.1.3. Thus the focussing of the beam around the designed closed particle trajectory in the synchrotron is essential for beam confinement and acceleration. This is done using magnetic forces especially at medium and high energy machines due to higher Lorentz forces provided by magnetic fields [14]. These magnetic lenses or quadrupoles are periodically arranged in the synchrotron such that the transverse dimensions of the beam are within the required specifications of the machine. This arrangement along with other magnets is referred to as beam lattice or beam optics. The tune is given by the number of oscillations, a particle of design energy will undergo during one turn while traversing the beam optics around the synchrotron. This designed machine tune is called the “bare tune” and the exact definition is given by Eq. 2.13. The important point to note is that, the bare tune is independent of the presence of beam in the machine, and completely given by the machine lattice settings. The bare tunes from both transverse planes are put together and called the “working point” of the machine. However, due to deviation in the particle momentum and other forces due to inter-particle interactions, beam storage ring interactions, particle tune may differ from the set or bare tune. This brings us to “another” definition, the tune of any single particle is the number of transverse oscillations it performs around its closed orbit during one complete turn around the synchrotron. This is also often called the “incoherent tune” of the particle and each particle has a different tune depending mainly on its relative position with respect to the synchronous particle and its instantaneous momentum. The measurement observable is often the center-of-mass (beam position) motion of all the particles rather than a single particle motion and this center-of-mass tune is called the “coherent tune”. Normal tune measurement systems deal with the coherent signal and thus the coherent tune, which depending on beam conditions, could be substantially different from bare tune or incoherent tunes. To put it all in perspective, if the beam intensity is very low such that all the intra-beam and beam-environment interactions can be neglected, and the momentum spread within the beam is also negligible, then the bare tune, incoherent tune and coherent tune, are equivalent.

The main objective of this work is to study, test and interpret the output of a fast, sensitive and high resolution method for measurement of the “tune spectrum” for bunched beams and further estimation of the coherent tune from the spectrum. This tune value is fed to the control system where appropriate actions are taken to correct it. The correction of drifting betatron tunes is essential to achieve high beam currents by avoiding any unexpected resonances and resulting emittance enlargement and/or beam losses. It also enables systematic machine studies and improvement of machine parameters.

The measurement and estimation of the coherent tune is a challenging task in bunched beams mainly because the tune spectrum contains several higher order “head-tail” [15] modes due to longitudinal synchrotron motion in addition to the 0^{th} order mode, which is the coherent tune for bunched beams. The relative amplitudes of these head-tail modes have a strong dependence on the machine chromaticity [16]. There are many instances when the highest peak in the spectrum may not be the coherent tune but rather a higher order head-tail mode. The spectra are further complicated by the presence of intensity dependent collective effects [17]. The collective effects stem from the presence of beam-storage ring coupling impedances [18, 19] and direct space charge forces which lead to coherent tune shifts [20, 21] and head-tail frequency shifts respectively in a rather non trivial way [22]. In addition to these, other factors such as coupling between the planes [23], Landau damping [24], initial beam conditions, interference noise and other spurious signals play a role in making for a complicated recipe of the transverse beam spectrum. Figure 1.4 gives a flavour of the complexity of the tune spectrum at a particular instance during acceleration.

There are two established methods to measure the tune spectrum: Transverse Schottky measurement and measurement of the beam transfer function (BTF) [25, 26]. Each of these “classical” methods of measurement have their own limitations: For example, Schottky measurements rely on the statistical fluctuations in the beam phase space and call for a very sensitive pick-up and long measurement times. In addition to that, in presence of space charge, the Schottky spectra become very complicated to analyse even for coasting unbunched beams [27]. Beam transfer function in its classical form is an appropriate method for machine studies, however its usage in terms of

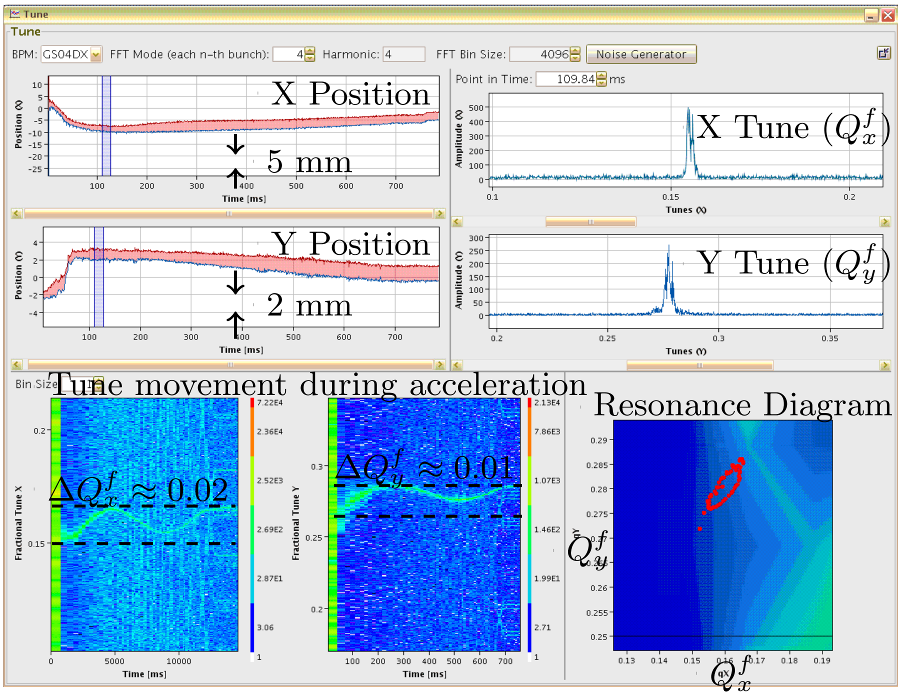

Tune

BPM: GS04DX FFT Mode (each n-th bunch): 4 Harmonic: 4 FFT Bin Size: 4096

Point in Time: 109.84 ms

Figure 1.4: The output of position and tune of both planes seen on a TOPOS screen shot. Single shot of tune spectra is shown on top right calculated out of the marked position on top left. The spectrum is quite complex especially in the y plane owing to higher space charge and wall impedances, as well as higher chromaticity. On the bottom left, is shown the well-known tune fluctuation during the acceleration ramp due to a change in the GSI SIS-18 beam optics settings [29]. The bottom right picture shows the calculated tune peak in both planes plotted over time on a "resonance diagram" [30].

regular operational tool is inconvenient due to frequency movements during acceleration and time required for each measurement. Another tune measurement method is the measurement of beam response after kicking the beam with a rapid excitation kicker [23, 28]. The kick based method is in principle a subset of the BTF, where instead of a frequency sweep, a fast kick is used. It satisfies the requirements on the measurement speed and reliability of measurement over the whole acceleration cycle. However, regular kicks are required for measurement over whole acceleration cycle, which leads to an emittance blow-up. More variants of this method based on different beam excitation types have been studied. The newer band-limited noise excitation method was studied in [29] and has been found to be appropriate for regular operational use. In addition to develop and optimise the excitation methods, efforts have been put into developing sensitive analyses of the beam pick-up data. This forms the basis to the two tune measurement systems presently under operation at SIS-18.

The Tune, Orbit and POSition measurement system deals with a digital analysis of BPM data with fast ADCs and FPGAs, where optimum position estimators are used to calculate the position. Those position data are analysed with high resolution frequency estimators to calculate the tune spectrum. The other tune measurement system (BBQ) was conceived at the CERN Beam Instrumentation group and bases itself on pick-up data processing directly in hardware. It uses diode based peak detectors, and detects the beam envelope immediately after pick-ups in hardware. The peak detected envelope signal is then conditioned with a custom-built chain of filters and amplifiers. The resulting signal is then analysed by spectrum estimators to find the tune spectra. As a part of this work, the band limited noise excitation method is refined by benchmarking it with other excitation types. A new position estimator is proposed for implementation in TOPOS FPGAs after rigorous off-line testing in comparison with previous algorithm. Further, non-parametric spectrum estimators superior to FFT technique in terms of resolution and variance have been identified and utilized for the first time in the domain of precise tune measurement.

Several measurement campaigns were performed using TOPOS to benchmark the excitation systems and their effect on the tune spectrum. Since summer 2011, the BBQ system was re-installed with some modifications for the betterment of the input stage and low frequency shielding. Both tune measurement systems were verified against each other and a relative sensitivity analysis was performed. Even though the prime motive of the experiments was to demonstrate the usage and sensitivity of the measurement systems as operational tools, important beam physics results were obtained from the synchronous usage of several beam diagnostic tools and careful data analysis. These campaigns led to fundamental findings on the measurement of incoherent tune shifts for bunched beams. They are also the first beam based measurement estimates for resistive wall impedances at SIS-18 [22]. In addition to that, novel method for chromaticity measurement was established based on frequency sweep excitation of individual head-tail modes. The chromaticity measurements were found to be in excellent agreement with previous measurements, based on other classical methods [27]. Other beam based measurements such as, beam coupling, influence of noise on position measurement etc. were also performed in the scope of these measurements.

Chapter 2 of this thesis summarizes important accelerator physics concepts required for the understanding of this work. It will also discuss advanced concepts like space charge effects on tune spectra at high intensities. Chapter 3 explains the technical details of the complete TOPOS and BBQ systems. The types and properties of the beam excitation and of the data acquisition signal chain are discussed. The measurement setups with measurement uncertainty calculations and noise considerations are described as well. Chapter 4 describes the BPM data processing methods for the position and tune calculations. Chapter 5 demonstrates the opportunities offered by the high resolution and parallel operation of both tune measurement systems. Important experimental results obtained using the data from both measurement systems in synchronization with other beam diagnostic systems over several machine studies are presented. Finally the outcome and outlook of this work is discussed with respect to the effectiveness of the measurement systems as a prototype for FAIR [1] and further research opportunities in the field of accelerator physics at SIS-18 and FAIR synchrotrons.

2 Beam Dynamics

This chapter presents the theoretical concepts and framework for interpreting the beam signals for a bunched beam in a synchrotron. The chapter is divided into three major segments; the first section presents basic fundamentals on the transverse and longitudinal beam dynamics and provides definitions of the various machine and beam properties. The second section gives an introduction to the theory of transverse beam signals for bunched beams i.e. Schottky signals and beam transfer function (BTF) measurement. The relation between Schottky signals, BTF measurement and the tune measurement system at GSI is discussed. The final section will discuss the collective effects in high intensity bunched beams and the resulting modification of the tune spectra. The discussions in this chapter essentially follow from the following sources [14, 19, 33].

2.1 Beam dynamics at low intensities

A charged particle beam is spatially confined in a synchrotron ring after its injection, during the acceleration until its extraction at the desired energy. The confinement (bending and focussing) is provided by various kinds of electromagnets which are collectively referred as the beam optics. We will discuss and derive the equations of motion for single particles under the assumption of linear beam optics in this section. Acceleration is usually provided by the standing or travelling wave cavities, however the acceleration of beams is not considered in this description, i.e. momentum $|\vec{p_0}|$ of the ideal/nominal/reference particle is constant. A useful result from the special theory of relativity, is the interrelation between the velocity $\vec{v}$ and the momentum $\vec{p}$ of a particle with rest mass m_pA and is given by,

$$\vec{p} = \gamma m_0 \vec{v} \approx \gamma m_p A \vec{v} \tag{2.1}$$

where $\gamma = \sqrt{\dfrac{1}{1-\beta^2}}$ is the Lorentz factor, $\beta = \dfrac{|\vec{v}|}{c}$ is the velocity divided by the speed of light in vacuum c, and m_0 is the rest mass of the nucleus taking into account the mass of proton, neutron and the binding energy [34]. However, the approximate result, where the rest mass of the particle is split into the proton mass m_p and the mass number A, which is equal to sum of number of protons and neutrons in the ion will be used for calculations in this thesis.

First we will define the reference orbit as the trajectory of an ideal (synchronous) particle with the nominal momentum $\vec{p_0}$. The reference orbit considered in this work is in the horizontal plane and it is required to be closed.

The shape of the reference orbit in synchrotrons is defined by the magnetic dipoles. In a homogeneous magnetic field of the flux density B_y, the particle moves on a circular trajectory with a radius R. The actual orbit in a synchrotron is comprised of arcs and straight sections, and is described by the mean radius $R = \frac{C}{2\pi}$ where C is the path length of one revolution. The product of B_y and R is called the magnetic rigidity. It is linked to the particle's charge $q = Ze$ and $|\vec{p_0}|$ by virtue of,

$$B_y R = \frac{|\vec{p_0}|}{q} \tag{2.2}$$

where e is the elementary charge and Z is an integer, specifying the ionic charge of the ion. The revolution frequency of the ideal particle is denoted by $f_0 = C/|\vec{v_0}|$ or by its angular frequency counterpart ω_0. It is also referred as f_{rev} at other places in the text to be explicit about the meaning of the term. A special curvilinear coordinate system called Frenet-Serret system is shown in Fig. 2.1. It is the commonly used coordinate system, suitable to describe the equations of motion for particle trajectories in the transverse plane. The origin of this coordinate system is moving

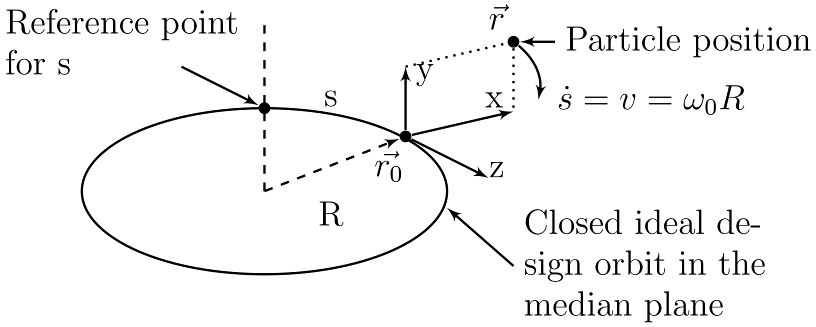

Figure 2.1: Frenet Serret coordinate system.

on the trajectory of the reference orbit. The motion of any non- ideal particle, deviating from the ideal path or momentum, if expressed in the six dimensional curvilinear coordinate system is given by,

$$\vec{r}_{ni} = \begin{pmatrix} x \\ x' \\ y \\ y' \\ z, \Delta t \\ \Delta p, \Delta W \end{pmatrix} \tag{2.3}$$

where x, y, z are the coordinates in the defined coordinate system such that z is oriented in parallel to the reference orbit. The unit vectors, spanning the coordinate system in real space, are denoted by $\vec{e}_x$, $\vec{e}_y$, and $\vec{e}_z$. x and y span the transverse plane such that x points to the horizontal direction and y to the vertical one. x' is defined as dx/ds, and y' correspondingly, and they express the local slopes of the actual orbit with respect to the reference orbit. The prime ($'$), represents the differentiation with respect to s in this thesis. The velocity is hence $v_0 = v_0\vec{e_z}$, and correspondingly $\vec{p_0} = p_0\vec{e}_z$. The longitudinal momentum deviation is normalized by the nominal momentum, i.e. $\dfrac{\Delta p}{p_0} = \dfrac{(p - p_0)}{p_0}$. In a stable beam, only small momentum deviations occur. Therefore we may assume x', y', $\frac{\Delta p}{p_0} \ll 1$. z can be associated with the delay or advance in time $\Delta t = \dfrac{z}{v_0}$ with respect to reference particle. This will be considered further in the longitudinal dynamics section.

2.1.1 Transverse beam dynamics

The equations for transverse motion for a single particle in the Frenet-Serret coordinate system are presented below. The position vector $\vec{r}$ of any particle is given by,

$$\vec{r} = \vec{r_0} + x\vec{e}_x + y\vec{e}_y \tag{2.4}$$

where $\vec{r_0}$ is the design orbit of the particle, and $\vec{e}_x$ and $\vec{e}_y$ are unit vectors in the x and y plane. The equations of motion are given by,

$$\ddot{\vec{r}} = \frac{q}{\gamma_0 m_0}\dot{\vec{r}} \times \vec{B} \tag{2.5}$$

After working out the above equation using the necessary transformations and taking the appropriate forces into account, closely following Ref. [14], we arrive at,

$$x''(s) + \Big(\frac{1}{R^2(s)} - \hat{k}_x(s)\Big)x(s) = \frac{1}{R(s)}\frac{\Delta p}{p_0} \tag{2.6a}$$

$$y''(s) + \hat{k}_y(s)y(s) = 0 \tag{2.6b}$$

where

$$|\hat{k}_{x,y}(s)| = \frac{q}{p}\frac{dB_{y,x}}{dx,y} \qquad \text{for } s \text{ in quadrupole} \tag{2.7a}$$

$$= 0 \qquad \text{for } s \text{ outside quadrupole} \tag{2.7b}$$

and $\hat{k}_x = -\hat{k}_y$ since a quadrupole focussing in one plane is defocussing in another plane. $R(s)$ is the bending radius of the dipole magnets present. Note the conversion of $(\dot{})$, representing derivative with respect to time to $(')$ the derivative with respect to s. The detailed steps can be followed in the excellent description given in [33]. If we solve the Eq. 2.6a for $\frac{\Delta p}{p_0} = 0$ (particle of nominal momentum) and $\frac{1}{R(s)} = 0$ (no bending magnet), we obtain the "Hill's type differential equation" in both planes. The solution of this equation in the horizontal plane is given by,

$$x(s) = \sqrt{\epsilon_x \hat{\beta}_x(s)} \cos(\hat{\Psi}_x(s) + \phi_x) \tag{2.8}$$

where ϵ_x and ϕ_x are fixed by the initial conditions and $\hat{\beta}_x(s)$ is the lattice amplitude function and $\hat{\Psi}_x(s)$ is the phase advance,

$$\hat{\Psi}_x(s) = \int\limits_0^s \frac{ds}{\hat{\beta}_x(s)} \tag{2.9}$$

Thus the orbit around the synchrotron is a function of s and is described by pseudo-harmonic betatron oscillations. The solution is shown only for horizontal plane to simplify the notations, and exactly the same treatment can be applied to the vertical plane by replacing x with y. The derivative of the trajectory function $x(s)$ is given by,

$$x'(s) = -\sqrt{\frac{\epsilon_x}{\hat{\beta}_x(s)}} \left[\hat{\alpha}_x(s) \cos(\hat{\Psi}_x(s) + \phi) + \sin(\hat{\Psi}_x(s) + \phi_x)\right] \tag{2.10}$$

with $\hat{\alpha}_x(s) = -\dfrac{\hat{\beta'}_x(s)}{2}$. Eq. 2.8 and Eq. 2.10 can be combined to find a famous result, the equation of the phase space ellipse or the so called "Twiss equation",

$$\hat{\gamma}_x(s)x^2(s) + 2(\hat{\alpha}_x(s)x(s)x'(s) + \hat{\beta}_x(s)x'^2(s) = \epsilon_x \tag{2.11}$$

where $\hat{\gamma}_x(s) = \dfrac{1 + \hat{\alpha}_x^2(s)}{\hat{\beta}_x(s)}$. Figure 2.2 shows the phase space ellipse at a particular position s_0, and the orientation of phase ellipse changes as it traverses through the synchrotron. However, the area of the phase space ellipse remains constant at any position (or time) in the synchrotron ring if the particle does not gain or dissipate energy due to acceleration, radiation or any other non-conservative interactions . Therefore the area of the phase space ellipse can be considered an invariant for non-accelerating ion beams and it is proportional to the initial property "emittance ϵ" of the particle as shown in Eq. 2.11.

Now moving to the time domain, if we consider the betatron motion with respect to time at any particular position s_0 in the synchrotron, it resembles a simple harmonic oscillator,

$$x_{s_0}(t_n) = \sqrt{\epsilon_x \hat{\beta}_x(s_0)} \sin(Q_x \omega_0 t_n + \phi_0^x) \tag{2.12}$$

where $t_n = nT$ are the times for the n^{th} passage through the azimuth $s = s_0$, ϕ_0^x is the phase of 0^{th} passage at s_0 and ω_0 is the angular frequency of revolution of the particle. Again, only the motion for horizontal plane is considered, and equations for vertical motion can be obtained by substitution of the subscript x by y. $a_{x,s_0} = \sqrt{\epsilon_x \beta_x(s_0)}$ is a constant depending on initial conditions; and from Eq. 2.9 when integrating for one complete turn of the ring,

$$Q_x = \frac{1}{2\pi} \int\limits_0^{2\pi R} \frac{ds}{\hat{\beta}_x(s)} \tag{2.13}$$

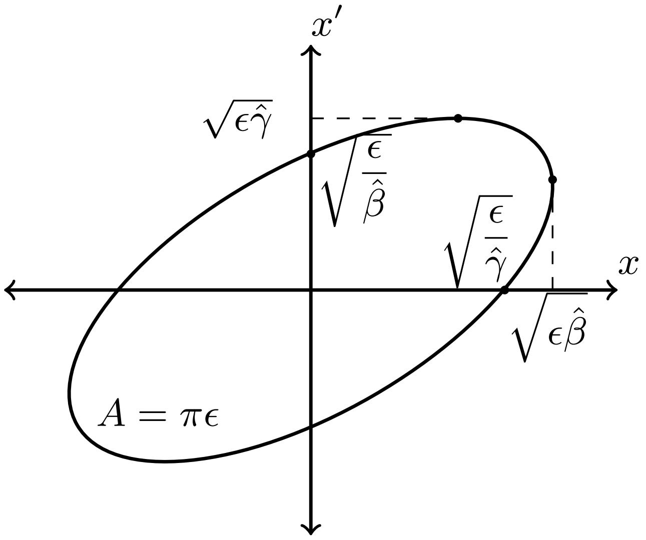

Figure 2.2: Phase ellipse orientation at a particular position s_0 in the synchrotron ring.

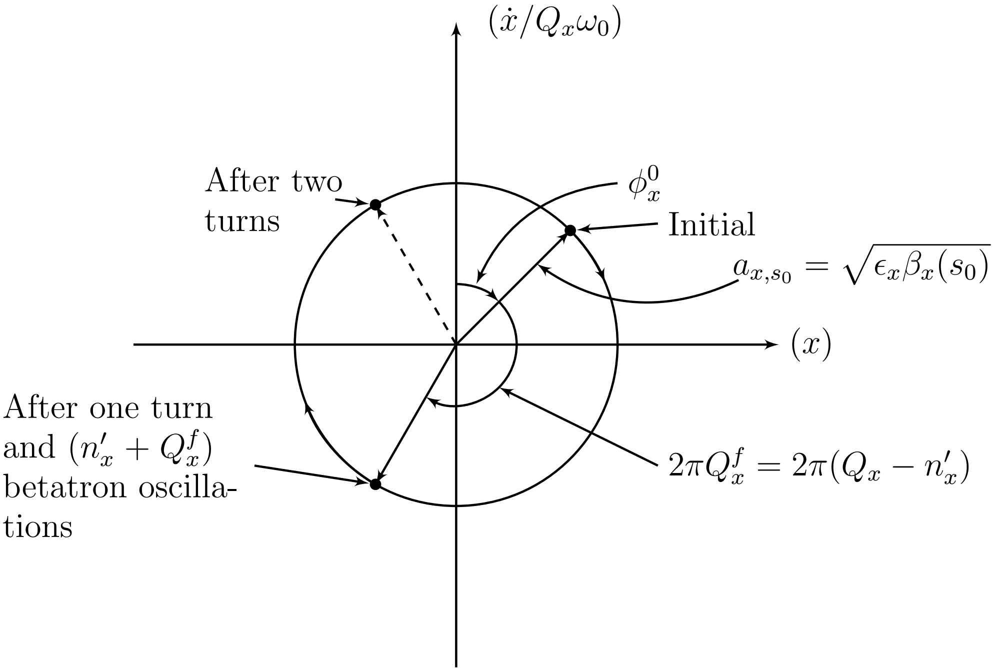

Figure 2.3: Turn by turn position in the polar diagram.

we obtain the definition of the betatron tune (bare tune), which is the number of betatron oscillations per one complete revolution. The betatron oscillations detected at a particular azimuth $s = s_0$, are due to its fractional part as the integer part is not visible due to aliasing. The amplitude and phase representation of linear betatron oscillations at a fixed azimuth are shown in Fig. 2.3 to give an understanding of the beam resonances. It also points out that the tune is a global property of the synchrotron.

$$x(t) = a_{x,s_0} \sin \phi_x(t) \tag{2.14}$$

$$\dot{x}(t) = a_{x,s_0} Q_x \omega_0 \cos \phi_x(t) \tag{2.15}$$

where $\phi_x = Q_x \omega_0 t + \phi_x^0$. The particles rotate in the $(x, \dot{x}/Q_x\omega_0)$ phase planes with angular frequency $Q_x \cdot \omega_0$ independent of the amplitude a_{x,s_0} in the linear regime. Looking into Fig. 2.3, one can observe that after one complete turn around the ring, the point (particle) in the phase space has made n'_x complete revolutions plus an angle of $2\pi Q_x^f$. In case of resonance, the point will return to the same position in phase space after a characteristic number of turns and may give rise to resonant growth due to any spontaneous disturbances caused by magnet alignment errors, field errors, or any unexpected forces. The condition for resonance, taking the coupling between the two planes into account, is given by, $mQ_x + nQ_y = l$ where m, n, l are integers, and order of resonance is given by $|m| + |n|$. Resonances of low orders should always be avoided. To understand the nature of disturbance sources, resultant resonance growth and the concept of stop bands, section 3.14.3 in [33] is recommended. The avoidance of these single particle resonances is the main driver behind the requirement of the precise measurement of tune.

A particle of longitudinal momentum $p = p_0 + \Delta p$ deviating from the design momentum p_R will execute its betatron oscillations about another closed orbit, radially displaced by $x_p(s) = x_0(s) + x_D(s)$ where $x_D(s) = D(s)(\frac{\Delta p}{p_R})$, and $D(s)$ is the dispersion function along the machine. The dispersion affects also the revolution frequency f of the non-ideal particle since it increases the length of the orbit for $\Delta p > 0$. Besides this effect, we have to consider the change of the speed and the mass according to Eq. 2.2. For $\beta \ll 1$, the change in speed is such that $df/dp > 0$, while for $\gamma \gg 1$ we have $df/dp < 0$. The energy with $df/dp = 0$ is called transition energy and the corresponding γ is denoted by γ_T . For small momentum deviations, the change of the revolution frequency is expressed by

$$\frac{\Delta f}{f_0} = -\eta_0 \frac{\Delta p}{p_0} \tag{2.16}$$

and the slippage factor

$$\eta_0 = \frac{1}{\gamma_T^2} - \frac{1}{\gamma^2} \tag{2.17}$$

The total horizontal displacement from the design orbit is given by $x(s) = x_0(s) + x_D(s) + x_\beta(s)$, where $x_\beta(s)$ is the betatron displacement. Orbit displacement due to Δp often has a negligible effect on the particle amplitude, while a rather big effect occurs from the modification of betatron tune due to Δp,

$$Q_x(p) = Q_x(p_0)\Big[1 + \xi_{x,nat}\Big(\frac{\Delta p}{p_0}\Big)\Big] \tag{2.18}$$

where $\xi_{x,nat}$ are the horizontal and vertical natural chromaticities of the ring. The first order chromaticity is the result of the dependence in focal length of magnetic lenses on the particle momentum and is given by,

$$\xi_{x,nat} = -\frac{1}{4\pi Q_x} \int_0^{2\pi R} \hat{\beta}_x(s) \hat{k}_x(s) ds \tag{2.19}$$

The chromaticity converts the momentum deviation into tune deviation, and plays an important role in beam stability. Here we have ignored the higher order contributions to chromaticity, coming from dependence on $\frac{\Delta p}{p_0}$, as well as from the higher order magnetic fields due to multipoles. Sextupoles are often installed to control the chromaticity values in synchrotrons.

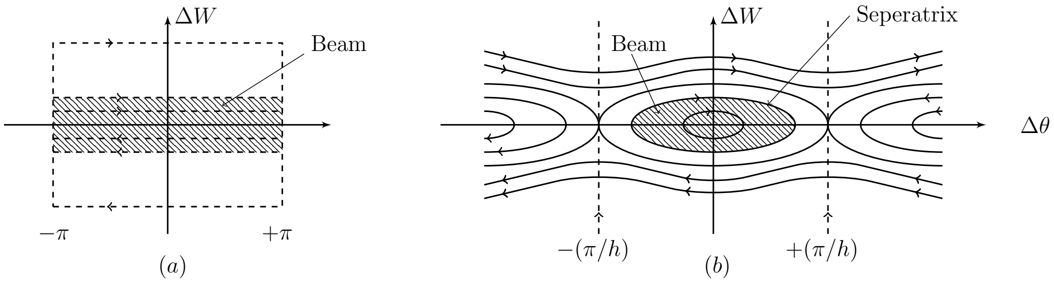

Figure 2.4: Longitudinal phase space for the coasting and bunched beams.

2.1.2 Longitudinal beam dynamics

Longitudinally, the particle motion occurs in two modes, i.e. in absence of any longitudinal forces (continuous coasting beam), or in presence of them (bunched beams). In case of continuous coasting beams, each particle drifts in a free streaming orbit with its own constant angular velocity. The beam fills the whole ring, and there are no longitudinal synchrotron oscillations. Each particle maintains its original momentum, and moves forward or backward relatively to the reference particle depending on its relative energy ΔW. Figure 2.4(a) shows the phase space representation of such a beam. The particle trajectories in phase space are marked by horizontal lines. These high intensity coasting beams are not the focus of this work. They have been considered in significant depth in [27].

In bunched beams, the sinusoidal rf potential $u\sin(\omega_{rf}\Delta t + \phi_0)$, generated by an rf cavity, longitudinally focuses the beam. The time deviation Δt from the reference particle is related to phase deviation ($\Delta\theta$) by,

$$\Delta\theta = \frac{2\pi\Delta t}{T_0} \tag{2.20}$$

The nominal particle with $\Delta\theta = 0$ finds the synchronous phase ϕ_0 of longitudinal electric fields at each turn. The particles with an energy deviation oscillate around the synchronous particle. The equations for longitudinal motion due to sinusoidal rf are given by,

$$\frac{d\Delta t}{dt} = \frac{\eta_0}{m_0 c_0^2 \beta_0^2 \gamma_0}\Delta W \tag{2.21a}$$

$$\frac{d\Delta W}{dt} = \frac{q\hat{u}}{T_0}(\sin(\omega_{rf}\Delta t + \phi_0) - sin(\phi_0) \tag{2.21b}$$

where Δt and ΔW is the relative distance and energy of any particle with the synchronous particle while W_0 is the energy, T_0 is the revolution time, β_0 is the relativistic beta and ϕ_0 are values for the synchronous particle. Following the treatment in [35], these equations for small $\Delta t \ll T_0$ (short bunches) can be written as,

$$\frac{d^2\Delta W}{dt^2} + {\omega_s}^2\Delta W = 0 \tag{2.22}$$

where

$$\omega_s = \frac{2\pi}{T_0}\sqrt{\frac{-\eta_0 quh\cos(\phi_0)}{2\pi W_0{\beta_0}^2}} \tag{2.23}$$

$f_s = \dfrac{\omega_s}{2\pi}$ is the synchrotron frequency in the longitudinal plane for bunched beams. Taking into account the canonical structure of the equations of motion Eqs. 2.21a and 2.21b, one can find the Hamiltonian for the longitudinal bunch motion which is given by,

$$H = -\frac{\eta_0}{W_0\beta_0^2}\frac{\Delta W^2}{2} - \frac{qu}{T_0}\Big(\frac{1}{\omega_{rf}}[\cos(\omega_{rf}\Delta t + \phi_0) - \cos\phi_0] + \Delta t \sin\phi_0\Big) \tag{2.24}$$

The saddle points of the Hamiltonian, with respect to ΔW and Δt represent the unstable points, which gives the equation of the separatrix. Fig. 2.4(b) shows the separatrix for the bunched beam i.e. $\phi_0 = 0$. The separatrix defines the bucket size, outside which the beam is not captured in any of the bunches and just "floats" around the whole synchrotron. These floating particles will be lost as soon as the acceleration starts.

2.1.3 Beam emittance

A beam in a synchrotron often consists of a large number of particles with randomly distributed initial phase-space coordinates. A beam is described by means of the statistical distribution of the one-particle coordinates. The general assumption is that the distributions are centred around the corresponding nominal values. The center-of-mass or the barycentre of the beam is then given by $\bar{x} = \langle x\rangle$, where the angular brackets $\langle ...\rangle$ indicate averaging over all particles in the beam. The volume in the six-dimensional phase space that is occupied by all particles is proportional to the total emittance of the beam [36, 37]. It is equal to the superposition of all single-particle ellipsoids. The projections of this phase-space ellipsoid, into the $x - x'$, $y - y'$ and $\Delta t - \Delta W$ subspaces yield the concept of horizontal, vertical and longitudinal emittance, respectively. These two-dimensional projections are conserved individually to the first order. The emittances for the single particles were already introduced in Eq. 2.11. The total emittance is defined by the particles with the largest single-particle emittances in each plane. However, this definition is often not useful especially for infinite distribution models, e.g. Gaussian distribution, where the total emittance is not even defined and a limit must be chosen. Often the emittance referring to one or two standard deviations (σ) of the distribution is considered. The 1σ beam size is given by,

$$\sigma_x = \sqrt{\langle x^2\rangle - \bar{x}^2} = \sqrt{\epsilon_{\sigma,x}\hat{\beta}_x} \tag{2.25}$$

The 1σ beam size is also often referred to as "rms beam size" where the assumption of zero mean ($\bar{x} = 0$) is implicitly made. Beams of different transverse density distributions are frequently compared by considering beams with the same transverse rms emittance, as proposed by the principle of rms equivalent beams [32]. In this way, beams with a non-linear profile are approximated by a beam with a constant transverse density. Such a beam is called K-V beam after I. M. Kapchinsky and V. V. Vladimirsky, who first studied its properties. Although K-V beams do not exist in reality, they are a useful approximation in many cases, for example in section 2.3.1 for space charge calculations. Longitudinal emittance is similarly defined. The standard deviation of the momentum distribution, σ_p, is defined as a measure for the momentum spread, and the longitudinal beam size is given by or in terms of 1σ bunch length σ_l. The concept of bunching factor is defined to account for the ratio of average current to peak current in the synchrotron for bunched beams.

2.2 Transverse bunch signals and measurement methods

Theoretical work on transverse beam signals for bunched beams with non-interacting particles is well documented in [19, 16, 51]. Here we will revisit some of the important theoretical concepts about measurement principles of beam signals. The first is the Schottky signal analysis where the inherent statistical fluctuations in the beam, due to finite number of particles, are sampled for long times using sensitive pick-ups to obtain information on the spectral content of the beam. The other method is the beam transfer function (BTF) measurement where the beam is excited using an external signal and the beam response is measured using the beam pick-ups (PU). This method allows the possibility of measuring the magnitude and phase response of the beam from which information on beam stability can be obtained. As mentioned before, a subset of BTF method is used in this work for the transverse betatron tune measurement. Thus, more details from the BTF measurement will be discussed to get a hint on the formal theoretical aspects of tune measurement in bunched beams.

Schottky signal analysis originates from the work of W. Schottky when he described spontaneous current fluctuations from DC electron beams [25]. The theory of Schottky signals induced by the beam given here, follow mostly from Ref. [19]. We will introduce the origin of the longitudinal and transversal Schottky signal for low intensity bunched beams. Important results about the properties of Schottky spectrum will be mentioned. However, theoretical interpretation in terms of propagating fluctuation modes and rigorous power calculations will be skipped in this section and can be followed in the reference aforementioned.

If $\Theta_n(t) = \omega_0 t + \theta_n \sin(\omega_s t + \psi_n^0) = \Big[\omega_0 t - \Delta\theta(t)\Big]$ represent the quasi-linear (i.e. sinusoidal orbits but with amplitude dependent synchrotron oscillation frequency $\omega_s(\theta_n)$) synchrotron oscillation of the n^{th} particle in the beam, where $\Theta_n(t)$ is the azimuthal position of n^{th} particle, θ_n is the synchrotron amplitude in radians, ω_0 is the angular revolution frequency and ψ_n^0 is the initial phase. The charge density signal is further modulated by the particle angular revolution frequencies $\omega_n = \omega_0 + \Delta\omega_n \cos[\omega_s(\theta_n)t]$. Then the longitudinal current density Schottky signal derived from a distribution of particles in a bunch, upon repeated traversals through a localized azimuth $\Theta = \Theta_P$ is given by,

$$I_n(t) = q\omega_n \sum_{m=-\infty}^{+\infty} \delta(\Theta_n(t) - \Theta_P - 2\pi m) \tag{2.26}$$

$$= \frac{q}{2\pi}\omega_n \left[\sum_{m=-\infty}^{+\infty} \exp(jm(\omega_0 t + \theta_n \sin(Q_s\omega_0 t + \psi_n^0)))\right] \tag{2.27}$$

The Fourier series representation of Eq. 2.27 is obtained for the train of delta functions in Eq. 2.26 at $\Theta = \Theta_P$ where $Q_s(\theta_n)$ is the amplitude dependent synchrotron tune of the n^{th} particle and m is the revolution frequency harmonic number. Further making use of the identity,

$$e^{jx\sin y} = \sum_{k=-\infty}^{+\infty} J_k(x)e^{jky} \tag{2.28}$$

where J_k is the ordinary Bessel's function of order k and summing over all the particles, we obtain,

$$I(t) = \sum_{n=1}^{N} I_n(t) = \sum_{n=1}^{N}\sum_{m=-\infty}^{+\infty}\sum_{k=-\infty}^{+\infty} r_{m,k}{}^{\pm}(n) \exp\Big[j\alpha_{m,k}{}^{\pm}(n)\Big] \exp\Big[j\Omega_{m,k}{}^{\pm}(n)t\Big] \tag{2.29}$$

where,

$$\Omega_{m,k}{}^{\pm}(n) = m\omega_0 + k\omega_s(\theta_n) \tag{2.30}$$

$$r_{m,k}{}^{\pm}(n) = qf_0 J_k\Big[m\theta_n\Big]\text{and} \tag{2.31}$$

$$\alpha_{m,k}{}^{\pm}(n) = (k\psi_n^0 + m\Theta_P) \tag{2.32}$$

Similarly the transverse Schottky signal of a beam is generated by the beam's dipole moment

$$d(t) = \sum_{n=1}^{N} x_n(t)I_n(t) \tag{2.33}$$

where $x_n(t)$ is the beam transverse offset and $I_n(t)$ the current of the n^{th} particle at the position of a pick-up (PU) in the ring. The sum extends over all N particles in the detector. The first term $x_n(t)$ in Eq. 2.33 denotes the transverse betatron oscillations (which modulates the particle amplitude) and the second term is $I_n(t)$ which takes the synchrotron oscillations along the beam axis into account(modulates the particle phase) as in the case of longitudinal Schottky signal. Using Eq. 2.12 and neglecting second order components, Eq. 2.33 is transformed into the following,

$$d_n(t) = a_n cos(Q_n\omega_0 t + \phi_n^0) q f_0 \left[\sum_{m=-\infty}^{+\infty} \exp(im\omega_0(t + \theta_n \sin(Q_s\omega_0 t + \psi_n^0))) \right] \tag{2.34}$$

where a_n, Q_n, ϕ_n^0 are the betatron amplitude, betatron tune and initial betatron phase of the n^{th} particle. Summing over all particles and expanding the phase modulation by using Bessel's function of first order result in,

$$d(t) = \sum_{n=1}^{N} d_n(t) = \sum_{n=1}^{N} \sum_{m=-\infty}^{+\infty} \sum_{k=-\infty}^{+\infty} r_{m,k}{}^{\pm}(n) \exp\left[j\alpha_{m,k}{}^{\pm}(n)\right] \exp\left[j\Omega_{m,k}{}^{\pm}(n)t\right] \tag{2.35}$$

where

$$\Omega_{m,k}{}^{\pm}(n) = (m \pm Q_n)\omega_0 + k\omega_s(\theta_n) \tag{2.36}$$

$$r_{m,k}{}^{\pm}(n) = q f_0 \frac{a_n}{2} J_k \left[((m \pm Q_n) - Q_n \frac{\xi}{\eta_0})\theta_n\right] \text{and} \tag{2.37}$$

$$\alpha_{m,k}{}^{\pm}(n) = (\phi_n^0 - k\psi_n^0 + m\Theta_P) \tag{2.38}$$

and ξ, η_0 are chromaticity and slippage factor respectively. The Schottky noise power spectrum as a function of the frequency f is defined as $S(f) = |D(f)|^2$ where $D(f)$ is the Fourier transformed PU signal $d(t)$. The formal transverse dipole fluctuation power spectrum can be obtained by calculating the autocorrelation of Eq. 2.35 and its Fourier transform. However it is not considered here.

As discussed above, for a bunched beam with N non interacting particles performing betatron and synchrotron oscillations, the transverse Schottky band of the equivalent "DC" beam splits into equidistant synchrotron satellites,

$$Q_{m,k} = (m \pm Q_0) + \Delta Q_k \tag{2.39}$$

where Q_0 is the machine tune, m is the harmonic number, $\Delta Q_k = \pm k Q_s$ and Q_s is the synchrotron tune. Since, we will mostly discuss baseband tune (i.e. $m = 0$), $Q_{m,k}$ is simply referred an Q_k. The relative amplitudes of the satellites are give by,

$$\mid d_k \mid \sim \mid J_k \left[((m \pm Q_0) - Q_\xi)\theta_m\right] \mid \tag{2.40}$$

where θ_m is the average longitudinal oscillation amplitude or half-bunch length (in rad) and $Q_\xi = Q_0\xi/\eta_0$ is the chromatic tune. The full bunch length $\theta_b = 2\theta_m$. J_k are the Bessel functions of order k. For any m such that $m \pm Q_0 \approx Q_\xi$ only the central line ($k = 0$) is important. It should also be noted that the length of bunch θ_b plays a major role is relative heights of synchrotron satellites. In the absence of transverse non-linear field components the width of each satellite with $k \neq 0$ is determined by the synchrotron tune spread $\delta Q_k \approx |k| Q_s \theta_b^2/64$. For a given side-band the relative amplitude of the synchrotron satellites resembles the momentum distribution in the bunch. Therefore the envelope of the Schottky power spectrum duplicates the power spectrum $S(f)$ for the equivalent coasting beam with the same rms momentum spread.

For the betatron bands, it should be noted that all the particles in the bunch are constrained to move with the same average orbital angular velocity ω_0; so the Q_0 appearing in the betatron side-band frequencies $Q_{m,k} = (m \pm Q_0) + \Delta Q_k$ is the same for all the particles, namely the tune of the nominal reference particle with angular velocity ω_0. Thus the chromaticity ξ does not appear in the observed frequencies at all. Therefore the only spread ΔQ in tune can come from the non-linear tune spread, arising from the multi-pole components of the machine. We thus see an important difference compared with continuous coasting beams, namely that as long as there is no non-linear tune spread, even a finite non-zero chromaticity, ξ does not alter the frequencies in the frequency space. The information about the machine chromaticity simply lies in the relative heights of the satellites $J_k\left[((m \pm Q_0) - Q_0\frac{\xi}{\eta_0})\theta_b/2\right]$ in the $\pm$ bands. This is the case even for high intensity beams as experimentally shown in chapter 5 of this report. For low revolution harmonics m, the fluctuation noise density of synchrotron

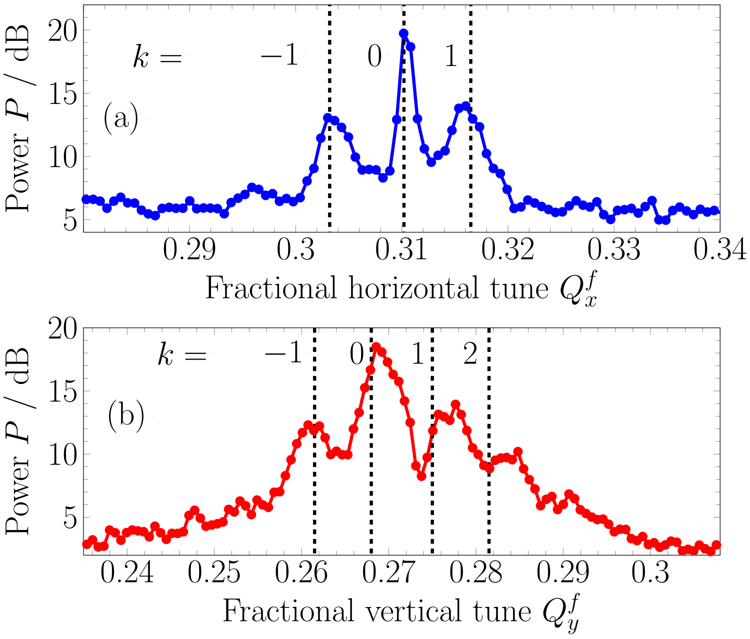

Figure 2.5: Measurement of baseband tune spectra for low intensity U^{73+} ion beams in SIS-18 for horizontal (a) and vertical (b) planes. The relative heights of $k = 0$ and 1 modes clearly indicate that the chromaticity values in vertical planes is higher compared to horizontal plane.

side-bands is enhanced by $\Gamma_k = (\omega_s/\Delta k\omega_s)$ compared with that of a continuous coasting beam, until the side-bands overlap, i.e. $\Gamma_k \leq 1$ for large m. This is so because the average power per full revolution (and betatron) band is the same for continuous and bunched beams. In the synchrotron-band overlapped region, different particles with different oscillation amplitudes generate the same frequency Ω through different synchrotron harmonics: with $\Omega = m\omega_0 + k\omega_s(\theta) = m\omega_0 + k'\omega_s(\theta')$. For still higher frequencies and hence harmonics m, even the revolution bands start to overlap, i.e. with $\Omega = m\omega_0 + k\omega_s(\theta) = n\omega_0 + k'\omega_s(\theta')$. The same holds for the betatron bands.

As we have seen, the longitudinal and transverse Schottky signals can provide a direct measurement of many beam parameters like momentum spread, betatron tune, chromaticity, synchrotron tune just by passive monitoring of the beam signals. If the transverse bunch signal is sampled with the revolution period T_0, then the positive frequency spectrum consists of only one set of lines $Q_k = Q_0 + \Delta Q_k$ due to aliasing, which is usually defined as baseband tune spectrum, where Q^f is the fractional part of the machine tune. A baseband tune spectra measurement using the BBQ system (described in chapter 3) is shown in Fig. 2.5 to highlight the relative heights of synchrotron satellites. The tune measurement systems described in this work are designed to measure only the baseband tune spectra.

A note on the unit of power spectral density (PSD) of transverse beam oscillation frequencies or tune spectra such as the one shown in Fig. 2.5 is essential. The excited transverse beam oscillations are translated by the beam pick-ups into the electrical signals which are amplified to suit the ADC range of operation. The data sampled by the ADCs is used to calculate the tune spectrum. The absolute power at each frequency is mainly a function of the excitation power, but also the beam current and the amplification chain when no normalization to the beam current is performed in the measurement system (in case of BBQ system). The absolute power spectral density is of negligible consequence to the tune measurement itself, while it would require the specification of exact measurement conditions such as the beam excitation power, beam current and signal amplification to give any extra information. Therefore, arbitrary units with the logarithmic scale (dB) are chosen for simplicity to indicate the relative power in the tune spectrum. It must be mentioned that PSD is usually given in W/Hz or dBm/Hz and that dB is not a unit of power but represents logarithmic arbitraty units (a.u.).

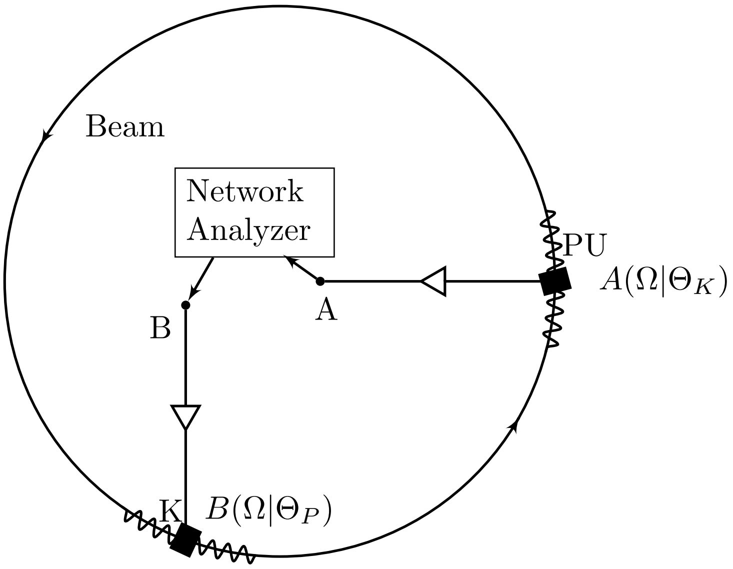

Figure 2.6: Experimental layout of a beam transfer function measurement in a synchrotron.

2.2.2 Beam transfer function measurement

In this section, we will discuss the coherent response generated in the coasting and bunched beams by an external excitation. We will briefly touch the formal considerations and assumptions in the traditional BTF theory and highlight the differences in coasting and bunched responses in longitudinal and transverse domains.

Transfer function is defined as the relation between the input and the output of a linear time-invariant system in frequency domain with zero initial conditions and zero point equilibrium. The beam transfer function is defined as the response of the beam-storage ring system to an external input or stimulus. A typical layout for the beam transfer function measurement is shown in Fig. 2.6. Small amplitude perturbing signals, applied at point B, excite the beam with an appropriate kicker K (which can be transverse, longitudinal, or both). The kicker fields introduce modulations in the beam, thus creating correlations between particles. These correlations or modulations are then propagated coherently by the beam back to the PU. The resulting PU signals are then carried back to point A. A network analyser then measures the amplitude and phase transmission from B to A. Such a beam transfer function (BTF) measurement, performed over a band of frequencies, is extremely useful since it contains information about the whole system, including its stability and phase delay properties over the band. In the measured transfer function, the extra electrical paths $B-K$ and $PU-A$, which may contain electrical elements such as amplifiers, filters, and cables are also included.

Since this work is primarily concerned with the transverse center-of-mass motion of the beam, by BTF we actually mean transverse dipolar BTF if not specified. If the beam is excited by an external signal $K(f)$ transversally and $D(f)$ is the measured dipole signal at the pick-ups, the transverse beam transfer function is defined as $R(f) = D(f)/K(f)$ [26, 38]. The tune measurement method used in this work is a subset of the classical BTF measurement principle described here. The main difference is that the excitation signal and beam response are not correlated to find the phase response (only $|D(f)|$ is measured for $|K(f)| = \text{constant}$). Basic results of the BTFs based on the detailed theory from [19] with emphasis on the bunched beams are given below.

For time-translation invariant systems (such as continuous coasting beams), excitation by a fixed frequency Ω at the kicker generates, in the linear approximation, a response at the PU at the same frequency $\Omega' = \Omega$ only. Repeating the measurement to excitations at other frequencies over the bandwidth of interest (either by single frequency sweep generators or by finite bandwidth noise generators) reveals the amplitude and phase response over the input range, indicating possible delay and stability properties. This is especially true at low frequencies, where revolution bands are separated and non-overlapping, $m\Delta\omega \leq \omega_0$, a fixed frequency Ω will only excite a single harmonic significantly, namely the harmonic satisfying the resonance condition $\Omega = m\omega(p)$. For non-overlapping bands, such a condition is satisfied by only one value of m. We can then speak of an observable response at a given harmonic m. The same is true for transverse response functions, where the concept of observable response at a given betatron harmonic $(m \pm Q_0)f_0$ is meaningful, based on whether the betatron bands overlap or not at the frequency of interest. In general, for high frequencies where revolution bands of the beam overlap, $m\Delta\omega > \omega_0$, perturbation at a fixed frequency Ω will excite a large number of harmonics m in the beam; for example, $\Omega = m\omega(p) = m'\omega(p') = ...$ (see section on Schottky signals 2.2.1) for the longitudinal response where $\omega(p) = \omega_0 + \Delta\omega(p) = \omega_0 + \eta_0\Delta p(\omega_0/p_0)$ describes the angular frequency dispersion in the continuous beam with a distribution of momentum offset Δp, and determined by the machine slip factor η_0. The response function then contains an intrinsic sum over all these excited harmonics m. Response at a given beam harmonic m is then experimentally meaningless, since it can never be isolated by a PU, although it exists theoretically.

For beams that are not invariant under time translations, perturbation at a frequency Ω will in general excite other frequencies Ω' also, including $\Omega' = \Omega$. The response of bunched beams fall into this category. Bunched beams are periodically non-stationary, i.e. it is invariant not with respect to arbitrary time translations but with respect to translations by a multiple m of the nominal revolution period $T_0 = 1/f_0 = 2\pi/\omega_0$ only, where $m = 0, \pm1, \pm2$ etc. An exciting frequency Ω at K will then generate excited frequencies at all the revolution-frequency translates of the beam: $\Omega' = \Omega + m\omega_0$, $m = 0, \pm1, \pm2, ...$ The response function, then, is not given by a single complex function at a given Ω, but by a matrix of complex functions, each element connecting response near harmonic l to an excitation near harmonic m. The analysis and measurement of the BTF of bunched beams are thus complicated compared to those for continuous beams.

In general, BTF can be measured in the response of some physical observable $\vec{A}$ of the beam due to perturbation in some other physically inducible variable $\vec{B}$ (not to be confused with magnetic flux density). The variables $\vec{A}$ and $\vec{B}$ may in general be vector quantities with components related to the two transverse dimensions and one longitudinal dimension of the beam. For example, $\vec{A}$ may be the transverse electric field excitation $\vec{E}(t)$ or the angular kick induced by the kicker $\alpha(t)$, and $\vec{B}$ is the resulting transverse dipole moment current modulation $d(t)$ at the PU. Alternatively, $\vec{B}$ may be the longitudinal voltage modulation $V(t)$ at K, and $\vec{A}$ the resulting longitudinal current modulation $I(t)$ at the PU. In a general case they may include both, which means that they are true three-component vectors $\vec{A}$ and $\vec{B}$. The response will usually be of the form

$$\vec{A} = H_{AB}\vec{B} + O(|\vec{B}|^2) + \cdots \tag{2.41}$$

For small excitation or perturbation signals $\vec{B}$ applied to the beam, we are interested in the linear response only and will neglect the higher order terms and the resultant non-linear response. In the time domain, the response matrix or tensor $\hat{H}_{AB}$ is simply a linear integral operator,

$$\vec{A}(t|\Theta_P) = \int_{-\infty}^{t} H_{AB}(t, t'|\Theta_P, \Theta_k)\vec{B}(t'|\Theta_K)dt' \tag{2.42}$$

An important assumption is that the system is stable against the disturbance $\vec{B}(t'|\Theta_K)$ and that the strength of the disturbance is sufficiently weak so that the induced quantity $\vec{A}$ may be represented by that part of the response which is linear in the disturbing field $\vec{B}$, thus guaranteeing the validity of the superposition principle embodied in Eq. 2.42. Such a representation then assumes the existence of a Green's function in the beam-storage ring system, describing the propagation characteristics of a disturbance applied at (Θ_K, t) and observed at (Θ_P, t) as an induced observable $\vec{A}$. We are also assuming that the response is "causal" which is reflected in the choice of the domain $(-\infty, t)$ for the range of t' integration in Eq. 2.42. Starting from an undisturbed state at $t = -\infty$, the quantity $\vec{A}$ is gradually induced in the beam owing to the application of the perturbation $\vec{B}$. This BTF or response function, as long as it represents a linear response relation as in Eq. 2.42, is determined solely by the properties of the beam-storage-ring system in the absence of the perturbation $\vec{B}$, i.e. by the zeroth order unperturbed trajectories and distribution of the particles in the beam. In general, the response is an integral operator in the frequency domain also, as can be seen by Fourier transform of Eq. 2.42 to the frequency space:

$$\vec{A}(\Omega|\Theta_P) = \frac{1}{2\pi}\int_{-\infty}^{\infty} \tilde{H}_{AB}(\Omega,\Omega'|\Theta_P,\Theta_K)\vec{B}(\Omega'|\Theta_K)d\Omega' \tag{2.43a}$$

$$\vec{A}(\Omega|\Theta_P) = \frac{1}{2\pi}\int_{-\infty}^{\infty} \tilde{R}_{AB}(\Omega-\Omega',\Omega'|\Theta_P,\Theta_K)\vec{B}(\Omega'|\Theta_K)d\Omega' \tag{2.43b}$$

where the equivalent response function R_{AB} is defined in time domain as,

$$R_{AB}(t,\tau|\Theta_P,\Theta_K) = R_{AB}(t,t-t'|\Theta_P,\Theta_K) = H_{AB}(t,t'|\Theta_P,\Theta_K), \qquad \tau = t-t' \tag{2.44}$$

For continuous coasting beams, the response is expected to be invariant under arbitrary time translations (τ), taking that into account and some straight forward manipulations of the various variables, Eq. 2.43a gives us,

$$\vec{A}(\Omega|\Theta_P) = \tilde{R}_{AB}(\Omega|\Theta_P,\Theta_K)\vec{B}(\Omega|\Theta_K) \tag{2.45}$$

$$\text{where } \tilde{R}_{AB}(\Omega|\Theta_P,\Theta_K) = \int_{0}^{\infty} \tilde{R}_{AB}(\tau|\Theta_P,\Theta_K)e^{j\Omega\tau}d\tau \tag{2.46}$$

and its inverse

$$\tilde{R}_{AB}(\tau|\Theta_P,\Theta_K) = \int_{C} \tilde{R}_{AB}(\Omega|\Theta_P,\Theta_K)e^{-j\Omega\tau}d\Omega \tag{2.47}$$

To make a short note on the causality (and convergence) of Eq. 2.45 and its inverse Eq. 2.47 demands that the frequency Ω be considered to have at least a small positive imaginary part $j\gamma, \gamma \to 0$. This is to guarantee the proper analytic structure in the frequency space and proper causal structure in real time for the physical response. The presence of this small imaginary part in Ω can be understood physically by imagining the perturbation at frequency Ω to have been adiabatically turned on from the infinite past, where the perturbation was zero. This is quite physical since the existence of a constant amplitude, single-frequency, sinusoidal perturbation for all time from the infinite past is rather unrealistic and we have to allow for switching on processes in order to avoid this artificial circumstance. One can also notice that the one sided Fourier transform in Eq. 2.45 in equivalent to a Laplace transform, which is exclusively studied and defined to transform such causal transform functions. A Laplace transform takes explicit account of initial conditions and causal boundary conditions for the response function defined in Eq. 2.42 for linear response. The Laplace transform variable s is set to $s = -j\Omega + \gamma$, with $\gamma \to 0^+$. The artificial introduction of $j\gamma$ is then avoided. Fig. 2.7 shows this complex frequency to Laplace conversion, and the Bromwich contour C for the inverse transformation.

The frequency response of bunched beams is uniquely different and has additional structure aside from the above considerations of analytic structure in the complex frequency space. A bunched beam interacting with the elements in the BTF measurement set-up is essentially a "sampled" system and is characterized by a non stationary time-varying response. However, the time variation is periodic, with the period being the revolution time-period of the reference synchronous particle in the bunch. Thus, it leads to a coupling of the exciting signal to the modulated output signal at all frequencies which are discrete translations of each other by multiples of the revolution frequency as follows:

$$H_{AB}(t,t'|\Theta_P,\Theta_K) = R_{AB}(t-t',t'|\Theta_P,\Theta_K) = \sum_{m=-\infty}^{\infty} R^m_{AB}(t,t-t'|\Theta_P,\Theta_K)e^{-jm\omega_0 t'} \tag{2.48a}$$

$$= \sum_{m=-\infty}^{\infty} S^m_{AB}(t,t-t'|\Theta_P,\Theta_K)e^{-jm\omega_0 t} \tag{2.48b}$$

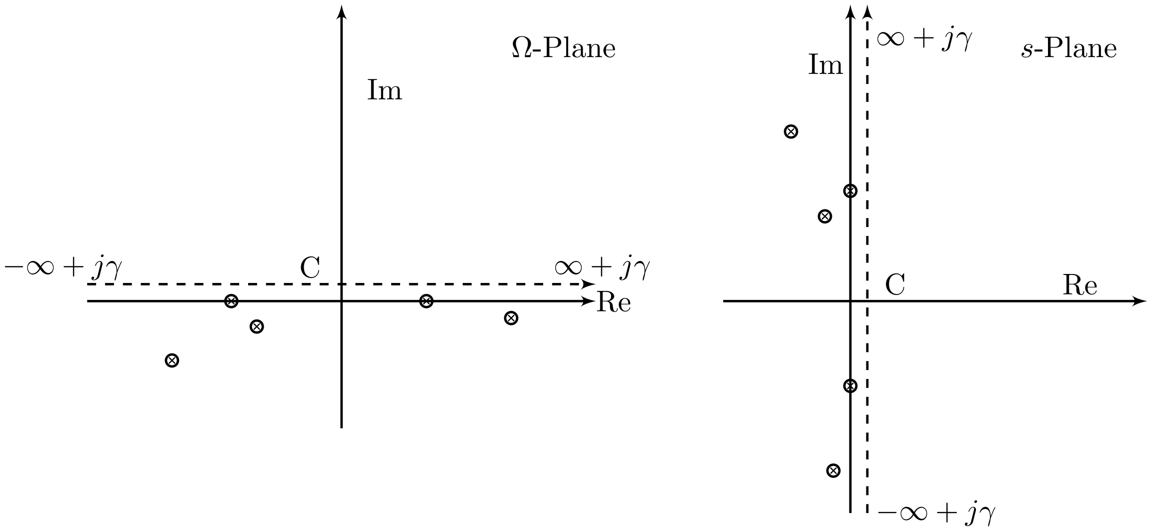

Figure 2.7: Bromwich integration contour for inverse transformation in complex frequency and Laplace domains for the beam response.

$$\tilde{H_{AB}}(\Omega, \Omega'|\Theta_P, \theta_K) = 2\pi \sum_{m=-\infty}^{\infty} \tilde{R}^m_{AB}(\Omega|\Theta_P, \Theta_K)\delta(\Omega - \Omega' - k\omega_0) \tag{2.49a}$$

$$= 2\pi \sum_{m=-\infty}^{\infty} \tilde{S}^m_{AB}(\Omega - m\omega_0|\Theta_P, \Theta_K)\delta(\Omega - \Omega' - m\omega_0) \tag{2.49b}$$

where in time domain,

$$S^m_{AB}(t, t - t'|\Theta_P, \Theta_K) = R^m_{AB}(t, t - t'|\Theta_P, \Theta_K)e^{-jm\omega_0(t-t')} \tag{2.50}$$

and in frequency domain,

$$\tilde{S}^m_{AB}(\Omega|\Theta_P, \Theta_K) = \tilde{R}^m_{AB}(\Omega + m\omega_0|\Theta_P, \Theta_K) \tag{2.51}$$

This leads to coupling of all the excitation signals to the modulated output signals at all frequencies which are discrete translations of each other by multiples of revolution frequency. The description is valid for both longitudinal and transverse planes. Often the excitation is applied at the single frequency Ω, given by $\vec{B}(\Omega|\Theta_K)$, one can find that the response is not only generated at the PU at the frequency Ω but also at the frequencies $\Omega + m\omega_0$ where $m = \pm 1, \pm 2, ...$ and is given by,

$$\vec{A}(\Omega + m\omega_0|\Theta_P) = \tilde{R}^m_{AB}(\Omega + m\omega_0|\Theta_P, \Theta_K)\vec{B}(\Omega|\Theta_K) \tag{2.52a}$$

$$= \tilde{S}^m_{AB}(\Omega|\Theta_P, \Theta_K)\vec{B}(\Omega|\Theta_K) \tag{2.52b}$$

Thus the response of the periodically time varying bunched-beam-storage-ring system can be characterized by the block-diagrammatic representation of Fig. 2.8 as an expansion in a parallel-series combination of a set of time invariant elements $\tilde{R}^m_{AB}(\Omega + m\omega_0|\Theta_P, \Theta_K) = \tilde{S}^m_{AB}(\Omega|\Theta_P, \Theta_K)$, each one modulated by sinusoidally time varying gains $e^{im\omega_0 t}$, the parallel branches ranging in $m = \infty, .., -1, 0, 1, ..., \infty$.

As in the case of coasting beams, the values considered for complex Ω, are analytic on the upper half plane $Im(\omega) > 0$, and all the considerations of analytic structure in the complex Ω plane elaborated before for time invariant beam

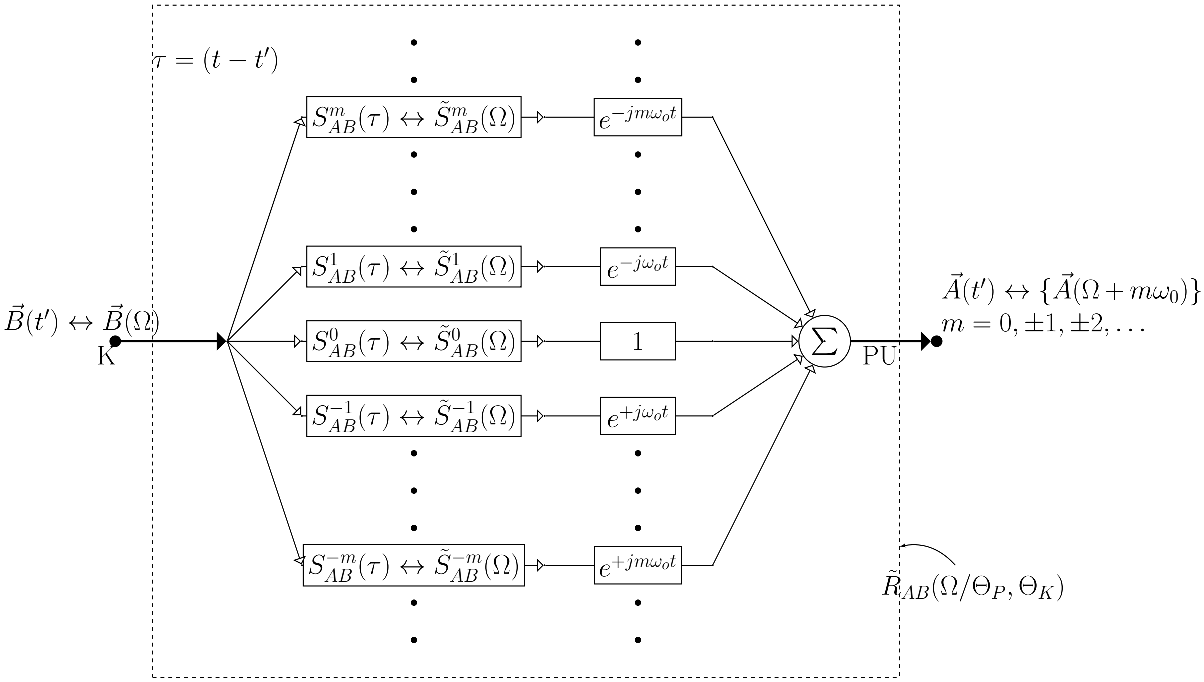

Figure 2.8: Feedback loop description for the beam transfer function of a bunched beam. The symbol ($\leftrightarrow$) corresponds to Fourier transform.

response (coasting beam case), now apply to each of the individual components $\tilde{S}^m_{AB}(\Omega|\Theta_P, \Theta_K)$for $m = 0, \pm 1, \pm 2$, etc., separately for bunched beams.

The coherent beam transfer function measurement is an important diagnostic tool also for estimating single-particle and collective effects, since it contains information about the beam-storage-ring impedance, the beam phase space distribution, and the incoherent and coherent frequencies of the whole system. The knowledge of the response properties of the beam is crucial for estimating the appropriate collective effect, be it the growth rate of a collective mode or the distortion of fluctuation signals, etc. The response also contains critical information about other aspects such as Landau damping and wave regeneration properties of the charged-particle beam [19]. Some of these aspects will be highligted again in chapter 5 where tune measurement results are discussed.

2.2.3 Relation of tune measurement with transverse Schottky and BTF measurement

Now that we have the description of both classical transverse signal measurement methods, the relation of these methods and a classical tune measurement system requires brief comments.

- In absence of collective effects (i.e. inter-particle interaction and beam-surrounding interaction) and small excitation, the tune measurement system and BTF magnitude response should give identical results in comparison with the Schottky measurements albeit with higher signal-to-noise ratio due to the correlations induced between the particles.
- As long as the amplitude of excitation in small enough, the tune measurement is a BTF measurement without the phase response. Excitation types like the frequency sweep and band-limited noise normally would fulfil this requirement. However a kick excitation significantly displaces the beam and the superposition principle, used in the whole section 2.42, is not strictly valid.
- In presence of collective effects dominated by inter-particle interaction, the incoherent frequencies of the particles change based on their relative position and momentum. In this case the Schottky and BTF spectrum

are not expected to be identical. The differences should be in principle a function of kick excitation strength. However, the self-consistent simulations for Schottky signals have predicted the results of the tune measurements for bunched beams in presence of collective effects quite well [22]. Further work have to be done to compare the Schottky and the BTF signals for bunched beams taking collective effects into account.

- Collective effects also may lead to instabilities, when the description, given above, breaks down, and the coherent response will be dominated by most unstable modes irrespective of the measurement method.

Major efforts are being made to extend the low intensity results to high intensity cases when collective effects strongly influence the beam signals [39]. Lately, lot of simulation work has been performed to better understand the influence of collective effects on the beam signals [27, 39].

2.3 Collective effects

With increase in beam intensity, the electromagnetic "self-fields" of the beam exerts an increasing force on each particle in the beam as well as interacts with the environment. The nature of the self-fields depend on the distribution of the particles and the beam environment. Electromagnetic interactions that are present in a beam only due to its distribution while neglecting its environment are called space-charge effects and are discussed in 2.3.1. However, particle beams in accelerators are always surrounded by materials which modify the boundary conditions for the self-fields. The impact of the beam environment on the beam is described with the concept of wake fields and impedances [40, 41], these effects are discussed in 2.3.2. The effects of space charge and impedances on the transverse beam signals of a weakly relativistic beam, such that $\beta \ll 1$ in a synchrotron will be discussed in the rest of this section.

2.3.1 Space charge and incoherent tune shifts

Space-charge effects are understood as the result of the interaction between the self-field, i.e. the field originating solely from the particles belonging to the beam, independently of the environment. Since particles with the same sign repel each other, the space-charge force is defocusing in both planes. However, this force is suppressed with increasing beam energy due to the Lorentz transformation. This effect can also be interpreted as a consequence of the force, balancing by the attractive force between the parallel currents represented by the particles with increasing γ. Thus space charge is most important at low energy (injection energy in case of a synchrotron). The space-charge force is different for each particle because it depends on the particle's position with respect to the barycentre of the beam. Furthermore, the force depends on the non-linear transverse particle distribution and is consequently non-linear, too. Unfortunately, a detailed analysis of the non-linear space-charge effects is quite involved. Therefore, simplified models are sought for the analysis of the data from measurements as long as they reflect the essential features of space charge. As a first simplification, we assume that we have a K-V beam (introduced in subsection 2.1.3). Such a beam is favourable for the modelling because it features a linear space-charge force. This approximation is justified only if the space-charge force is weak enough to neglect the non-linear components. The second major simplification used is called rigid beam assumption. A beam is said to oscillate rigidly if its cross-section is not altered by the oscillation. It is only under this condition that the particle density is constant in time or with respect to s. Further commentary on these assumptions is given in [42].

Figure 2.9 shows a homogeneous elliptical K-V beam with an arbitrary offset $\bar{x}$ and a test particle at x_j. Following the treatment in [21], if we apply Maxwell's equations to such a beam, it yields the expression for incoherent tune shift ΔQ_{sc} for each particle,

$$\Delta Q_{sc} = \frac{q I_p R}{2\pi\epsilon_0 c W_0 {\gamma_0}^2 \beta_0^3 \left(\epsilon_x + \sqrt{\epsilon_x \epsilon_y \frac{Q_{x0}}{Q_{y0}}}\right)} \tag{2.53}$$

where I_p is the bunch peak current, q the particle charge and $W_0 = \gamma_0 m_0 c^2$ the energy. The relativistic parameters are γ_0 and β_0, the ring radius is R and the emittance of the rms equivalent K-V distribution is ϵ_x (which is equivalent to 2σ emittance of a gaussian beam profile). For the vertical plane the procedure is the same, with x replaced by y.

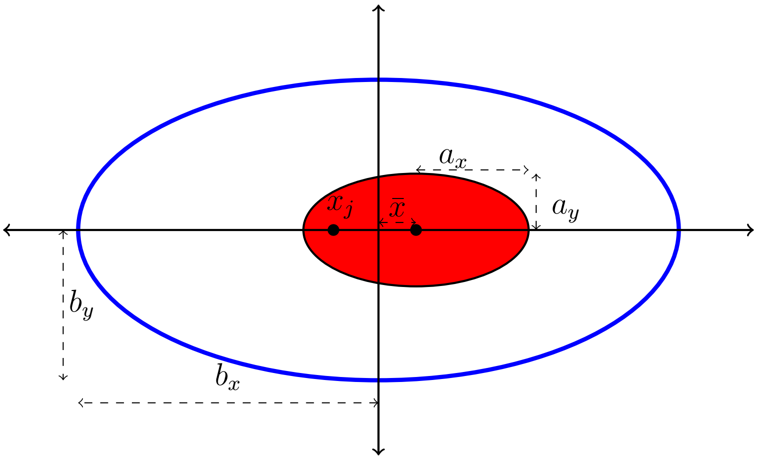

Figure 2.9: The schematic description of an elliptical beam pipe, and a horizontally displaced beam.

2.3.2 Transverse impedances and coherent tune shift

In the previous section, we studied the direct field interaction of various particles in the beam under some assumptions. The self-field of the beam is also influenced by the beam environment. Quantitatively this effect is described with (coupling) impedances. In this work only dipolar transverse impedances are considered. These impedances deflect the beam. Higher order impedances, which may for instance focus the beam, are disregarded. Let $\vec{E}$ be the electric and $\vec{B}$ the magnetic field produced by the interaction of a beam with the current dipole-moment $I_p\bar{x}$ with the surrounding accelerator components. The transverse impedance of an accelerator component of length L_d is defined by the integral [18].

$$Z_\perp(\omega) = -\frac{j}{\beta_0 I_p \bar{x}} \int_0^{L_d} \left[\vec{E}(s,\omega) + \vec{v} \times \vec{B}(s,\omega)\right]_T ds \tag{2.54}$$

The assessment of impedances is an area of active research at many accelerator facilities including at GSI e.g. for FAIR devices [43]. For devices with a complicated geometry, numerical simulations have to be performed. The most simple and relevant example of an impedance is that of a perfectly conducting beam pipe. The beam pipe contributes strongly to the total impedance of an accelerator because it surrounds the beam almost along its entire length and especially important for low frequency measurements. For an elliptical pipe of a perfectly conducting material and of radii $b_{x,y}$, as sketched in Fig. 2.9, the purely imaginary impedance is given by

$$Z_{\perp,x} = -j\frac{Z_0 \xi_{ff}}{2\pi(\beta_0\gamma_0 b_x)^2} \tag{2.55}$$

where Z_0 is the characteristic impedance of vacuum, and ξ_{ff} is a form factor based on exact shape and surroundings of beam pipe and falls under the framework of Laslett's coefficients [20]. For the vertical plane the procedure is the same, with x replaced by y. This impedance is purely reactive because the resistivity is neglected. The fact that it is independent of the frequency is a peculiarity of the perfectly conducting beam pipe. Taking the finite resistivity of the beam pipe into account gives an impedance with a real part, and complicates the evaluation significantly. This is not important for the work here, however [43] and references therein discuss these calculations in detail.

The imaginary impedances cause a real shift of the frequency of the coherent beam oscillation, referred as coherent tune shift. For the perfectly conducting beam pipe, whose impedance is given in Eq. 2.55, the coherent tune shift is given by,

$$\Delta Q_{c,x} = -j\frac{q I_p R^2 Z_{\perp,x}}{2 Q_{x0} \beta_0 W_0} \tag{2.56}$$

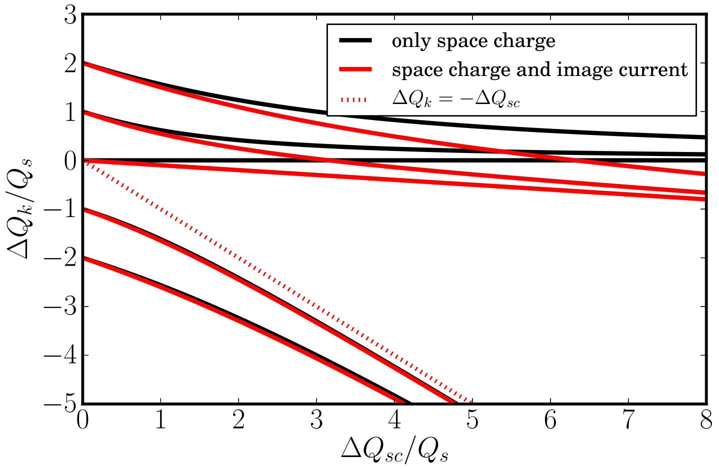

Figure 2.10: Head-tail mode frequencies as a function of the space charge parameter. The red curves represent the result obtained for $q_c = 0.1 q_{sc}$.

In case the impedances are not only given by Eq. 2.55 but have a real part, there is a corresponding imaginary part in coherent tune shift. The real part of impedance can lead to an exponential growth or damping of the beam oscillations depending on its sign and the growth or decay rate is given by the magnitude.

2.3.3 Head-tail modes with space charge and image currents

In the presence of incoherent space charge, represented by the tune shift ΔQ_{sc} or image currents effects, represented by a real coherent tune shift ΔQ_c, the shift of the Schottky satellites in bunches can be reproduced rather well by [39],

$$\Delta Q_k = -\frac{\Delta Q_{sc} + \Delta Q_c}{2} \pm \sqrt{(\Delta Q_{sc} - \Delta Q_c)^2/4 + (kQ_s)^2} \tag{2.57}$$

where the + is used for $k > 0$. For $k = 0$ one obtains $\Delta Q_{k=0} = -\Delta Q_c$. These satellites in the above expression are referred as the head-tail eigenmodes of the order k for an airbag bunch distribution in a barrier potential [44] with the eigenfunctions

$$\bar{x}_k(\theta) = \cos(k\pi\Delta\theta/\theta_b)\exp(-j\chi\Delta\theta/\theta_b) \tag{2.58}$$

where $\bar{x}_k$ is the local transverse bunch offset of the k^{th} mode, $\chi = \xi\theta_b/\eta_0$ is the chromatic phase, θ_b is the full bunch length and η_0 is the slip factor. The airbag model is given by a constant transverse charge density (K-V distribution), square well potential and longitudinal momentum distribution give by $f(p) = \delta(p - p_0) + \delta(p + p_0)$ and is further discussed in [44]. Figure 2.11 shows the eigen-functions for some example values of chromaticity.

The head-tail mode frequencies obtained from Eq. 2.57 are shown in Fig. 2.10. In Ref. [44] the analytic solution for the eigenvalues Eq. 2.57 is obtained using a simplified approach, where the transverse space charge force is assumed to be constant for all particles (K-V beam). This assumption is correct if there are only dipolar oscillations. In Ref. [39] Eq. 2.57 has been successfully compared to Schottky spectra, obtained from 3-D self-consistent simulations for realistic bunch distributions in rf buckets. Analytic and numerical solutions for Gaussian and other bunch distribution were also presented in [45, 46].

In an rf bucket the synchrotron tune Q_s is a function of the synchrotron oscillation amplitude. For short bunches Q_s corresponds to the small-amplitude synchrotron tune

$$Q_{s0}^2 = \frac{quh|\eta_0|}{2\pi m_0\gamma_0\beta_0^2 c^2} \tag{2.59}$$

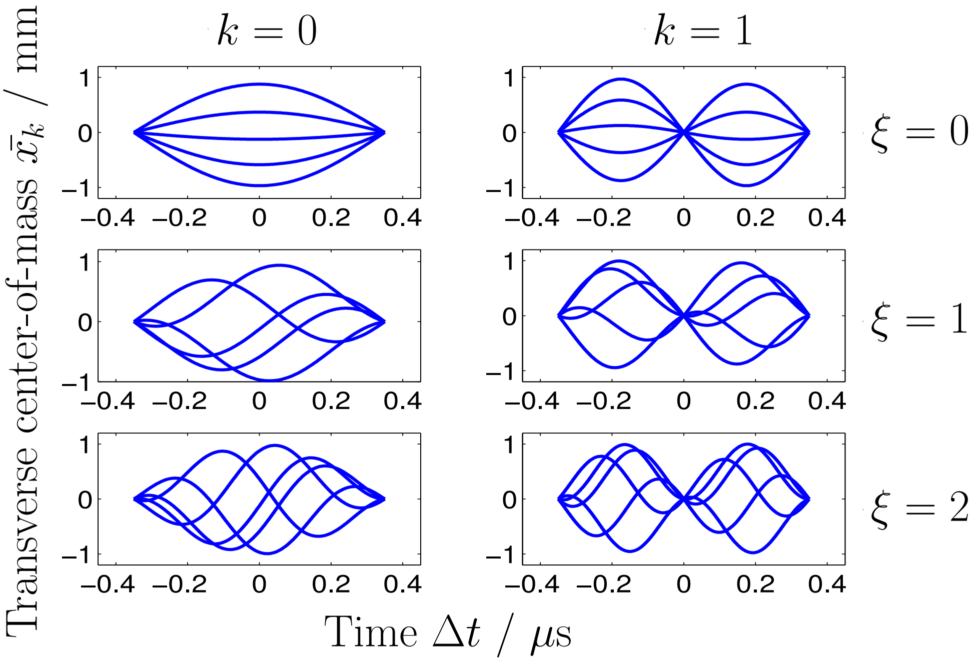

Figure 2.11: The transverse center-of-mass for head-tail modes of the order $k = 0$ and $k = 1$ for chromaticity values $\xi = 0, -1, -2$. Chromaticity at SIS-18 is measured by excitation of these modes as shown in Fig. 5.17a.

where u is the rf voltage amplitude and h is the rf harmonic number. For head-tail modes, the space charge parameter is defined as a ratio of the space-charge tune shift (Eq. 2.53) to the small-amplitude synchrotron tune,

$$q_{sc} = \frac{|\Delta Q_{sc}|}{Q_{s0}} \tag{2.60}$$

and the image current parameter as

$$q_c = \frac{|\Delta Q_c|}{Q_{s0}} \tag{2.61}$$

An important parameter for head-tail bunch oscillations in long bunches is the effective synchrotron frequency which will be different from the small-amplitude synchrotron frequency in short bunches. For an elliptic bunch distribution (parabolic bunch profile) with the bunch length $\theta_b = \sqrt{10}\sigma_l$ (rms bunch length σ_l), one obtains the approximate analytic expression for the longitudinal dipole tune [52],

$$\frac{Q_{s1}}{Q_{s0}} = \sqrt{1 - \frac{\sigma_l^2}{2}} \tag{2.62}$$

Using Q_{s1} instead of Q_{s0} in Eq. 2.57 shows a much better agreement with the simulation spectra for long bunches in rf buckets.

For Gaussian bunches with a bunching factor $B_f = 0.3$ ($B_f = I_0/I_p$, I_0 is the DC current and I_p is the peak current), the transverse tune spectra obtained from PATRIC simulations [39] for different space charge factors and thin beams ($q_c = 0$) are shown in Fig. 2.12. The dotted vertical lines indicate the positions of the head-tail tune shifts, obtained from Eq. 2.57 with $Q_s = Q_{s1}$. For the low-k satellites there is a good agreement between Eq. 2.57 and the simulation results. Peaks with $k > 2$ can barely be identified in the simulation spectra. The positions of the satellites for $k = 0, 1$ and 2 together with the predicted head-tail tune shifts from Eq. 2.57 are shown in Fig. 2.13. The error bars indicate the obtained widths of the peaks in the tune spectra.

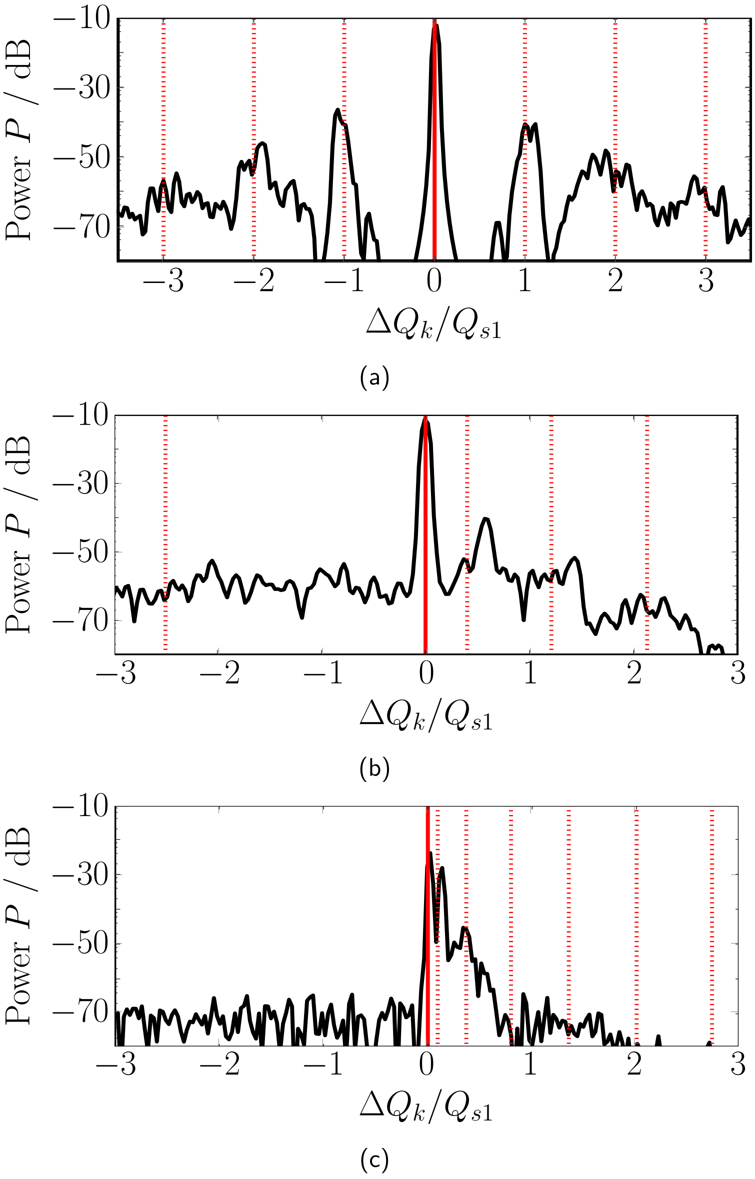

(a)

(b)

(c)

Figure 2.12: Tune spectrum obtained from the simulation for $q_{sc} = 0$ (a),2 (b) and 10 (c) at $q_c = 0$. The dotted vertical lines indicate the positions of the head-tail tune shifts obtained from Eq. 2.57. Simulations by [55].

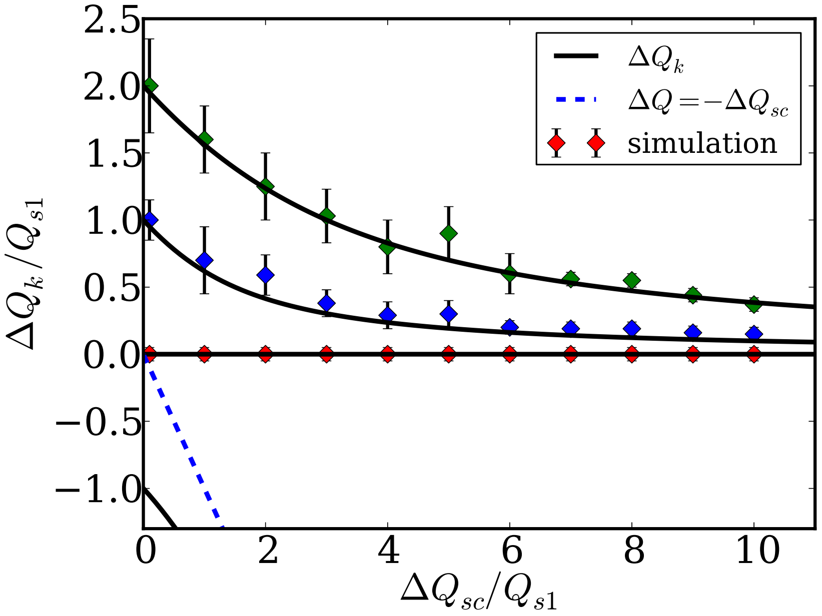

Figure 2.13: Head-tail tune shifts and their width obtained from the simulations for $q_c = 0$. The error bars indicate the widths of the lines. Simulations by [55].

It is important to notice that the simulations for moderate space charge parameters ($q_{sc} \lesssim 10$) require a 2.5D self-consistent space charge solver. The theoretical studies rely on the solution of the Möhl-Schonauer equation [50], which assumes a constant space charge tune shift for all transverse particle amplitudes. In PATRIC simulation tool [39], one can chose between a fully self-consistent 2.5D space charge solver and a rigid slice model, which corresponds to the Möhl-Schönauer equation. The PATRIC simulation studies using the Möhl-Schönauer model gave tune spectra with pronounced, thin satellites also for large k, in contrary to the PATRIC results obtained using the self-consistent model. In order to account for the intrinsic damping of head-tail modes [45, 46, 47], which is the main cause of the peak widths obtained from the simulations, a self-consistent treatment is required.

For thick beams (here $q_c = 0.15q_{sc}$, which corresponds to the conditions at injection in the SIS-18) the positions of the synchrotron satellites, obtained from the simulations, are indicated in Fig. 2.14. Again, the error bars indicate the widths of the peaks. From the plot we notice an increase in the spacing between the $k = 0, 1, 2$ satellites, relative to the analytic expression. Also the peak width for $k = 1, 2$ does not shrink with increasing q_{sc}.

The tune spectra obtained for $q_{sc} = 3$, $q_{sc} = 5$ and $q_{sc} = 10$ are shown in Fig. 2.15. One can observe that for thick beams (here $a \approx 0.4b$) the $k = 1$ peak remains very broad up to $q_{sc} = 10$.

2.3.4 Space charge induced damping of head-tail modes

The width of the peaks in the tune spectrum is directly related to the Landau damping rate of the respective head-tail mode. At low intensities and in the absence of transverse non-linear field components, the width of each satellite with $k \neq 0$ is determined by the synchrotron tune spread $\delta Q_k \approx |k|Q_s\theta_m^2/16$. In intense bunches, Landau damping arises due to the tune spread caused by the variation of the transverse space charge tune shift along the bunch. This intrinsic Landau damping has been analysed in previous studies using analytical as well as simulation models (see Refs. [45, 46, 47]).

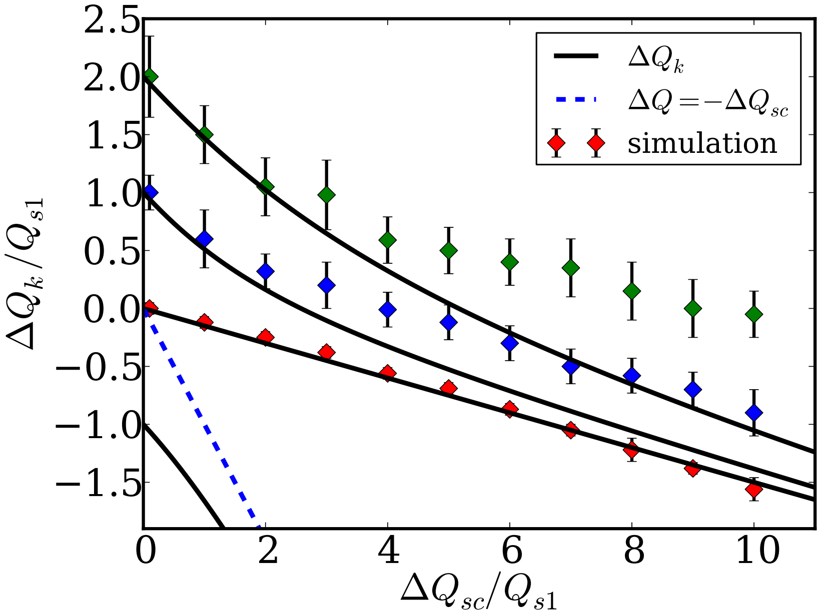

Figure 2.14: Head-tail tune shifts and their width obtained from the simulations for $q_c = 0.15q_{sc}$. The error bars indicate the widths of the peaks. Simulations by [55].

In Ref. [47] it has been shown that there is a distinctive upper q_{sc} threshold for every k. Above this threshold Landau damping is lost. For low k's, the threshold in q_{sc} is also lower. In the following we will present simplified expressions for this threshold, including the effect of the coherent tune shift due to image currents. For a Gaussian bunch profile, the maximum incoherent tune shift, including the modulation due to the synchrotron oscillation is

$$\Delta Q_{\max} = -\Delta Q_{sc} + kQ_s \tag{2.63}$$

where ΔQ_{sc} is determined by Eq. 2.53. The minimum space charge tune shift is (see Refs. [46, 47])

$$\Delta Q_{\min} = -\alpha_{sc} q_{sc} Q_s + kQ_s \tag{2.64}$$

where α_{sc} is determined from the average of the space charge tune shift along a synchrotron oscillation with the amplitude θ_m. For a parabolic bunch we obtain $\alpha_{sc} = 0.5$. For a Gaussian bunch and bunch half-length $\theta_m = 3\sigma_l$, we obtain $\alpha_{sc} = 0.287$. Each band of the incoherent transverse spectrum has a lower boundary determined by the maximum tune shift $\Delta Q_{\max}$ and an upper boundary determined by $\Delta Q_{\min}$. Landau damping, in its very approximate treatment, requires an overlap of the coherent line with the incoherent band. The head-tail tune for low q_{sc} can be approximated as

$$\Delta Q_k = -\frac{1}{2}\left(\Delta Q_{sc} + \Delta Q_c\right) + kQ_s \tag{2.65}$$

The distance between the coherent line and the upper boundary of the incoherent band for fixed k is

$$\delta Q_k = \left(\frac{1}{2} - \alpha_{sc}\right)\Delta Q_{sc} + \frac{1}{2}\Delta Q_c \tag{2.66}$$

For large q_{sc} the head-tail modes with positive k converge towards $Q_k = -\Delta Q_c/2$. For a given k the mode is still inside the incoherent band if

$$k \gtrsim \alpha_{sc} q_{sc} - \frac{1}{2} q_c \tag{2.67}$$

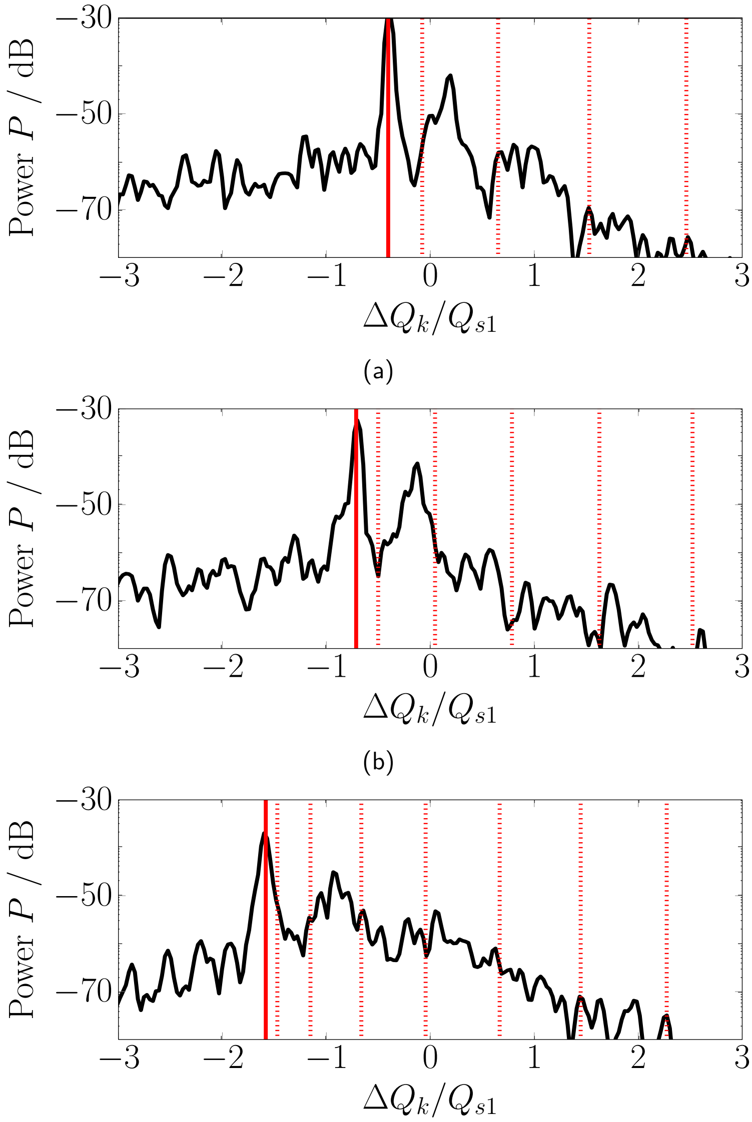

(a)

(b)

(c)

Figure 2.15: Tune spectrum obtained from the simulation for $q_{sc} = 3$ (a), 5 (b), 10 (c) at $q_c = 0.15q_{sc}$. The dotted vertical lines indicate the positions of the head-tail tune shifts obtained from Eq. 2.57. Simulations by [55].

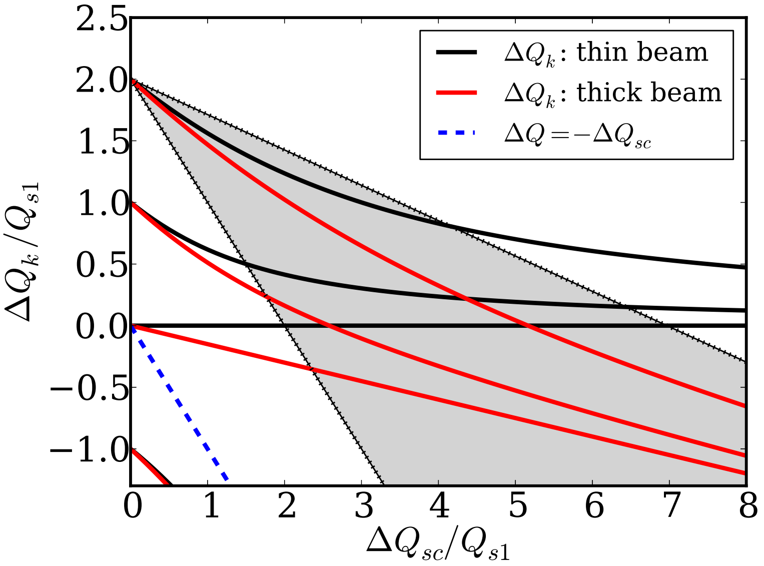

Figure 2.16: Head-tail mode frequencies as a function of the space charge parameter. The grey shaded area indicates the incoherent band for a Gaussian bunch and $k = 2$. The red curves represent the head-tail mode frequencies obtained for $q_c = 0.15q_{sc}$.

holds. In order to illustrate the above analysis the incoherent band for $k = 2$ is shown in Fig. 2.16 (shaded area). For $q_c = 0$ the coherent head-tail mode frequency crosses the upper boundary of the band at $q_{sc} \approx 4.5$. For $q_c = 0.15q_{sc}$ the head-tail mode remains inside the band until $q_{sc} \approx 12$. Similarly for the $k = 1$ modes the above analysis leads to threshold of $q_{sc} \approx 2$ for $q_c = 0$ (thin beams) and $q_{sc} \approx 6$ for $q_c = 0.15q_{sc}$. It is also worth to notice that for $q_c \gtrsim \alpha_{sc}q_{sc}$ (with $\alpha_{sc} = 0.287$ for Gaussian bunches) the $k = 0$ mode should be Landau damped.

The strongly enhanced Landau damping in thick beams can also serve as an explanation for the deviations of the $k = 1, 2$ head-tail tune shifts obtained from the simulations (shown in Fig. 2.14) and the predictions by Eq. 2.57. The theoretical model underlying Eq. 2.57 does not account for Landau damping. Within a more accurate approach the eigenvalues should be obtained from a dispersion relation including the real and the imaginary parts of the head-tail eigenfrequencies.

It is important to point out that the negative head-tail modes ($k < 0$) always reside inside the incoherent band. Therefore they can be neglected for strong space charge ($q_{sc} \gtrsim 1$). In addition it was pointed out in Ref. [39] that for strong space charge the negative-k head-tail modes develop a dominant envelope oscillation amplitude.

2.3.5 Modification of tune spectra at high intensity

Figure 2.17 summarizes the relevant effects developed in this section on the experimental observable i.e. tune spectra. It shows the gradual modification of the low intensity tune spectra due to space charge, image current and Landau damping of negative modes at $q_{sc} \approx 1, 4$. The major observations are,

- There is a downward shift of the whole spectra due to image current induced coherent tune shift.
- The distance between $k = 0$ and $k = 1$ modes decrease as a function of space charge parameter in accordance to Eq. 2.57.
- The relative heights of head-tail modes are given by the machine chromaticity.
- Intrinsic Landau damping of negative modes at high q_{sc}.

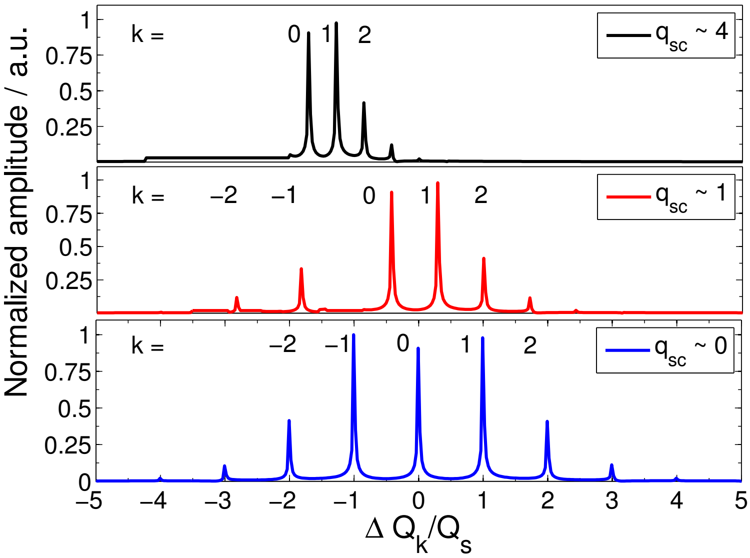

Figure 2.17: Schematic showing qualitative transformation of low intensity tune spectra into the high intensity tune spectra as a function of the space charge parameter. The relative heights of the modes are calculated for the nominal vertical chromaticity values at SIS-18.

- Due to damping of negative modes, a beating will be observed in the beam position envelope with the time scale given by the difference of the frequencies of neighbouring excited modes. If $f_{k,0}$ and $f_{k,1}$ is the frequency of the excited modes $k = 0, 1$, then $t_{beat} = \dfrac{1}{f_{k,0} - f_{k,1}}$. This observation is also presented in [56, 49].

2.4 Summary

1. Basic concepts of single particle beam dynamics in a synchrotron are revisited.
2. Basic theory of Schottky and BTF measurements are described in view of interpretation of the measurement results in this work.
3. Important collective effects in a high intensity bunched beam are discussed.
4. Modification of tune spectra due to mentioned collective effects are qualitatively demonstrated and supported by simulation results.

3 Tune Measurement Systems

GSI SIS-18 has two parallel tune measurement systems installed presently. The first is called the Tune, Orbit and POSition measurement system (TOPOS) which relies on digital processing of the BPM data to obtain bunch-by-bunch position and betatron tune from it. The other system is known as Base Band Tune (Q) measurement system (BBQ) which is a dedicated tune measurement hardware conceived at CERN-Beam Instrumentation. The prototype installed at SIS-18 is similar to the ones installed at PSB and LEIR machines at CERN. The beam is excited for reliable tune measurements during the whole acceleration cycle at SIS-18. Thus, a separate subsystem for beam excitation system, which is used by both tune measurement systems, is under operation at SIS-18. First, the beam excitation system and the beam excitation signals will be discussed. This will be followed by the detailed description of both tune measurement systems. The chapter will end with a comparison of both of these systems.

3.1 Beam excitation system

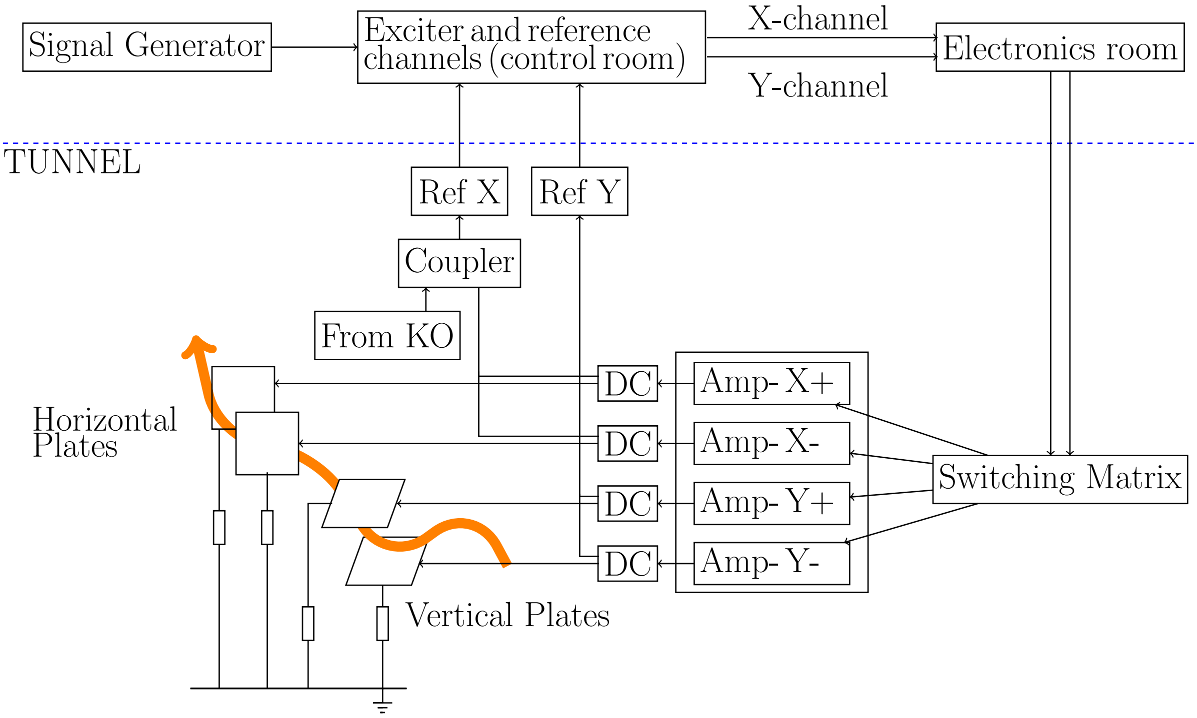

Figure 3.1: Beam excitation signal chain from the control room and back showing all the major components.

The full schematic of the beam excitation system is shown in Fig. 3.1. It is also referred to as the BTF excitation in the control system. It consists of a signal generator, whose output can be fed to either/both of the exciter ports for x and y plane in the control room. The excitation scheme is identical for both planes, so we will refer only to the x plane for conciseness of the notations. The signal for each plane is routed via electronics room to the SIS-18 tunnel where it is fed to a hybrid switch, which generates the original signal and its instantaneous inverse. These signals are further fed to two identical 25 W, 50 dB fixed power amplifiers. The output of the amplifier is supplied via the main output of the 40 : 1 dB directional coupler (marked as DC) to the two strip-line plates each terminated downstream with a 50 Ω resistor. The minor output of the directional coupler is sent back to the control room as

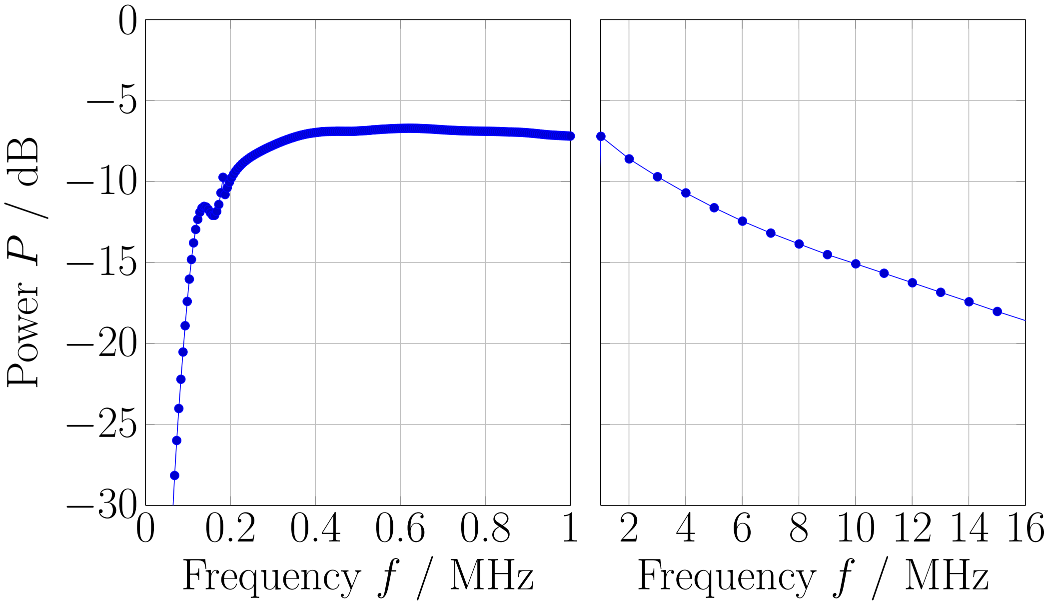

Figure 3.2: The frequency response of the beam exciter system measured using frequency sweep utility of the network analyzer.

the reference signal. These reference signals give information on the cable and amplifier responses, and can be used to calculate the phase response of the beam. The present limitation for exciter plates in the x plane is that they are used in a switch mode for both of the described modes, BTF excitation mode and the knock-out excitation mode for slow extraction. This has to be correctly specified in the control system. This section discusses the motivation and types of beam excitations used in this dossier. Figure 3.2 shows the measured frequency response of the excitation chain using an Agilent E5071C ENA® series network analyzer by sweeping the frequency ranging from 9 kHz to 20 MHz [57].

3.1.1 Signal generator

Traditionally a kick excitation (Q Kicker) was used at GSI SIS-18 to measure betatron tune. However a short-term excitation, e.g. by a fast kicker magnet, leads to a decoherence of beam centroid after a few 100 turns due to beam momentum spread and any transverse variation of the beam centroid is no longer measurable. Moreover, since the kick type beam excitation causes an increase in the beam emittance, it cannot be used for regular operations. In addition, from Chapter 2 we concluded that the beam excitation should be as small as possible such that the original BTF of unperturbed beam is not significantly modified.

In principle a white noise excitation can be applied to the beam, and the beam will respond on its resonances (mainly betatron tune frequency) throughout the acceleration cycle. However, using this procedure, most of the applied power is not utilized, and only a fraction of it will lead to a coherent response by the beam. Since an approximate value of betatron tune is known from optics settings, a band limited noise can be applied, which provides a more efficient beam excitation. An efficient excitation is especially important at higher energies where the beam is more rigid and higher power is required to induce sufficient oscillation amplitudes. The beam oscillation amplitude is directly proportional to signal-to-noise ratio of the tune spectrum and thus to the reliability of the measurement. Two alternatives to a simple white noise beam excitation, namely the band limited noise excitation and the frequency sweep, were extensively used in course of this work.

The idea of band limited noise excitation emerged when the advanced methods for transversal knock-out extraction (RF-KO) were being developed in HIMAC, Japan and at GSI [63, 64]. After its successful operation for knock-out extraction, a similar excitation system was built for application in tune measurements (for both transverse planes). The main difference between a KO excitation system and a BTF excitation system is the power requirement. The power required for tune measurement is much less compared to that for beam extraction, thus the power amplifiers of lower ratings were installed when compared to the RF-KO amplifiers [63].

The generation of this signal is done in the following way; the RF f_{rf} is transformed to the reference revolution frequency f_0 by a frequency divider. Then the revolution frequency ($f_0 = f_{rf}/h$) is mixed with the Direct Digital Synthesis (DDS) generated fractional tune frequency $(Q - \left[Q\right]) \cdot f_0 = Q^f \cdot f_0$, and we obtain a spectra with the power distributed in the following frequencies,

$$f_c = (m + Q - \left[Q\right]) \cdot f_0 \tag{3.1}$$

where $m = 0, \pm 1, \cdots$ and $\left[Q\right]$ is the integer part of the tune. The resulting carrier signal f_c also contains higher order harmonics ($m \neq 0$) due to technical realization of the division and mixing process [63]. The carrier signal is further modulated by a pseudo random sequence resulting in a band limited noise signal (source) around the tune frequency. Let the random sequence $X_b(t)$ be modelled by a random binary waveform $[0, \pi]$ which toggles or remains the same every t_t seconds. The interval t_t is defined by the required bandwidth around the signal to be modulated. So, the noise signal is

$$N(t) = A\cos(2\pi f_c t + X_b(t)) \tag{3.2}$$

$$N(t) = \cos(2\pi f_c t) \cdot Y(t) \tag{3.3}$$

where $Y(t)$ is a random binary waveform with two values $\pm A$ which toggles or remains same with equal probability every t_t seconds. Figure 3.3 shows the $Y(t)$ and corresponding $N(t)$. Taking a Fourier transform of Eq. 3.2, we obtain,

$$N(f) = \delta(f \pm f_c) * Y(f) = Y(f \pm f_c) \tag{3.4}$$

Calculation of PSD of a binary random process $|Y(f)|^2$ is closely followed from [92].

$$|Y(f)|^2 = A^2 t_t^2 |\text{sinc}(f t_t)|^2 \tag{3.5}$$

where $sinc(x) = \frac{\sin \pi x}{\pi x}$. It is clear from the Eq. 3.5 that the width of the main lobe of the *sinc* function in the frequency domain is inversely proportional to the time t_t. This result is utilized in creating a tunable band limited noise simply by changing the frequency of the pseudo-random binary waveform $Y(t)$. This has been highlighted in Fig. 3.3. Using Eq. 3.4, we obtain the PSD of the pseudo random noise,

$$|N(f)|^2 = a_{nf} \left[\frac{\sin(\pi(f \pm f_c)t_t}{\pi(f \pm f_c)t_t)}\right]^2 \tag{3.6}$$

Here a_{nf} is a normalization factor. A typical frequency spectrum of the noise applied to the beam spectrum is shown in Fig. 3.4. It shows the variation of the carrier frequency f_c with the acceleration RF signal. The beginning of the recorded data shows the injection plateau and then the acceleration when the spectrum is moving with time. The set parameters during the recording were: $f_c = 0.25 \cdot f_0$, $\mathrm{d}f = 0.05 \cdot f_0$, $P = 10.7$ W. The revolution frequency f_0 at injection is ≈ 212 kHz and increases during acceleration up to $\approx f_0 = 1$ MHz. The relatively broad excitation of

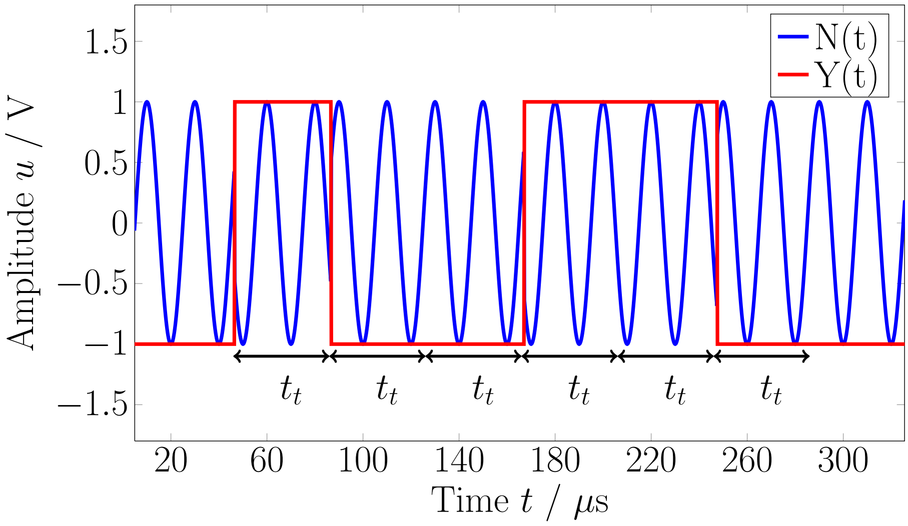

Figure 3.3: The blue waveform shows the pseudo-random noise $N(t)$ due to phase jumps in accordance to the pseudo-random binary sequence $Y(t)$ at each time interval t_t.

$0.05 \cdot f_0$ makes sure that the unknown betatron frequency is in the range of excitation. The width of the excitation signal spectrum plays an important role since the efficiency of power delivered, to the beam, directly depends on it. Proper choice of excitation width will play an important role in operation of FAIR accelerators, since the beam deflection reduces (or electric rigidity increases) with $\beta^2\gamma$ as seen in Eq. 3.9.

There are two main advantages of this system; first it is an easily tunable excitation source available during the whole acceleration ramp. Second is that the band limited nature of this noise results in an efficient excitation of the beam in comparison to white noise excitation. The main drawback is the difficulty in correlation of the resultant tune spectrum with the excitation signal.

Frequency sweep

Frequency sweep also called chirp or harmonic excitation is used by a network analyser for BTF measurements which is an established method primarily for beam stability analysis [38]. However, using this method for tune measurements during acceleration is not trivial, and thus the method is not suitable for tune measurements during the whole acceleration cycle. Nevertheless, this method offers advantages compared to the previous excitation method for careful interpretation of tune spectrum in storage mode, e.g., injection plateau or extraction flat top when the tune frequency is relatively constant. Thus frequency sweep has been extensively used during the measurements at injection plateau to compare and understand the dependence of tune spectra on the type of excitation and isolate individual modes. The parameters for sweep excitation are sweep time, sweep bandwidth and sweep power. A slower sweep gives the beam longer time to respond, but induces bigger perturbations to the beam distribution and consequently emittance blow-up.

3.1.2 Amplifiers and strip-line exciters

The signal generated is fed to the hybrid switch which generates the original signal and its instantaneous inverse. These signals are fed to two fixed 50 dB amplifiers each with a specified maximum power rating of 25 W. The maximum power delivered by the amplifiers has been found to exceed its maximum power rating by factor ≈ 2 in experiments without saturation [65]. This power is fed to the strip-line exciters terminated with $R_{ex} = 50\ \Omega$ resistors. The length of strip-line exciter plates is $L_s = 0.75$ m, and the inter-plate separation of $d_s = 0.07$ m in vertical and 0.2 m in horizontal plane. The input power spectrum density of any generated signal $P_{in}(f)$ is given in

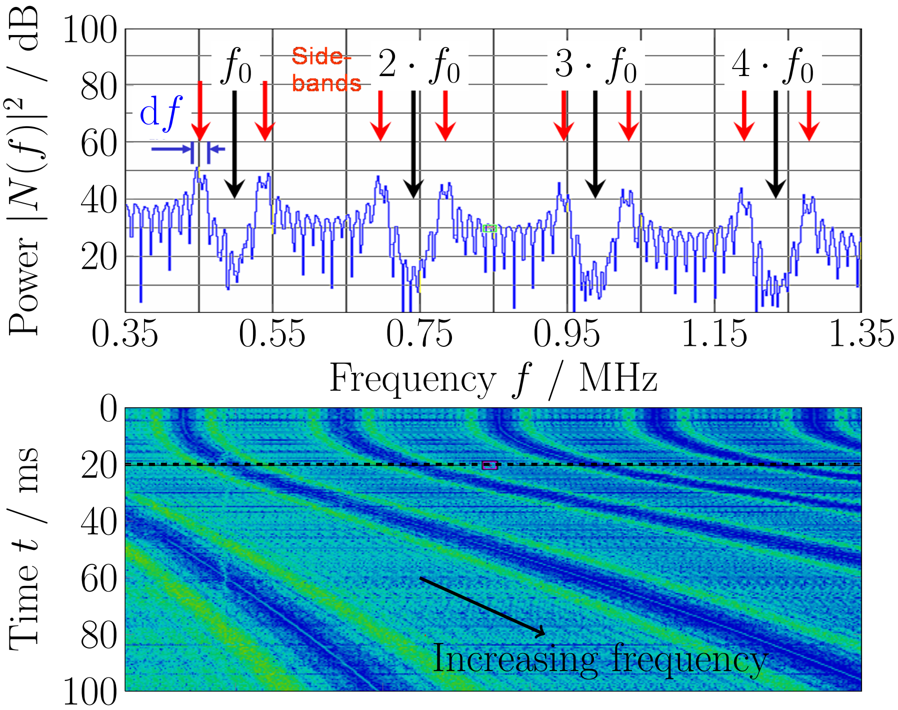

Figure 3.4: The output of band limited exciter during an acceleration ramp [74]. The spectrum shown at the top is taken at the time instance marked by the dotted line in the spectrogram on the bottom.

the unit of mW/Hz. However, if we consider P_{in} as the total input power of the excitation signal in a narrow band Δf around the tune frequency f_b, the electric field acting on the beam due to this signal is,

$$E_{ex} = \frac{u}{d_s} = \frac{2\sqrt{2 * 10^{(\frac{50}{10})} \cdot P_{in} \cdot R_{ex}}}{d_s} \tag{3.7}$$

where the factor 2 comes from the opposite voltages between the exciter plates, and the 50 dB amplification is also taken into account. The electric field induced between the exciter plates causes a deflection of the beam p_x. The particles in the beam with a momentum p_0 are deflected by an angle,

$$x'_{ex} = \frac{p_x}{p_0} = \frac{qE_{ex}t_p}{m_0 c \gamma_0 \beta_0} \tag{3.8}$$

where $t_p = \frac{L_s}{\beta_0 c}$ is the time spent by the particles in the electric field within the strip-line plates, $q = Ze$ is the total charge of the ions , $m_0 \approx A \cdot m_p$ the rest mass of the accelerated ion, c the speed of light, β_0 and γ_0 are the relativistic Lorentz factors of the velocity of the ions. Expanding the parameters in Eq. 3.8, we obtain

$$x'_{ex} = \frac{Z}{A} \cdot \frac{L_s}{d_s} \cdot \frac{e}{m_p c^2 \beta_0^2 \gamma_0} u \tag{3.9}$$

Z/A is the charge-to-mass ratio in the observed ions. In all the above calculations, we have ignored the effect of magnetic field generated due to the current flowing in the strip-line which is considered in [58]. The current flowing in the strip-line plate generates magnetic fields, which would exert forces on the beam depending on its velocity.

In this section, we will discuss each constituent of the tune measurement system in detail. Figure 3.5 shows the schematic description of the Tune, Orbit and Position measurement system along with the beam excitation subsystem.

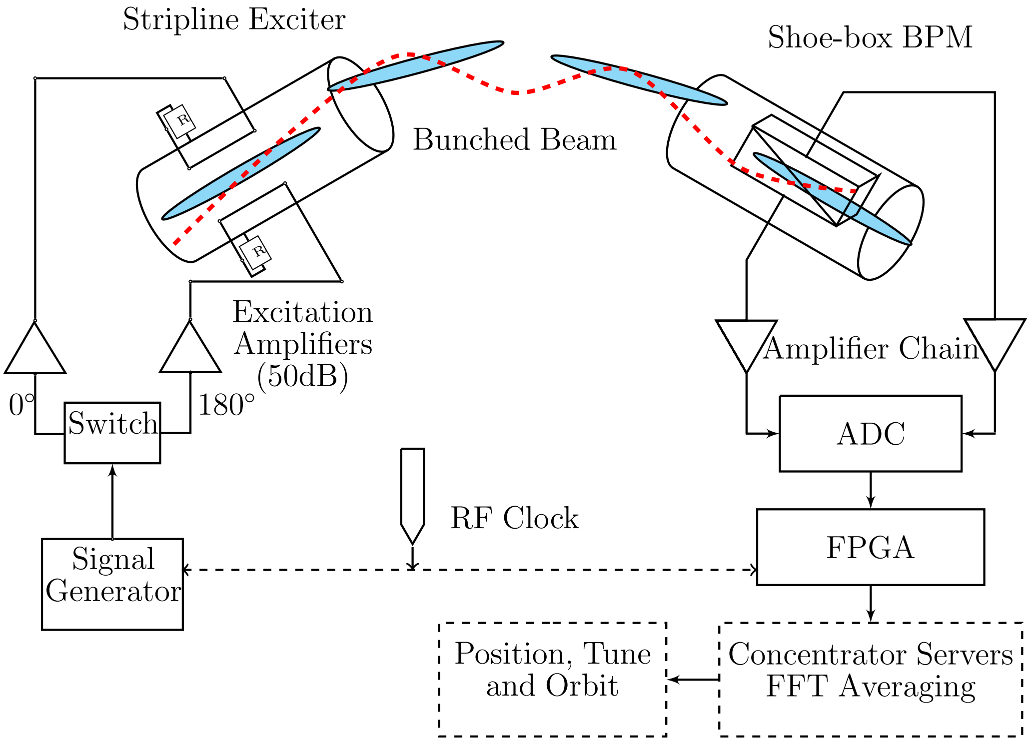

Figure 3.5: The schematic of Tune, Orbit and POSition measurement system along with the beam excitation system.

3.2.1 Beam Position Monitors (BPMs)

Beam position measurements can be done in many different ways, hence many different devices qualify to be called as BPMs. Invasive methods are very impractical for synchrotrons since the particles undergo many million turns around the synchrotron from injection to extraction and small deflections per turn could lead to huge losses in beam intensity. Thus, non invasive capacitive pick-ups are the most commonly used device for the monitoring the beam position in the synchrotron and hence they are almost invariably given the title of BPMs while actually they are just pick-ups. We will refer to them as pick-ups or BPMs interchangeably. These pick-up designs often come in the form of shoe-boxes or buttons. Their working principle is simple, two isolated conductor plates (pick-ups) are placed on the either side of the beam. Whenever a bunched beam passes through them, its electric field induces image charges on the plates. The image charges in turn drive a current and induce a voltage in the connected circuit for each plate. The difference of the measured current or voltage between the two plates provide information about the position of the beam. They are referred as "capacitive pick-ups" since no DC signal is passed through the plates and a continuous beam would not induce any measurable non-transient voltage or current. More detailed description can be found in [67]. The schematic of the shoe-box pick-up used at SIS-18 is shown in Fig. 3.6

The important parameters of a BPM is its transfer impedance and the position sensitivity. Both of these parameters are a function of the pick-up shape, dimensions and frequency and independent of the magnitude of the beam current.

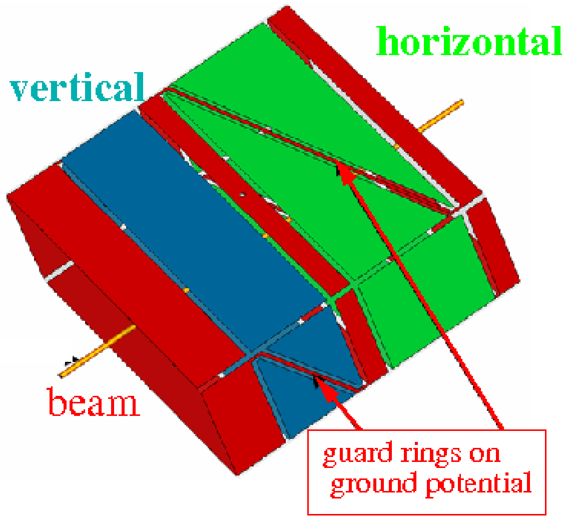

Figure 3.6: The model of the Shoe-box pick-up installed in SIS-18.

Figure 3.6 shows the shoe-box or linear-cut BPM installed at SIS-18. The transfer impedance is defined as the ratio of voltage induced at the input of the head amplifier to the beam current. The transfer impedance of the pick-up can be calculated in different ways. A common way is to model the induced image charges as a current source. This current source is then connected to the following circuit which in this case is a parallel combination of capacitance of the cables and the input impedance of the following amplifier [67]. However, we take a different approach here which perhaps is more intuitive. We model the pick-up as a capacitor formed by the pick-up electrode and a virtual plate at the centre of the beam pipe. The capacitance is thus a constant for a particular pick-up design and installation. This capacitance, as a rule of thumb, will be proportional to the pick-up plate area, and inversely proportional to the distance of pick-up from the center of beam pipe and the exact calculation requires taking pick-up dimensions and shape into account. The virtual plate is connected to a dependent voltage source which is driven by the beam current via image charges. The voltage source takes into account the magnitude of beam current and position with respect to the center as shown in Fig. 3.7.

Here, we show the calculation of the transfer impedance for the prescribed simplified model when beam is centred in the beam pipe. The impedance of BPM electrodes (plates) is given by $Z_1 = \frac{-j}{\omega C_1}$, which are terminated with a high impedance amplifier, $Z_2 = R_1 || C_2$ is the parallel combination of cable and amplifier input capacitance (C_2) and input resistance (R_1) of the pre-amplifier [62] as shown in Fig. 3.7. If $U_{beam}(\omega)$ is the voltage induced on the pick-up plates due to beam passage through the pick-ups, it is transformed into the voltage at the input of the pre-amplifier $U_{in}(\omega)$ by the voltage divider equation,

$$U_{in}(\omega) = \frac{Z_2}{Z_1 + Z_2} U_{beam}(\omega) \tag{3.10}$$

$$U_{in}(\omega) = \frac{C_1}{C_1 + C_2} \frac{j\omega R_1 (C_1 + C_2)}{1 + j\omega R_1 (C_1 + C_2)} U_{beam}(\omega) \tag{3.11}$$

Now substituting $U_{beam}(\omega)$ by $I_{beam}(\omega)$,

$$U_{beam}(\omega) = k(\theta, \omega) \cdot I_{beam}(\omega) \tag{3.12}$$

where $k(\theta, \omega)$ is a factor of proportionality between U_{beam} and I_{beam}, and θ is the beam position with respect to the center. $k(\theta, \omega)$ relates the image charges induced on the plates to the position and shape of the beam bunches.

$$k(\theta, \omega) = \varphi(\omega)(1 + K(\omega)\theta) \tag{3.13}$$

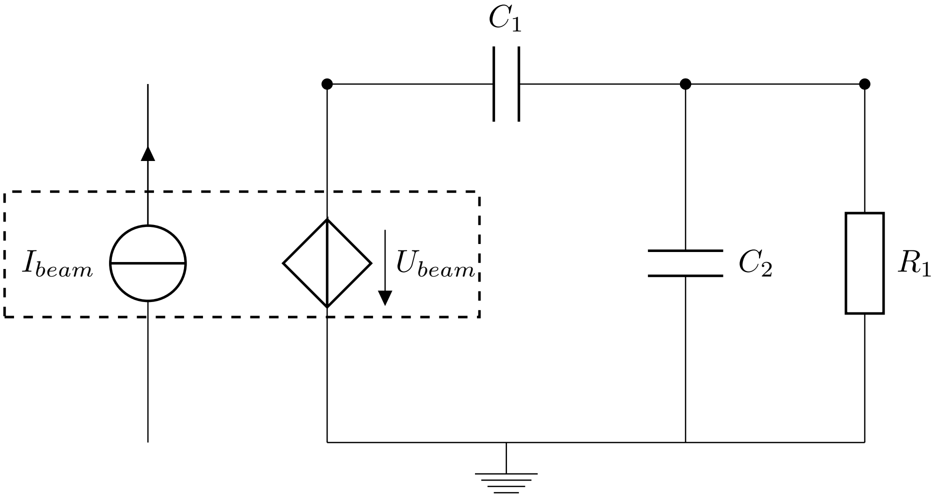

Figure 3.7: Pick-up terminated with a high impedance amplifier.

where $\varphi(\omega)$ is the monopolar response of the pick-up and $K(\omega)$ is the dipolar response or the position sensitivity. However, we have defined the transfer impedance for a beam centered in the pick-up and beam pipe, so $k(\theta, \omega) = \varphi(\omega)$. $\varphi(\omega)$ is often independent of frequency (by careful BPM design) in the interesting range of the BPM operation, thus it is included as a constant in the Eq. 3.14.

$$U_{in} = \frac{\varphi C_1}{C_1 + C_2} \frac{j\omega R_1(C_1 + C_2)}{1 + j\omega R_1(C_1 + C_2)} I_{beam} \tag{3.14}$$

$$Z_T = \frac{U_{in}}{I_{beam}} = \frac{\varphi C_1}{C_1 + C_2} \frac{j\omega R_1(C_1 + C_2)}{1 + j\omega R_1(C_1 + C_2)} \tag{3.15}$$

Figure 3.8 shows the high pass frequency response of this circuit for $C_1 = C_2 = 50$ pF, $R_1 = 1$ MΩ and $\varphi = 1$ Ω. The time required for the output to reach the steady state is given by $\tau_{BPM} = R_1(C_1 + C_2)$ which is the inverse of low cut-off frequency of the high pass circuit shown in Fig. 3.7. Figure 3.9 shows the transient response of the the BPM equivalent circuit (Fig. 3.8) to the input $u_{beam}(t)$ which is a sequence of square shaped longitudinal bunches, modulated by periodic beam offset and sinusoidal betatron oscillations. The response or output is shown as $u_{in}(t)$. Though the frequency response of the pick-up along with its termination is shown to be high pass, the total frequency response is actually a band pass with the higher cut-off frequency defined by the bandwidth of the head-amplifier ≈ 100 MHz.

The shape of shoe-box type BPMs has been designed to provide linearity in position calculation. To ensure position linearity, the function $k(\theta, \omega)$, defined in Eq. 3.14, should be a linear function of bunch position and independent of bunch shape i.e it should be independent of frequency in the relevant frequency bands. These conditions are expressed in the given equation,

$$k(\theta) = \varphi(1 + K\theta) \tag{3.16}$$

where K represents the position sensitivity of the pick-up. For a beam displaced by θ in the x-plane, we obtain two signal voltages $U_{in,l}$ and $U_{in,r}$ from the left and right pick-up plates. Using Eq. 3.14 and Eq. 3.16, we obtain a more practical definition of position sensitivity,

$$K_x = \frac{1}{\theta} \frac{U_{in,l} - U_{in,r}}{U_{in,l} + U_{in,r}} \tag{3.17}$$

$$= \frac{1}{\theta} \frac{\Delta U_x}{\Sigma U_x} \tag{3.18}$$

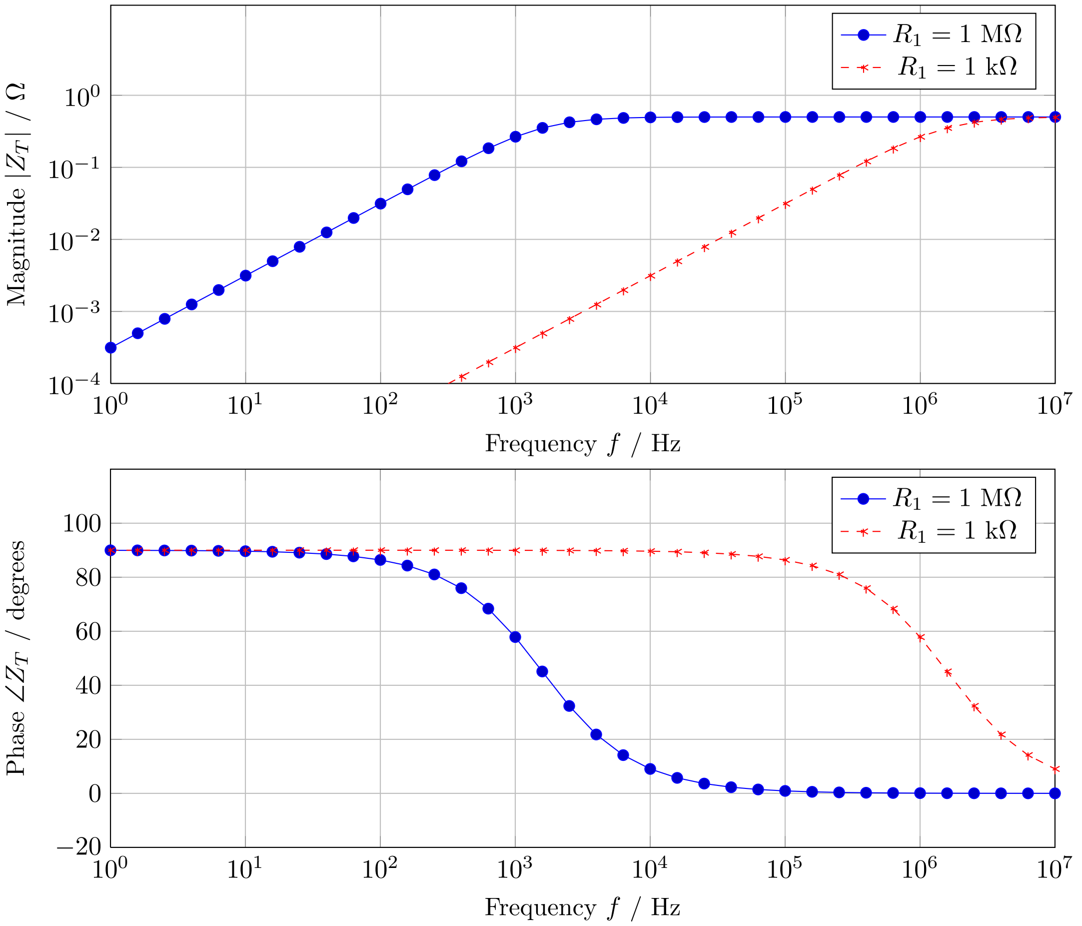

Figure 3.8: The magnitude and phase of the transfer impedance for a capacitive pick-up along with the termination, shown in Fig. 3.7, using Simulation Program with Integrated Circuit Emphasis (SPICE). The blue curve shows the curves for high impedance termination (1 MΩ), while the red is for a low impedance (1 kΩ).

The unit of sensitivity is given in %/ mm. The approximate values for TOPOS BPM sensitivities in horizontal plane is calculated to be $K_x = 0.442\%/$ mm and vertical plane $K_y = 1.595\%/$ mm. There is often a constant offset due to the difference between the “electric” beam center and pick-up center as well as pick-up design tolerances. A complete list of sensitivities and offset for each SIS-18 BPM can be found in [29]. An example for the sensitivity for shoe-box BPM is shown in Fig. 3.10. The top three legends represent the vertical(top and bottom) BPM plate measurement samples when the vertical position is fixed, and the horizontal position is swept in the range of -60 mm to 60 mm compared to the electrical center of the pick-up. The lower three legends represent the vertical(top and bottom) BPM measurement samples when the horizontal position is fixed, and the vertical position is swept in the mentioned range. The influence of beam position in one plane on another, often referred as coupling, is negligible in this case. For tune measurements, a higher sensitivity of the pick-ups is desired. However, the requirement of pick-up linearity is important for preciseness and convenience in position calculation. Since TOPOS is designed to be a position and tune measurement system, a proper balance between both has to be obtained during pick-up design.

It is important to note that C_1 and $k(\theta, \omega)$ represent two separate physical aspects of a capacitive pick-up. C_1 describes the frequency response of the pick-up, taking the “capacitive” nature of the pick-up into account which by definition is independent of the beam and only depends the pick-up design and installation. k on the other hand represents the induction of image charges on the plates and its dependence on bunch position and bunch shape with respect to the pick-up plates.

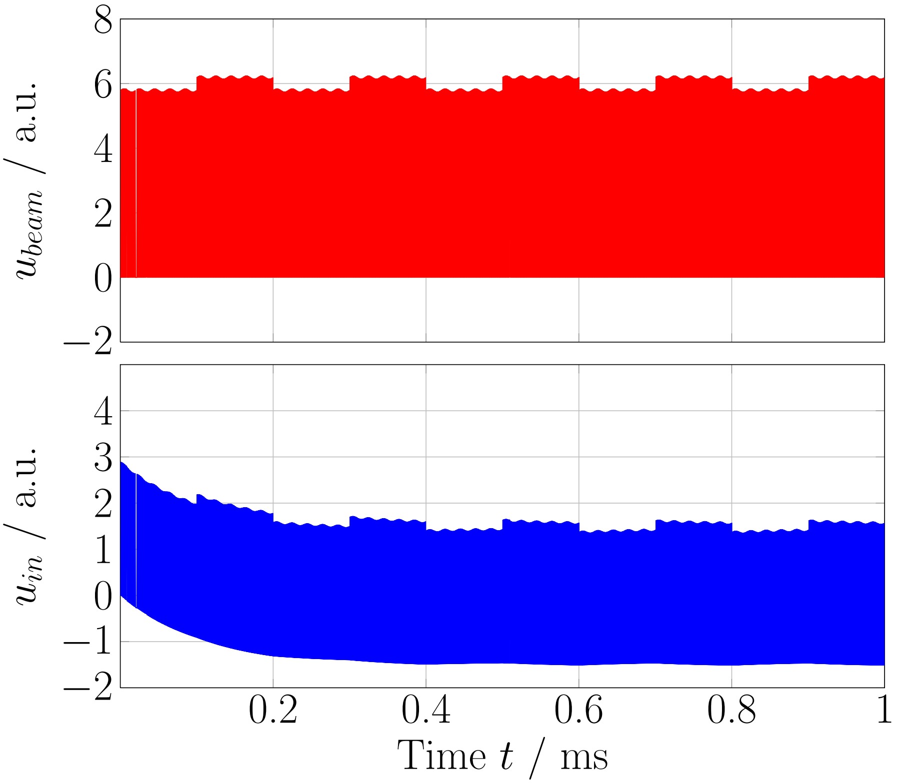

Figure 3.9: Simulation of the transient response of the BPM with a high impedance termination. The bunched beam signal is modeled by a square pulses at 1 MHz which are modulated by sinusoidal betatron oscillations (at 25 kHz) and periodic closed orbit distortion (at 5 kHz). The time required to reach the steady state in inversely proportional to the low cut-off frequency of the circuit.

3.2.2 Signal transfer chain and noise considerations

As seen in the previous section, the signal from the BPMs are terminated with a high impedance termination. This brings the lower cut-off frequency considerably below the region of interest. Then the signal passes through a series of switchable attenuators and amplifiers from the BPM electrodes to the ADCs, where they are digitized and processed. Figure 3.12 shows the schematic description of the signal chain. In principle the signal chain is divided into 3 parts, the head amplifier, the driving amplifier and the post amplifier. Each of them has switchable attenuators which are controlled by relay switches. The reason for this complex configuration of the signal chain is the high dynamic range required during regular machine operations. The signal voltage range of BPM electronics lies between ≈ 10 μV to 100 V. The switchable attenuators give a possibility of switching in a dynamic range of 90 dB i.e −40 to 50 dB. Whenever a value of gain is set in the control room, the switches are configured such that the signal to noise ratio is the highest.The amplifiers have a 3 dB bandwidth of 170 MHz. Characteristics of each stage is detailed in [29]. The amplifiers are connected to signal generators for their regular calibration. In addition, the post amplifier unit also has a built-in sum and difference unit which was the basis of the previously used position calculation program POSI.

The sensitivity of a system is defined by the smallest signals it can resolve from the background noise coming from various sources. The strongest noise sources in the TOPOS signal chain come from the amplification and termination of the signals. It is also well known that the first amplification stage is the biggest source of noise, and the later stages have negligible contribution to the overall noise, since the the input noise of first stage has been already amplified by it. Due to the complex combination of the attenuators, in certain cases, when all the attenuators

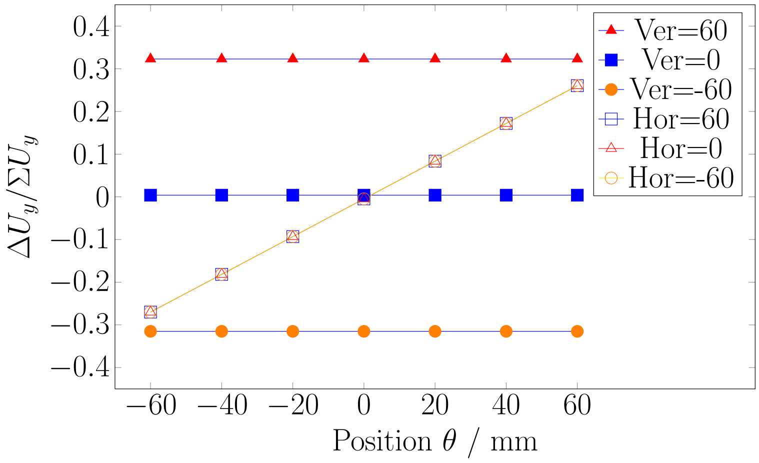

Figure 3.10: An example of position sensitivity calculation for horizontal plane for SIS-18 shoe-box BPM using simulations [68]. $\frac{\Delta U_y}{\Sigma U_y}$ is a linear function of beam position (θ_y) in the plane under investigation (vertical plane). The position calculation in the vertical plane is independent of horizontal position (θ_x) of the beam.

between head-amplifiers (pre-amplifiers) and post-amplifiers are connected, the noise from the second amplification stage also contributes significantly.

Let us begin with a simple model of various noise sources in the circuit, shown in Fig. 3.13. The thermal noise of the discharge resistor R_1 represented by i_{nR} in the form of Norton's equivalent circuit; the noise current of the high impedance amplifier is given by i_{nA} and the noise voltage of the amplifier is given by u_{nA}. The capacitance C_2 due to cable capacitance, input capacitance of the amplifier and any stray capacitance forms a low-pass filter of first order which filters away noise above certain frequencies in i_{nR} and i_{nA}.

$$u_{n,TOPOS} = \sqrt{u_{nA}^2 + Z_{RC}^2(i_{nR}^2 + i_{nA}^2)} \tag{3.19}$$

where $|Z_{RC}|$ is the magnitude of the RC filter impedance,

$$|Z_{RC}| = \frac{R_1}{\sqrt{1 + (\omega R_1 C_2)^2}} \tag{3.20}$$

The thermal noise current squared of the resistor is,

$$i_{nR}^2 = \frac{4k_B T}{R_1} \tag{3.21}$$

where k_B is the Boltzmann constant and T is the temperature.

$$u_{n,TOPOS} = \sqrt{u_{nA}^2 + Z_{RC}^2\left(\frac{4k_B T}{R_1} + i_{nA}^2\right)} \tag{3.22}$$

The values for $R_1 = 1$ MΩ, $C_2 \approx 50$ pF, $i_{nA} = 0.1 - 1$ pA/$\sqrt{\text{Hz}}$ and $u_{nA} = 5$ nV/$\sqrt{\text{Hz}}$ can be found in [62]. The frequency of revolution for SIS-18 varies from ≈ 200 kHz to 1 MHz. The equivalent noise bandwidth of the amplifiers in the TOPOS chain is limited to ≈ 100 MHz. Putting all these values in Eq. 3.22, we obtain the input noise amplitude at the head amplifier to be

$$u_{n,TOPOS} = \sqrt{5^2 + 0.4^2 + 0.2^2} \cdot 10^{-9}\text{V}/\sqrt{\text{Hz}} \tag{3.23}$$

$$\approx 5\text{nV}/\sqrt{\text{Hz}} \tag{3.24}$$

where the filter response Z_{RC} is calculated at 1 MHz. The output noise after 50 dB amplification is $\approx 300 \cdot 5 \cdot 10^{-9} \cdot 10^4 = 15$ mV rms. This corresponds to 120 ADC points which is consistent with the measurements. The above calculation was for the worst case scenario, when none of the attenuators between head amplifier and driving amplifier are connected. The best case scenario gives a noise output of ≈ 8 mV rms.

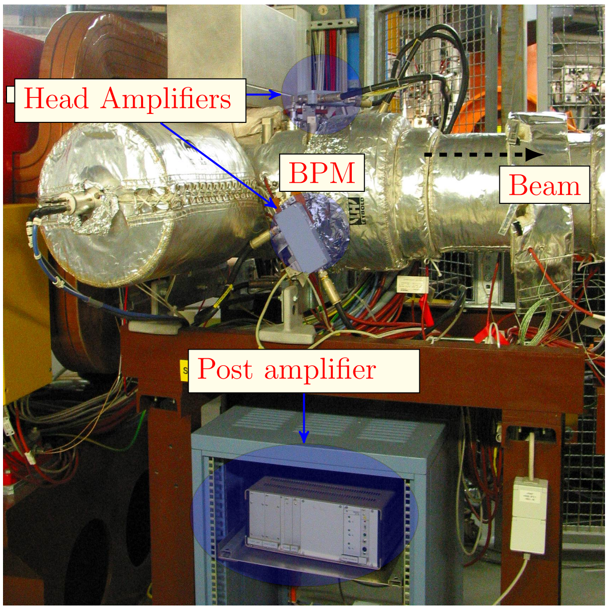

Figure 3.11: The pick-ups along with head and driving amplifier in SIS-18 tunnel [74].

3.2.3 Libera ADCs and FPGAs

The digitization and processing of the data from all the four BPM plates after passing through the signal chain is performed by a single "Libera Hadron®" unit for each of the 12 BPMs. This system is produced by Instrumentation Technologies and has digitization rate of 125 MSa/s per channel at a nominal resolution of 14 bits, the Xilinx Virtex II Pro® FPGA, a single board computer (SBC) and a built-in 256 MB of DDR RAM memory. The Libera unit is synchronized by the timing signals of the accelerator, which can be customized on the GUI, as explained later. The programming of FPGA is done to calculate the position from the BPM signals and forms the subject on the next chapter. While the Libera Hadron can calculate the position of the whole acceleration cycle, it can store only 256 ms of the raw data due to the limited memory size. A detailed discussion on exact position calculation procedure is postponed till chapter 4.

3.2.4 Concentrator server and GUI

The position values thus calculated in the each Libera FPGAs are transmitted to two concentrator PCs where they are further processed to find quantities such as orbit and tune. A GUI client then requests the data each cycle from these concentrator PCs to display the tune, position, orbit or longitudinal profile in the control room. A typical GUI screenshot for the bunch-by-bunch mode along with tune is shown in Fig. 1.4.

3.3 BaseBand tune(Q) measurement system (BBQ)

Baseband tune measurement system was conceived at CERN-Beam instrumentation group by M. Gasior et al. [60]. The system went into successful operation in all the CERN synchrotrons, RHIC, FermiLab etc. [71, 72]. Given the similarity of SIS-18 to CERN-PSB and LEIR, first attempt of BBQ system installation was performed at SIS-18 in 2008 as part of the previous work [29]. Some calculations and measurements were also performed in line with [60] and the system was shown to have no advantage in terms of "gain factor" compared to the then developing TOPOS system. The system was reinstalled again in 2011 with a few modifications as part of this work and is found to

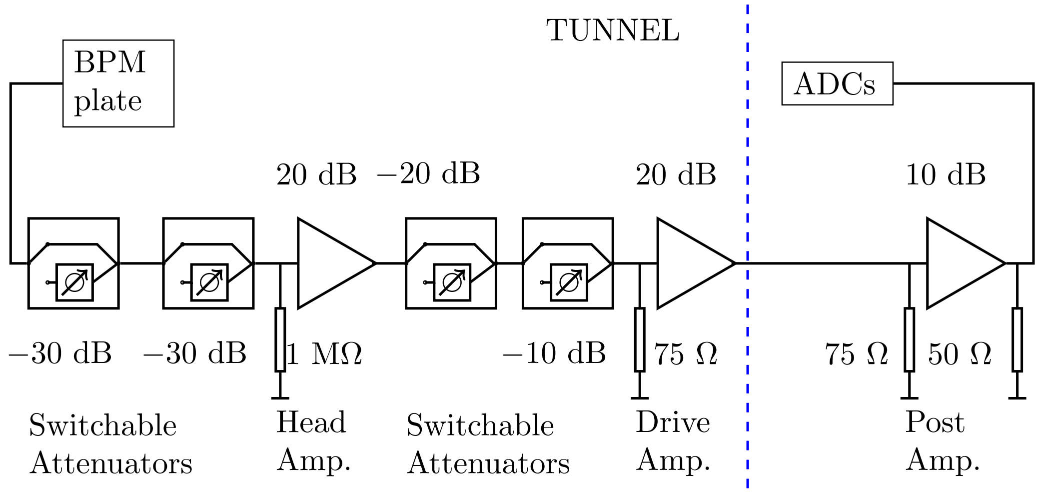

Figure 3.12: The TOPOS signal chain from BPM plates to the ADCs. It is divided into three distinct stages. Each stage consists of switchable attenuators and amplifiers.

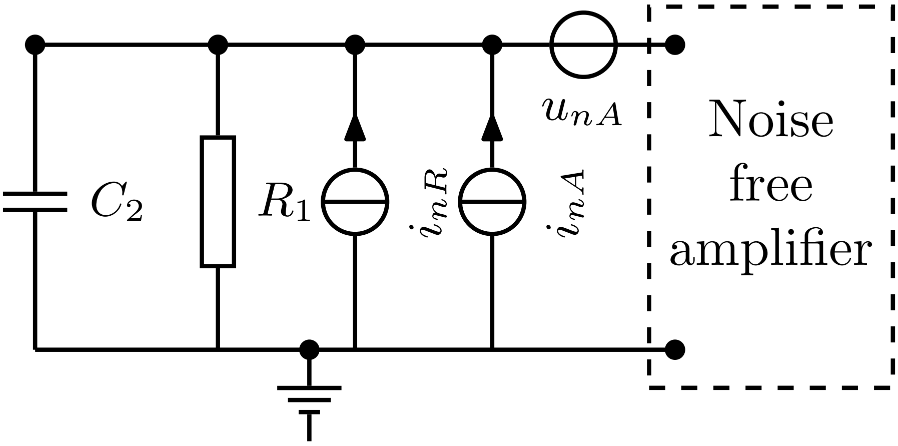

Figure 3.13: Noise model for the TOPOS.

perform satisfactorily. This section closely follows the first treatment given in [60] for the BBQ system while focussing on the conditions and challenges specific to SIS-18 such as the dynamic range of the system and the signal-to-noise ratio in comparison to the TOPOS system.

3.3.1 Principle of operation

The simple schematic of BBQ system configuration at SIS-18 is shown in Fig. 3.14. The BBQ front-end system is divided into two distinct parts; a diode based peak detector and an analog signal processing chain consisting of input differential amplifier (DA), a variable gain amplifier and filter chain with 1 MHz bandwidth. The peak detector stretches the bunch signal to the inter-bunch spacing which is effectively a sample and hold operation at the peak of each bunch. In this way, it suppresses the revolution frequency and folds down the beam spectrum into the baseband. The DC part of the resulting signal is rejected using coupling capacitors. Following this, the signal is passed through an input differential stage where any common-mode signal (interference signal) is rejected and the differential betatron signal is amplified.

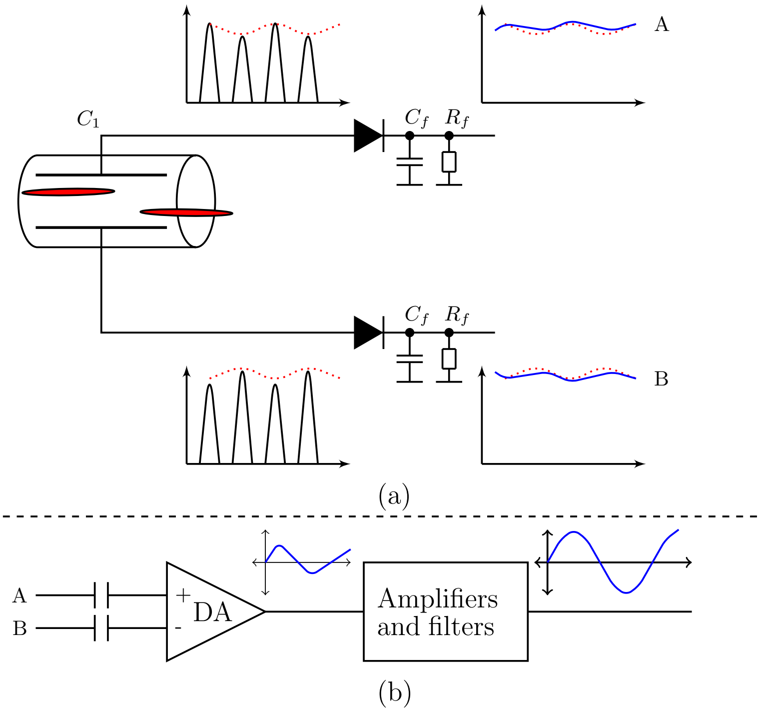

Figure 3.14: Schematic of the BBQ system.

3.3.2 Analytical model and noise characteristics

The treatment in this section follows closely the first treatment of this system [60], and thus same notations are chosen for easy reference. For a bunch with longitudinal profile $\hat{Q}(t)$, oscillating with betatron frequency $f_b = Q \cdot f_0$ in any plane (either x or y), the repetition time is considered as one machine revolution period $T_0 = \frac{1}{f_0}$. Signals $s_1(t)$ and $s_2(t)$ of opposite pick-up (PU) electrodes of an off-axis beam is given by,

$$s_1(t) = \hat{Q}(t)(1 + K\theta)(1 + \theta_\beta \cos(2\pi f_b t)) \tag{3.25}$$

$$s_2(t) = \hat{Q}(t)(1 - K\theta)(1 - \theta_\beta \cos(2\pi f_b t)) \tag{3.26}$$

where θ represents the relative beam offset, while θ_β describes the relative betatron oscillation amplitude. Opposite signs are used to reflect the fact that a signal increase on one electrode implies a decrease of the signal on the opposite electrode. The most important parameter for this device is the time constant of the peak detectors $\tau_{PD} = R_f C_f$. As we will see, the values of R_f and C_f play a major role in successful operation of this device. The choice of time constant is constrained by two effects, the lower limit is given by the suppression of the revolution frequency component in the transverse spectrum. The highest possible time constant is limited by the so called “dragging" effect as well as the signal to noise considerations as explained below. To understand the relation between suppression of revolution frequency and time constant, let us consider a single plate signal in Eq. 3.25 with a centered beam ($\theta = 0$).

$$s_1(t) = A_b s_{PD}(t) * \cos(2\pi f_b t) \sum_{n=-\infty}^{\infty} \delta(t - nT_0) + A_o s_{PD}(t) * \sum_{n=-\infty}^{\infty} \delta(t - nT_0) \tag{3.27}$$

where $\hat{Q}(t)$ has been replaced by a infinite train of delta pulses, A_b and A_o are the relative amplitudes of revolution and betatron components, and the capacitor discharging function $s_{PD}(t)$. It is a section of an exponential curve with a length corresponding to the machine revolution period T_0,

$$s_{PD}(t) = (\hat{u}(t) - \hat{u}(t - T_0)) \cdot \mathsf{e}^{\left(\frac{-t}{\tau_{PD}}\right)} \tag{3.28}$$

$\hat{u}(t)$ is a unit step function used to construct the one turn window. The magnitude of Fourier transform of Eq. 3.28 gives,

$$S_{PD}(f) = \tau_{PD} \left| \frac{1 - \mathsf{e}^{\left(-j2\pi f T_0 - \frac{T_0}{\tau_{PD}}\right)}}{1 + \mathsf{e}^{(-j2\pi f T_0)}} \right| \tag{3.29}$$

The main parameter suppression ratio $\tilde{\xi_s}$ can be found for the worst case value of betatron frequency $f_b = f_0/2$,

$$\tilde{\xi_s} = \frac{S_{PD}(\frac{f_0}{2})}{S_{PD}(f_0)} = \sqrt{4 - \frac{3T_0^2}{T_0^2 + \pi^2 \tau_{PD}^2}} \tag{3.30}$$

A value of $\tau_{PD} = 100T_0$ gives a suppression ratio of $\approx$ 50 dB. Revolution frequency suppression (due to peak detection) forms one of the main advantages of BBQ over TOPOS system with respect to proper utilization of the dynamic range of the ADCs and amplifiers.

The limiting factor for increasing the filter time constant is the need to discharge the storage capacitor faster than the bunch amplitude decreases due to betatron motion. This condition can be expressed as,

$$\Delta_c > \Delta_b \tag{3.31}$$

where Δ_c is the relative discharge of the storage capacitor, assuming one bunch in the machine, the reference period for these changes is one revolution period T_0,

$$\Delta_c = 1 - \mathsf{e}^{\frac{-T_0}{\tau_{PD}}} \tag{3.32}$$

and Δ_b is the maximal decrease of the betatron modulation envelope, the change in the modulation envelope is fastest around the zero crossing of the betatron motion and is given by,

$$\Delta_b = 2\theta_\beta \sin(2\pi f_b \frac{T_0}{2}) \tag{3.33}$$

This gives us the upper limit for τ_{PD},

$$\tau_{PD} < \frac{T_0}{2\theta_\beta \sin(\pi f_b T_0)} \tag{3.34}$$

which if not satisfied results in the dragging effect. One should also note that, the limit is dependent on the specific tune value as well as on the amplitude of betatron oscillations. The amplitude of betatron oscillations is a difficult quantity to predict since it depends on numerous factors. However, dragging does not lead to any dramatic consequences in the resulting output, it reduces the signal amplitude. Thus we conclude that the value of τ_{PD} should be large i.e. $\tau_{PD} \geq 100\ T_0$, and any further increase is mainly limited by the signal-to-noise ratio considerations which are discussed next.

Figure 3.15 shows the main noise sources in the BBQ system. The noise current source i_{nD}, representing the shot noise associated with the diode leakage current with reverse polarity; the thermal noise of the discharge resistor R_f

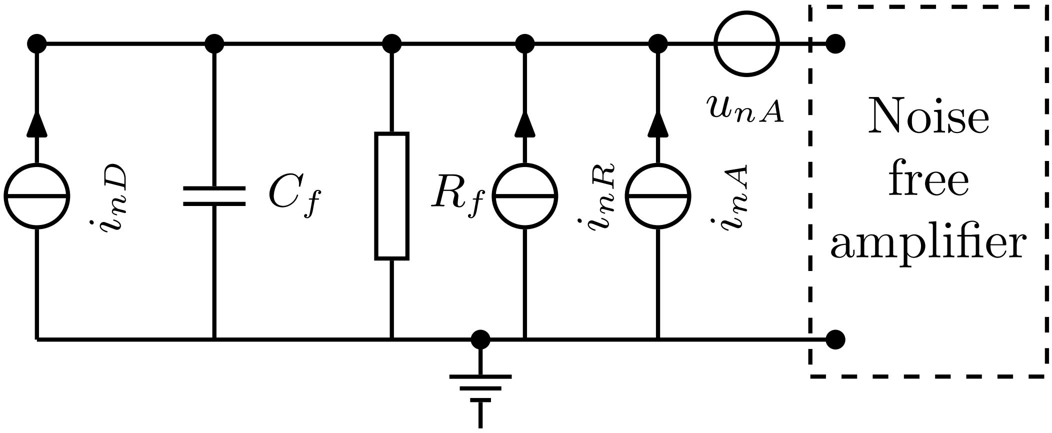

Figure 3.15: Noise model for the front-end of the BBQ system.

represented by i_{nR} in the form of Norton's equivalent circuit; the noise current of the high impedance amplifier, i_{nA}; the noise voltage of the amplifier, u_{nA}.

$$u_{n,BBQ} = \sqrt{u_{nA}^2 + Z_{RC}^2(i_{nD}^2 + i_{nR}^2 + i_{nA}^2)} \tag{3.35}$$

where $|Z_{RC}|$ is the magnitude of the RC filter impedance,

$$|Z_{RC}| = \frac{R_f}{\sqrt{1 + (\omega R_f C_f)^2}} \tag{3.36}$$

The shot noise current squared of the diode leakage current is

$$i_{nD}^2 = 2eI_{RD} \tag{3.37}$$

where e is the elementary electron charge and I_{RD} is the DC diode leakage current with reverse polarity. It should be noted that I_{RD} is given in A, unlike all the noise current sources e.g. i_{nD}, i_{nR} which are normalized to the bandwidth and given in the units of A/$\sqrt{\text{Hz}}$. The thermal noise current squared of the resistor is

$$i_{nR}^2 = \frac{4k_B T}{R_f} \tag{3.38}$$

where k_B is the Boltzmann constant and T is the temperature. Putting all the terms back in Eq. 3.35, we obtain

$$u_{n,BBQ} = \sqrt{u_{nA}^2 + \frac{R_f^2}{1 + (\omega R_f C_f)^2}\left(2eI_{RD} + \frac{4k_B T}{R_f} + i_{nA}^2\right)} \tag{3.39}$$

The parameters related to BBQ circuitry, namely $C_f = 50$ pF, $R_f = 10$ MΩ, $I_{RD} = 5$ nA, $i_{nA} = 1$ pA/$\sqrt{\text{Hz}}$ and $u_{nA} = 5$ nV/$\sqrt{\text{Hz}}$, were found from [73, 74]. The frequency of revolution for SIS-18 varies from ≈ 200 kHz to 1 MHz. The bandwidth of the amplifiers in the BBQ chain is limited to 1 MHz. Putting all these values in Eq. 3.39, one can calculate the output noise ≈ 1 mV rms after 50 dB amplification. We thus notice that the BBQ system noise is an order of magnitude lower than that of TOPOS.

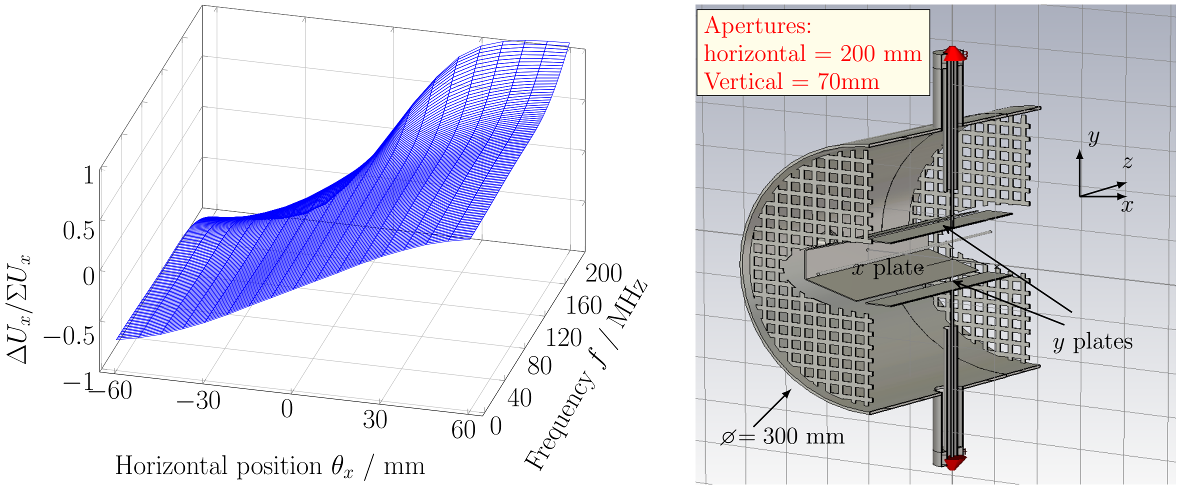

(a) (b)

Figure 3.16: (a) Quadrupole pick-up horizontal position sensitivity against beam position and frequency. (b) The vertical cross-section of the simulated structure of quadrupole pick-up.

3.3.3 Quadrupolar pick-up simulations

When comparing BBQ and TOPOS system, one has to emphasize that the pick-ups used by both systems are different. In this subsection, we have simulated the so called “Quadrupolar pick-up” which was originally designed to measure the transverse quadrupolar oscillations but was used as pick-up for the BBQ system. The pick-up was simulated by CST Microwave Studio® [75]. The results are presented in Fig. 3.16a for the vertical plane. The sensitivity is dependent on the position, and calculated as 2.14%/mm in vertical plane and 1.42%/mm in horizontal plane at the center of the pick-up below ≈ 30 MHz. The sensitivity has a dependence on the signal frequency, however the dependence is far above the frequency range of interest ≤ 10 MHz. The vertical cross-section of the simulated structure of quadrupole pick-up is shown in Fig. 3.16b.

3.3.4 BBQ prototype measurements

A picture of the BBQ system installation at SIS-18 is shown in Fig. 3.17. The diode detectors are directly connected to the pick-ups with the values $R_f = 10\ \mathrm{M\Omega}$ and $C_f = 50$ pF. The output of the diode detectors is connected to the “BBQ Box” containing amplifier and filter chain using low capacitance cables. The cables are shielded with metal wire casing to reject the low frequency noise. The amplification of the amplifier chain is remotely controlled in the range of 55 dB to 90 dB. The frequency response of the BBQ signal chain is shown in Fig. 3.18. The measurement shown is for channel 1 at the default gain of 55 dB. A 50 dB attenuator is placed to compensate for the default amplification. The measured response of all channels are identical, which is prerequisite for optimum operation of the device.

3.3.5 Comparison of BBQ and TOPOS

The major differences between the systems are in terms of sensitivity, operational ease and versatility. The TOPOS system, as described earlier, has several subsystems and is a large system, which makes it prone to instabilities from various factors such as, network connections, firmware updates, etc.. It requires substantial maintenance and continuous calibration. BBQ system is relatively small and less complex in this sense.

The absolute tune sensitivity is difficult to determine for each system since it depends on beam conditions, machine settings, etc.. However, a relative value for both systems under the same beam conditions can be ascertained. If

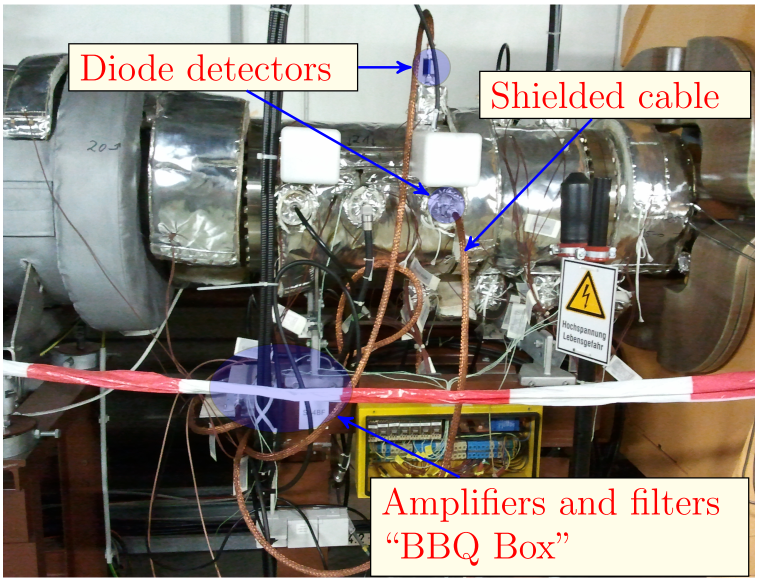

Figure 3.17: Picture showing the BBQ installation in SIS-18.

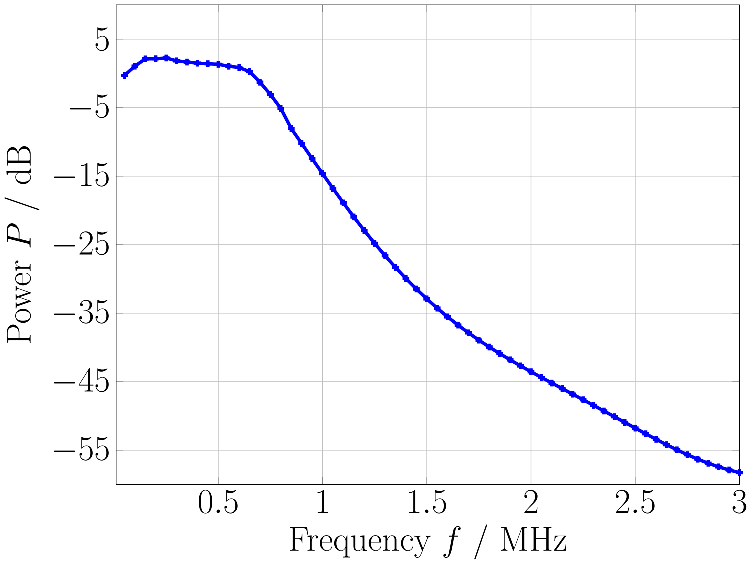

Figure 3.18: The frequency response of the BBQ amplifier and filter chain.

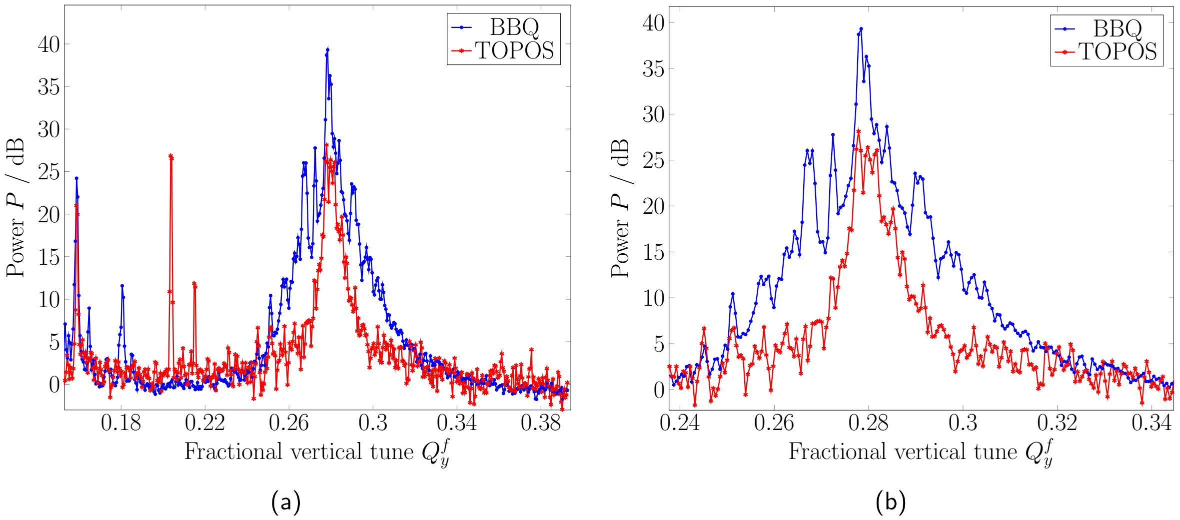

(a) (b)

Figure 3.19: (a) A comparison of the tune spectra for BBQ and TOPOS systems under the same conditions. (b) A zoomed version of Fig. (a). The noise level of BBQ system is ≈ 15 dB lower than the TOPOS system. However, for clarity, the spectra obtained from both systems are adjusted to the same noise level, which gives an impression of broader tune peak in case of BBQ system.

the beam is performing a θ_β mm betatron oscillations, the difference voltage registered in the data acquisition for TOPOS and BBQ systems will be,

$$\Delta U_{TOPOS} = |Z_{T,TOPOS}| K_{TOPOS} \theta_\beta \tag{3.40}$$

$$\Delta U_{BBQ} = |Z_{T,BBQ}| K_{BBQ} \theta_\beta \tag{3.41}$$

where Z_T and K is the transfer impedance and position sensitivity of the respective systems. The ratio of Z_T is given by the relative dimensions of the pick-ups, $\dfrac{Z_{T,BBQ}}{Z_{T,TOPOS}} \approx 0.5$ while $\dfrac{K_{BBQ}}{K_{TOPOS}} \approx 3.5$ using the values estimated from simulations in section 3.2.1, 3.3.3. Thus the calculated relative SNR can be found using Eqs. 3.39 and 3.23,

$$\frac{SNR_{BBQ}}{SNR_{TOPOS}} = \frac{\Delta U_{BBQ} \cdot u_{n,TOPOS}}{\Delta U_{TOPOS} \cdot u_{n,BBQ}} \approx 5 \tag{3.42}$$

This corresponds to a ≈ 15 dB higher SNR of BBQ in comparision to TOPOS. It should be noted that $u_{n,TOPOS}$ used in Eq. 3.42 is ≈ 3 lower compared to what is calculated in Eq. 3.23, since all the points within a bunch are integrated to find out the position in TOPOS, which is further processed to calculate the spectrum while only single value per bunch is considered for BBQ spectrum calculation presently. BBQ offers higher tune sensitivity due to lower noise floor compared to TOPOS system. It is also more robust compared to TOPOS since lot of data reduction is performed directly in hardware using the peak detectors and this reduces the digital analysis considerably. However the robustness and sensitivity comes at the cost of high frequency data rejection and the versatility of digital analysis as in case of the TOPOS system. Another important difference is that BBQ works on averaged mode or peak mode based on relative intensities of the bunches and the time constant of the peak detector [60]. Thus, users have no “gating” possibilities to find out the tune for each bunch separately. TOPOS does not have these restrictions and it allows for “gating” of any bunch.

While BBQ was instrumental in the discovery of head-tail modes at GSI SIS-18, it would have been impossible to separate them from suspected “intermodulations” without the high resolution time domain data from TOPOS. Both systems complemented each other, and played important roles in full understanding of the tune spectrum. In addition to that, they cross-checked each other for ruling out any other technical errors.

In Fig. 3.19, the spectrum at the same time computed by both systems on the injection plateau with 10^9 N^{7+} ions is displayed. The beam was excited with a band limited noise of ≈ 1 mW/Hz. To make a fair comparison between

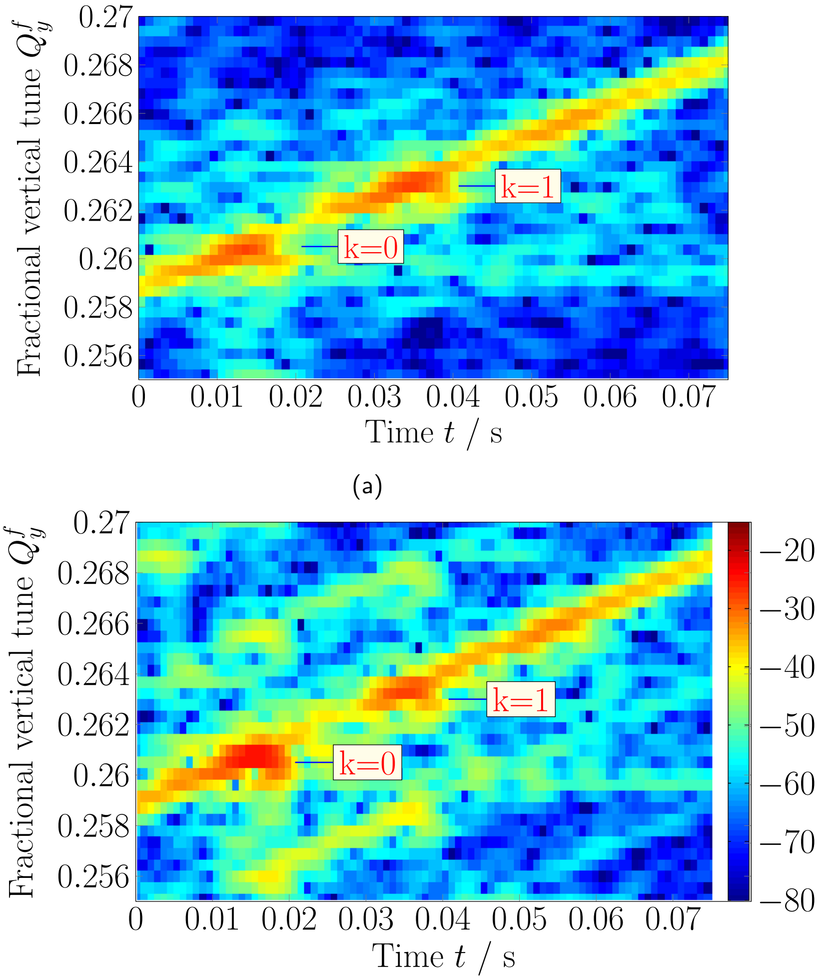

Figure 3.20: Tune spectrum for a sweep excitation from (a) TOPOS and (b) BBQ system. The colour code depicts the power level in dB.

the two systems, BBQ data was acquired using a fast ADC system in LeCroy® oscilloscope with 25 MHz sampling rate. The data is decimated by a factor of 25 such that the number of samples, obtained by the BBQ system, were similar to the number of position samples obtained from TOPOS system (i.e. one sample per bunch). Further all the data analysis was performed off-line for both systems with similar spectrum estimation techniques. For the BBQ spectrum, a sharp peak can be seen at $Q_y^f \approx 0.262$ which is always present irrespective of the beam conditions. Similarly, TOPOS spectrum shows a anomalous peak at $Q_y^f \approx 0.20, 0.22$ which is the “signature” noise peak of the pick-up $S04 - DX$ which is used to calculate the TOPOS spectrum in this particular example. Similarly another example of the spectra, computed by the BBQ and TOPOS systems for a frequency sweep excitation, is shown in Fig. 3.20 for 10^9 N^{7+} ions on the injection plateau. The various head-tail modes are excited as the excitation frequency is swept through them. Both spectra are similar while more “structure” is visible in the BBQ spectra above the noise level.

Based on the arguments and examples above, several observations can be made with respect to BBQ and TOPOS systems.

- The internal structure for the various head-tail modes in the tune spectra obtained from both systems is very similar i.e. the tune spectra are equivalent irrespectively of the system details.

Table 3.1: Comparison of the TOPOS and BBQ system.

Parameters	TOPOS	BBQ
Observables	Tune, Orbit, Position, Longitudinal profile	Tune
System size	Several subsystems	Single “box”
Bunch gating	Yes	No
Tune sensitivity	Low	High
Status	Operational	Expert

- The signal-to-noise ratio of BBQ is 10 dB better compared to TOPOS, which matches the predications of noise analysis.
- There are different interference sources for both systems, since they are placed at different places in the ring.
- At $Q_y^f = 0.16$ in Fig. 3.19a, the coupling from the horizontal plane is seen in both systems.

Table 3.1 summarizes the comparison of the two systems.

3.4 Summary

1. The beam excitation scheme along with the types of excitation types are studied.
2. The various constituents of the TOPOS system such as BPMs, signal chain and FPGA electronics are described.
3. The principle of operation of the BBQ system is studied, along with its noise characteristics, and optimization parameters.
4. The TOPOS and BBQ systems are compared with emphasis on their symbiotic operation.

The primary outcome of this chapter is the description of the installation of two parallel and consistent tune measurement systems, namely the TOPOS and BBQ. The details of the working principles and their respective regimes of operation were discussed.

4 BPM Data Processing

This chapter describes the major steps in BPM data processing. The first major step is position estimation from the "raw" BPM data and the second is tune spectra calculation from the estimated position. Position estimators are first discussed in terms of robustness and computation requirements. Tune spectrum calculation from position pose specific challenges for SIS-18 due to the fast measurement times required and the presence of higher order head-tail modes. High resolution non-parametric spectrum estimators are discussed and compared, utilizing the measured bunch-by-bunch beam position during various stages of beam acceleration.

4.1 Problem statement

The transverse BPM signal level is a function of three variable components; peak beam current, beam excitation and signal amplification chain. The pre-amplifier noise and local interference noise specific to each ring section are found to be the main noise contributions to the transverse signal. The first problem statement is to find an efficient, real-time, unbiased, minimum variance estimator for position determination for the full accelerating cycle and beam intensity range. To perform reliable tune measurements at any given current level, the beam has to be excited with sufficient excitation power. The excitation level often depends on the machine settings and beam conditions and is further commented in section 5.3.7. It is important to find the optimum beam excitation to get a significant signal-to-noise ratio in the tune spectra while avoiding any excitation induced beam losses. The second problem statement is to compare the various spectrum estimation methods and find the best spectrum estimation method for the complete beam acceleration cycle, and find the bare tune from the tune oscillation spectra thus obtained.

4.2 Position determination

The digitized BPM signals are processed in an FPGA as mentioned in chapter 3. In this section, we will discuss two separate serial procedures implemented in the FPGAs which are used to determine beam position from the BPM signals. First is the bunch detection procedure where the bunch is detected using a robust and versatile approach, such that it can operate under extreme variations in beam conditions and bunch manipulations [76] at SIS-18. The second part is the position estimation from these detected bunch samples. The current algorithm under operation for position estimation is a combination of baseline restoration (BLR) and weighted mean [78, 29]. The working principle is similar to the CERN PS trajectory system [77]. As shown further in this section, the baseline restoration is a computationally expensive procedure, and prone to error under certain beam conditions. Thus a new proposal for beam position estimation is introduced. This proposal for position estimation algorithm removes the need of baseline restoration procedure by using regression based algorithms like ordinary least square error estimator (OLS) or the total least square estimator (TLS). Finally the current and proposed algorithms are compared for their characteristics such as bias, variance and speed to establish the optimum algorithm.

4.2.1 BPM signals

Let $a(t)$ and $b(t)$ be the beam signal induced on the top and bottom (or left and right) linear cut or shoe-box BPM plates due to a bunch passage shown in Fig. 4.1 and are given by,

$$a(t) = \hat{Q}(t) \cdot (1 + K\theta) \tag{4.1a}$$

$$b(t) = \hat{Q}(t) \cdot (1 - K\theta) \tag{4.1b}$$

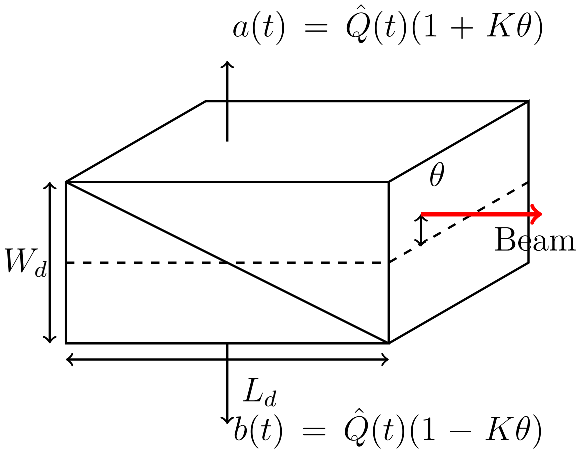

- $\hat{Q}(t)$ is the longitudinal beam profile, W_d is width of the pick-up and L_d is the length of the pick-up
- Sensitivity $K = f(W_d, L_d)$
- θ is the vertical position

Figure 4.1: Beam signals from the shoe-box pick-up.

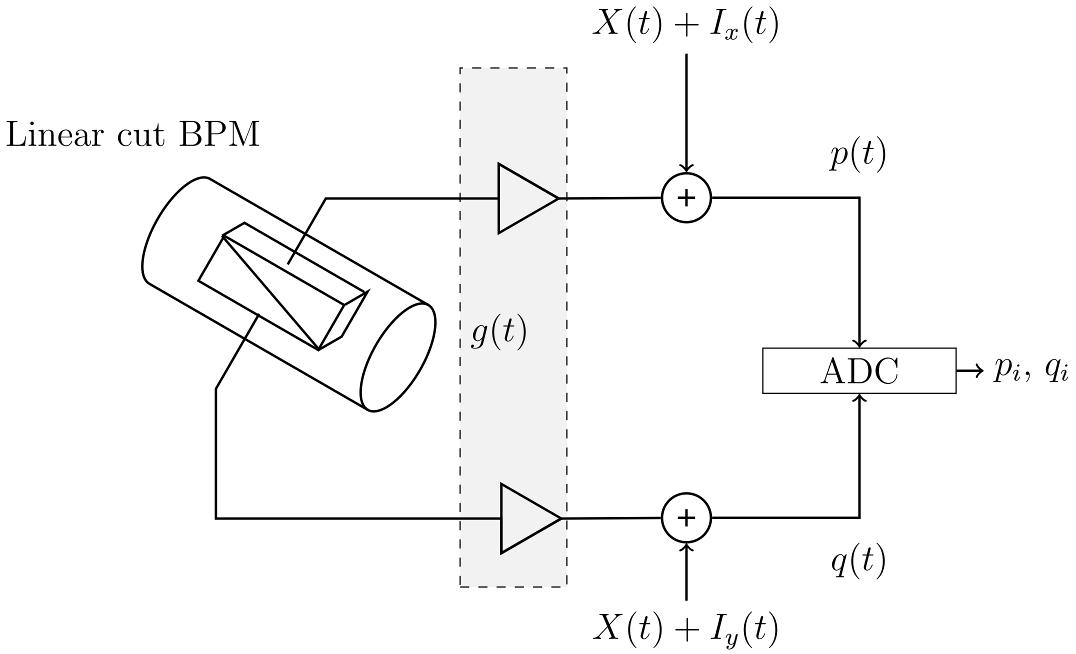

Figure 4.2: Beam signals passing through the signal chain towards the digitizers.

where $\hat{Q}(t)$ is the longitudinal bunch charge profile, θ is the beam offset position and K is the position sensitivity. The signals are periodically induced at rf frequency when the bunch traverses through the BPMs. However, the pick-up has a certain termination and signal chain before the signals are recorded in the ADCs as shown in Fig. 4.2. The amplifier chain is modelled as additive white Gaussian noise (AWGN) channel with $X(t)$ as the random variable and a non-stationary interference noise source which is denoted by $I_x(t)$ and $I_y(t)$. The nature of interference noise makes it complicated to model since it could have spatial and temporal dependence on parameters or sources which are not fully understood or changing with time. It is different at each BPM location stationed in each section of the SIS-18 ring. The transformation of induced voltage from BPM plates to the output of signal chain is given by $p(t)$ and $q(t)$,

$$p(t) = a(t) * g(t) + X(t) + I_x(t) \tag{4.2a}$$

$$q(t) = b(t) * g(t) + X(t) + I_y(t) \tag{4.2b}$$

where $g(t)$ is the impulse response of the system formed by the pick-up and the pre-amplifier. The frequency response $G(f)$ is given by the Fourier transform of $g(t)$. In our case, it is the frequency response of the TOPOS system shown in Eq. 3.11 (Section 3.2). The signal $p(t)$ and $q(t)$ are sampled at 125 MSa/s with 14-bit ADCs as discussed in section 3.2. This results in input data samples p_i and q_i for the digital signal processing part of the TOPOS system. The digital processing of the sampled signal is done in the FPGA in two serial stages. The first is the bunch detection stage, which identifies the presence of the bunches and passes the detected samples to the next stage where position estimation is performed. In general, the definition of an estimator is “a procedure one applies to a data set to estimate some property of the parent distribution from which the data is drawn” [81]. In this case, this parent distribution is the position “submerged” in the electronics and interference noise. Thus the task of the position estimator is to use the signal p_i and q_i over the bunch length N whose range is between 10 and 150 number of samples (varying due to acceleration) and estimate the position parameter θ.

4.2.2 Bunch detection

Bunches are first detected from the signal samples p_i and q_i using the double threshold algorithm explained below. A finite state machine (FSM) diagram of the procedure is shown in Fig. 4.3. The steps are the following:

1. A minimum S_{min} of any of the BPM signal p_i or q_i is found which should be less than an initial value $S_{min,in}$. $S_{min,in}$ is regularly updated which is an average of data between the samples.
2. Using the minimum level, two thresholds are calculated at $T_{11} = T_{12} = \frac{1}{2}S_{min}$ and $T_{21} = T_{22} = \frac{-5}{8}S_{min}$. These threshold values were found empirically in [29].
3. When the bunch signal passes through all these thresholds in the order $T_{11}, T_{12}, T_{21}, T_{22}$, a bunch is detected and their respective time stamps are recorded $t_{11}, t_{12}, t_{21}, t_{22}$. A “time out” is imposed on each state to bring the algorithm back to initial state in case of unexpected data.
4. Time windows (W_{sn}, W_{en}) for the n^{th} bunch is calculated using the time stamps, $W_{sn} = t_{11} - m_n(t_{12} - t_{11})$ and $W_{en} = t_{21} + m_n(t_{22} - t_{21})$. The data in the windows are passed to the next stage i.e. the position estimation. m_n is a “magic number”, which is empirically found by testing of the algorithm with various bunch shapes.

The steps of the mentioned procedure applied to the pick-up signals are shown in Fig. 4.4.

Advantages

- Simple, real-time and bunch based algorithm.
- Does not require any a priori knowledge of rf system and number of harmonics during the whole acceleration cycle which may be advantageous in case of special bunch gymnastics like bunch merging during regular operations [76].

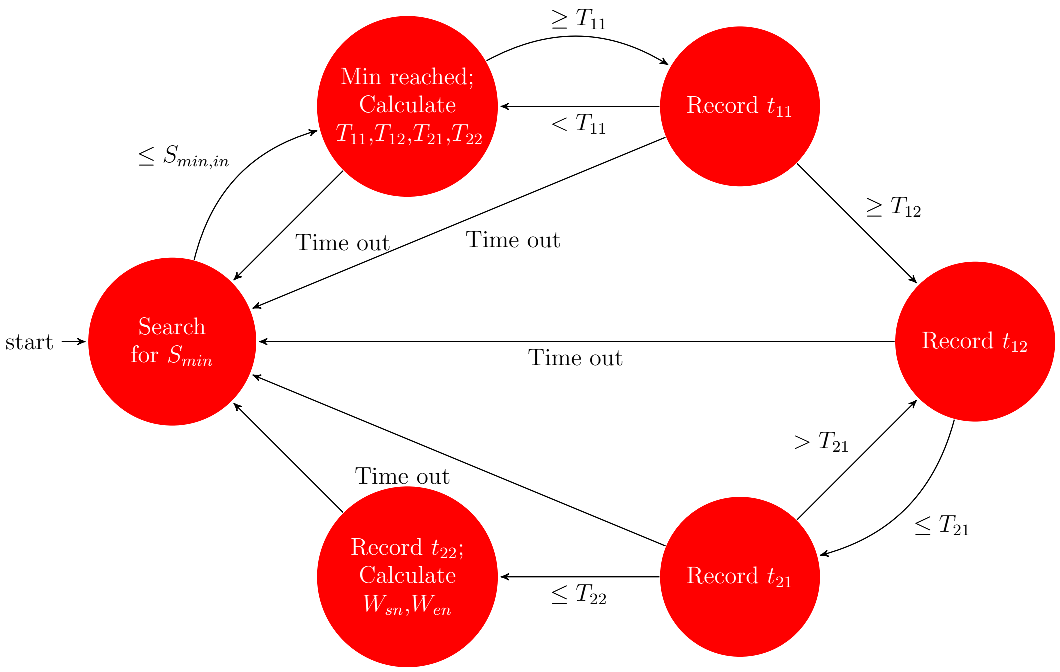

Figure 4.3: Finite state machine representation of double threshold algorithm for bunch detection.

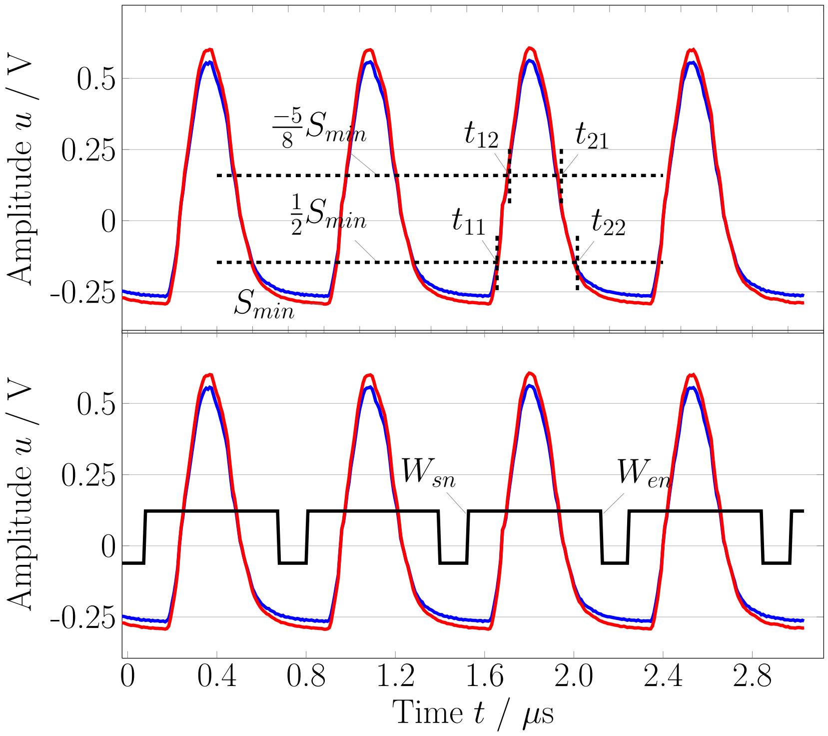

Figure 4.4: Double threshold algorithm for bunch detection and time window calculation.

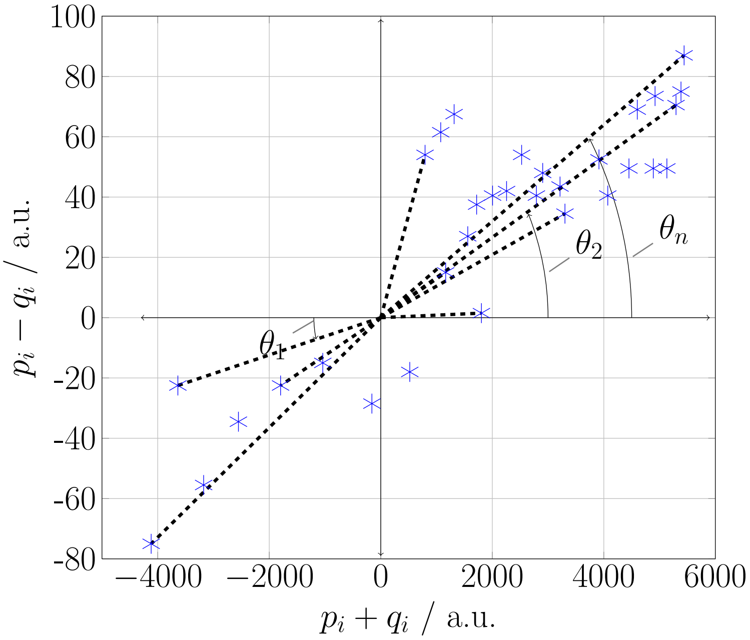

Figure 4.5: Data during injection where $p_i - q_i$ (Δ) is plotted against $p_i + q_i$ (Σ) where $i = 1 \cdots N$ denotes the samples within one bunch. Position (θ_n) are given by the slope (marked by black dashed lines) of each of the N points in the bunch. Larger data samples are more immune to noise, and give slopes with smaller errors. A weighted mean of all the slopes with higher weightage, given to the slopes obtained from larger samples, forms the basis of weighted mean algorithm.

Limitations and failure scenarios

- It does not use any information from the readily available rf cavity signal which is “by definition” synchronized with the bunches.
- Since the method is bunch based, it depends on bunch parameters like bunch shape, amplitude and signal-to-noise-ratio (SNR). In case of a very low intensity beam, inappropriate amplifier settings or glitches in the beam signal, this method is prone to errors.

An rf based bunch detection algorithm was studied in previous work [29] to overcome the mentioned limitations. It was found to be unfeasible due to a slow drift in rf with respect to the bunches, and a further careful consideration is required.

4.2.3 Position estimation

The problem of digital position evaluation and the various methods were recently discussed in [80]. Various scenarios and algorithms based on different hardware configurations for both orbit and bunch-by-bunch (B2B) position were discussed. Since a bunch-by-bunch position measurement is specified for SIS-18, only the methods satisfying this requirement are considered here. The sampling rate of the ADCs is 125 MSa/s and the number of samples within a bunch is in the range $10 \leq N \leq 150$ during the acceleration cycle. Since each sample in the bunch has complete position information, we have an overdetermined system for the position estimation problem. Therefore, we will focus only on the algorithms which directly utilize this overdetermined system for optimum position calculation.

Figure 4.5 helps visualizing the position estimation problem. It shows a plot of $p_i - q_i$ against $p_i + q_i$ signals in terms of ADC amplitude values for a single bunch, where $i = 1, 2, \cdots N$ and N is the number of samples in the bunch. In principle, each data sample in the bunch contains the full position information, and thus position can be obtained by finding the "difference over sum" or slope at any data sample as shown in Fig. 4.5. Since there is always a finite noise $X(t)$, $I_x(t) \neq 0$ added to the signal due to amplifiers and interference from the surroundings, the larger samples will give better accuracy to the slope or position also depicted in Fig. 4.5. The overdetermined nature of the system (i.e. many samples providing the same information are available) can be used to reduce the noise by using several data samples in the bunch for position calculation. Thus, a simple estimator for θ can be arrived at,

$$\hat{\Theta} = \frac{\sum\limits_{i=1}^{N} W_i \cdot \theta_i}{\sum\limits_{i=1}^{N} W_i} \tag{4.3}$$

where

$$\theta_i = \frac{p_i - q_i}{p_i + q_i} \tag{4.4}$$

Looking in Fig. 4.5, it is equivalent to calculating position using the slope of each sample and a weighted mean over all samples in the bunch.

In Eq. 4.3, if uniform weight $W_i = w$ is applied for each sample within the bunch, the obtained estimator is

$$\hat{\Theta} = \frac{1}{N} \sum_{i=1}^{N} \frac{p_i - q_i}{p_i + q_i} \tag{4.5}$$

It is clear that the precision of the obtained result would be poor due to equal weightage given to slopes irrespective of the sample amplitude. A better choice would be such that the weighting coefficients are based on the magnitude of the samples. Thus, if $W_i = p_i + q_i$, we arrive at the traditionally used "difference over sum" or more aptly the "weighted mean" equation for position calculation,

$$\hat{\Theta}_{wm} = \frac{\sum\limits_{i=1}^{N} p_i - q_i}{\sum\limits_{i=1}^{N} p_i + q_i} \tag{4.6}$$

It is known from section 3.2.1 that capacitive pick-ups have a finite lower cut-off frequency depending on the impedance of pick-up termination. Finite lower cut-off frequency means that, $G(f) \approx 0$ for $f \leq f_{cut}$. Thus, the "DC" part of the signal is removed from the bunch. Thus Eq. 4.6 will give erroneous results in cases where $\sum\limits_{i=1}^{N} W_i = p_i + q_i \approx 0$. So Eq. 4.6 cannot be used in its present form without conditioning the data. There are two ways to avoid this problem:

1. Deconvolve the data with an appropriate filter. This has to be a non-linear process since a linear filter cannot produce frequencies missing in the input data [82].
2. Choose the weighing coefficients such that $\sum\limits_{i=1}^{N} W_i \gg 0$. The choice of weighting coefficients should be such that the noise mitigation is not compromised.

Correcting the data points by the deconvolution is possible in principle, but has the following drawbacks;

- It is a computationally expensive procedure, more so when done in real time.
- It requires the knowledge of the transfer function of the amplifier chain and the noise model which is found to be non time-invariant.
- It would create technical difficulties for obtaining the raw data and calculated position simultaneously.

Thus, another simpler method to restore the DC part of the signal was devised. It is called the baseline restoration procedure (BLR). It takes the advantage of very slowly moving baseline due to high impedance termination also shown in Fig. 3.9. Ref. [78] explains the implemented baseline restoration procedure. The simplified procedure is as follows; If p_{nj} and q_{nj} are the j^{th} samples in the n^{th} bunch window of length N generated by bunch detection algorithm. The baseline restored $p_{r,nj}$ is calculated as

$$p_{r,nj} = p_{nj} - \frac{p_{nj+N/2} + p_{nj-N/2}}{2} \tag{4.7}$$

The same procedure is followed for the other BPM signal q_{nj}. This procedure results in the doubling of noise power i.e. $Y(n) = \sqrt{2} \cdot X(n)$. In the next step, the Eq. 4.6 is easily applied to the restored signals $p_{r,nj}$ and $q_{r,nj}$,

$$p_n = \frac{\sum\limits_{i=W_{sn}}^{W_{en}} p_{r,ni} - q_{r,ni}}{\sum\limits_{i=W_{sn}}^{W_{en}} p_{r,ni} + q_{r,ni}} \tag{4.8}$$

The operation of baseline restoration is equivalent to averaging the data samples between the bunches and adding to rest of the data samples in the bunches. Visualizing in terms of Fig. 4.5, baseline restoration procedure will translate all the data samples in the positive quadrant with an averaged slope of all samples on either side of the detected bunch.

Limitations

- Adds noise to the signal. No optimization for noise reduction is performed.
- High latency i.e. baseline restoration takes 2/3 of total position calculation time.
- When the bunch spacing is less than $N/2$, the efficient implementation of baseline restoration algorithm (Eq. 4.7) fails and other high latency workarounds are implemented.

Proposed method: Linear regression fit

In principle, the N samples obtained from both plates in the time window can each be used by the estimator to obtain the position parameter θ using the relation Eq. 4.5. Thus it is a linear overdetermined system which can be written as

$$\mathbf{Y} = \mathbf{S}\theta + \mathbf{X} \tag{4.9}$$

where $\mathbf{Y} = \begin{bmatrix} Y_1 \\ \vdots \\ Y_N \end{bmatrix}$ is the measured signal, $\mathbf{S} = \begin{bmatrix} S_1 \\ \vdots \\ S_N \end{bmatrix}$ is the errorless independent variable and $\mathbf{X} = \begin{bmatrix} X1 \\ \vdots \\ X_N \end{bmatrix}$ is the noise matrix. The problem can now be seen as standard linear regression fitting problem, where each sample has complete information on the estimated parameter θ. Thus, a linear estimator for θ is of the form $\hat{\Theta} = \mathbf{AY}$ where $\mathbf{A}$ is not a function of $\mathbf{Y}$. For a given estimate $\hat{\theta}$, the squared residuals $E_{ols} = \left\|\mathbf{Y} - \mathbf{S}\hat{\Theta}\right\|^2$ give the measure of error in fitting and should be minimized.

$$\begin{aligned} E_{ols} &= \left\| \mathbf{Y} - \mathbf{S}\hat{\Theta} \right\|^2 \\ \frac{\mathrm{d}E_{ols}}{\mathrm{d}\hat{\Theta}} &= 2\mathbf{S}^T\mathbf{S}\hat{\Theta} - 2\mathbf{S}^T\mathbf{Y} = 0 \\ \hat{\Theta}_{ols} &= (\mathbf{S}^T\mathbf{S})^{-1}\mathbf{S}^T\mathbf{Y} \end{aligned} \tag{4.10}$$

$\hat{\Theta}$ is also referred to ordinary least square (OLS) estimator or linear regression fit, and it can be shown that, it is the maximum likelihood estimate (MLE) if $X(t)$ can be modelled by *i.i.d* and a normal distribution [83].

If $\mathbf{Y} = \begin{bmatrix} p_1 - q_1 \\ \vdots \\ p_N - q_N \end{bmatrix}$ are the difference of measured signals between the plates, $\mathbf{S} = \begin{bmatrix} p_1 + q_1 \\ \vdots \\ p_N + q_N \end{bmatrix}$ is the signal intensity which varies along the bunch shown in Fig. 4.5 and $\mathbf{X} = \begin{bmatrix} X_1 \\ \vdots \\ X_N \end{bmatrix}$ is the noise matrix, we obtain a system of equations equivalent to Eq. 4.9.

$$p_i - q_i = (p_i + q_i)\theta + X_i \tag{4.11}$$

Here we assume that S is an errorless variable which is a reasonable assumption since $\dfrac{p-q}{p+q} \ll 1$. Finally, we obtain the solution of the system of equations given by Eq. 4.11 using Eq. 4.10,

$$\hat{\Theta}_{ols} = \frac{\sum\limits_{i=1}^{N}(p_i + q_i)(p_i - q_i)}{\sum\limits_{i=1}^{N}(p_i + q_i)^2} \tag{4.12}$$

If the weighting factor W_i in Eq. 4.3 is chosen as $(p_i + q_i)^2$, a result equivalent to Eq. 4.12 is arrived. This demonstrates a connection between the seemingly ad-hoc choice of the weighting factor $W_i = (p_i + q_i)^2$ and a more systematic estimation theory.

Limitations

- Assumes variable matrix $\mathbf{S} = p + q$ to be noise free, which is not entirely true for the given problem at hand.
- It should be noted that Eq. 4.12 is equivalent to ordinary least squares method only under the constraint or implicit assumption that $\sum\limits_{i=1}^{N} p_i + q_i = 0$ and $\sum\limits_{i=1}^{N} p_i - q_i = 0$ (zero mean data samples), which leads to a dependency on the window length for obtained estimates when the mentioned constraints are not fulfilled.

Error in variables approach

The solution to one of the issues of linear regression fit (OLS) can be addressed by the error in variables approach [88]. The error in variables approach considers the noise in the $\mathbf{S}$ matrix, and a total least square (TLS) estimator is found for the problem posed in (Eq. 4.11).

Input: $\mathbf{Y}$ and $\mathbf{S}$ as defined in the previous section

1. Compute the singular value decomposition $[\mathbf{YS}] = \mathbf{U\Sigma V}^T$.
2. **if** $\mathbf{V_{22}}$ is non-singular **then** set $\Theta_{tls} = -\mathbf{V_{12}}\mathbf{V_{22}^{-1}}$.

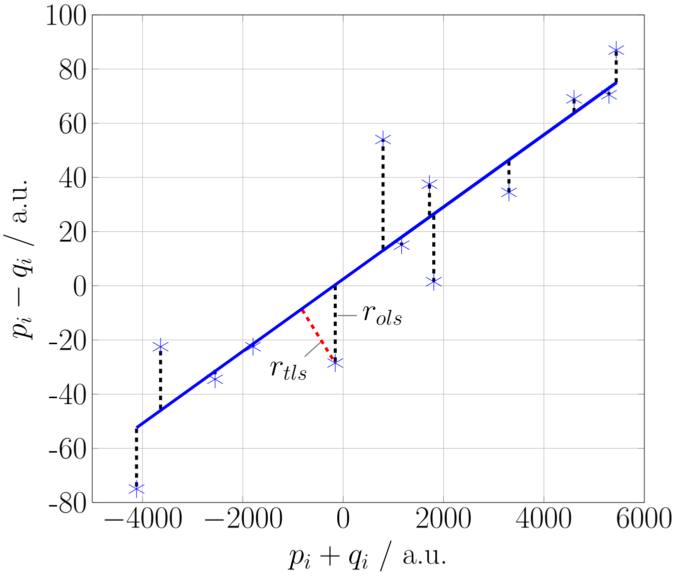

Figure 4.6: Geometric interpretation of OLS and TLS. Ordinary least squares estimate is calculated by fitting a line such that sum of squares of the vertical distances to all the data samples (r_{ols}) in minimized. Total least squares estimate is obtained by the fitting a line such that the sum of squares of the shortest perpendicular distances (r_{tls}) to all the points is minimized.

3. **else** No solution

Output: $\hat{\theta}_{tls}$, is the total least squares estimate of $\mathbf{Y} \approx \mathbf{S}\theta$. Total least square involves performing an SVD which can be easily solved using numerical algorithms, however it is difficult to implement in FPGA for online position calculation and considered here just for completeness. The difference between OLS and TLS estimation is highlighted in Fig. 4.6.

Interpretation in the frequency domain

Equation 4.10 obtained for regression fit gives additional insights for data processing in the frequency domain. When the frequency transform of the input signal $\mathbf{Y}$ and $\mathbf{S}$ is performed, each frequency (bin) contains its position information in its magnitude, thus the problem is to select the “best bin” to calculate the position. Thus, if a Fourier transform of Eq. 4.10 is performed,

$$\hat{\Theta}_{ols} = \frac{I_{lp}(f) \cdot (S(f) * Y(f))}{I_{lp}(f) \cdot (S(f) * S(f))} \tag{4.13}$$

where $I_{lp}(f)$ is the frequency response of an integrator [84], which acts as a first order low pass filter. The convolution in Eq. 4.13 is effectively mixing the difference signal with the predominant frequency. The low pass filtering is then performed by integrator. Mixing and low pass filtering could also be replaced by a single stage band pass filtering. These operations are thus equivalent to a band pass filter operating at the frequency with highest SNR and therefore could be seen as optimum estimator in the frequency domain as well.

4.2.4 Comparison of algorithms

The performance of various algorithms, with respect to the bunch-by-bunch position resolution and bias, should be viewed along with the signal chain response and the corresponding noise model discussed in section 3.2. When the

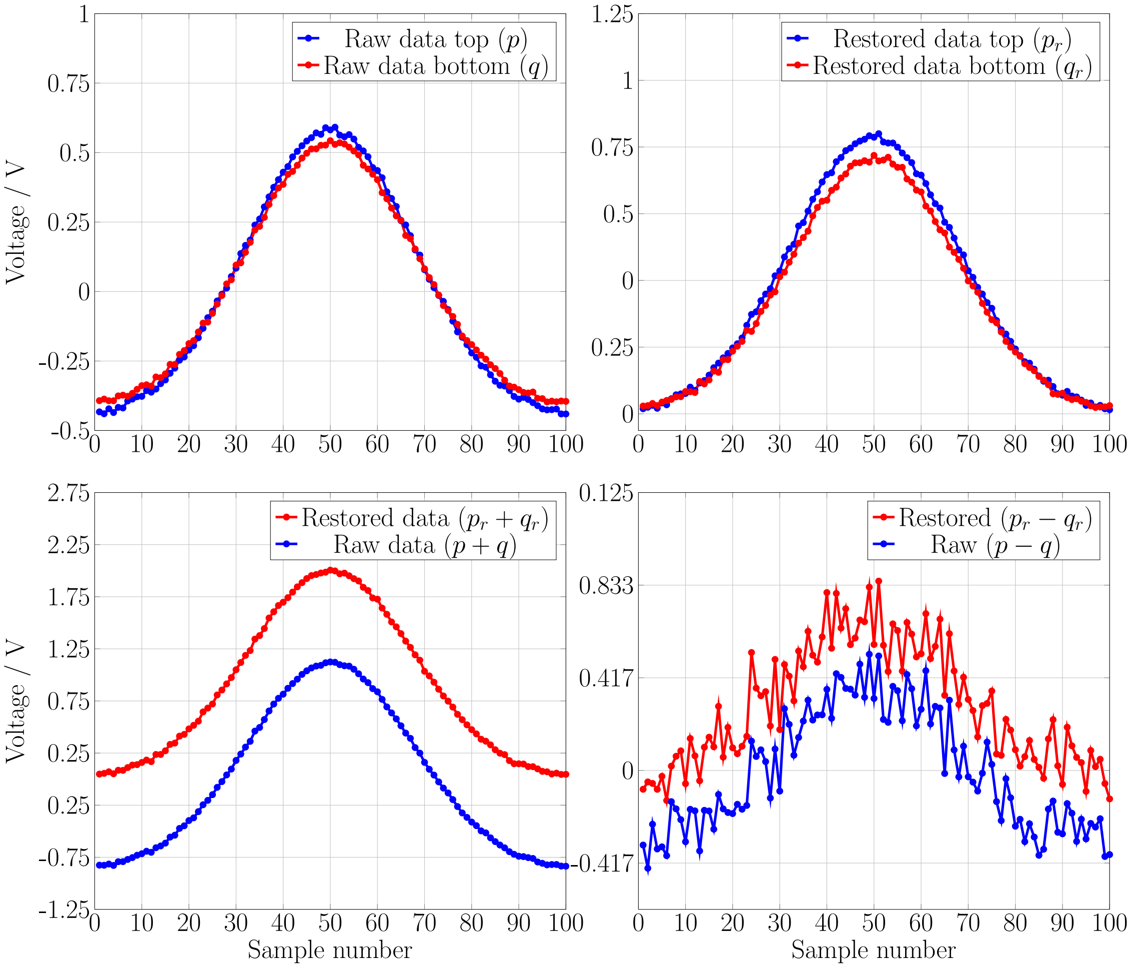

Figure 4.7: Simulated bunches at 6 mm position added with a white Gaussian noise.

BPM data reaches a steady state for a fixed beam position, it can be shown that the total least square estimator (TLS) (with or without BLR) is the best position estimator for a Gaussian noise distribution. However, TLS requires complex operations which makes it difficult to implement in real time, thus it will be ignored in any further analysis.

To compare the performance of the other two algorithms i.e. the weighted mean and regression fit (OLS) with and without BLR, first an ideal test data is generated (simulated) for different levels of the additive Gaussian noise. Position is calculated for this data with both algorithms and the results are compared. Then the measured data during two extremes of acceleration cycle i.e. at injection and extraction are evaluated again using both algorithms, and results are interpreted based on the characteristics such as bias, robustness, speed and resolution. As mentioned in section 4.2.1, the data is digitized at 125 MSa/s, which corresponds to sampling interval of 8 ns.

Simulated bunches

Figure 4.7 shows the simulated BPM data for injection energies. The data is generated assuming 6 mm position offset, and noise is added to emulate the measured BPM electronics noise. The specific position offset is a realistic value, and is chosen for clarity in the figure. Figure 4.8a shows the calculated mean position $\bar{\hat{\theta}}$ using 500 bunches with respect to the number of data samples within the window (referred as window length in the figure caption) for following four cases,

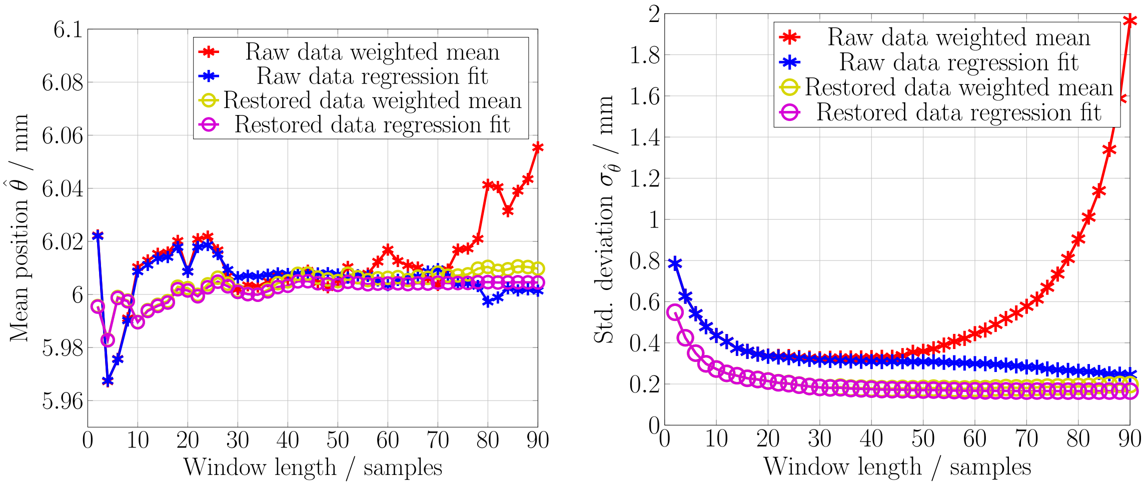

(a) (b)

Figure 4.8: Mean $\bar{\hat{\theta}}$ and std. deviation $\sigma_{\hat{\theta}}$ of the 500 calculated position values using both algorithms with and without BLR against the window length.

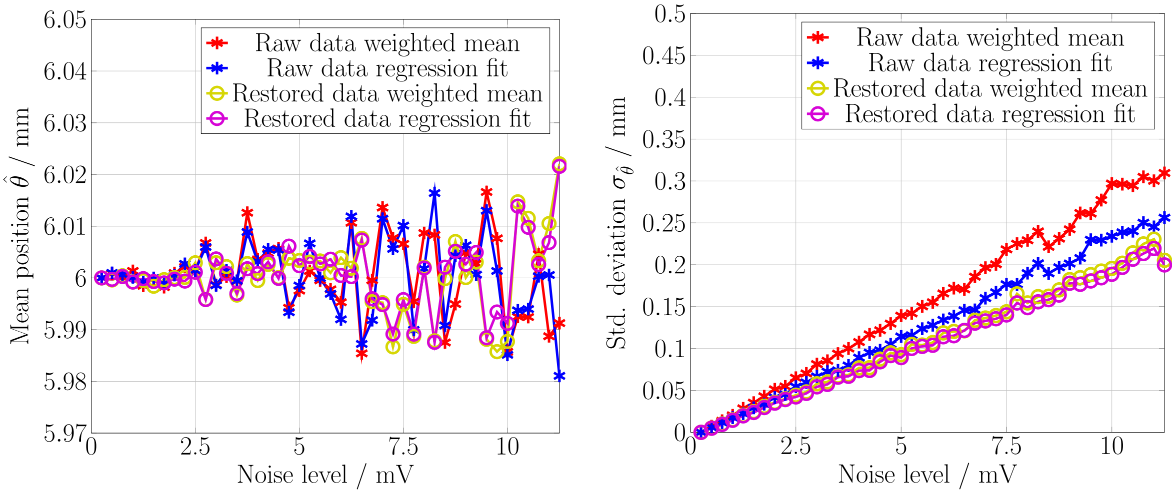

(a) (b)

Figure 4.9: Mean and std. deviation of the 500 calculated position values using both algorithms with and without BLR against the added noise amplitude.

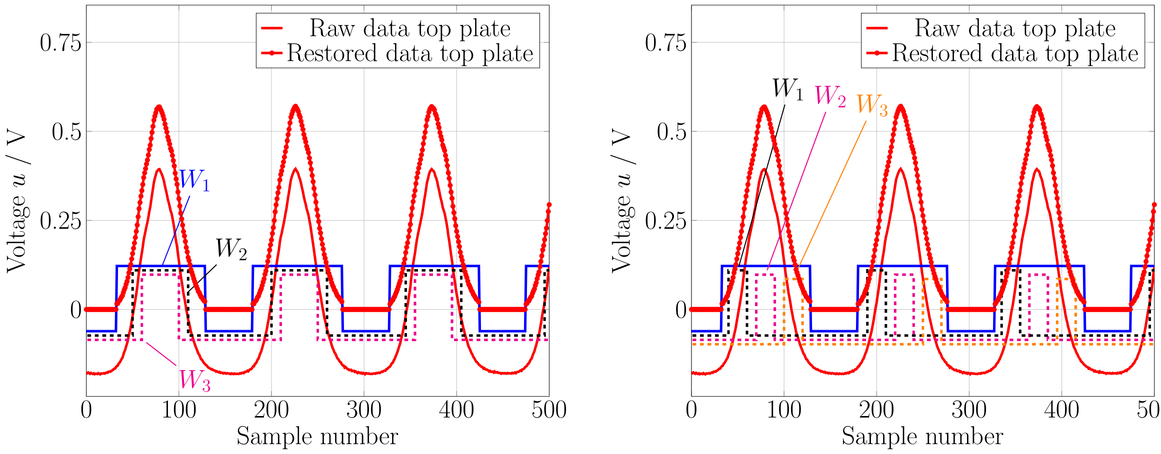

(a) Window length.

(b) Window position.

Figure 4.10: Windows of varying lengths and position with respect to the bunch are used to study their influence on the calculated position. Window length is represented in number of samples, and window position is with respect to the "head" of the bunch. The sampling period is 8 ns.

- Weighted mean with raw data (without BLR)
- Weighted mean with restored data (with BLR)
- Regression fit with raw data
- Regression fit with restored data

Each data sample in the bunch adds information of the position (overdetermined system) and thus the bias of calculated position value reduces with increase in the number of samples as clearly seen in the figure. Figure 4.8b is more interesting since, the std. deviation $\sigma_{\hat{\theta}}$ blows up for weighted mean algorithm without BLR as soon as negative values are taken into account as expected from Eq. 4.6.

Figures 4.9a and Fig. 4.9b show the variation in mean position and std. deviation with increase in noise amplitude for a fixed window length of 50 samples. These figures simply extrapolate the results shown in Figures 4.9a and 4.9b and establish a direct correlation of the input noise level to the measured bias and variance.

Measured bunches at injection

Figure 4.10a shows a data sample measured at injection where the lower red curve (without symbols) is the direct raw data from the ADCs, while the upper red curve (with symbols) is the baseline restored data as discussed in the previous subsection 4.2.3. There are around $120 - 150$ samples in a typical bunch at injection depending on beam intensity and bunch shape. There are three different window lengths marked with respect to the bunch center such that $W_1 > W_2 > W_3$. Position is calculated with respect to continuously varying window lengths starting from only data samples at the center of the bunch to points at the bunch edge. Position is calculated over several turns for each window length, and the bias and variance of the obtained position data distribution is plotted as shown in Fig. 4.11a and Fig. 4.11b. The windows defined in Fig. 4.10a are marked in Fig. 4.11a and also apply to Fig. 4.11b.

The important observations are:

- The weighted mean algorithm diverges for raw data as soon as negative data samples are taken into account. This is an expected behaviour from Eq. 4.6, and baseline restoration is essential for error free operation of the weighted mean algorithm.
- There is a bias between the position calculated from the raw data and the restored data for both algorithms. This bias can be understood as an error either due to improper baseline restoration or zero mean assumption

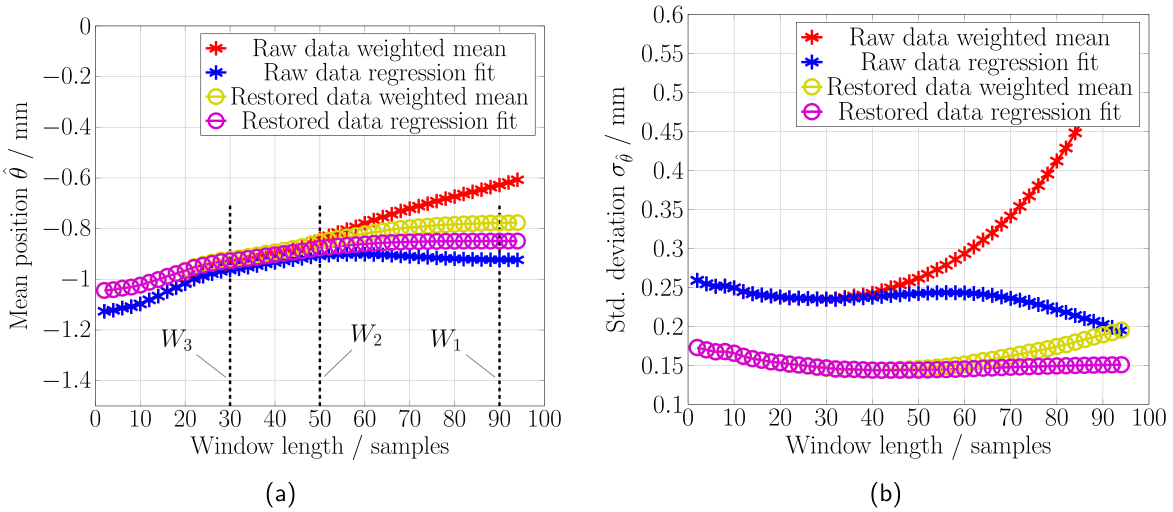

Figure 4.11: Mean $\bar{\hat{\theta}}$ and std. deviation $\sigma_{\hat{\theta}}$ of the 500 calculated position values using both algorithms with and without BLR against the window length. The marked window lengths (W_1, W_2, W_3) correspond to Fig. 4.10a. The sampling interval is 8 ns.

encapsulated in Eq. 4.12 for regression fit. The bias is well within the specifications of precision and resolution (≤ 0.2 mm), and much smaller than other system dependent error sources like the BPM frequency response, alignment of the BPM, etc.

- There is a monotonic movement in the calculated position for both restored and raw data, and the position value stabilizes after 60-70 data samples. This movement can be completely understood only by the noise model. However, this movement is acceptable since it is within the precision and resolution requirements.
- $20 - 30$ data samples provide enough precision in position calculation for both weighted mean algorithm with BLR and regression fit (with or without BLR) in this specific example at injection energy. A generalization of this observation, would be to use $\approx 30 - 50\%$ of samples at the center of the bunch. This information can be used to optimize the computational complexity in the FPGA.

Figure 4.10b shows the same data sample as Fig. 4.10a, however with three different window positions with respect to the bunch “head”. The effect of window position on the calculated position is used to understand the robustness of each position estimator to errors caused by window detection.

Figure 4.12a and Fig. 4.12b shows the mean position and std. deviation calculated against the window position each with a size of 20 samples. Weighted mean with raw data is very sensitive to the position of the window and diverges very fast compared to rest of the three cases as evident in Fig. 4.12b, and therefore is not shown in Fig. 4.12a for maintaining clarity. The window positions are with respect to the “head” of the bunch, i.e. the window position of the three windows shown in Fig. 4.10b are such that $W_1 < W_2 < W_3$. Thus, the most stable values are expected at the center of x axis. These plots report the robustness of the algorithm against the bunch detection errors. The important observations are:

- The weighted mean algorithm with raw data diverges as soon as negative data samples are taken into account similar to the simulated data case. This is an expected behaviour from Eq. 4.6, and a proper baseline restoration is essential for error free operation of the weighted mean algorithm. Regression fit, gives “sane” values (less than 5% error) over the whole window range of window position.
- Even with restored data, weighted mean algorithm is less robust compared to linear regression fit, as the values diverge faster when the edge of bunch is approached (see Fig. 4.12b). The reason lies in the efficient noise mitigation of regression fitting procedure.
- Regression fit algortihm is more robust to the output of bunch detection algorithm, and it completely removes the need of the complicated and rather ad-hoc approach of baseline restoration.

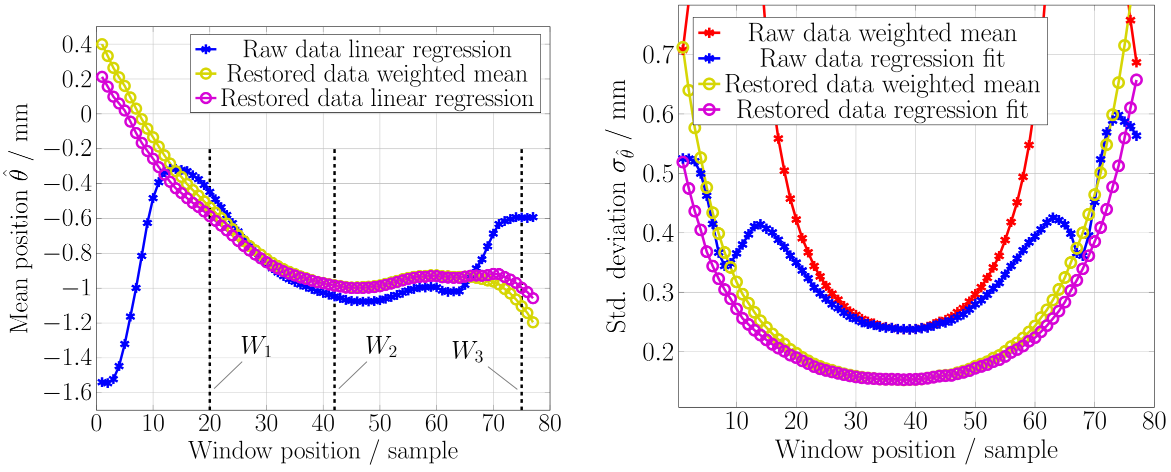

(a)

(b)

Figure 4.12: Mean $\bar{\hat{\theta}}$ and std. deviation $\sigma_{\hat{\theta}}$ of the 500 calculated position values using both algorithms with and without BLR against the window position. The marked window positions (W_1, W_2, W_3) correspond to Fig. 4.10b.

Measured bunches during acceleration

One instance of a bunch at the end of acceleration is shown in Fig. 4.13a. The blue curve is the direct raw data from the ADCs, while the red curve is the baseline restored data as discussed in the previous subsection. There are around 15 to 35 samples in the bunch. Fig. 4.13b shows the bunch-by-bunch position for 90 turns using regression fit algorithm for raw and restored data. There is a bias between the position calculated from the raw data and the restored data. This bias can be understood as an error due to the zero mean data assumption in Eq. 4.12. The bias and variance characteristics with respect to beam position are not shown, since they are similar to that of injected bunches.

Figure 4.14a and Fig. 4.14b show the mean position and std. deviation of accelerated bunches with respect to window position in line with Fig. 4.10b with each window consisting of 10 data samples. The observations are similar to the injection case. The only difference is that the sensitivity of position calculation on window position is higher due to less data samples in the detected bunch window and due to the narrow and steep bunch shapes.

The general conclusions of this section are:

1. The bias and variance for the position distribution with respect to window length and position for long bunches at injection and short bunches at the end of acceleration is studied.
2. During the whole acceleration cycle, the regression fit algorithm provides a more robust position estimation irrespectively of whether the baseline restoration procedure is used or not. Weighted mean algorithm can only be used with a "proper" baseline restoration.
3. There is a bias between position calculated from raw and restored data. The reason for the bias is an implicit assumption of "zero mean" data used while deriving Eq. 4.12.

Implementation details

Here we detail some of the computational complexity issues for each of the position estimation procedures. The implementation of the mentioned algorithms is performed in the Libera Hadron® FPGA Xilinx Virtex 2 Pro®, modell:2vp30ff1152-6 at the GSI beam instrumentation group [85, 86]. The resources required in terms of FPGA "area" and time for each implementation for 10 bit resolution is calculated by the ISE synthesizer for Xilinx Virtex 2 Pro®, modell:2vp30ff1152-6. The resources in percentage of total resources is shown in the Table 4.1.

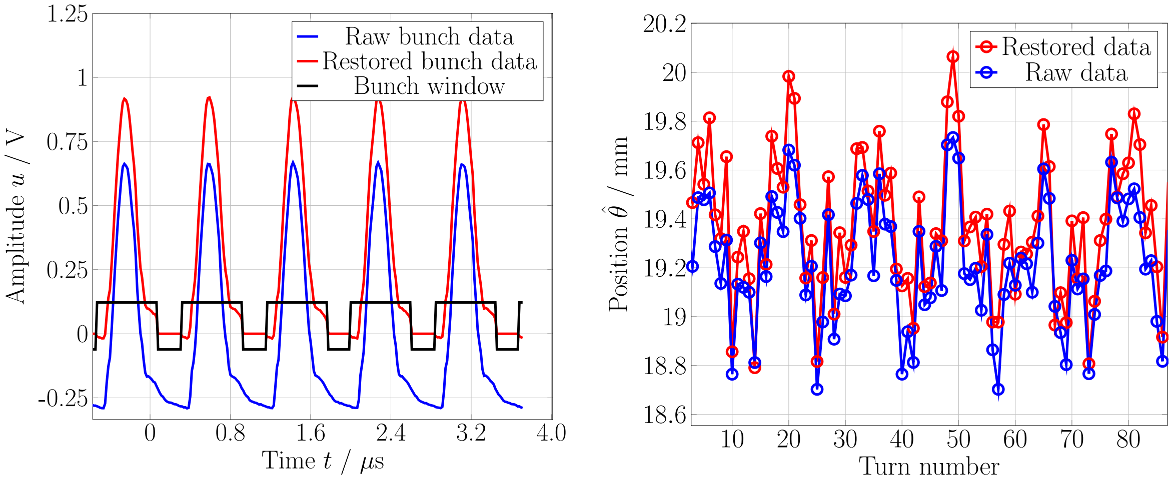

(a) (b)

Figure 4.13: The raw and restored bunches at the end of acceleration cycle are shown. Position is calculated by regression fit algorithm. There is clear bias between the position calculated from raw data and restored data.

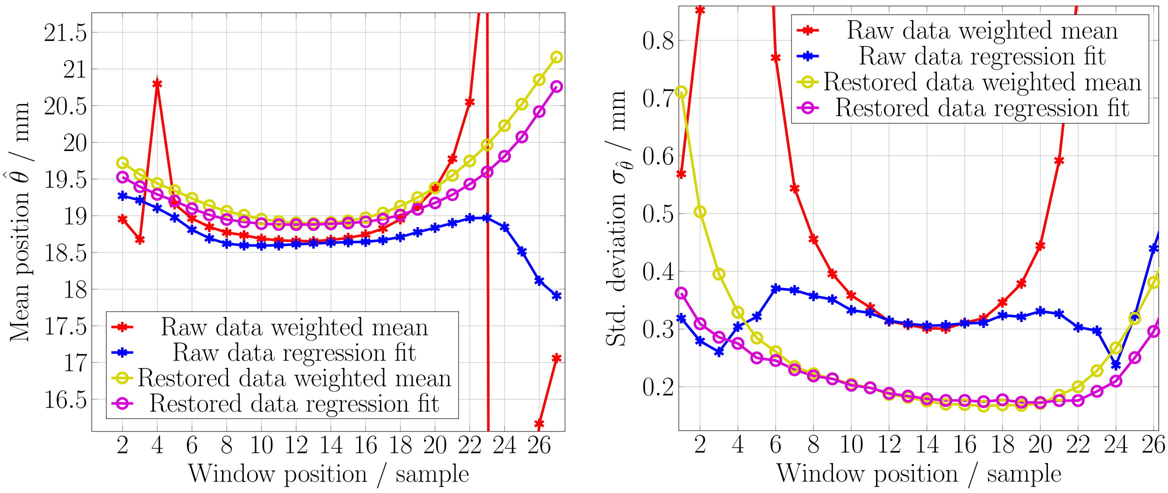

(a) (b)

Figure 4.14: Mean and std. deviation of the 500 calculated position values using both algorithms with and without BLR against the window position. The sampling period is 8 ns.

Table 4.1: Comparison of the two estimators in terms of resources and time required for 10 bit implementation in the FPGA.

Resources	Weighted mean with BLR	Linear Regression
Number of Slices	2%	5%
Number of Slice Flip Flops	2%	4%
Number of 4 input LUTs	1%	2%
Number of Block RAMs (1Kbyte)/multipliers	3%	2%
Latency	154 clock cycles	62 clock cycles

A slice is the basic resource unit in an FPGA, and consists of flip-flops, look up tables (LUTs) etc. and is specific to the family and model of the FPGA being used. Block Rams and multipliers (MULT18X18s) share a common pool in this particular FPGA model and thus are mentioned together. Weighted mean with BLR requires less resources, but has higher latency primarily due to the baseline restoration routine. Thus we conclude that weighted mean with BLR does not offer any significant advantage over linear regression algorithm from the FPGA implementation perspective.

SNR and resolution

Some comments on the relation between signal-to-noise ratio of the BPM signals and the position resolution are presented below.

- Noise is given by the (often static) amplifier configuration. Bunch-by-bunch position resolution is a function of SNR and the number of samples within the detected bunch.
- Position resolution is often quoted with a frequency i.e. 100 Hz or 1 kHz which is the rate at which one position or orbit value is calculated after averaging over all the values obtained in that period. This definition of resolution is only valid when the beam position at the BPM is known to be stationary below the quoted resolution which is often the case in storage rings.
- Determining position resolution from the real data is challenging since the beam centre-of-mass is a dynamic quantity, and it is important to differentiate between actual bunch motion and the noise contribution.

4.3 Tune spectrum estimation

Before the spectral estimation problem is formulated, it is necessary to specify the type of signal that will be studied, and how the spectrum that we want to estimate is defined. In the context of non-parametric spectral estimation, it is assumed that the signal under consideration is a sum of sinusoids embedded in stationary noise, i.e., that Eq. 4.14 holds, and consequently that the amplitude spectrum in Eq. 4.14 is the quantity of interest. On the other hand, signals observed in practice may not necessarily consist of superimposed sinusoids; if the signal is not a superposition of sinusoids then the estimation of the amplitude spectrum apparently amounts to implicitly approximating the signal with such a sum of sinusoids. Doing so may be useful in a wide range of applications. For instance, the presence of a hidden periodicity in the data can be revealed by estimating the relative amplitudes of many fictitious sinusoidal component in the data and estimating its frequency.

The problem of precise tune spectra determination can be found in literature[89, 90, 69, 91]. However,in [89, 90], only a small subset out of the large variety of methods are considered i.e. DFT, APA etc. and no specific details on their performance with measured data is mentioned. Similarly [69, 91] considers only tune determination assuming it as a single sinusoid. Thus, it mainly considers interpolation or iterative algorithms like SUSSIX or NAFF which may suffice for the LHC data but definitely not suitable for SIS-18. The challenges for tune spectra estimation during injection and acceleration a SIS-18 are fundamentally different. The ever changing beam conditions, along with space charge effects bring out complex frequency spectra which changes during acceleration due to change in machine optics. In addition to that, there are strong sinusoidal interferences depending on BPM locations which can be easily mis-identified as the tune peak, if algorithms searching for single sinusoids are used. The examples and the suitable methods for the transverse tune spectrum determination at SIS-18 are highlighted in this section.

4.3.1 Methods of spectrum estimation

The classical approach to spectrum analysis is invariantly the Discrete Fourier Transform (DFT), often visible/realised as FFT in practical implementations due to its computational efficiency. The spectral resolution of DFT based methods is considered poor in the domain of high resolution spectrum estimation methods, even though it is a robust method without any a priori assumptions about the data. On the other hand, there exist several parametric high-resolution methods that exhibit an excellent capability to resolve spectral peaks. This class of methods includes MUSIC [94], and other subspace-based methods [100]. In contrast to the DFT-based methods, these parametric techniques rely heavily on the assumption that the observed data consist of a known number of sinusoids in white noise or any other noise model, and unfortunately they often fail in applications where these assumptions are not perfectly satisfied. In this work, we will not consider parametric methods at all, even though some of them may be suitable for tune spectrum estimation. Another class of non-parametric methods are the so called filter bank based methods, which provide higher resolution compared to DFT based methods with a trade-off between resolution and robustness or statistical parameters. The basic idea behind these methods is to utilize the data properties in the design of the “matched filters” for each frequency of investigation [100]. Thus, these methods are in general data and frequency dependent. Capon method is one of the prominent examples among these methods which will be considered in this section. Here we will describe the various spectrum estimation methods under the common framework of weighted least squares (WLS) closely following the treatment in [99]. As examples for demonstrating the properties of various estimators, we will use two real position samples, one during injection and another during acceleration and calculate the spectrum using DFT, Averaged DFT (a variant of Welch method), and the Capon method.

Weighted least squares estimators

To put the method in perspective, a general class of spectral estimation method using weighted least squares is defined. Let $x(n)$ be a 1-D time series. For a given frequency (ω), $x(n)$ can be decomposed into a sinusoidal component of amplitude $\alpha(\omega)$ and residue $w_\omega(n)$.

$$x(n) = \alpha(\omega)\mathrm{e}^{j\omega n} + w_\omega(n) \tag{4.14}$$

where $w_\omega(n)$ includes all other sinusoids in $x(n)$ and the noise components. So, the problem of spectral estimation of $x(n)$ becomes finding $\alpha(\omega)$ for each ω given $x(n)$. Let us assume that we are given N consecutive samples of $x(n)$, viz., $x(n)$ for $n = 0, \cdots, N-1$. Let $M \leq N/2$ be a user parameter, whose choice will be discussed subsequently. If we rearrange Eq. 4.14 in the following matrix form,

$$\mathbf{Y} = \alpha(\omega)\mathbf{A}(\omega) + \mathbf{W}(\omega) \tag{4.15}$$

where the observed data $x(n)$ in arranged in an $M \times L$ Hankel matrix as follows:

$$\mathbf{Y} = [\mathbf{y}_0, \mathbf{y}_1, \cdots, \mathbf{y}_{L-1}] = \begin{bmatrix} x(0) & x(1) & \cdots & x(L-1) \\ x(1) & x(2) & \cdots & x(L) \\ \vdots & \vdots & \cdots & \vdots \\ x(M-1) & x(M) & \cdots & x(N-1) \end{bmatrix} \tag{4.16}$$

with $L = N - M + 1$. $\mathbf{A}(\omega)$ is defined as the following matrix,

$$\mathbf{A}(\omega) = \mathbf{a}_M(\omega)\mathbf{a}_L(\omega)^T \tag{4.17}$$

where $\mathbf{a}_P(\omega) = \begin{bmatrix} 1 \\ \mathrm{e}^{j\omega} \\ \vdots \\ \mathrm{e}^{j(p-1)\omega} \end{bmatrix}$ and $\mathbf{W}(\omega) = [\mathbf{w}_0(\omega), \mathbf{w}_1(\omega), \cdots \mathbf{w}_{L-1}(\omega)]$ is defined similarly as $\mathbf{Y}$ in matrix 4.16.

Eq. 4.15 expresses the typical linear regression problem between observed data and the quantity of interest. All the so-called parametric subspace methods [100] rely on an equation equivalent to Eq. 4.15 which is essential in order to formulate a low-rank signal model. The DFT method, certain averaged DFT methods, as well as the Capon and APES algorithms are also based on Eq. 4.15. In the present framework, the latter methods simply compute a WLS estimate of $\alpha(\omega)$ as follows:

$$\hat{\alpha}(\omega) = \underset{\alpha(\omega)}{\text{argmin}} \left| \phi^{\frac{-1}{2}}(\omega)\Big(\mathbf{Y} - \alpha(\omega)\mathbf{A}(\omega)\Big) \right|^2 \tag{4.18}$$

where $\boldsymbol{\phi}(\omega)$ is a weighting matrix and $(.)^{\frac{1}{2}}$ denotes the square root of a Hermitian matrix. The WLS criterion in Eq. 4.18 effectively pre-whitens the columns of $\mathbf{Y}$ with an ω-dependent weight matrix $\boldsymbol{\phi}(\omega)$ to account for a possible colouration of the residual signal $w_\omega(n)$, and then fits a single sinusoidal model to the pre-whitened data. The well known solution to Eq. 4.18 can be found as,

$$\hat{\alpha}(\omega) = \frac{\mathbf{a}_M^H(\omega)\boldsymbol{\phi}^{\frac{-1}{2}}\mathbf{g}(\omega)}{\mathbf{a}_M^H(\omega)\boldsymbol{\phi}^{\frac{-1}{2}}\mathbf{a}_M(\omega)} \tag{4.19}$$

where $(.)^H$ denotes the complex conjugate transpose and

$$\mathbf{g}(\omega) = \frac{1}{L}\mathbf{Y}\mathbf{a}_L^*(\omega) \tag{4.20}$$

The difference between the DFT, Averaged DFT and Capon methods is the choice of M and $\boldsymbol{\phi}(\omega)$. For many of the estimates presented below, the matrix $\boldsymbol{\phi}(\omega)$ is a function of the covariance sequence of $x(n)$. In a strict sense, this covariance sequence is only well-defined if $x(n)$ is a stationary random process. Under the assumption that $x(n)$ is stationary, the following covariance matrix is well-defined:

$$\mathbf{R} = E[\mathbf{y}_k\mathbf{y}_k^H] \tag{4.21}$$

(and is independent of k). Moreover, since $\mathbf{w}_k(\omega)$ are identically distributed, the covariance matrix

$$\mathbf{Q}(\omega) = E[\mathbf{w}_k(\omega)\mathbf{w}_k^H(\omega)] \tag{4.22}$$

is also well defined (and independent of k). Finally, under the same assumption, it follows (after some steps given in [99]) that,

$$\mathbf{Q}(\omega) = \mathbf{R} - E[|\alpha(\omega)|^2]\mathbf{a}_M(\omega)\mathbf{a}_M^H(\omega) \tag{4.23}$$

An ideal choice of weighting matrix for the WLS problem would be to use $\boldsymbol{\phi}(\omega) = \mathbf{Q}(\omega)$ since this yields a Markov-like estimate that is known to have optimal (in a certain sense) statistical properties [100]. This matrix effectively captures the statistics of the residual term $w_\omega(n)$ in 4.14. In practice $\mathbf{Q}(\omega)$ is unknown, thus $\mathbf{R}$ is used as the weighting matrix which has a certain proportional relation with $\mathbf{Q}(\omega)$ evident from Eq. 4.23.

DFT

If we consider $M = 1$, consequently we have $L = N$. In this case, $\boldsymbol{\phi}(\omega)$ disappears from both, the formulation in Eq. 4.18 and from the solution Eq. 4.19 of the LS problem. The resulting spectral estimate Eq. 4.19 reduces to the well-known DFT estimate:

$$\hat{\alpha}_{DFT}(\omega) = \frac{1}{N}\mathbf{a}_N^H(\omega)\mathbf{y} = \frac{1}{N}\sum_{n=0}^{N-1} x(n)e^{-j\omega n} \tag{4.24}$$

This directly corresponds to a periodogram or a modified periodogram in case of data conditioning by applying windows.

Averaged DFT

If $M > 1$, and $\boldsymbol{\phi}(\omega) = \mathbf{I}$, an averaged version of FFT is obtained,

$$\hat{\alpha}_{A-DFT}(\omega) = \frac{1}{M}\mathbf{a}_M^H(\omega)\mathbf{g}(\omega) = \frac{1}{LM}\sum_{l=0}^{L-1}\sum_{m=0}^{M-1} x(l+m)e^{-j\omega(l+m)} \tag{4.25}$$

Effectively, in this case the parameter M can be interpreted as a smoothing lag that trades spectral resolution for improved statistical stability (variance). This method corresponds to Welch estimator, and to the Bartlett estimator, in case the segments are not overlapped i.e. $N = ML$.

Capon method

The Capon method can easily be described in the current framework by choosing an ω independent weighting matrix $\boldsymbol{\phi}(\omega)$ that is a sample estimate of the data covariance matrix $\mathbf{R}$,

$$\phi_{Capon}(\omega) = \hat{\mathbf{R}} = \frac{1}{L}\mathbf{Y}\mathbf{Y}^{\mathbf{H}} = \frac{1}{L}\sum_{l=0}^{L-1}\mathbf{y}_l\mathbf{y}_l^H \tag{4.26}$$

The resulting estimator is

$$\hat{\alpha}_{Capon}(\omega) = \frac{\mathbf{a}_M^H(\omega)\mathbf{R}^{-1}\mathbf{g}(\omega)}{\mathbf{a}_M^H(\omega)\mathbf{R}^{-1}\mathbf{a}_M(\omega)} \tag{4.27}$$

As mentioned earlier, Capon estimator makes use of Eq. 4.23 for a reasonable approximation of $\mathbf{Q}(\omega)$ and uses the covariance matrix defined in Eq. 4.22 as $\boldsymbol{\phi}(\omega)$. Even though it is not the most optimum solution of optimization problem, defined in Eq. 4.15, it gives much better "resolving power" compared to simple DFT or averaged DFT estimates as discussed later. This method is also referred as amplitude-spectrum Capon (ASC) estimator which should be distinguished from power spectrum Capon. More adavanced methods, such as APES, take a step further in this respect but referred to dedicated texts [100] on signal processing. All the above derivations can be derived from a more intuitive matched filter-bank interpretation discussed in the appendix 7.

Properties of the estimators

Detailed derivations of the estimator properties for DFT and Averaged DFT can be found [93]. To understand the detailed properties of Capon method, the reader is referred to [99]. However the important properties are highlighted here,

- DFT in an inconsistent estimator, its variance $Var(DFT)$ does not $\rightarrow 0$ as the sample length $N \rightarrow \infty$. However, it is asymptotically unbiased i.e. $Bias(DFT) \rightarrow 0$ as $N \rightarrow \infty$.
- Averaged DFT trades resolution for improving the variance characteristics of DFT.
- Capon is a slightly downward biased estimator, and possesses better leakage properties compared to the DFT for short data segments.
- FFT algorithm to calculate DFT is computationally more efficient i.e $O(NLogN)$ when compared to the Capon method (and similar filter bank based methods), where the available algorithms have the complexity of at least $O(N^3)$ [99].

Further we compare the performance of the DFT which is the most commonly used method for calculating spectrum with the Capon estimator, used mostly in specialized domains such as radar array data processing. An example each for the estimated spectrum from the BPM data on the injection plateau and during acceleration is presented below.

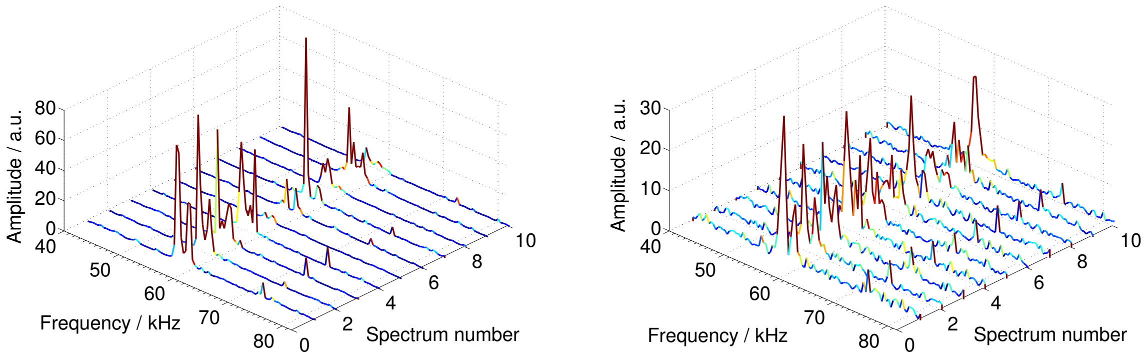

(a) (b)

Figure 4.15: The vertical tune spectra at injection revolution frequency of 214 kHz using 512 samples is calculated using the Capon and FFT methods . The Capon method (a) is found to have a lower noise floor and higher “resolving power” compared to FFT (b). The various head-tail modes are visible.

Injection example

Figure. 4.15 shows a waterfall plot of the vertical tune spectrum at injection revolution frequency of 214 kHz using 512 samples per spectra calculated using the Capon and FFT methods. One of the spectra from Fig. 4.15 is shown in Fig. 4.16. The Capon method (a) is found to have a lower noise floor and higher “resolving power” compared to FFT (b). The various head-tail modes are visible with their relative amplitudes varying over time due to the noise excitation.

Acceleration example

The surface plot in Fig. 4.17 shows the vertical tune spectra using the BPM data from the TOPOS system during acceleration. One spectra is obtained with 512 samples as comparison of Capon (a) vs FFT (b) method. The Capon clearly shows a better performance.

Comparison between the spectrum estimators

The results obtained from the data clearly favour the Capon method over DFT. Similar results were obtained, for empirical studies have shown that the ability of the Capon method to resolve fine details of a PSD, such as closely spaced peaks, is superior to the corresponding performance of the periodogram based methods [99]. The reason for this could be understood from the following argument concerning the “resolution” and “resolving power” from [100]. It should be stressed that the notion of “resolution” refers to the ability of the theoretically averaged spectral estimate $E(\hat{\alpha}(\omega))$ to resolve fine details in the true PSD $E(\alpha(\omega))$. This resolution is roughly inversely proportional to the window’s length or the bandpass filter impulse response’s aperture. The “resolving power” corresponding to the estimate $\hat{\alpha}(\omega)$ is more difficult to quantify, but of course it is what interests the most. It should be clear that the resolving power of $\hat{\alpha}(\omega)$ depends not only on the bias of this estimate (i.e., on $E(\hat{\alpha}(\omega))$, but also on its variance. A spectral estimator with low bias-based resolution but high statistical accuracy may be better able to resolve finer details in a studied PSD than can a high resolution/low accuracy estimator. Since the periodogram may achieve better bias-based resolution than the Capon method, the higher (empirically observed) “resolving power” of the latter should be due to a better statistical accuracy (i.e., a lower variance).

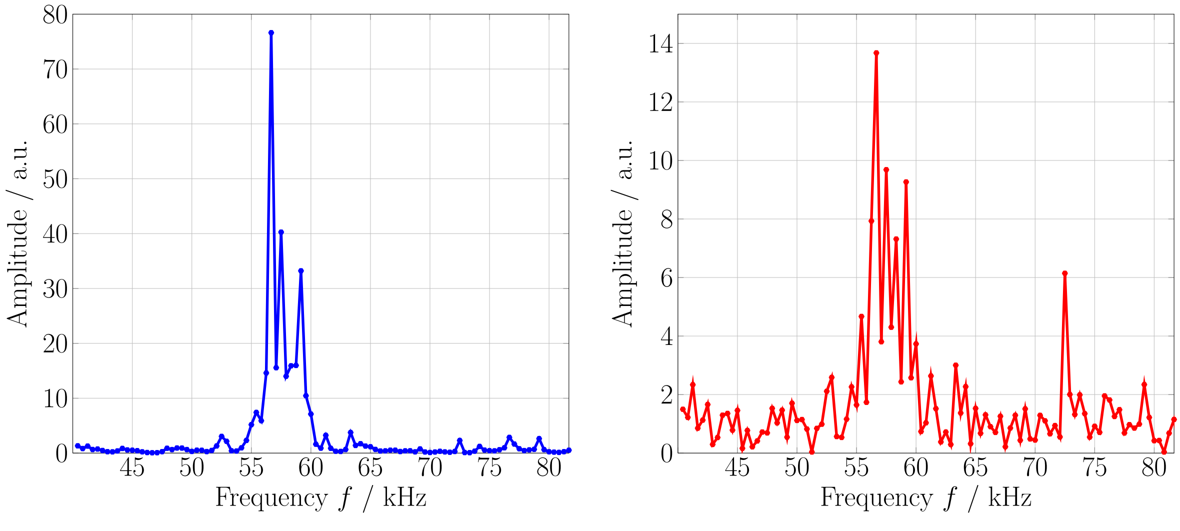

(a) (b)

Figure 4.16: One "snapshot" spectrum from Fig. 4.15 showing higher resolution for Capon method (a) in comparison to FFT method (b).

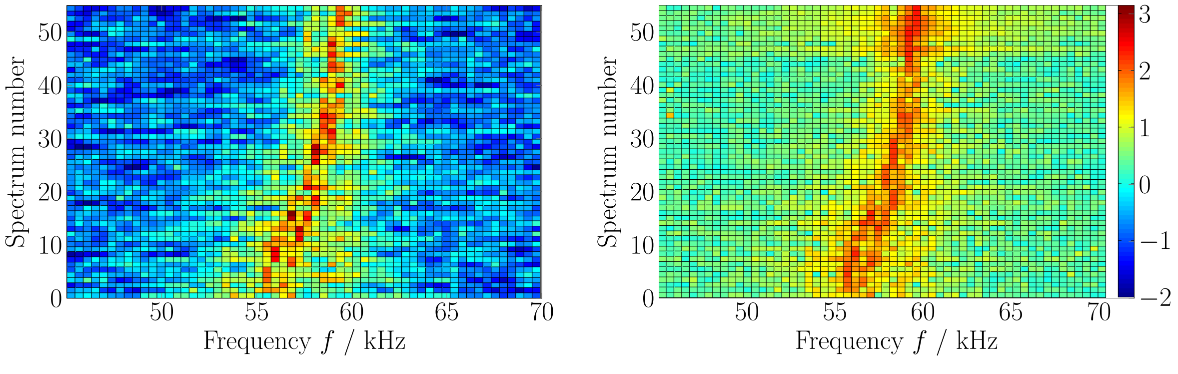

(a) (b)

Figure 4.17: Surface plot showing the vertical tune spectra during acceleration. Each spectrum is calculated using 512 samples both with Capon (a) and FFT (b) method. The Capon estimator clearly shows a better performance.

4.3.2 Tune calculation from spectrum

With the challenges of higher order head-tail modes excited near the tune frequency $k = 0$ mode, finding bare tune requires more information than just the spectrum at hand. It requires the information on the beam profile, the beam current and the chromaticity. This will be further detailed in the next chapter.

4.4 Summary

1. The details of each step from raw BPM data to tune spectra calculation are discussed.
2. Position estimation using two alternate methods i.e. weighted mean and linear regression fit (with and without BLR) are described.
3. The two algorithms are compared for bias, resolution, robustness and computation overhead with simulated and measured BPM data at the injection energy and at higher energies.
4. Linear regression fit is found to be advantageous in terms of robustness, and computation time. Bias and resolution performance is comparable in both cases.
5. Other high resolution non-parametric method i.e. Capon method is discussed in comparison with conventional DFT, with examples of tune spectra calculation of measured data in SIS-18.

5 Experiments and Results

This chapter will give a short description of the major beam diagnostics instruments used during the experiments. Then the general measurement setup, beam parameters and measurement errors will be discussed. Finally the major results will be presented in context of the theory presented in the previous chapters.

5.1 Beam diagnostics

Several beam diagnostic instruments were used in synchronism with position and tune measurement systems discussed in previous chapters to arrive at the results described in this chapter. This includes mainly Schottky monitor, DC current transformer (DC-CT) and Ionization profile monitor (IPM).

5.1.1 DC current transformer

The working principle of the DC current transformer is shown in Fig. 5.1. The beam pipe is enclosed by two tori, each consisting of 3 windings. The first windings of each torus with opposite orientation are used as a modulator. The modulation frequency is typically $1 - 10$ kHz. The amplitude of the modulation current I_{mod} is high enough to force the torus into magnetic saturation at the opposite ends of hysteresis curve twice a period. The secondary windings with equal orientation act as a detector for the modulated signal. Assuming perfectly identical magnetic characteristics of both tori, the detector signal, as shown in the scheme, should be exactly zero if there is no beam current flowing through the tori. However, an asymmetric shifting of the hysteresis curve results if a DC-beam is fed through the toroids, because of the additional magnetic field from the beam. The sum voltage signal u_S thus generated by I_{sense} is different from zero with a modulation twice the modulation frequency. Then the u_S is rectified and a proportional current I_{comp} is generated in the feedback compensation circuit which forces the output signal back to zero. The applied feedback current is the measured DC beam current which flows through the third winding of both tori. Due to the extremely specific requirements concerning the matching of the magnetic characteristics for a pair of tori, the design of a magnetic modulator with high resolution and DC-stability is rather complex and the success depends very much on the selection and treatment of the core-material as discussed in [104].

The applied feedback circuit for the zero flux compensation makes the device very sensitive and linear. The time resolution of the full device installed at GSI SIS-18 is ≈ 20 μs. The current resolution is about ≈ 1 μA. The offset drifts are mainly caused by the magnetic properties of the tori, and are of the order of ≈ 20 μA per day and can be compensated when no beam is present in the synchrotron. More details about the exact construction and material properties can be found in [104].

5.1.2 Schottky diagnostics

The theory of longitudinal and transverse Schottky beam signals is presented in section 2.2.1. Here we will discuss the practical installation and operation of a Schottky measurement system. Figure 5.2a shows the photo of Schottky pick-up installed in the storage ring at GSI. A similar device with some modifications is installed in SIS-18. The concave shaped plates are oriented horizontally and vertically to form the capacitors in respective planes. The operational principle is thus similar to the capacitive pick-ups explained in section 3.2.1 in the context of TOPOS BPMs. The main difference here is the large pick-up design which offers high sensitivity. Detailed description of the design considerations and hardware is given in [102]. The sensitivity of the pick-up can be adjusted by varying the distance between the plates.

The scheme for the measurements is shown in Fig. 5.2b. The sum of the pre-amplified outputs from a pair of plates yields a signal proportional to the beam current. Thus the sum of the signals indicates the longitudinal Schottky

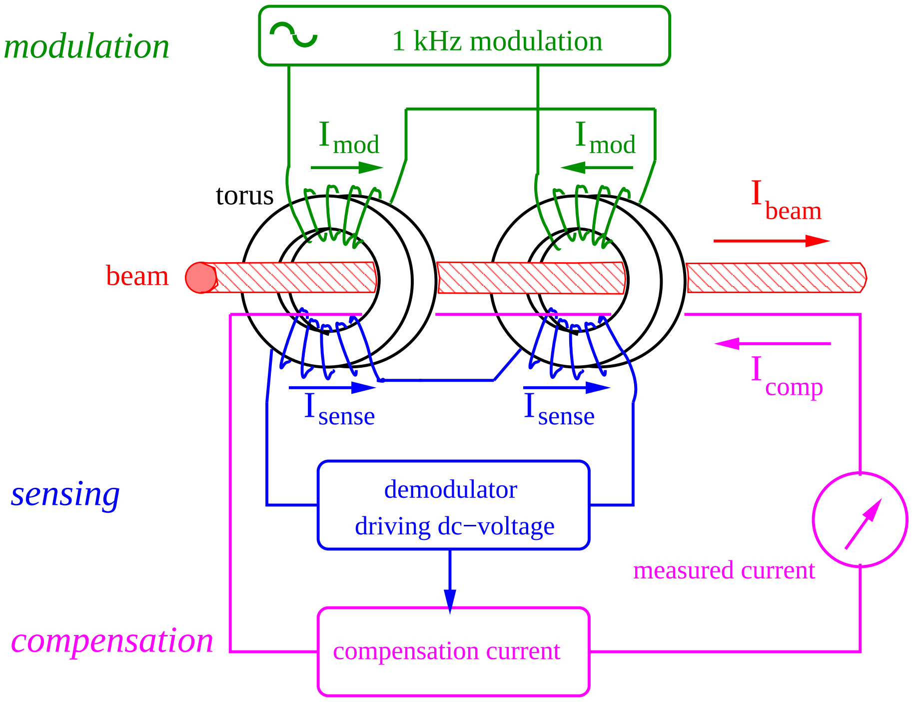

Figure 5.1: The working principle of the DC current transformer [67].

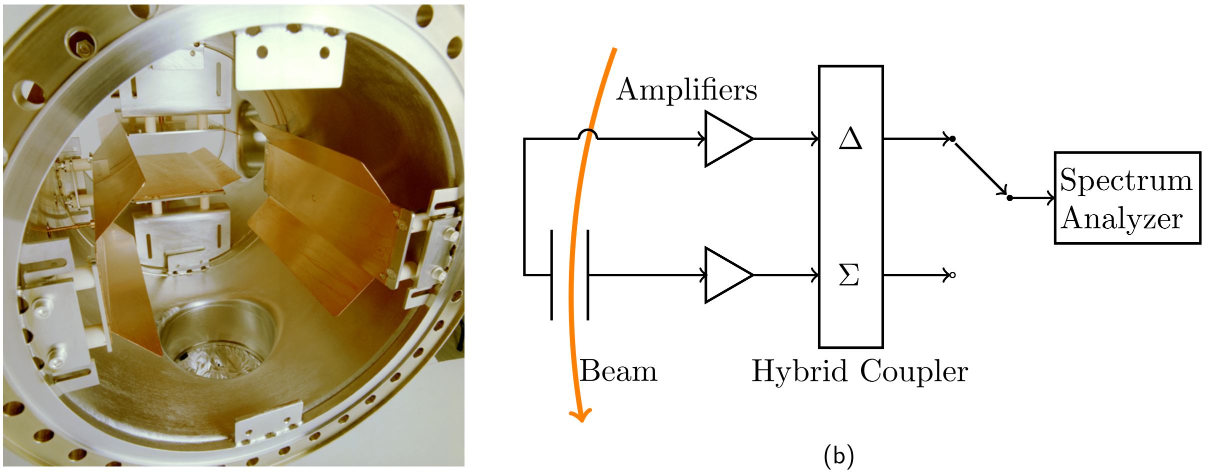

(a)

(b)

Figure 5.2: The Schottky pick-up installed in ESR (a)(Courtesy A. Zschau). The scheme for longitudinal and transverse Schottky measurements at SIS-18 (b).

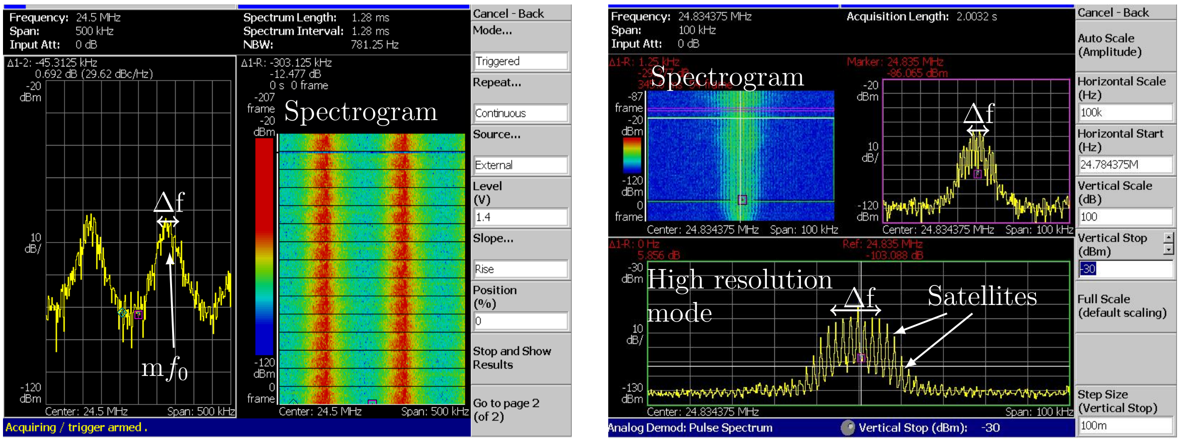

Frequency: 24.5 MHz
Span: 500 kHz
Input Att: 0 dB
Spectrum Length: 1.28 ms
Spectrum Interval: 1.28 ms
NBW: 781.25 Hz
Δ1-2: -45.3125 kHz
0.692 dB (29.62 dBc/Hz)
Δ1-R: -303.125 kHz
-12.477 dB
0 s 0 frame
Center: 24.5 MHz Span: 500 kHz
Mode... Triggered
Repeat... Continuous
Source... External
Level (V) 1.4
Slope... Rise
Position (%) 0
Acquiring / trigger armed .

Frequency: 24.834375 MHz
Span: 100 kHz
Input Att: 0 dB
Acquisition Length: 2.0032 s
Δ1-R: 1.25 kHz
Marker: 24.835 MHz
-86.065 dBm
Center: 24.834375 MHz Span: 100 kHz
Δ1-R: 0 Hz
5.856 dB
Ref: 24.835 MHz
-103.088 dB
Horizontal Scale (Hz) 100k
Horizontal Start (Hz) 24.784375M
Vertical Scale (dB) 100
Vertical Stop (dBm) -30
Step Size (Vertical Stop) 100m
Analog Demod: Pulse Spectrum
Vertical Stop (dBm): -30

(a) (b)

Figure 5.3: Longitudinal Schottky of a coasting beam (a) and bunched beam (b).

spectrum of the beam. On the other hand, the difference of the signals provides a measure for the current dipole moment which is the transverse Schottky spectrum. The signal in either of the cases is measured by using a real time spectrum analyser, RSA3303A®, from Tektronix® [103]. The transverse signal is measured similarly using the difference signal. The primary usage of this device during the work is to measure beam momentum spread. A longitudinal Schottky measurement screenshot during a coasting beam operation and bunched beam operation at SIS-18 is shown in Fig 5.3b. The momentum spread (2σ) can be measured using Eq. 2.16 which is repeated here,

$$\frac{\Delta f}{m f_0} = -\eta \frac{\Delta p}{p_0} \tag{5.1}$$

where Δf is the 2σ bandwidth of the Schottky band indicated in Fig. 5.3a. One can recall from section 2.2.1, that the momentum spread of a bunched beam can be found by using the envelope around the synchrotron satellites, and using the 2σ bandwidth of the envelope indicated in Fig. 5.3b.

5.1.3 Ionization profile monitor

The ionization profile monitor (IPM) or residual gas monitor (RGM) is a transverse beam profile measurement device installed at SIS-18. There are distinct devices for measurement of the transverse profile for each plane. The working principle is shown in Fig. 5.4a and the photo of device installed in SIS-18 is shown in Fig. 5.4b. The ion beam, circulating in SIS-18, ionizes the residual gas in the beam pipe. An electric field, with a field strength of ≈ 300 to 450 V/cm, is applied to these ions for transportation to a micro-channel plate (MCP) with the dimensions 100×30 mm. Directly behind the MCP is a wire mesh consisting of 64 wires each having a diameter of 1.5 mm and a wire spacing of 0.6 mm. The current induced by the ions on the wire mesh is transformed to a voltage, amplified, digitized and registered by the data acquisition system. The recording time of a single measurement can be chosen between either 0.5 ms and 5 ms. A read-out is made every 10 ms and a new measurement is automatically started, the data is compressed and stored in a file on a PC [105]. The wire diameter and spacing define the measurement resolution of 2.1 mm per channel for a single measurement. However, the acquired data is integrated over several turns and the actual measurement resolution is better, see section 5.1.4.

An example of the IPM GUI screenshot is shown in Fig. 5.5. An Ar^{18+} ion beam is accelerated from 11.4 MeV/u to 140 MeV/u. The beam profile measurements in horizontal (a) and vertical planes (b) are shown. Top right (c) in the Fig. 5.4 shows the dipole magnet ramp and the output of beam current transformer (DC-CT). Furthermore, (d) shows the integrated beam profiles over time (bottom left, red = horizontal, vertical = blue), by adding up all the signals on each wire. The beam positions for both planes are found by finding an average (e). Fig. 5.4(f) shows the rms beam width of the profiles. The digital recording of the profile data was used throughout this work for all measurement accelerator cycles.

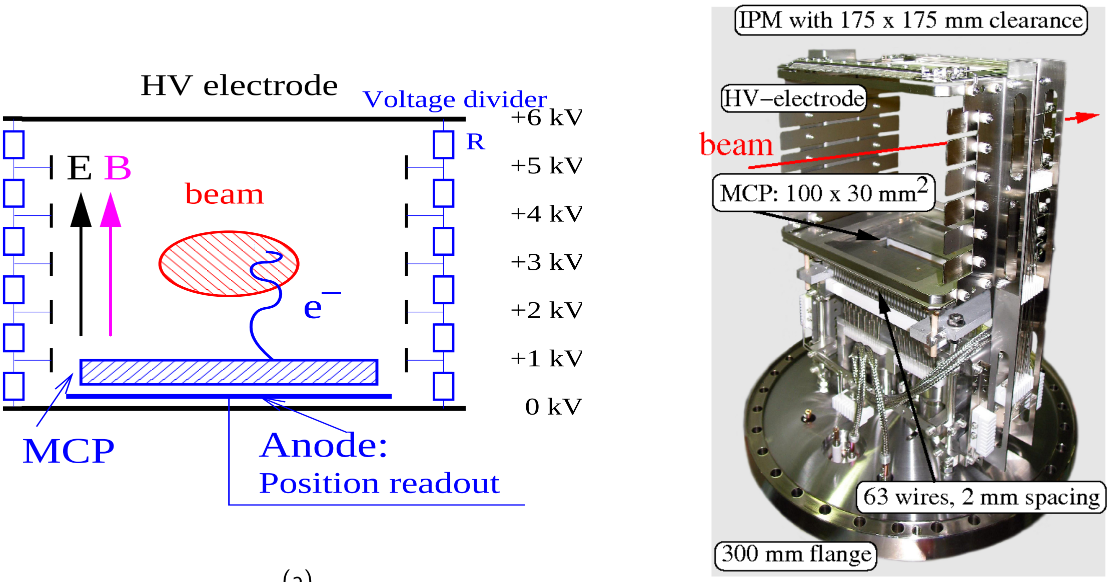

(a)

(b)

Figure 5.4: Working principle of the IPM (a) [67]. Photograph of the IPM installed at SIS-18 (b)(Courtesy T. Giacomini).

5.1.4 Measurement uncertainties

The calculation of high intensity effects such that ΔQ_{sc} from Eq. 2.53 has a dependence on measured current, transverse beam profiles, longitudinal beam profiles and the Twiss parameters. The measurement uncertainty on each of these measured parameters at GSI SIS-18 were commented in the detailed analysis in [112]. Even though some parameters and the associated uncertainties are correlated, any correlations are neglected in the simplified analysis. Uncertainties in each measured parameter are propagated to find the error bars on the calculated and measured incoherent tune shifts.

Reproducing from Ref. [112], the relative random uncertainty (std. deviation) in beam profile width (σ_x) measurements is given by Eq. 5.2.

$$\frac{\delta\sigma_x}{\sigma_x} = \frac{0.043}{B} + 0.33 \cdot \delta N_i \tag{5.2}$$

where $\Delta x_s = 2.1$ mm is the wire spacing and $\delta N_i = \frac{1}{2^8}$ is the ADC resolution of the IPM and B is defined as $\sigma_x/\Delta x_s$. If the error bars are derived from j measurements, the measured profile is given by

$$\sigma_{av,x} = \langle\sigma_x\rangle_j,\ \delta\sigma_{av,x} = \sqrt{\langle\sigma_x^2\rangle_j - \langle\sigma_x\rangle_j^2 + \langle\delta\sigma_x\rangle_j^{\ 2}} \tag{5.3}$$

For each tune measurement at the given intensity and excitation power, 5-8 transverse beam profiles were measured, and the relative error is obtained $\approx 5\%$ using Eq. 5.2 and Eq. 5.3. The relative systematic error (bias) in transverse beam width measurements is $< 1\%$ [112] and ignored in this analysis.

The uncertainty in the injected current is dominated by fluctuations in the source and the relative uncertainty is estimated to be $\approx 5\%$ based on 5-8 measurements at the same intensity settings for each measurement point. Bunch length and bunching factor vary by $\approx 2-3\%$ due to long term beam losses only under high intensity beam conditions. The maximum relative bias in the lattice parameter $\hat{\beta}$ is assumed to be $\approx 5\%$ at the IPM location. Taking all the

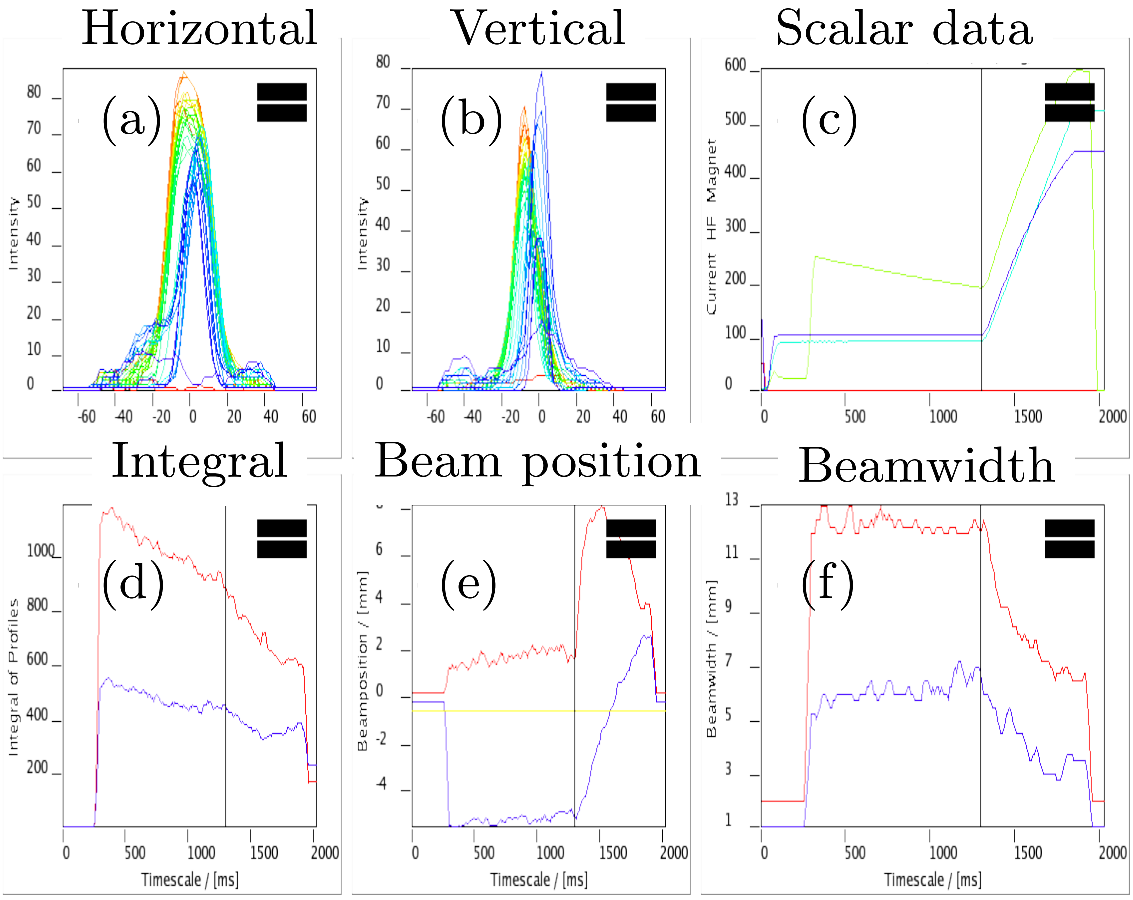

Figure 5.5: IPM GUI showing the evolution of beam profiles and other machine settings over time. (a) Horizontal profiles, (b) Vertical planes, (c) shows the dipole magnet ramp (blue) and the output of beam current transformer (DC-CT) (yellow), (d) shows the integrated beam profiles over time (red = horizontal, blue = vertical), by adding up all the signals on each wire,(e) Beam centroid for both planes and (f) shows the rms beam width of the profiles (red = horizontal, blue = vertical).

relative errors, uncertainty propagation using familiar Eq. 5.4 gives relative error for estimated incoherent tune shifts $\approx 12\%$.

$$\frac{\delta\epsilon_{av,x}}{\epsilon_{av,x}} = \sqrt{4(\frac{\delta\sigma_{av,x}}{\sigma_{av,x}})^2 + (\frac{\delta\hat{\beta}_x}{\hat{\beta}_x})^2}$$
$$\frac{\delta\Delta Q_{sc}}{\Delta Q_{sc}} = \sqrt{(\frac{\delta\epsilon_{av,x}}{\epsilon_{av,x}})^2 + (\frac{\delta I_p}{I_p})^2} \tag{5.4}$$

Tune measurements, done by averaging over long intervals, contribute to the width of modes due to long term beam losses. Beam losses lead to change in coherent tune especially in the vertical plane where the image current effects are larger. This has been highlighted at appropriate sections in the text.

Calculation of bunching factor

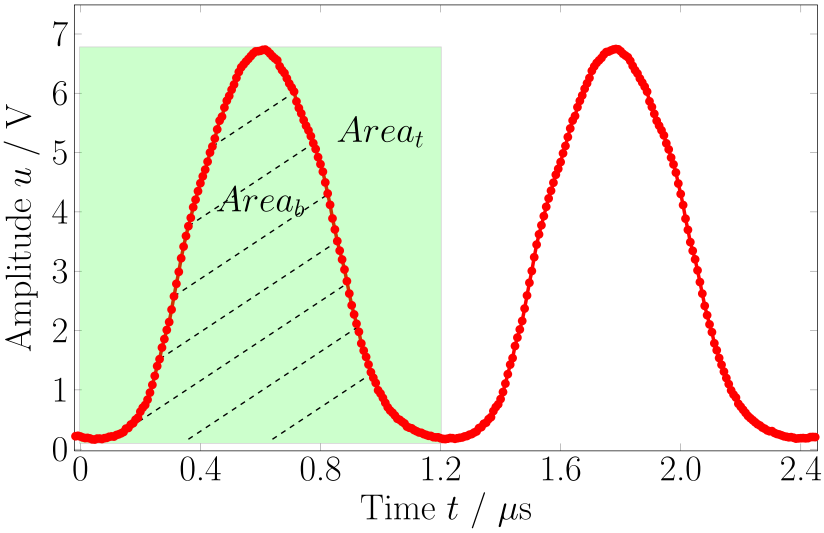

Figure 5.6: A typical normalized longitudinal beam profile from TOPOS system. The length of the rf period is $\approx 1.2\mu s$.

Figure 5.6 shows a typical longitudinal profile of the bunch. The bunching factor is calculated by the Eq. 5.5.

$$B_f = \frac{Area_b}{Area_t} = \frac{\sum_{n=1}^{N} u_n}{max(u_n) \cdot N} \tag{5.5}$$

where u_n is the voltage at time instant n and N is the number of samples in one rf period (≈ 150 at injection). The TOPOS system samples the bunch at 125 MSa/s, thus the difference between adjacent samples is 8 ns.

5.2 Experimental details

A typical acceleration cycle in SIS-18 is comprised of the following steps. The beam is injected from the UNILAC via the transfer channel into the SIS-18 with no longitudinal rf voltage (no bucket-bucket transfer) over ≈ 20 turns (multi-turn injection). Injection is a crucial step in the acceleration cycle in terms of beam quality and requires neat optimization. The coasting (dc) beam, thus injected, is captured in four radio frequency buckets using adiabatic bunching and then accelerated. Figure 5.7 shows one of the special ramp cycle used during one of our experiments. The signals of interest in the description here are *S02BE1_Amp* which is the amplitude of SIS-18 rf and *SIS_HF_Frequenz* is the SIS-18 rf frequency. The beam is injected at time **(a)** and the adiabatic bunching starts at **(b)**, at **(c)** the rf voltage is switched off and the bunch is de-bunched. Starting from **(d)**, the beam acceleration starts, as the ramp frequency and dipole magnetic field increase in synchronism according to Eq. 2.2. The state of the synchrotron after acceleration ramp is called flat top where the beam is extracted**(e)** and is followed by the ramping down of rf frequency and magnetic fields in **(f)**. Most of the experiments, performed in the scope of this thesis, were on the bunched injection plateau i.e. between **(b)** and **(c)**. Data are obtained during long injection plateaus of 600 ms where the beam excitation is applied. Some data was also recorded during the acceleration and on the "flat top".

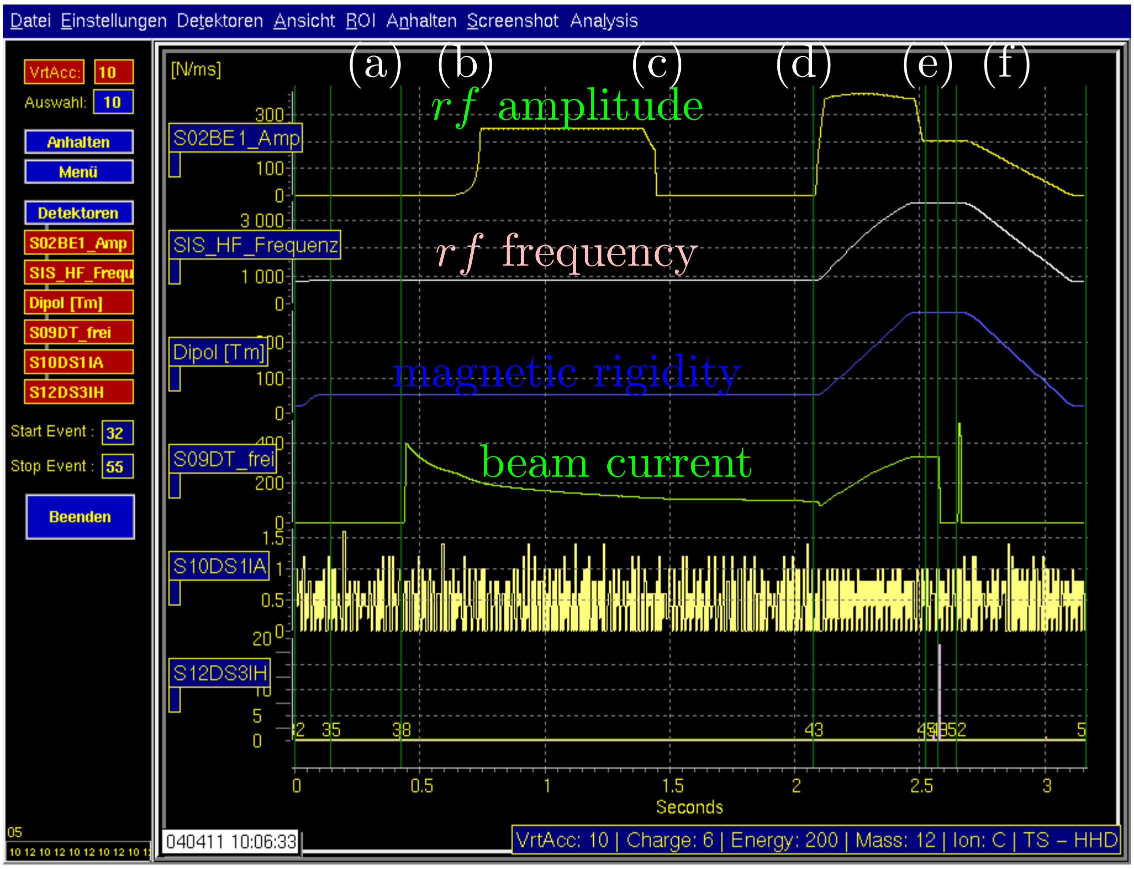

Figure 5.7: Various signals from the ABLASS measurement tool, see text.

5.2.1 Measurement set-up

The experiments described here were carried out using N^{7+} and U^{73+} ion beams at the SIS-18 injection energy of 11.4 MeV/u. At injection energy, the space charge effects are usually strongest. Four bunches are formed from the initially coasting beam during adiabatic rf capture. The experiment was repeated for different injection currents. At each intensity level several measurements were performed with different types and levels of beam excitation in both planes.Tune measurements were done simultaneously using the TOPOS and BBQ systems. The beam current and the transverse beam profile are measured using the beam current transformer [104] and the ionization profile monitor (IPM) [105] respectively. A typical transverse beam profile is shown in Fig. 5.8. The dipole synchrotron tune (Q_{s1}) is deduced using the residual longitudinal dipole fluctuations of the bunches. Q_{s1} has been used as an effective synchrotron tune for all experimental results and will be referred as Q_s from here-on. The momentum spread is obtained from longitudinal Schottky measurements [106].

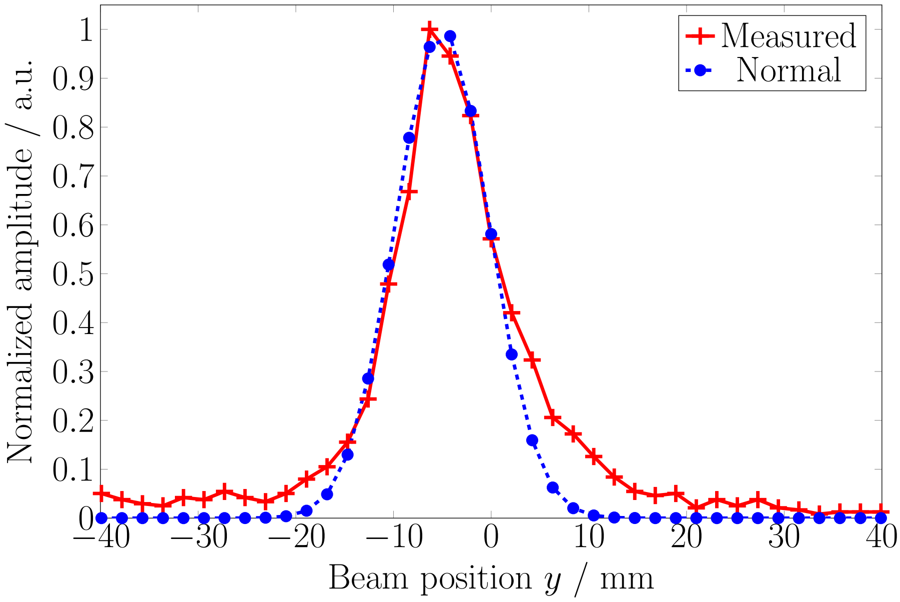

Figure 5.8: Normalized transverse beam profile in the vertical plane with $N^{7+} = 15 \cdot 10^8$ ions at injection. The dotted lines shows the normal distribution for the rms width obtained by evaluation of beam profile around its centre.

5.2.2 Beam parameters during the measurements

Important beam parameters during the experiment are given in Tab. 5.1 and Tab. 5.2. It is important to note that all the parameters required for analytical determination of q_{sc}, q_c were recorded during the experiments.

From Tab. 5.1 and Tab. 5.2 one can estimate that in the measurements, the space charge and image current parameters, were in the range $q_{sc} \lesssim 10$ and $q_c \lesssim 0.2q_{sc}$ for the horizontal and vertical planes. $\hat{\beta}_{x,trip}$ and $\hat{\beta}_{y,trip}$ are the lattice parameters for the SIS-18 triplet lattice, which is used at the injection plateaus.

5.2.3 Adiabatic capture

An unbunched charged particle beam i.e. coasting or dc beam in SIS-18 is captured by "switching ON" the rf voltage slowly enough such that to preserve the longitudinal emittance during the whole capturing process as well as to capture all the particles in the beam. This is known as the adiabatic capture [35] of the DC beam. The reference time scale for the particle motion in the longitudinal phase space is the period of synchrotron motion T_s. For the adiabatic capture, the increase in the amplitude of the rf voltage u should be slow enough to result in a linear variation of the phase space parameters, synchrotron period T_s and synchrotron frequency ω_s [107, 108], to avoid dilution of phase space. Although there are many possibilities and conditions to obtain adiabatic ramps, the following condition, shown in Eq. 5.6, is most often used to obtain the iso-adiabatic ramp,

$$\alpha_{ia} = \frac{1}{2\pi}\left|\frac{dT_s}{dt}\right| = \left|\frac{1}{\omega_s^2}\frac{d\omega_s}{dt}\right| \ll 1 \tag{5.6}$$

where t_{ramp} is the ramping time, which is time required to reach the final value u_f from its initial value u_i and the voltage values u_i and u_f. Putting in synchrotron tune values from 2 in Eq. 5.6, one obtains the following condition for iso-adiabatic ramps,

$$u(t) = \frac{u_i}{\left(1 - \dfrac{t}{t_{ramp}}\dfrac{\sqrt{u_f} - \sqrt{u_i}}{\sqrt{u_f}}\right)^2} \tag{5.7}$$

Table 5.1: Beam parameters during the U^{73+} experiment

Beam/Machine parameter	Symbol	Value
Atomic mass	A	238
Charge state	Z	73
Kinetic energy	W_{kin}	11.4 MeV/u (measured
Number of particles	N_p	$1, 5, 12 \cdot 10^8$ (measured)
Tune	Q_x, Q_y	4.31, 3.27 (set value)
Chromaticity	ξ_x, ξ_y	-0.94, -1.85 (set value)
Transverse emittance	$\epsilon_x, \epsilon_y(2\sigma)$	$45, 22$ mm-mrad (measured)
Slip factor	η	0.94
Bunching factor	B_f	0.4 (measured)
Synchrotron tune	Q_{s0}, Q_{s1}	0.007,0.0065 (measured)
Momentum spread	$\frac{\Delta p}{p}(1\sigma)$	0.001 (measured)
Lattice parameter	$\hat{\beta}_{x,trip}, \hat{\beta}_{y,trip}$	5.49, 7.76
Beam pipe width	b_x, b_y	120, 40 mm

Table 5.2: Beam parameters during the N^{7+} experiment

Beam/Machine Parameter	Symbol	Value
Atomic mass	A	14
Charge state	Z	7
Kinetic energy	W_{kin}	11.56 MeV/u (measured)
Number of particles	N_p	$3, 6, 11, 15 \cdot 10^9$ (measured)
Tune	Q_x, Q_y	4.16, 3.27 (set value)
Chromaticity	ξ_x, ξ_y	-0.94, -1.85 (set value)
Transverse emittance	$\epsilon_x, \epsilon_y(2\sigma)$	$33, 12$ mm-mrad (measured)
Slip factor	η	0.94
Bunching factor	B_f	0.37 (measured)
Synchrotron tune	Q_{s0}, Q_{s1}	0.006,0.0057 (measured)
Momentum spread	$\frac{\Delta p}{p}(1\sigma)$	0.0015 (measured)
Lattice parameter	$\hat{\beta}_{x,trip}, \hat{\beta}_{y,trip}$	5.49, 7.76

Iso-adiabatic ramps have been used for adiabatic capture in this work, however there are other types of ramps such as parabolic or linear ramps which are frequently used for the capturing process. The adiabatic capture process and the ramp parameters have been studied in detail at GSI SIS-18 in [107].

For adiabatic capture during experiments, a data-table consisting of the voltage amplitude and time information is generated by a custom ramp generator software obtained from rf group [109]. This data is remotely fed to an Arbitrary Waveform Generator (AWG) whose output is then fed to the driving cavity. The measured output from an experiment can be seen in *S02BE1_Amp* detector output in Fig. 5.7.

5.3 Results

The major results obtained during the several beam experiments using both tune measurement systems are presented in this section.

5.3.1 Interpretation of tune spectra at high intensities

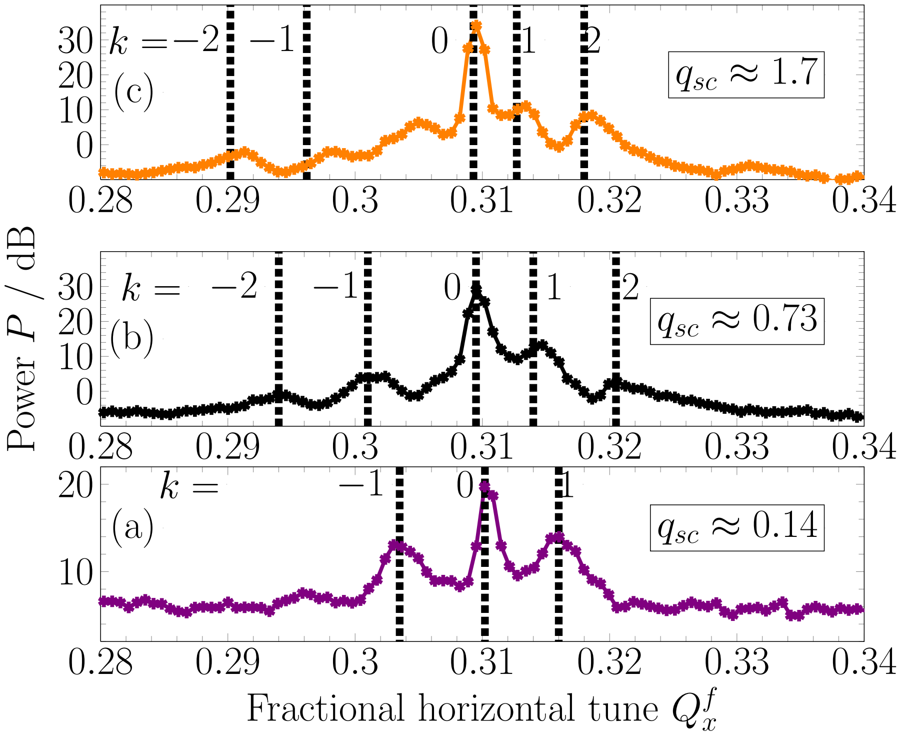

Figure 5.9: Horizontal tune spectra for U^{73+} ions and beam parameters given in Tab. 5.1 (see text). The dashed lines indicate the head-tail tune shifts from Eq. 2.57.

Figure 5.9 shows the horizontal tune spectra obtained with the BBQ system using band-width limited noise at different beam intensities. Figure 5.9(a) shows the horizontal tune spectrum at low intensity. Here the $k = 1, 0, -1$ peaks are almost equidistant, which is expected for low intensity bunches. The space charge parameter obtained using the beam parameters and Eq. 2.53 is $q_{sc} \approx 0.14$. The vertical lines indicate the positions of the synchrotron satellites obtained from Eq. 2.57 (with $Q_s = Q_{s1}$). Figure 5.9(b) shows the tune spectrum at moderate intensity ($q_{sc} \approx 0.73$). The $k = 2, -2$ peaks can both still be identified. Figure 5.9(c) shows the tune spectra at larger intensity ($q_{sc} \approx 1.7$). An additional peak appears between the $k = 0$ and $k = -1$ peaks which can be attributed to the mixing product of diode detectors (since at this intensity $30 - 40V$ acts across the diodes pushing it into the non-linear regime). The $k = 0, 1, 2$ peaks can be identified very well, whereas the amplitudes of the lines for negative k already start to decrease (see section 2.3.3). In the horizontal plane the effect of the pipe impedance and the corresponding coherent tune shift can usually be neglected because of the larger pipe diameter.

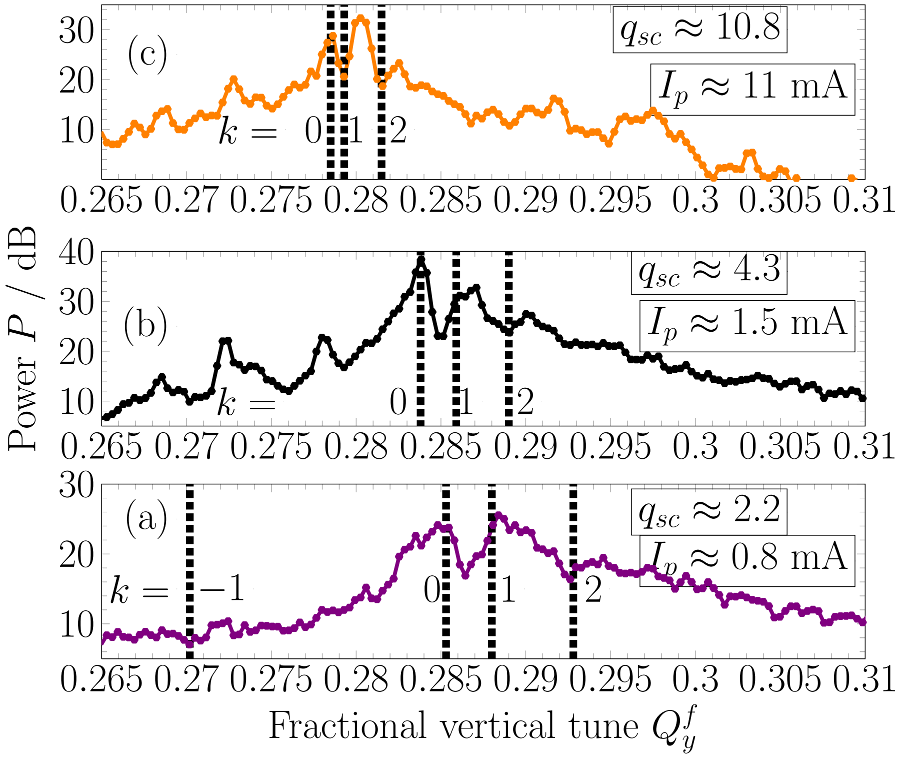

Figure 5.10: Vertical tune spectra for N^{7+} ions and beam parameters given in Tab. 5.2. The dashed lines indicate the head-tail tune shifts from Eq. 2.57.

Figure 5.10 shows the vertical tune spectrum obtained by the BBQ system with band limited noise excitation for N^{7+} beams with q_{sc} values larger than 2. Here the negative modes ($k < 0$) could not be resolved anymore. In the vertical plane the coherent tune shift is larger due to the smaller SIS-18 beam pipe diameter ($q_c \approx q_{sc}/10$). The shift of the $k = 0$ peak, due to the effect of the pipe impedance, is clearly visible in Fig. 5.10.

In the measurements the width of the peaks is determined by the cumulative effect of non-linear synchrotron motion, non-linearities of the optical elements, closed orbit distortion, tune fluctuation during the measurement interval as well as due to the intrinsic Landau damping (section 2.3.3). From the comparison to the simulations we conclude that the intrinsic Landau damping is an important contribution to the width of the $k = 1, 2$ peaks.

5.3.2 Coherent and incoherent tune shift measurements

Coherent tune shift measurements

The coherent tune shift ΔQ_c can be obtained by measuring the shift of the $k = 0$ line as a function of the peak beam current. The location of $k = 0$ modes, in both planes similar to Fig. 5.9 and Fig. 5.10 along with data from previous high current Ar^{18+} beam experiments [56], are used to obtain coherent tune shift as a function of peak beam current as shown in Fig. 5.11. The transverse impedance is thus obtained by a linear least square error fit of the measured shifts in both planes to Eq. 2.56. The impedance values are calculated in the horizontal and vertical planes at injection energy are $Z_{\perp,x,meas} = -j(0.23 \pm 0.04)$ MΩ/m^2 and $Z_{\perp,y,meas} = -j(1.78 \pm 0.04)$ MΩ/m^2 respectively. If we revisit the Eq. 2.55 and calculate the transverse impedance values by substituting the machine and beam parameters and the average beam pipe radii of the SIS-18 at injection energy, i.e $Z_0 = 377\Omega$, $\beta_0 = 0.16$, $\gamma_0 = 1.01$, $b_x = 120$ mm and $b_y = 40$ mm.

$$Z_{\perp,x,y} = -j\frac{Z_0}{2\pi(\beta_0\gamma_0 b_{x,y})^2} \tag{5.8}$$

$Z_{\perp,x,calc} = -j0.17\ \mathrm{M}\Omega/m^2$ and $Z_{\perp,y,calc} = -j1.54\ \mathrm{M}\Omega/m^2$ which are within 20% of the measured values. The difference could be attributed to the various unaccounted insertions in the machine during the calculations.

Incoherent tune shift measurements

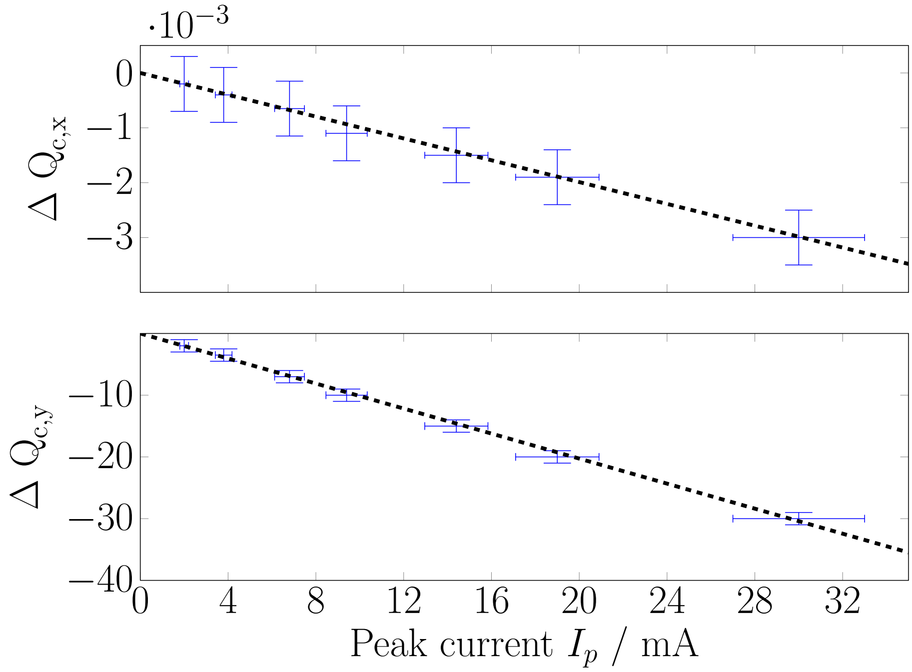

Figure 5.11: Coherent tune shift obtained from the measurement for the horizontal and for the vertical planes as a function of the peak beam current. The dotted lines correspond to a linear least square error fit. The error bars in the horizontal plane are due to uncertainties in the current measurements. In the vertical plane errors result from the width of $k = 0$ mode. The FFT resolution is $\approx 5 \cdot 10^{-4}$ and is always kept higher than the mode width.

Figures 5.12a, 5.12b, 5.13a and 5.13b show the measured positions of the peaks in the tune spectra for different intensities. In comparison the analytical curves (solid lines) obtained from Eq. 2.57 for the head-tail tune shifts are plotted using q_{sc} estimated from the beam parameters in tables 5.1 and 5.2 for each intensity. The error bars in the vertical plane ($\delta q_k = \frac{\delta Q_k}{Q_s}$) correspond to the 3 dB width of the measured peak due to accumulation of various effects (see section 5.3.1). In the horizontal plane, error bars (δq_{sc}) are estimated by propagation of parameter uncertainties mentioned in section 5.1.4.

In this subsection, we introduce another space charge parameter $q_{sc,m}$ which is the measured space charge parameter using the following method. It is not to be confused with q_{sc} which is predicted for a given set of beam parameters by Eq. 2.53. The incoherent space charge tune shift can be determined directly from the tune spectra by measuring the separation between the $k = 0$ and $k = 1$ peaks, i.e. ($q_{k,01} = \frac{\Delta Q_{k,01}}{Q_s}$) and fitting it with the parameter q_{sc} in the predictions from Eq. 2.57. The value of q_{sc} for the best fit is denoted as $q_{sc,m}$.

$$q_{sc,m} = \frac{1 - q_{k,01}^2}{\lambda q_{k,01}} \qquad 0 \leq q_{k,01} \leq 1 \tag{5.9}$$

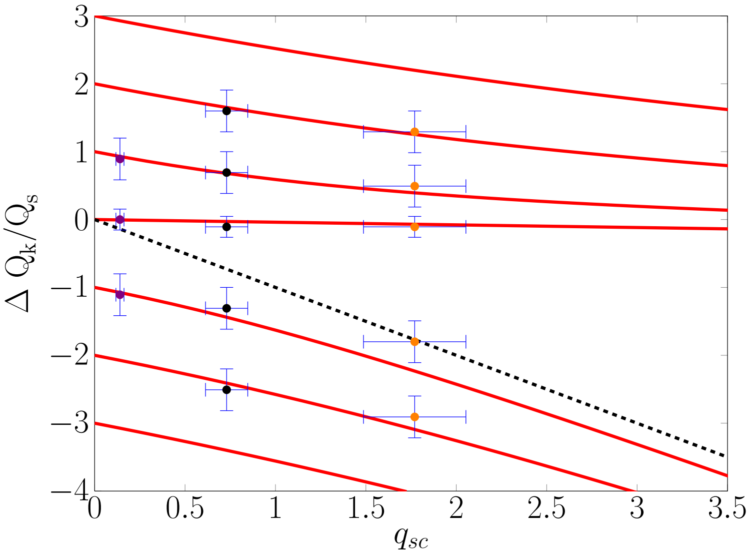

(a) The measured positions of the peaks in the horizontal tune spectra for different U^{73+} beam intensities together with the analytical curves from Eq. 2.57 using the space charge tune shift estimated from the beam parameters in Tab. 5.1. The colour of data points correspond to the three plots in Fig. 5.9. The dotted line corresponds to the incoherent tune shift. The error bars for the vertical plane correspond to the width of measured modes (see text). In the horizontal plane the error bars are estimated by the propagation of uncertainties (see text).

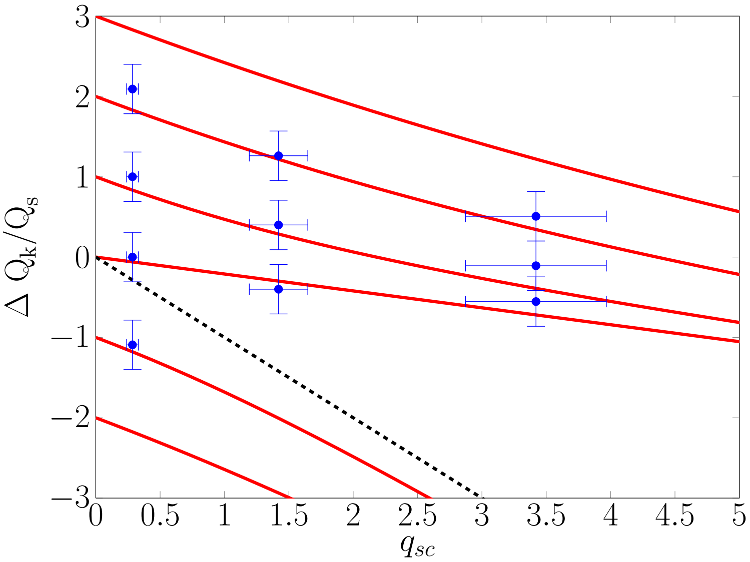

(b) This plot shows the predicted shifts from analytical Eq. 2.57 and measured head-tail mode frequencies are overlaid in vertical plane for U^{73+} ion beam at various current levels (Tab. 5.1).

Figure 5.12

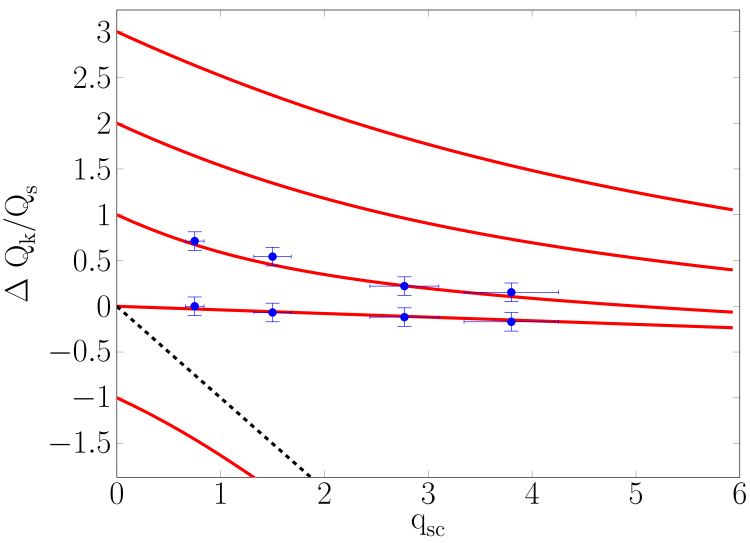

(a) This plot shows the predicted shifts from analytical Eq. 2.57 and measured head-tail mode frequencies are overlaid in horizontal plane for N^{7+} ion beam at various current levels (Tab. 5.2).

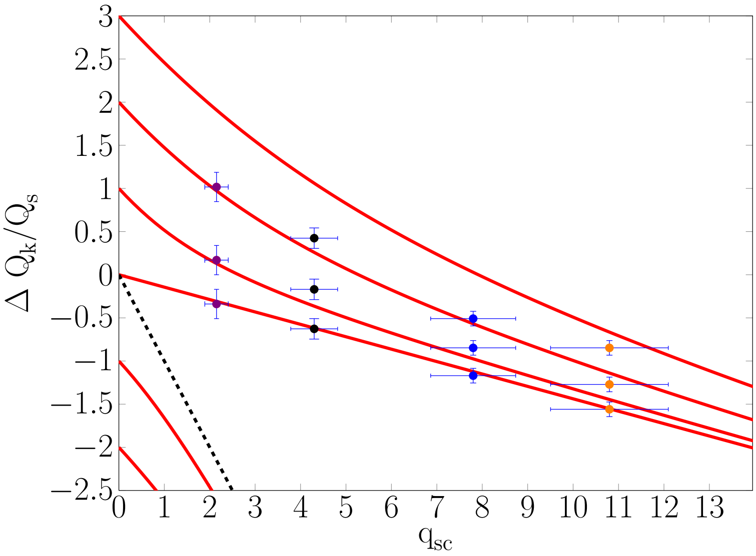

(b) This plot shows the predicted shifts from analytical Eq. 2.57 and measured head-tail mode frequencies are overlaid in vertical plane for N^{7+} ion beam at various current levels (Tab. 5.2). The colour of data points correspond to the three plots in Fig. 5.10.

Figure 5.13

Eq. 5.9 is obtained by rearranging Eq. 2.57 for $k = 0, 1$ while $\lambda = \frac{q_{sc} - q_c}{q_{sc}}$. The linearized absolute error on measured $q_{sc,m}$ $(\delta q_{sc,m})$ is given by

$$\delta q_{sc,m} = \frac{-(1 + q_{k,01}^2)}{\lambda q_{k,01}^2} \cdot \delta q_{k,01} \tag{5.10}$$

$\delta q_{k,01}$ is given by either the width of the $k = 0, 1$ lines or by the frequency resolution of the system. In a typical tune spectrum measurement using data from 4000 turns, the frequency resolution of the spectrum gives the measurement uncertainty of $q_{k,01}$ i.e. $\delta q_{k,01} \approx 0.04$. The absolute error is a non-linear function of q_{sc} in accordance to the Eq. 5.9. It is possible to define the upper limit of q_{sc} where this method is still adequate based on the system resolution and Eq. 5.9. If we define a criterion that, $q_{k,01} \gtrsim \delta q_{k,01}$ to resolve the head-tail modes. This gives the limit to be $q_{sc} \lesssim 8$ where the measurement error is still within the defined criterion.

Figure 5.14 shows a plot of the predicted space charge tune shifts (q_{sc}) versus the ones measured from the tune spectra, using the above procedure $(q_{sc,m})$. For $q_{sc} \lesssim 3.5$ the space charge tune shifts, measured from the tune spectra, are systematically lower by a factor $= 0.74$ than the predicted shifts. It is shown by the dotted line in Fig. 5.14 which is obtained by total least squares fit of the measured data points. For larger q_{sc} the factor decreases to ≈ 0.4. Thus the method for measuring the incoherent tune shift based on head-tail tune shifts is found to be satisfactory only in the range $q_{sc} \lesssim 3.5$. A possible explanation is the effect of the pipe impedance. Similar observations are made by the results of self-consistent simulations in section 2.3.3, where for $q_{sc} \gtrsim 2$ the separation of the $k = 0$ and $k = 1$ peaks observed is underestimated by Eq. 2.57.

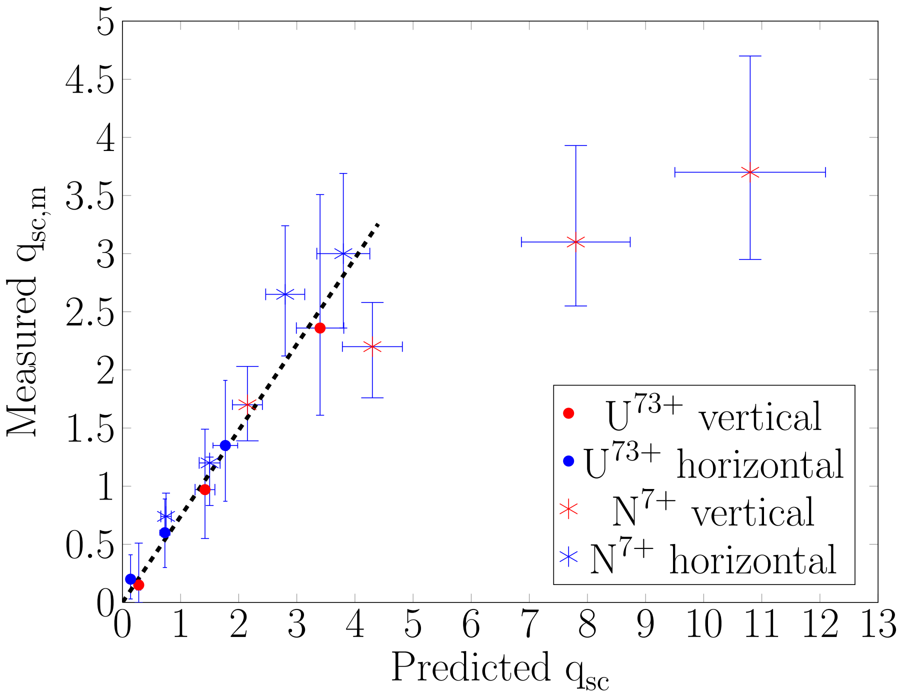

Figure 5.14: Combining the results from the Figures 5.12a, 5.12b, 5.13a and 5.13b, a plot of predicted q_{sc} using Eq. 2.53 against measured q_{sc} using the distance between modes $k = 0$ and $k = 1$ is obtained.

5.3.3 Effect of excitation parameters on tune spectrum

Figure 5.15a presents the tune spectra obtained from BBQ system at various excitation power levels of band limited noise. The beam is excited with 0.25, 1.0 and 2.25 mW/Hz power spectral density on a bandwidth of 10 KHz. Signal-to-noise ratio (SNR) increases with excitation power whereas the spectral position of various modes is independent of excitation power.

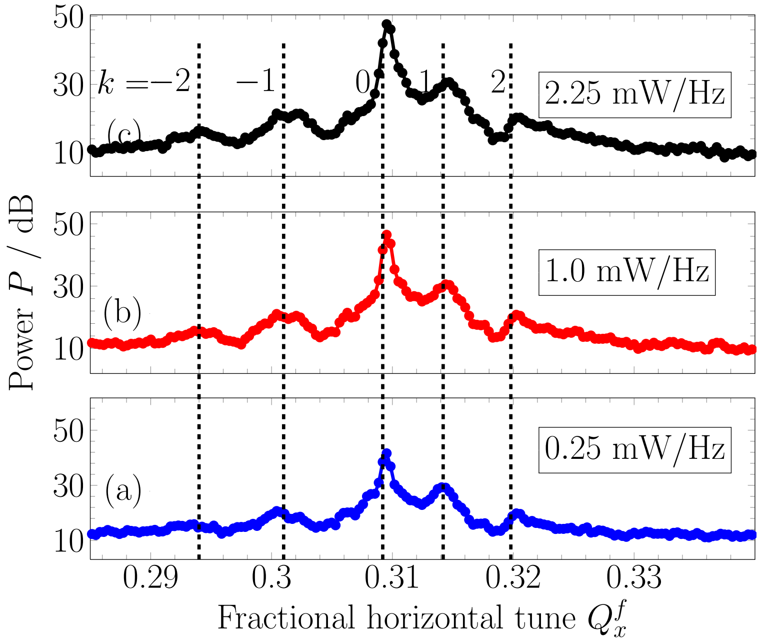

(a) Horizontal tune spectra for U^{73+} beam with $N_p = 5 \cdot 10^8$ at injection energy which is excited with three different excitation amplitudes. The beam is excited with 0.25, 1.0 and 2.25 mW/Hz power (blue, red and black respectively). The dotted lines mark the relative positions of the head-tail modes. The frequencies of various head-tail modes are unaffected by the excitation power.

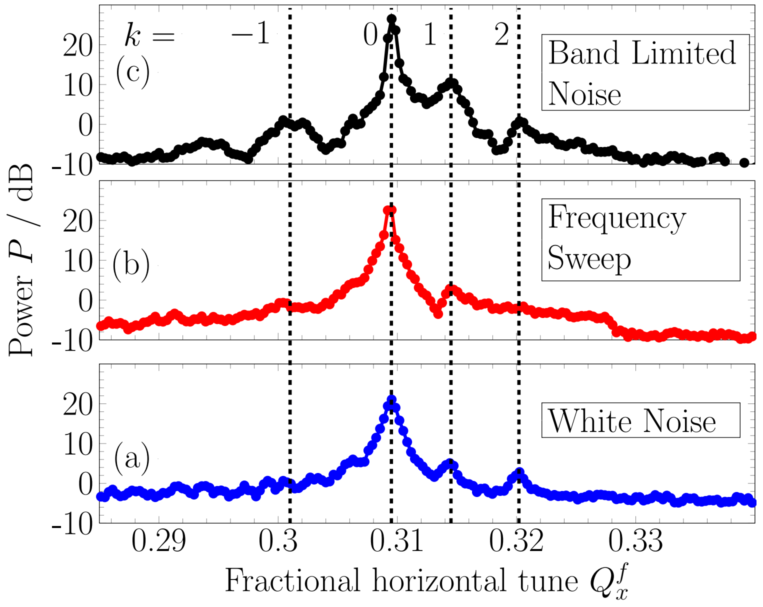

(b) Horizontal tune spectra with U^{73+} beam consisting of $5 \cdot 10^8$ particles with band limited noise (rf Noise), frequency sweep (chirp noise) and white noise (top to bottom). The dotted lines mark the relative positions of the head-tail modes.

Figure 5.15

Beam excitation using two other excitation types i.e. frequency sweep and white noise is also performed to study the effect of excitation type on the tune spectra. Figure 5.15b shows the tune spectra under the same beam conditions for different types of beam excitation obtained from the BBQ system. The frequencies of various modes in the tune spectra are independent of the type of excitation. The signal-to-noise ratio (SNR) is optimum for band limited noise, due to the long averaging time, compared to “one shot” spectra from sweep excitation.

5.3.4 Time domain identification of head tail modes

Figure 5.16a shows the 2-D contour plot for frequency sweep excitation in the vertical plane, obtained from the TOPOS system, where various head-tail modes are individually excited as the excitation frequency crosses them. Frequency sweep excitation allows resolving the transverse center-of-mass along the bunch for various modes which helps in identifying each head-tail mode in time domain. This serves as a direct cross-check for the spectral information and leaves no ambiguity in identification of the order (k) of the modes. Figure 5.16b shows the corresponding transverse center- of-mass along the bunch for $k = 0, 1$ and 2 at the excited time instances. This method works only with sweep excitation and requires high signal-to-noise ratio in the time domain, which amounts to higher beam current or high excitation power.

5.3.5 Measurement of the chromaticity and its effect on relative amplitude of head tail modes

As highlighted in the previous section, the frequency sweep allows to resolve the different head-tail modes both spectrally and temporally. This procedure can be used for the precise determination of the chromaticity by fitting the analytical expression for the head-tail eigenfunction Eq. 2.58 to the measured bunch offset, with the chromaticity (ξ) as the fit parameter as shown in Fig. 5.17a for $k = 0, 1$ and 2. The measured chromaticity is independent of the order of head-tail eigenfunction used to estimate it.

The fitting method is shown in Eq. 5.11; the head-tail eigenfunction $\bar{x}_k(\Delta t)$ from Eq. 2.58 is multiplied with the beam charge profile $\hat{Q}(\Delta t)$ and corrected for the beam offset Δx at the BPM where the signal is measured, we obtain the expected center-of-mass along the bunch for the k^{th} mode $F_k(\Delta t, \xi, A_k)$.

$$F_k(\Delta t, \xi, A_k) = \Delta x \cdot \hat{Q}(\Delta t) \cdot (1 + A_k \cdot \bar{x}_k(\Delta t)) \tag{5.11}$$

If $\hat{x}_{m,k}(\Delta t)$ is the measured transverse center-of-mass for the k^{th} mode along the bunch, then the fit error $E(\xi, A_k)$ is reduced as a function of two independent variables; chromaticity ξ and head-tail mode amplitude A_k for each of the mode k. The best fit gives the value of measured chromaticity ξ_m.

$$E(\xi, A_k) = (\hat{x}_{m,k}(\Delta t) - F_k(\Delta t, \xi, A_k))^2 \tag{5.12}$$

The fit error gives the goodness of the fit. It is used to determine the error bars on the measured chromaticity ξ_m. The error on chromaticity can be reduced, by several simultaneous measurements using different orders of head-tail modes. In Fig. 5.17a, three different modes, ($k = 0, 1$ and 2) are used to calculate chromaticity.

This method has been utilized for the determination of chromaticity at SIS-18 as shown in Fig. 5.17b. The set and the measured chromaticity can be fitted by linear least squares to obtain the form $\xi_{s,y} = 1.187\xi_{m,y} + 0.804$ as shown by red dashed line in Fig. 5.17b. Figure 5.17b also shows a coherent tune shift, due to change in sextupole strength which is used to adjust the chromaticity. This is due to uncorrected orbit distortions during these measurements. These chromaticity measurements agree with the previous chromaticity measurements at SIS-18 using established methods [27].

It is also possible to determine the relative response amplitude of each head-tail mode with TOPOS to the beam excitation, both in time and frequency domains. Figure 5.18a shows the tune spectrum obtained with sweep excitation for different chromaticity values. The beam parameters are kept the same ($N^{7+}, 14 \cdot 10^9, q_{sc} \approx 10$) for all the measurements points. The spectral positions and relative amplitudes of each head-tail mode peak are confirmed using the time domain information (see Fig. 5.16b). In Fig. 5.18b the single particle response amplitudes for different k (Eq. 2.40) are plotted as a function of the chromaticity. The measured relative amplitudes are indicated by the coloured symbols. The comparison indicates that the simple single particle result (Eq. 2.40) describes quite well the dependence of the relative height of the peaks obtained from the TOPOS measurement. An alternative hypothesis specifically for kick excitation proposing a similar trend is discussed in [49].

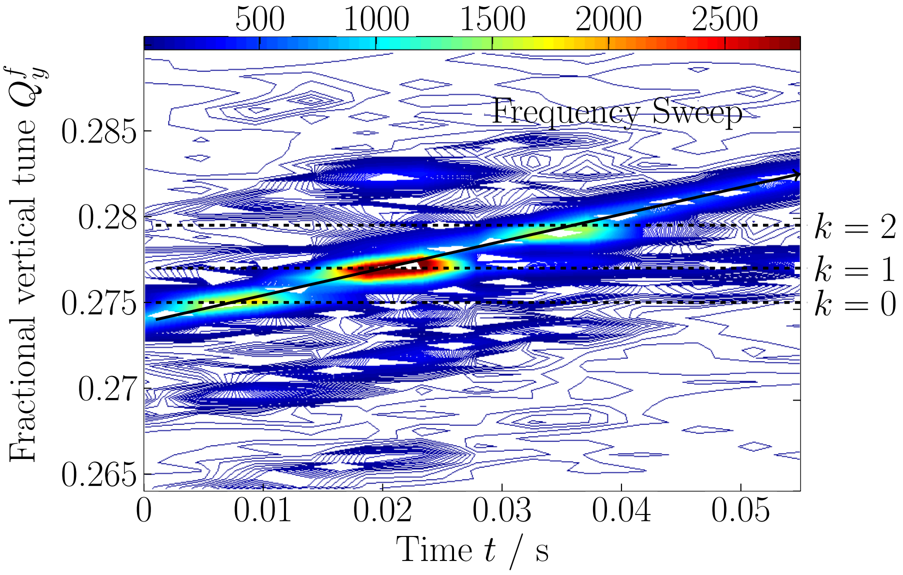

(a) Vertical tune spectra with frequency sweep over time at N^{7+} with $1.5 \cdot 10^9$ particles. The various modes get individually excited as the sweep frequency (marked by the arrow) coincides with the mode frequency. The $k = 0, 1, 2$ modes are marked. Symmetric sidebands, due to coherent longitudinal oscillations, are visible around the sweep frequency spaced with Q_s and can be clearly distinguished from the head-tail modes.

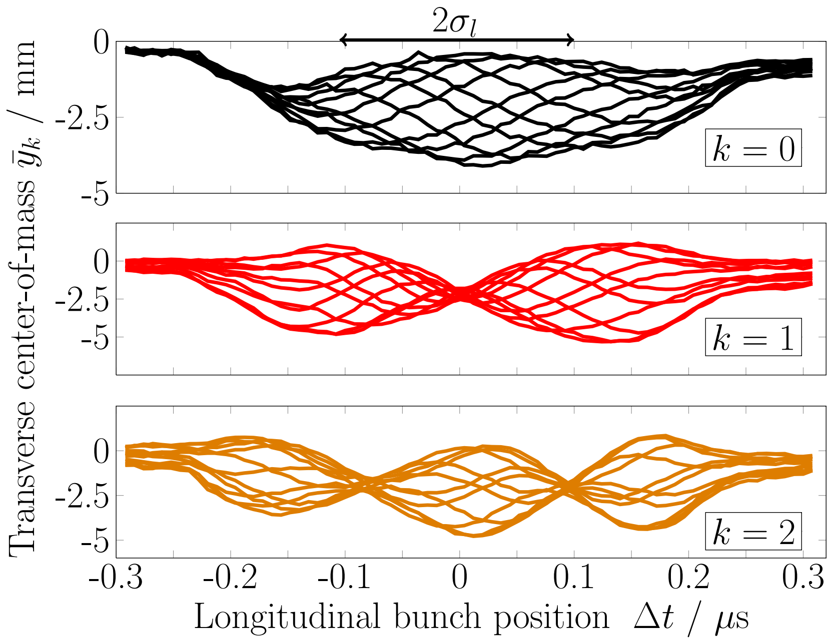

(b) Transverse center-of-mass along the bunch for $k = 0, 1$ and 2 modes corresponding to Fig. 5.16a. Frequency sweep is used to excite the beam which enables to resolve the distinct head-tail modes temporally. The rms bunch length ($2\sigma_l$) is indicated.

Figure 5.16

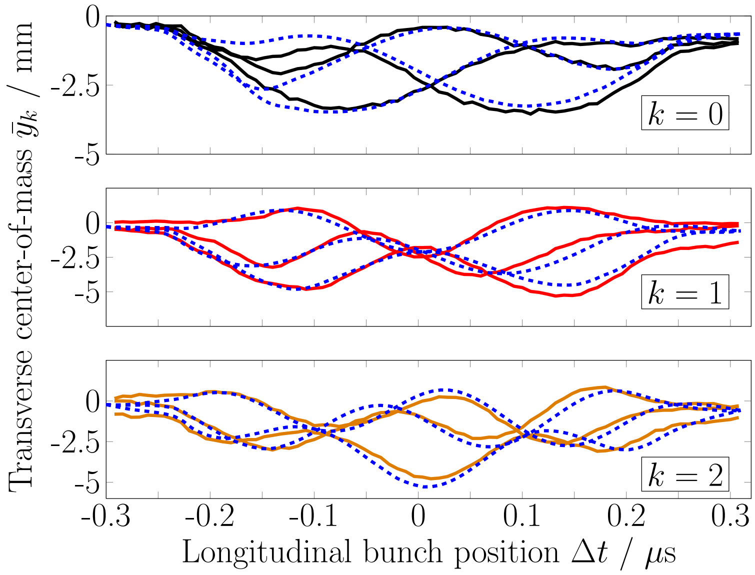

(a) Analytical curves from Eq. 2.58 (dotted) are fitted to the local transverse offset for the $k = 0$ and $k = 1$ modes with the head-tail phase shift as the fit parameter. This method has been used for the precise determination of the chromaticity.

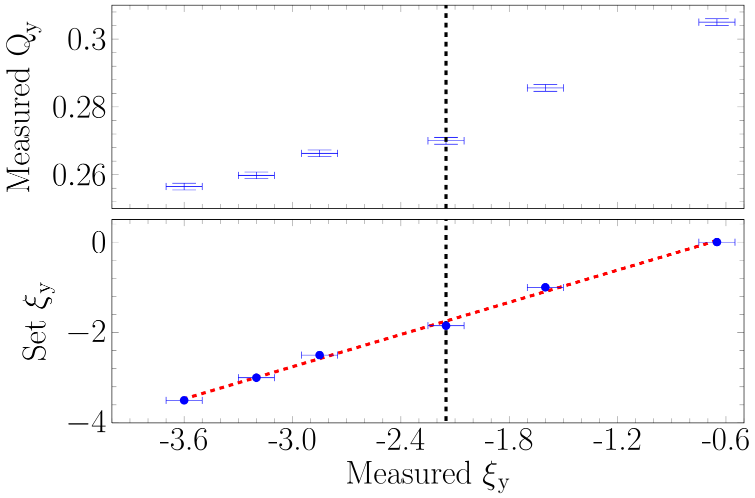

(b) Chromaticity measurement using the method shown in Fig. 5.17a over the possible range of operation at SIS-18. The black dashed line marks the natural chromaticity of SIS-18. The error bars for the chromaticity measurement are determined mainly by the electronic noise in the amplifier chain of the TOPOS system.

Figure 5.17

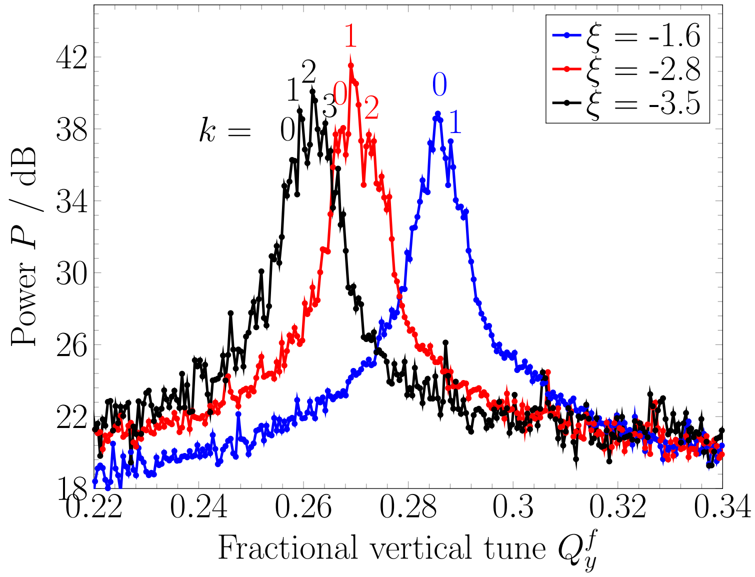

(a) Relative signal amplitudes of various head-tail modes are plotted with respect to the measured chromaticity. The centroid of the spectrum moves toward higher order modes with increase in chromaticity.

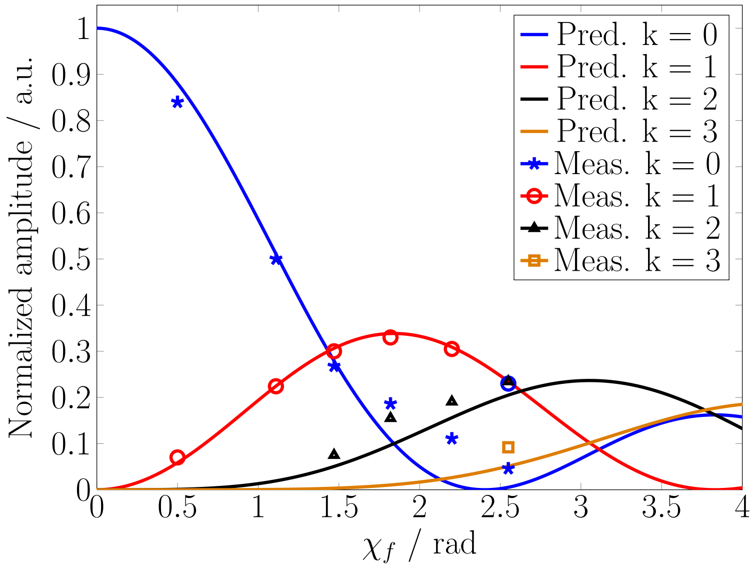

(b) Relative signal amplitudes of various head-tail modes are plotted with respect to the coefficient of Bessel's function in Eq. 2.40 ($\chi_f = \chi/2$). All the modes are relative to k=1 mode, which has a significant amplitude during the whole measurement range.

Figure 5.18

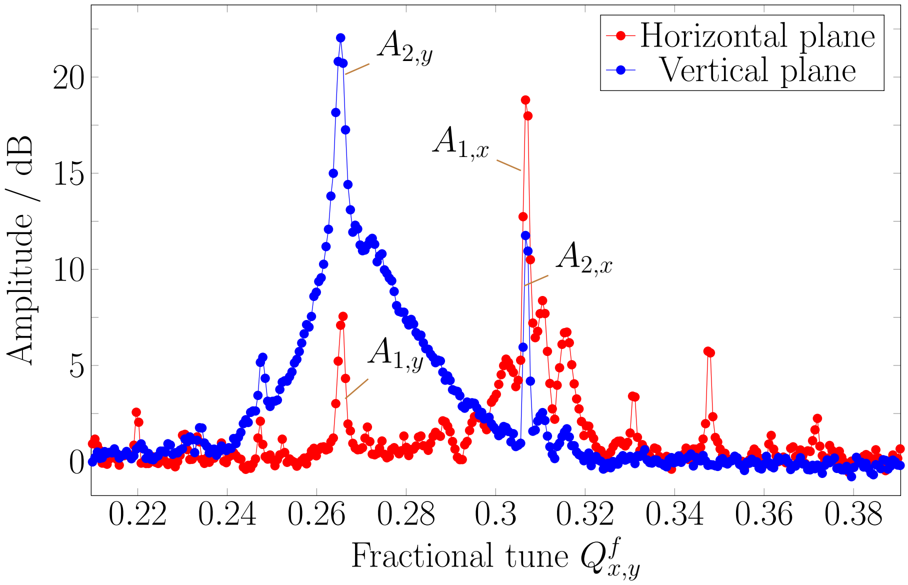

Figure 5.19: The regular and cross terms shown in the tune spectra, obtained from both planes.

5.3.6 Linear coupling between transverse planes

A systematic estimation of the coupling coefficient (C^-) of linear betatron coupling, using the eigenmode amplitude ratio and the closed tune approach [110, 69], is presented for the specific machine settings of the presented measurement beam time.

Eigenmode amplitude ratio approach

This approach allows reconstructing both real and imaginary parts of the betatron coupling. Regular and cross term amplitudes $A_{1/2,x/y}$ of the eigenmodes are measured. Fig. 5.19 shows a typical tune spectrum from both planes with the measured amplitudes $A_{1/2,x/y}$ shown in logarithmic scale, which should be converted to the linear scale. Then, using the measured amplitudes of the eigenmodes, one can find the coupling coefficient

$$r_1 = \frac{A_{1,y}}{A_{1,x}}, \ r_2 = \frac{A_{2,x}}{A_{2,y}} \tag{5.13}$$

$$C^- = |Q_x - Q_y| \cdot \frac{2\sqrt{r_1 r_2}}{1 + r_1 r_2} \tag{5.14}$$

$$\Delta = |Q_x - Q_y| \cdot \frac{1 - r_1 r_2}{1 + r_1 r_2} \tag{5.15}$$

The coupling coefficient C^- was estimated to be 0.005 ± 0.001 as shown in table 5.3. These measurements can be used to correct the coupling by appropriate skew-quadrupole settings.

Closed tune approach

Another method of find coupling between both planes, called the closed tune method, is described. In this method, the set tune in one of the planes is varied across a narrow region while ensuring a cross-over with the tune value in the other plane. The closest approach of two measured tune values in both planes gives a direct measurement

Table 5.3: Linear betatron coupling

Set Tune $Q_{x,y}$	Measured Tune	Δ	C^-
0.29,0.27	0.3115,0.2695	0.0411	0.0053
0.28,0.27	0.3017,0.2701	0.031	0.0063
0.27,0.27	0.2925,0.2701	0.0217	0.0055
0.265,0.27	0.2874,0.2701	0.0154	0.006
0.26,0.27	0.2834,0.2701	0.0119	0.0059
0.255,0.27	0.2786,0.2701	0.0074	0.0041
0.25,0.27	0.2727,0.2701	0.0005	0.0025
0.245,0.27	0.2664,0.2731	0.0042	0.0052
0.24,0.27	0.2619,0.2727	0.0093	0.0056
0.23,0.27	0.2527,0.2727	0.0194	0.0048

of coupling between the planes. In our experiment, the horizontal tune value is swept from 0.29 to 0.23 while the vertical tune is set to a fixed value of 0.27 by the control system. The closest they come to each other is then measured to find the coupling coefficient. Figure 5.20 shows the tune values obtained from the BBQ tune spectrum. The coupling coefficient is found to be ≈ 0.003 using this method. The problem with this method is the high sensitivity of beam to the change in machine optics (tune settings). There were large beam losses when the tunes crossed each other during these measurements, and thus tune values were calculated under poor SNR in the spectrum. Thus, eigenmode amplitude ratio should be considered more reliable. However, Fig. 5.20 provides a direct evidence showing the presence of a systematic offset between the measured and set tune of ≈ 0.0215 in the horizontal plane.

It is important to mention that other studies for measurement of coupling coefficient at GSI SIS-18 were performed based on transverse emittance exchange process [111]. The estimated coupling coefficient C^- in those studies was 0.008 ± 0.003. These studies were used to optimize the injection process and the associated beam losses.

5.3.7 Beam excitation required for continuous tune monitoring

The beam excitation, required to obtain reasonable signal-to-noise ratio for reliable tune measurements, is often strongly correlated with the machine injection settings, closed orbit, beam current, etc. which are not carefully controlled during normal synchrotron operation. In this section, empirical determination of appropriate beam excitation for tune measurements during entire acceleration cycle is presented. Figure 5.21a shows a plot of signal-to-noise ratio and beam losses with respect to band limited beam excitation power for Ar^{18+} ions at 11.4 MeV/u i.e. on the injection plateau at two current levels. The tune spectrum is calculated by FFT of position data from 4096 turns. The peak in the tune spectrum (after filtering interference noise lines) is used to calculate the SNR. As expected, the SNR increases with increase in beam excitation, however at beam excitation levels higher than 2 mW/Hz, significant particle losses start to occur at both current settings measured by a DC-CT. It should be pointed out that during long injection plateau at high beam intensities, there are particle losses due to single particle resonances [112], and thwe beam losses mentioned here, are relative to these single particle resonance type losses. Thus, the working range beam excitation at injection energies should be $\lesssim$ 2mW/Hz. As mentioned earlier, this number should only be used as a “rule of thumb”, and could considerably vary depending on exact machine settings and beam conditions.

Figure 5.21b shows the SNR and beam losses against beam excitation levels for Ar^{18+} ions during acceleration ramp. In the ramp case, the SNR used is obtained at the end of the ramp $\approx$ 300 MeV/u, where the beam has highest electric rigidity. Here only 1024 turns are used to find the tune spectrum and thus the SNR due to movement of tune during the ramp. Again the signal-to-noise ratio increases with beam excitation, but is lower than the injection case. There are no significant beam losses in the range of beam excitation. Thus, the beam excitation levels upto 2.5 mW/Hz are suitable for tune measurements during acceleration ramp.

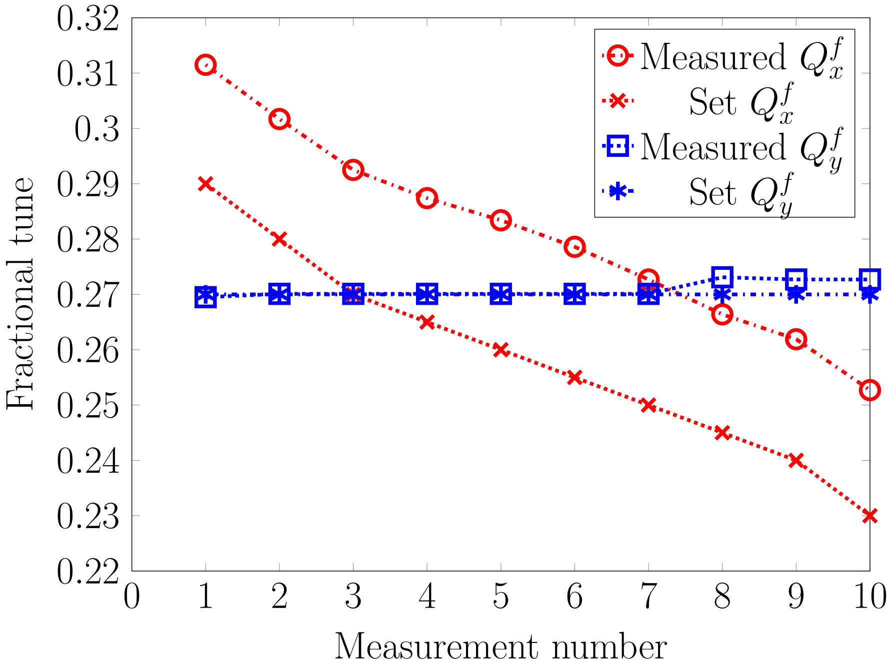

Figure 5.20: Measurement of betatron coupling using closed tune approach. The error bars are given by the tune resolution and are smaller than the symbol sizes used in the figure.

5.4 Applications of tune measurements

In this section we will discuss the application of our results to tune measurements in the SIS-18 and in the projected SIS-100, as part of the FAIR project at GSI [3]. As shown in the previous section, the relative amplitudes of the synchrotron satellites in the tune spectra are primarily a function of chromaticity and possibly the excitation mechanism. In order to determine the coherent tune with high precision the position of the $k = 0$ mode has to be measured. Depending on the machine settings, if the relative height of the $k = 0$ peak with respect to the other modes is small, then the $k = 0$ mode may not be visible at all. To estimate the bare tune frequency in this case, the information of space charge parameter, coherent tune shift and chromaticity are all simultaneously required with good precision.

5.4.1 Tune measurements during acceleration

Another important point is the tune measurement during acceleration. The space charge parameter for $1 \cdot 10^{10} Ar^{18+}$ stored ions in the SIS-18 from injection to extraction reduces only by $\approx 20\%$ as shown in Fig. 5.22a. The dynamic shift of head-tail modes during acceleration is shown in Fig. 5.22b obtained from the TOPOS system under the same conditions. The asymmetry of $k = 1, -1$ modes around the $k = 0$ mode can only be understood in view of the space charge effects predicted by Eq. 2.57. Thus, a correct estimate of this parameter plays an important role in understanding the tune spectra, not only during dedicated experiments performed on the injection plateau, but also during regular operations.

The measurement time, required to resolve the various head-tail modes (ΔQ_k), is a complex function of Q_s, q_{sc}, beam intensity and excitation power. To give some typical numbers for SIS-18; on a measurement time of 600 ms on the injection plateau, if one spectrum is obtained in $\approx$ 20 ms ($\approx$ 4000 turns), an improvement of factor ≈ 6 in the SNR can be achieved by averaging 30 spectra. Following the calculations in section 5.3.2, $q_{sc} \lesssim 8$ can be resolved under typical injection operations. However, the constraints on measurement time are much higher during

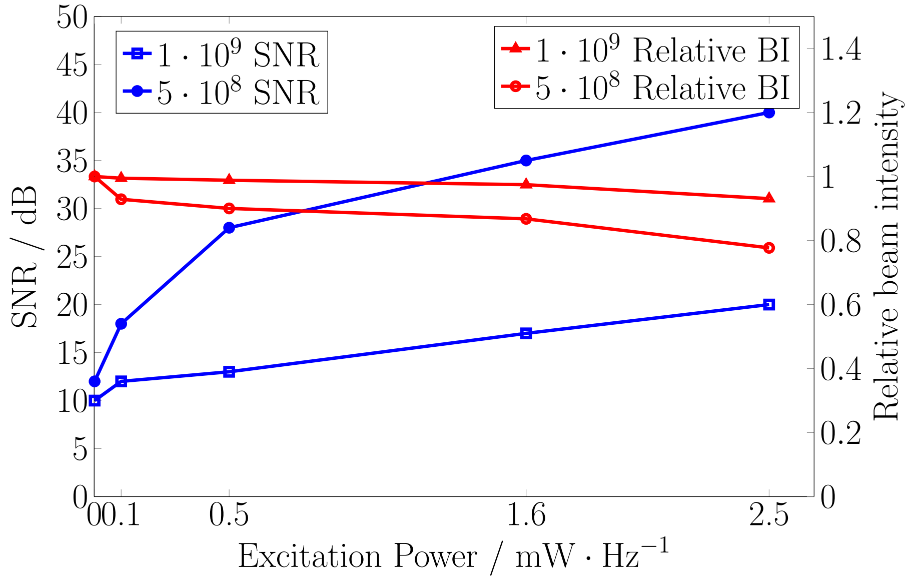

(a) Injection

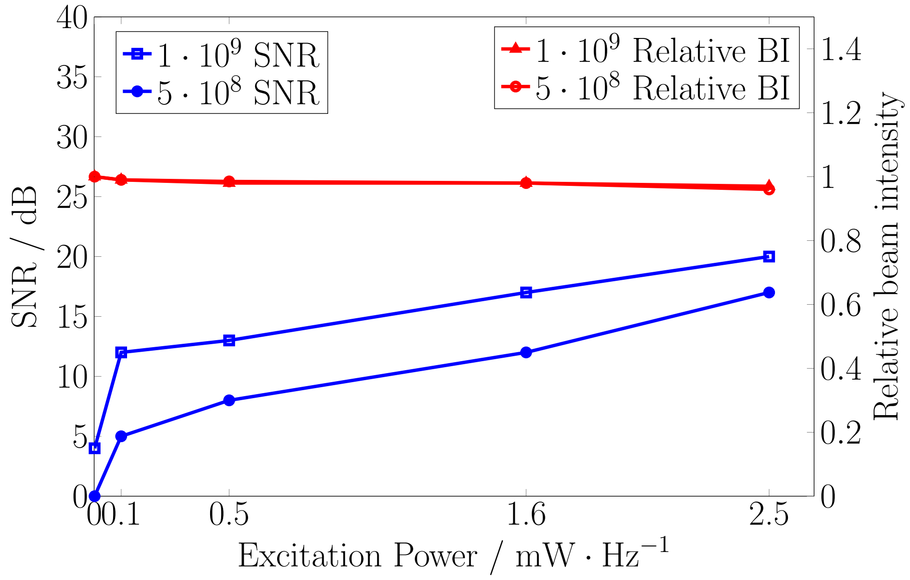

(b) Acceleration

Figure 5.21: (a) SNR in the tune spectrum as a function of beam excitation power at the injection plateau. The beam intensity (BI) normalized to the intensity of the non-excited beam show the beam losses as a function of excitation power. (b) SNR and relative beam intensity as a function of beam excitation power at the end of acceleration.

acceleration, where the tune/revolution frequency increases due to acceleration. This allows the measurement of a single spectrum typically only over $500 - 1000$ turns (depends on ramp rate as well). There are no averaging possibilities since the tune is moving during acceleration due to dynamic changes in machine settings as seen in Fig. 5.22b. In addition, the synchrotron tune reduces with acceleration making it practically very difficult to resolve the fine structure of the head-tail modes for $q_{sc} \gtrsim 2$.

5.4.2 Beam blow-up at high intensities

Transverse beam profiles at two current levels $I_1(N^{7+} = 15 \cdot 10^9)$ and $I_2(N^{7+} = 30 \cdot 10^9)$ are shown in Fig. 5.23a and 5.23b. At the injection, the beam width is similar for both intensities. However, as soon as bunches are formed ($t \approx 50$ms), the transverse emittance of higher current case I_2 blows-up while there is no blow up in case of I_1. Intuitively this can be attributed to the higher incoherent tune spread of I_2 as soon as the bunches are formed. This is easily verified if we observe the tune spectrum for both cases shown in Fig. 5.24. First the coherent tune shift (ΔQ_c) in the vertical plane is measured to be -0.01 for I_1 and -0.02 for I_2 which are directly proportional to the current level. However, $q_{sc} = \Delta Q_{sc}/Q_s$ has an inverse quadratic dependence of the beam width, thus the measured $q_{sc} \approx 3.5$ is case (I_2) which is smaller than the lower current case (I_1) where the measurement shows $q_{sc} \approx 4.8$ (maximum incoherent tune shift ≈ -0.07). It is also visually evident from the distance between $k = 0$ and $k = 1$ for the two spectrum. The maximum incoherent tune shift for I_2 for the same profile width as in case I_1 (just after bunch forming) would be ≈ -0.15 which lead to a crossing of several machine resonances and thus the blow-up. A simple qualitative explanation like this, supported by the high resolution tune measurements and transverse profile measurements, takes one step forward in quick interpretation of the beam behaviour due to incoherent resonance crossing [112] and/or to undertake required remedial actions.

5.5 Summary

1. The major diagnostic devices, used in the experimental campaigns, are described and the measurement uncertainties of each device is estimated.
2. Interpretation of tune spectrum at high intensities in terms of head-tail mode shifts in accordance with theory, presented in chapter 2, is performed.
3. Incoherent tune shifts are measured for bunched beams at SIS-18 based on head-tail frequency shifts.
4. Coherent tune shifts, due to resistive wall impedance, is measured for both planes.
5. Linear betatron coupling measurements under normal operating conditions are performed.
6. Novel chromaticity measurement technique, using the head-tail mode structure, is presented.
7. Empirical studies on the typical beam excitation levels, required for reliable tune measurements, are shown.
8. Selected applications of tune measurement systems, for better understanding of the beam dynamics at SIS-18, are discussed.

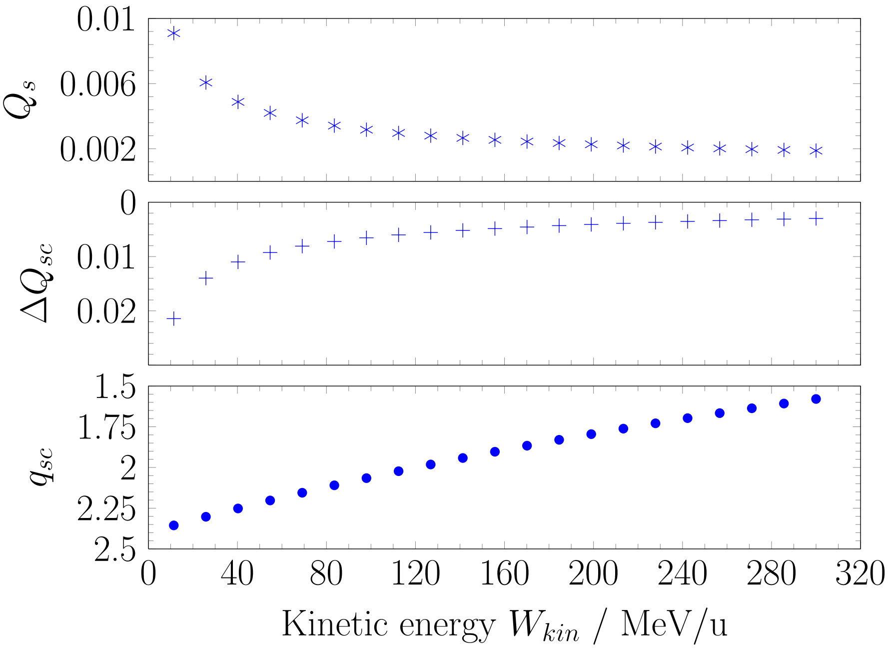

(a) Change in synchrotron tune and space charge tune shift on acceleration from injection to extraction for Ar^{18+} with $1 \cdot 10^{10}$ particles. The estimated space charge parameter reduces by $\approx 20\%$ in this typical case from injection at 11.4 MeV/u to 300 MeV/u at extraction.

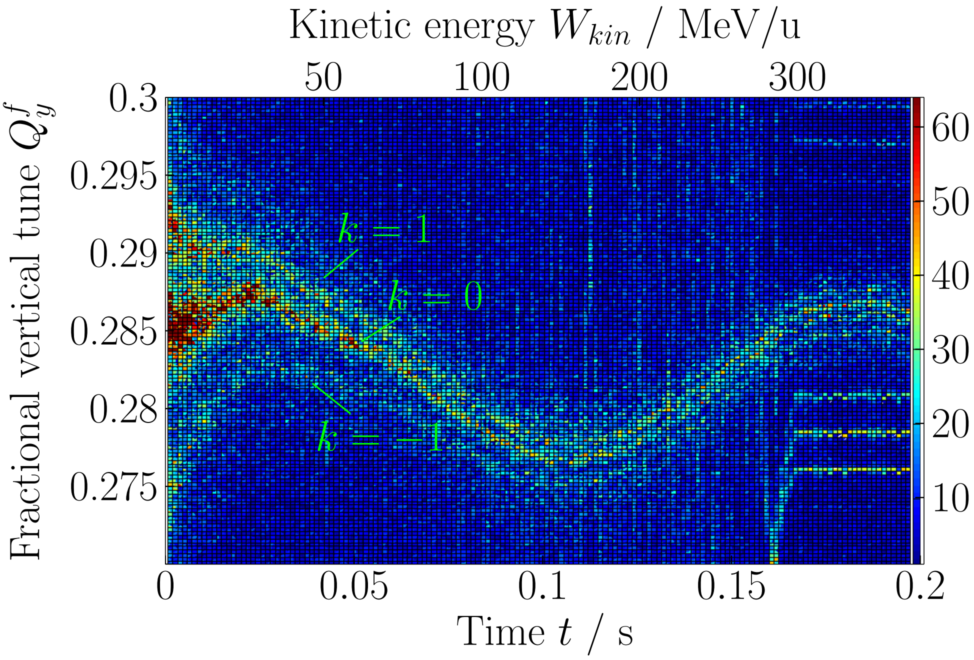

(b) The movement of head-tail modes during acceleration. The head-tail modes are getting closer since the synchrotron tune reduces with acceleration, but the asymmetry of the $k = 1$ and $k = -1$ modes around $k = 0$ is maintained throughout the ramp which depends primarily on the space charge parameter (q_{sc}).

Figure 5.22: (a) Evolution of space charge parameter during the acceleration ramp in SIS-18. (b) Measurement of head-tail modes during acceleration.

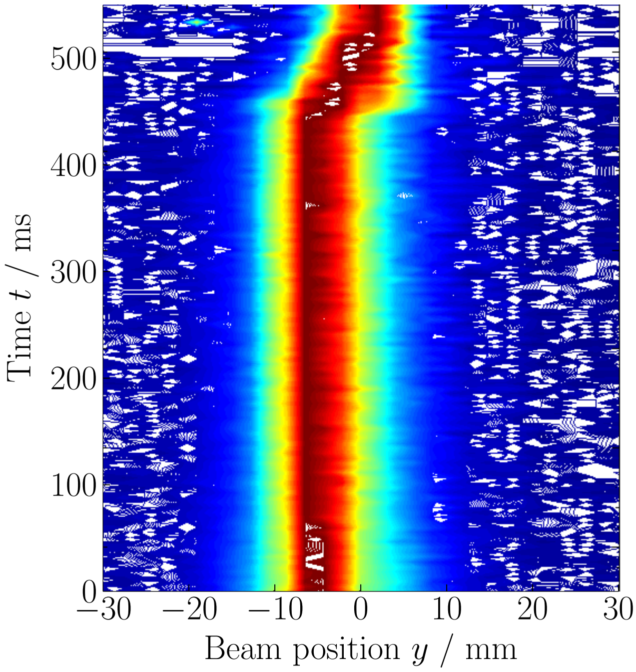

(a) Case I_1: Evolution of transverse beam profile in vertical plane on injection plateau at $N^{7+} = 15 \cdot 10^9$ ions. The profile remains conserved until acceleration starts at $\approx t = 500$ ms.

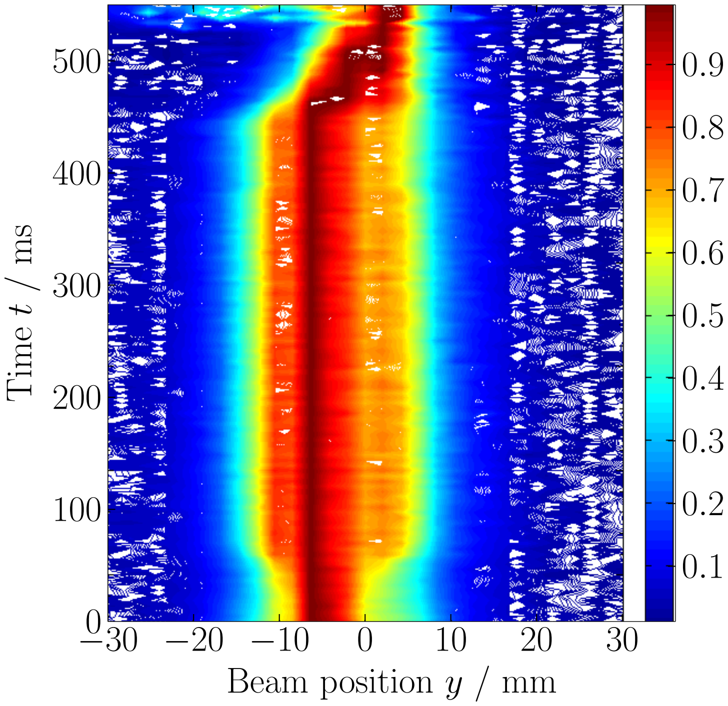

(b) Case I_2: Evolution of transverse beam profile in vertical plane on injection plateau at $N^{7+} = 30 \cdot 10^9$ ions. The enlargement of beam profile is visible immediately after bunching at $\approx t = 50$ ms.

Figure 5.23: Beam blow-up with increase in intensity, and its relation with the space charge parameter.

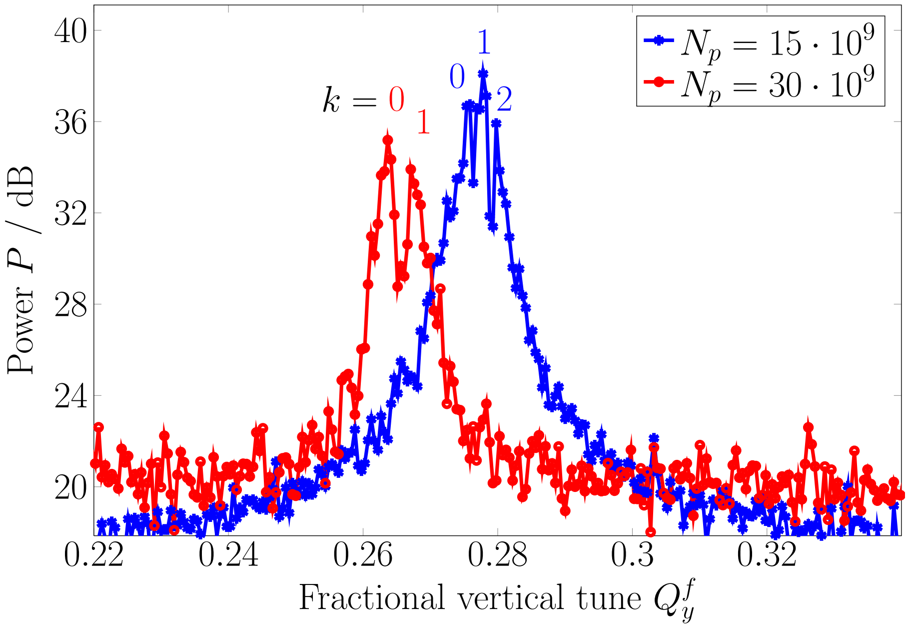

Figure 5.24: Vertical tune spectra from TOPOS for the two current settings: case 1 (blue): $N_p = 15 \cdot 10^9$ and case 2 (red): $N_p = 30 \cdot 10^9$. The space charge parameters(q_{sc}) measured are $\approx$ 4.8 (blue) and red (3.5).

6 Outcome and Outlook

In this chapter, we present the major outcomes of this work, and the directions in which this work can be continued.

6.1 Outcome

The outcomes of this work can be divided into two major segments. The first segment is the contribution in the technical realization, installation and operation of the two parallel and consistent tune measurement systems namely the Tune, Orbit and POSition measurement system (TOPOS) and Baseband Tune (Q) measurement system (BBQ). It should be clarified that the contribution to the technical realization of both systems is only partial and both systems existed before the commencement of this work. However, the testing, verification and comparison of both systems for SIS-18 was performed during the course of this thesis. A detailed description of each component of both systems for their comparision is presented in this thesis. The second part involves the measurement set-up and results obtained during dedicated beam physics investigations with high intensity beams. These measurements extensively utilized these tune measurement systems along with other beam diagnostics instrumentation at SIS-18. The experimental part and data analysis of these studies are part of this work in their entirety. The beam dynamics simulations were performed by the Beam Physics Group [55] to fully understand some aspects of the experimental results.

The contribution to the development and testing of both tune measurement systems are as follows. In the TOPOS system, the present bunch detection scheme and position calculation algorithm for BPM data processing were evaluated for their stability and reliability. The present position calculation algorithm i.e. weighted mean with baseline restoration is found to be non-optimal and is the result of a rather ad-hoc approach. A new position estimator based on linear regression was thus introduced and implemented for “offline” analysis. It was compared to the existing weighted mean with baseline restoration algorithm and established as a more robust and optimal position estimation procedure. The outcome of the offline analysis resulted in online tests for comparing the efficiency and computational complexity of both algorithms with respect to their FPGA implementation. These tests were performed in the Beam Diagnostics Group [86].

The BBQ system for tune measurements was first installed in course of a previous work [29]. However, it was discarded due to low frequency noise issues and importantly it was shown to have no advantage over the TOPOS system for SIS-18 beam conditions. In the course of this work, the BBQ system was reinstalled with change in input impedance of the peak detectors and better shielding with assistance from the CERN Beam Instrumentation Group [73]. It was brought into operation and compared with the TOPOS system in terms of measurement sensitivity and operational ease. Both systems were compared during routine acceleration operation and their respective regimes of operation were discussed. It was concluded that the BBQ system provides higher reliability and sensitivity in measuring tune, though it specializes only in tune measurements. On the other hand, TOPOS also provides bunch-by-bunch BPM data which can be analyzed for obtaining other beam and parameters such as beam position, closed orbit, chromaticity, etc. in addition to tune spectra. The problem of spectrum estimation is common to both systems. Advanced non-parametric spectrum estimators are discussed in the general weighted least square (WLS) framework with focus on the Capon method in comparison with commonly used periodogram and Welch estimators. The Capon estimator (ASC) is shown to have a higher resolving power when compared with the DFT based methods.

During the technical realization and testing of the tune measurement systems under various beam conditions, complex tune spectra were obtained for high intensity beams during several machine experiments. Such spectra were not observed earlier in SIS-18 and therefore called for detailed interpretation. On further investigations, various analytical and numerical studies were found in literature [44, 39], which predicted such complex tune spectra under high intensity conditions similar to SIS-18. These spectra were the result of head-tail mode frequency shifts and Landau damping of some modes as a function of beam intensity. Further experiments were performed to verify these studies by means of the high sensitivity and resolution provided by the tune measurement systems. Even though the shifts of head-tail modes were explained by the theoretical predictions, the magnitude of shifts did not exactly match with them for very high intensity conditions ($q_{sc} \geq 4$), and thus additional simulations were performed by the GSI Beam Physics Group taking the SIS-18 transverse impedances into account. These simulations confirmed the experimental findings and explained the reasons for disagreement between theory and measurements. These head-tail frequency shifts gave a direct measurement of the incoherent tune shift in the bunched beams. Further application of these detailed investigations provided the measurement of the coherent tune shift as a function of the beam current, from which the transverse machine impedances were extracted.

The tune spectra were measured with various beam excitation types such as band-limited noise, wide-band (white) noise, frequency sweep and kick excitation. The results were compared to understand the influence of beam excitation on the tune spectrum. The tune spectrum was found to be largely independent of the type of excitation. The frequency sweep excitation was used to excite each head-tail mode individually, which facilitated in resolving them both in time and frequency domain. This coupled with the high sampling rate of the TOPOS system resulted in the development of a novel chromaticity measurement technique. Further, measurement of linear betatron coupling using eigen-mode amplitude ratio approach was successfully performed. Empirical studies on the beam excitation levels required for sufficient SNR in tune spectrum for robust tune monitoring during acceleration were also performed. Though the measurements originally aimed to demonstrate the utility of these tune measurement systems, they resulted in detailed measurements of several elusive beam and machine parameters in GSI SIS-18. These studies are especially relevant for FAIR machines due to similar space charge regimes expected there.

6.2 Outlook

The natural outlook of this work is to extend and optimize the systems for FAIR machines on the technical front. The main directions for the system development would be:

- The development of a dedicated back-end system for data analysis and display for the BBQ system and bring it under regular operation. This is already planned to be performed in the near future.
- Refining the bunch detection techniques for position calculation in the TOPOS system to increase its robustness in varying beam conditions.
- Fast implementation of the other spectrum estimation techniques. Parametric spectrum estimators were ignored in this work, but would be explored and compared with non-parametric spectrum estimators for tune spectrum calculations.
- From a longer perspective, a tune feedback or feed-forward system is foreseen in association with the new control system LSA.

From the beam physics point of view, the tune spectrum measurements and interpretation in beam conditions similar to FAIR should be performed. These measurements would complement or help benchmarking the several ongoing simulations studies for FAIR machines. The major directions to proceed would be:

- Incorporating all the offline data analysis into an online mode. Immediate example would be an online chromaticity estimation tool based on the technique developed in this work.
- Bulk of the data recorded during the course of this work was analyzed in view of specific parameters and results. The data could yield host of other information, such as dependence of head-tail mode frequencies on the bunch shape. For example, in some experiments, the order of head-tail mode excited was different for each of the four bunches for the same excitation frequency. These higher order effects will be pursued further to get more insights into the SIS-18 beam dynamics.
- Tune measurements for the dual RF bunch is already being proposed and would provide important hints for beam dynamics in FAIR machines.
- Machine impedance measurements studies based on the growth or damping rates of the head-tail modes.

7 Appendix

7.1 A1 : Noise at the BPMs

Interference sources, specific to the location of the BPMs, cause problems in tune peak determination. Figure 7.1 shows tune spectrum obtained for the same bunches using three BPMs placed in different sections. Since tune is a global property, the spectrum is independent of the BPM location. However, the interference sources, and the noise floor is different for each spectrum. It is important to measure the “signature noise” for each BPM location regularly to understand the spurious noise sources, as well as to avoid them during analysis of the tune spectrum.

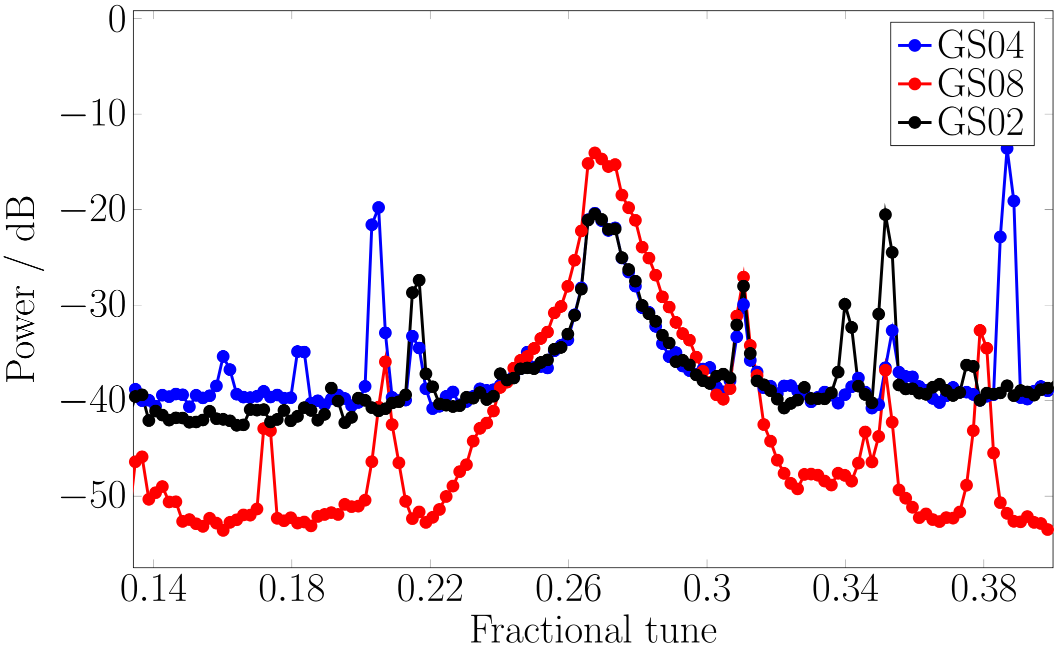

Figure 7.1: The vertical tune spectra evaluated from the data at three BPMs at the same time instant. While the spectra are similar, irrespectively of the BPM data used, the interference noise peaks are very dissimilar to each other and strongly depend on the location of the pick-up.

7.2 A2 : Matched filter-bank interpretation

The periodogram, averaged periodogram and the Capon estimators, described in chapter 4, can be interpreted in an adaptive filterbank framework. Although this interpretation is somewhat ad-hoc, it does provide additional insight into the characteristics of the different methods [99]. All the notations are the same as in section 4.3.

In the context of filterbanks, for each frequency ω of interest the nonparametric methods filter the data with a normalized finite-impulse response (FIR) filter $h(\omega)$ of length M. The variable M is a user parameter which is the same as the length of the snapshots in the matrix 4.16. The filter $h(\omega)$ is chosen according to a criterion which is different for the various spectral analysis methods, but with the common constraint that a sinusoid with frequency ω should pass the filter without distortion. Following the filtering, a sinusoid is fitted to the filtered data in a least square sense, and the amplitude of the so-obtained sinusoid $\alpha^p(\omega)$ is taken as the estimate of the amplitude spectrum $\alpha^p(\omega)$ at the frequency ω of interest.

The idea behind the filtering is easy to understand intuitively as follows. Clearly, filtering $x(n)$ with $h(\omega)$ reduces the number of available samples from N to L; yet, if the filter is properly designed, the increase in signal-to-noise ratio (SNR) in the filtered data will counterbalance this reduction and the amplitude of a sinusoidal component with frequency ω can be estimated more accurately from the filtered data than from the original signal.

Again, let $x(n)$ be a finite time series, and y_n be defined according to previous equation. If

$$\mathbf{h}(\omega) = [h_0(\omega)...h_{M-1}(\omega)]^T \tag{7.1}$$

is a M vector that contains the co-efficient of the FIR filter, the filtered data can be written as

$$z(l) = \sum_{m=0}^{M-1} x(l+m)h_m(\omega) = \alpha(\omega)\mathbf{h}^H(\omega)\mathbf{a}_M(\omega) + \mathbf{h}^H(\omega)\mathbf{w}_L \tag{7.2}$$

for $l = 0, 1..., L-1$. So, the problem of estimation in matched filter intepretation is thus defined as: $\mathbf{h}^H(\omega)\mathbf{w}_L$ has to be minimized constrained to the condition that $\mathbf{h}^H(\omega)\mathbf{a}_M(\omega) = 1$. Results similar to section 4.3 can be obtained for both DFT and Capon estimator using this intuitive approach.

7.3 A3 : Symbols and abbreviations

Table 7.1: Abbreviations

a.u. :	Arbitrary units
ACT :	Alternating Current Transformer
ADC :	Analog to Digital Converter
APA :	Averaged Phase Advance
APES :	Amplitude and Phase EStimation
ASC :	Amplitude Spectrum Capon
AWG :	Arbitrary Waveform Generator
AWGN :	Additive White Gaussian Noise
BBQ :	BaseBand tune (Q) measurement system
BLR :	BaseLine Restoration algorithm
BPM :	Beam Position Monitor
BTF :	Beam Transfer Function
B2B :	Bunch-by-Bunch
CAS :	CERN Accelerator School
CERN :	Organisation Européenne pour la Recherche Nucléaire
CST :	Computer Simulation Technology GmbH
DAQ :	Data AcQuisition
dB :	Decibel
DC :	Direct Current, Directional Coupler
DC-CT :	Direct Current- Current Transformer
DDR-RAM :	Double Data Rate Random Access Memory
DDS :	Direct Digital Synthesis
DFT :	Discrete Fourier Transform
ECR :	Electron Cyclotron Resonance
EH :	Experimental Hall
ER :	Single Gap Resonators
ESR :	Experimental Storage Ring

FAIR :	Facility for Antiproton and Ion Research
FCT :	Fast Current Transformer
FFT :	Fast Fourier Transform
FPGA :	Field Programmable Gate Array
GSI :	GSI Helmholtzzentrum für Schwerionenforschung GmbH
GUI :	Graphical User Interface
HIMAC :	Heavy Ion Medical ACcelerator in Chiba (Japan)
HLI :	High charge state injector
HSI :	High current injector
IPM :	Ionization Profile Monitor
ISE :	Integrated Synthesis Environment
K-V :	Kapchinsky-Vladimirsky distribution
LEIR :	Low Energy Ion Ring
LHC:	Large Hardon Collider
LUT :	Look Up Table
LSA :	LHC Software Architecture
MCP :	Micro-Channel Plate
MLE :	Most Likelihood Estimate
OLS :	Ordinary Least Squares
PSB :	Proton Synchrotron Booster
PSD:	Power Spectral Density
PU :	Pick-Up
RF :	Radio Frequency
RF-KO :	Radio Frequency- Knock Out
RFQ :	Radio Frequency Quadropole
RGM :	Residual Gas Monitor
RHIC :	Relativistic Heavy Ion Collider
RSA :	Realtime Spectrum Anlyzer
SBC :	Single Board Computer
SIS :	Schwerionensynchrotron
SNR :	Signal-to-Noise Ratio
SVD :	Singular Value Decomposition
TK :	Transfer channel between LINAC and SIS
TLS :	Total Least Squares
TOPOS :	Tune, Orbit and POSition measurement system
UNILAC :	UNIversal Linear ACcelerator
WLS :	Weighted Least Squares
1-D,2-D :	1-Dimensional, 2-Dimensional

Table 7.2: Symbols

Symbol	Definition	Unit
A :	Atomic mass number, total number of neutrons and protons	-
a_{x,y,s_0} :	Amplitude of betatron oscillations at azimuth s_0 in the synchrotron	m
$\mathbf{a}_P(\omega)$:	Column vector of complex exponentials $\mathrm{e}^{jn\omega}$ with $n = 0, \cdots, P-1$	-
α_{ia} :	Iso-adiabiticity parameter	-
α_{sc} :	Average space charge tune shift along a bunch	-
$\hat{\alpha}_{x,y}$:	Twiss parameter	-
$\hat{\alpha}_{DFT}$:	DFT as the spectrum estimator	-
$\hat{\alpha}_{Capon}$:	Capon method as the spectrum estimator	a.u.

$b_{x,y}$:	Elliptical beam pipe radius	m
B_f :	Bunching factor	-
β :	Velocity divided by speed of light in vacuum	-
β_0 :	Relativistic beta for the reference particle	-
$\hat{\beta}_{x,y}$:	Twiss parameter, Lattice amplitude function	m
$\hat{\beta}_{x,trip}$:	$\hat{\beta}_x$ at the IPM at injection (triplet) optics	m
$\vec{B}$:	Magnetic flux density	T
C :	Accelerator circumference	m
C^- :	Coupling coefficient	-
c :	Speed of light in vacuum, $2.998 \cdot 10^8$	m-s^{-1}
D :	Dispersion function	m
$D(f)$:	Dipolar signal in frequency domain	a.u.
Δp :	Momentum deviation from the reference particle	Kg-m-s^{-1}
$\Delta\theta$:	Delay or advance in phase w.r.t the reference particle	rad
Δt :	Delay or advance in time w.r.t the reference particle	s
ΔQ_{sc} :	Space charge tune shift	-
ΔQ_c :	Coherent tune shift	-
ΔQ_k :	Separation of k^{th} head-tail mode with respect to the bare tune	-
ΔQ_{k01} :	Spectral separation between k=0 and k=1 mode	-
ΔW :	Energy deviation from the reference particle	eV
$d(t)$:	Dipolar PU signal	a.u.
$d_n(t)$:	Dipolar PU signal due to the n^{th} particle	a.u.
d_s :	Inter-plate separation of the stripline exciter	m
$\delta(Arb)$:	Uncertainty or error in the measured parameter Arb	-
δQ_k :	Synchrotron tune spread of the k^{th} mode	-
$\delta(t)$:	Dirac delta function with the variable t	-
e:	Charge of a proton or an electron, $1.602 \cdot 10^{-19}$	C
$\epsilon_{x,y}$:	Transverse emittance	m-rad
ϵ_σ :	1σ emittance	m-rad
ϵ_0 :	Permittivity in vacuum, $8.854 \cdot 10^{-13}$	F-m^{-1}
E_{ols} :	Squared residue due to ordinary least squares fitting	-
$E[Var]$:	Expectation of a random variable or array	-
$\vec{E}$:	Electric field	V-m^{-1}
η_0 :	Slip factor	-
f:	Frequency	Hz
f_{rf} :	Frequency of rf cavity	Hz
f_0 :	Revolution frequency of the reference particle	Hz
f_c :	Carrier frequency for pseudo-random noise generation	Hz
f_s :	Synchrotron frequency, , $Q_s \cdot f_0$	Hz
f_b :	Betatron tune frequency, $Q_0 \cdot f_0$	Hz
$f_{k,r}$:	Frequency of the r^{th} head-tail mode, $Q_r \cdot f_0 = (Q_0 + \Delta Q_r) \cdot f_0$	Hz
γ :	Relativistic gamma	-
γ_0 :	Relativistic gamma for the reference particle	-
γ_T :	Relativistic gamma at transition energy	-
$\hat{\gamma}_{x,y}$:	Twiss parameter	m^{-1}
h :	Harmonic number	-
$\hat{H}_{AB}$:	Linear response matrix relating observable $\vec{A}$ and inducible variable $\vec{B}$	a.u.
I :	Electric current	A
I_{beam} :	Beam current	A
I_n:	Current due to n^{th} particle	A
I_p :	Peak beam current	A
$I_{lp}(f)$:	Low pass frequency response of an integration operation	-

i_n :	Noise current normalized to bandwidth	A-Hz$^{-1/2}$
J_k :	Ordinary Bessel's function of order k	-
j :	Imaginary unit	-
K :	Beam position sensitivity	%/m
$K(f)$:	Amplitude spectrum of the excitation signal in BTF measurement	a.u.
$\hat{k}_{x,y}$:	Quadrupole strength	m^{-2}
k :	Head-tail mode number, synchrotron satellite number	-
k_B :	Boltzmann's constant, $1.380 \cdot 10^{-23}$	J-K^{-1}
L_d :	Length of a device	m
L_s :	Length of the stripline exciter	m
m :	Revolution frequency harmonics	-
m_p:	Mass of proton, $1.67 \cdot 10^{-27}$	Kg
m_0 :	Mass of the nucleus	Kg
N:	Number of samples in a bunch	-
N_p:	Number of particles in the beam	-
n :	Discrete sequence index	-
Ω, ω :	$2\pi f$, angular frequency	rad-s^{-1}
P:	Power	W
$P(f)$:	Power spectrum	W-Hz^{-1}, a.u.
$\vec{p}$:	Momentum, $p\vec{e}_z$	Kg-m-s^{-1}
$\vec{p}_0$:	Momentum of the reference particle	Kg-m-s^{-1}
$\hat{\Psi}(s)$:	Betatron phase advance from a reference point to s	rad
ϕ_0 :	Synchronous phase	rad
ϕ_n^0 :	Initial betatron phase of the n^{th} particle	rad
ψ_n^0 :	Initial longitudinal phase of the n^{th} particle	rad
φ :	Relation between V_{beam} and I_{beam} for a centered beam	Ohm (Ω)
$Q_0, Q_{x,y,0}$:	Machine horizontal or/and vertical tune	-
$Q_{x,y}^f$:	Fractional horizontal and vertical tune	-
$[Q]$:	Integer part of tune	-
Q_k :	Tune of the k^{th} head-tail mode $Q_0 + \Delta Q_k$	-
Q_s :	Synchrotron tune	-
Q_{s0} :	Synchrotron tune for short bunches	-
Q_{s1} :	Effective synchrotron tune	-
Q_ξ :	Chromatic tune	-
q :	Particle charge	C
q_{sc} :	Calculated space charge parameter, ΔQ_{sc} normalized to Q_s	-
$q_{sc,m}$:	Measured space charge parameter using the separation between head-tail modes	-
q_c :	Image current parameter, ΔQ_c normalized to Q_s	-
q_k :	ΔQ_k normalized to Q_s	-
$q_{k,ab}$:	Separation between q_a and q_b	-
R :	Mean bending radius of the synchrotron	m
$R(f)$:	Beam transfer function (BTF)	a.u.
R_b :	Magnet bending radius of the synchrotron	m
$\mathbf{R}$:	Auto-covariance matrix	a.u.
$\tilde{R}_{AB}(\Omega\|\Theta_P, \Theta_K)$:	Beam transfer function of the beam between the kicker and beam PU in frequency domain	a.u.
$\vec{r}$:	Position vector	m
$\vec{r}_0$:	Design orbit of the synchrotron	m
$\vec{r}_{ni}$:	Six dimensional vector of the non-ideal particle in the curvilinear cordinate system	-
σ :	Std. deviation of a distribution	a.u.
σ_l :	1σ (rms) bunch length	m

$\sigma_{x,y}$:	1σ (rms) transverse beam width	m
$\sigma_{\hat{\theta}}$:	Std. deviation of the distribution of estimated beam position values	m
T :	Temperature	K
T_0 :	Revolution time	s
T_s :	Synchrotron motion period	s
Θ_P :	Location of pick-up for BTF measurement	rad
Θ_K :	Location of exciter for BTF measurement	rad
$\hat{\Theta}$:	Beam position estimator	m
t :	Time	s
t_{ramp} :	Ramping time	s
t_t :	Toggle time for pseudo-random noise generator	s
τ :	Difference between two time instances	s
τ_{BPM} :	Time constant of the pick-up along with the input termination	s
τ_{PD} :	Time constant of the BBQ peak detector	s
θ :	Beam position	m
$\hat{\theta}$:	Estimated beam position	m
$\bar{\hat{\theta}}$:	Mean of estimated beam position	m
θ_b :	Full bunch length	rad
θ_m :	Amplitude of synchrotron oscillations in the bunch, or half-bunch length	rad
θ_β :	Amplitude of betatron oscillations	m
U, u :	Voltage or electric potential difference	V
U_{beam} :	Voltage induced by the beam on pick-up plates	V
U_{in} :	Voltage induced by the beam on the pre-amplifiers	V
u_n :	Noise voltage normalized to bandwidth	V-Hz$^{-1/2}$
$\hat{u}$:	Unit step function	-
$\vec{v}$:	Velocity	m-s^{-1}
$\vec{v}_0$:	Velocity of the reference particle	m-s^{-1}
W_d :	Width of a device	m
W :	Energy	eV
W_0 :	Energy of the reference particle	eV
W_{kin} :	Kinetic energy	eV
$\mathbf{W}$:	Weighting matrix	a.u.
$\mathbf{X}$:	Noise matrix	a.u.
$x(n)$:	Signal sequence	a.u.
x, y :	Tranverse coordinates	m
x', y' :	Slope of transverse motion with respect to the nominal orbit	rad
$\dot{x}, \dot{y}$:	Time derivative of transverse motion with respect to the nominal orbit	m-s^{-1}
x_n, y_n :	Transverse coordinate of n^{th} particle in the beam	m
$\xi_{x,y,nat}$:	Natural chromaticity of the lattice	-
ξ_{ff} :	Form-factor for calculating transverse impedance (one of the Laslett's coefficient)	-
$\bar{x}, \bar{y}$:	Transverse beam position, barycenter of the beam	m
$\vec{e}_x, \vec{e}_y, \vec{e}_z$:	Orthonormal basis unit vectors	a.u.
$\mathbf{Y}$:	Signal matrix	a.u.
Z :	Charge state of the ion	-
Z :	Impedance	Ohm (Ω)
Z_0	Characterstic impedance of vacuum, 377	Ω
Z_T :	Transfer impedance	Ω
$Z_\perp$:	Transverse machine impedance	Ω
z :	Longitudinal coordinate	m

Bibliography

[1] H. H. Gutbrod, I. Augustin, H. Eickhoff, K.-D. Groess, W. F. Henning, D. Kraemer and G. Walter, “FAIR baseline technical report”, technical report, GSI, 2006.

[2] “FAIR Green Paper, The Modularized Start Version”, October 2009.

[3] O. Boine-Frankenheim, “The FAIR accelerators: Highlights and challenges”, Proc. of IPAC 2010, Japan, 2010.

[4] B. Franczak, “SIS parameter list”, technical report, GSI, 1987.

[5] M. Steck et al., “Fast beam accumulation by electron cooling in the heavy ion synchrotron SIS”, In Proc. of EPAC96, 1996.

[6] https://www.gsi.de/en/gsiwork/forschungsabteilungen.htm

[7] B. Jakob, J. Splinter, M. Durante, and G. Taucher-Scholz, “Live cell microscopy analysis of radiation-induced DNA double-strand break motion”, Proc. of the National Academy of Sciences, 106(9):3172,3177, 2009.

[8] http://www-alt.gsi.de/informationen/wti/library/scientificreport2011/

[9] P. Spiller, K. Blasche, U. Blell, O. Boine-Frankenheim, P. Forck, P. Hülsmann, G. Moritz, H. Ramakers, and S. Ratschow, “SIS100/300 Conceptual Design Studies”. Technical report, GSI, 2004.

[10] http://www.fair-center.de/de/oeffentlichkeit/

[11] Th. Stöhlker,T. Beier, et al., “Atomic physics with highly-charged ions at the future FAIR facility: A status report”, NIM in Physics Research Section B-Beam Interactions with Materials and Atoms 261(1-2): 234-238, 2007.

[12] B. Friman et al., “The CBM physics Book”, Series: Lecture Notes in Physics, Vol. 814, 2011.

[13] H. Geissel et al., “The Super-FRS project at GSI”, In Nuclear Instruments and Methods in Physics Research, volume B of 71, 2003.

[14] J. Rossbach and P. Schmüser, “Basic course on accelerator physics”, Proc. of CAS 1992, Finland, 1994.

[15] M. Sands, SLAC TN-69-8 and TN-69-10, 1969.

[16] F. J. Sacherer, “Transverse space-charge effects in circular particle accelerators”, UCRL-18454, 1968.

[17] L. Vos, “Decoherence from space charge”, presented at the XVIIth Int. Conf. High Energy Part. Accel., Dubna, Russia, September 1998, Internal Report CERN SL-98-056 AP, 1998.

[18] A. W. Chao, “Physics of Collective Beam Instabilities in High Energy Accelerators”, Beam Physics and Accelerator Technology. Wiley, 1993.

[19] S. Chattopadhyay, “Some fundamental aspects of fluctuations and coherence in charged particle beams in storage rings”, Super Proton Synchrotron Division, CERN 84-11, 1984.

[20] L. J. Laslett, “On intensity limitations imposed by transverse space-charge effects in circular particle accelerators”, Summer Study on Storage Rings, BNL Report 7534, p. 325-367, 1963.

[21] K. Schindl, “Space Charge”, Joint US-CERN-Japan-Russia School on Particle Accelerators, Montreaux, Switzerland, 1998.

[22] R. Singh et al., “Interpretation of transverse tune spectra in a heavy-ion synchrotron at high intensities”, Phys. Rev. ST Accel. Beams 16, 034201, 2013.

[23] F. Zimmermann, “Accelerator optics”, Proc. of Joint US-CERN-Japan-Russia School on Particle Accelerators, Montreaux, Switzerland, 1998.

[24] A. Hofmann, “Landau damping”, In Proc. of CERN Accelerator School 2003, CERN 2006-02, DESY, Zeuthen, 2006.

[25] W. Schottky, “Über spontane Stromschwankungen in verschiedenen Elektrizitätsleitern”, Annalen der Physik, 57:541, 1918.

[26] J. Borer, G. Guignard, A. Hofmann, E. Peschardt, F. Sacherer, and B. Zotter, “Information from beam response to longitudinal and transverse excitation”, In Proc. of PAC 1979, volume NS-26, 3, 1979.

[27] S. Paret, “Transverse Schottky Spectra and Beam Transfer Functions of Coasting Ion Beams with Space Charge”, PhD Thesis, TU Darmstadt, Germany, 2009.

[28] H. Schmickler, “Beam Diagnostics”, Proc. of Joint US-CERN-Japan-Russia School on Particle Accelerators, Montreaux, Switzerland, 1998.

[29] U. Springer, “High resolution measurement of betatron tune at SIS-18”, PhD Thesis, Goethe university Frankfurt, 2010.

[30] G. Franchetti et al., “ Beam losses and resonance diagram”, GSI Scientic report, 2003.

[31] H. Weidemann, “Particle accelerator Physics”, ISBN 978-3-540-49043-2, 2007.

[32] M. Reiser, “Theory and design of charged particle beams”, ISBN 978-3-527-40741, 2008.

[33] K. Wille, “The Physics of particle accelerators, an introduction”, ISBN 978-0-19-850550-1, 2009.

[34] R. Nave, “Nuclear Binding Energy”, Hyperphysics - a free web resource from GSU, Georgia State University, Retrieved 2013-05-30, 2010.

[35] H. Klingbeil, “Lecture notes of acceleration of charged particle beams”, TU Darmstadt, Germany, 2011.

[36] C. Prior, “Dynamics of Non-Linear Beams with Space-Charge”, CAS, Bilbao, Spain, 2011

[37] S. Sykora, “Volume Integrals over n-Dimensional Ellipsoids”, in Stan’s Library, Ed.S.Sykora, Vol I, 2005.

[38] D. Boussard, “Schottky Noise and Beam Transfer Function Diagnostics”, CERN Accelerator School, Fifth Advanced Accelerator Physics Course, 1995.

[39] O. Boine-Frankenheim, V. Kornilov, Phys. Rev. ST Accel. Beams, **12**, 114201, 2009.

[40] G. Palumbo, V. Vacarro and M. Zobov, “Wake fields and impedance”, LNF-94/041, 1994.

[41] R. Wanzenberg, T. Weiland, “Wakefields and Impedances”, CCAS- CAT-CERN Accelerator School, Vol. 1, Proc., Indore, India, 7-16 November 1993, pp. 140-180, 1993.

[42] K. Y. Ng, “Physics of Intensity Dependent Beam Instabilities”, ISBN 981-256-342-3, 2006.

[43] U. Niedermayer et al., “Analytical and numerical calculation of beam pipe impedances at low frequencies for applications to thin SIS-100 pipe”, IPAC 2011, Japan, 2011.

[44] M. Blaskiewicz, Phys. Rev. ST Accel. Beams **1**, 044201, 1998.

[45] A. Burov, Phys. Rev. ST Accel. Beams **12**, 044201, 2009.

[46] V. Balbekov, Phys. Rev. ST Accel. Beams **12**, 124402, 2009.

[47] V. Kornilov, O. Boine-Frankenheim, Phys. Rev. ST Accel. Beams,**13**, 114201, 2010.

[48] R. Singh et al., “High intensity effect on Betatron tune at GSI SIS-18”, Proc. of BIW’12, Newport News, U.S.A, 2012.

[49] V. Kornilov, O. Boine-Frankenheim, Phys. Rev. ST Accel. Beams,**15**, 114201, 2012.

[50] D. Möhl, “Stochastic Cooling”, Proc. CERN Acc. School, Fifth Advanced Course, p. 587, CERN 95-06, 1995.

[51] T. Linnecar and W. Scandale, “A Transverse Schottky Noise Detector For Bunched Beams”, Proc. of PAC 1981, p. 2147, 1981.

[52] O. Boine-Frankenheim, T. Shukla, Phys. Rev. ST Accel. Beams **8**, 034201, 2005.

[53] Proc. of CAS 1992, Edited by S. Turner, University of Jyväskylä, Finland, ISBN 92-9083-057-3, 1994.

[54] Proc. of Joint US-CERN-Japan-Russia School on Particle Accelerators, Edited by Lee, Kurokawa, Turner, Pereyentsev, 1998.

[55] Simulations performed by O. Boine-Frankenheim, Private communication, GSI Beam Physics Group, 2012.

[56] R. Singh, P. Forck, W. Kaufmann, P. Kowina, “Tune measurements with high intensity ion beams at GSI SIS-18”, DIPAC 2011, Hamburg, Germany, 2011.

[57] Agilent application note, “Understanding the Fundamental Principles of Vector Network Analysis”, Retrieved May 2013.

[58] S. Sorge, “Magnetostatic contribution to the RF noise of the SIS-18 RF-KO exciter”, PHN-ACC-RD-18, 2011.

[59] P. Kowina et al., “Digital baseband tune determination”, Proc. of BIW’10, Santa Fe, U.S.A, 2010.

[60] M. Gasior, R.Jones, “The principle and first results of betatron tune measurement by direct diode detection”, LHC-Project-Report 853, 2005.

[61] M. Gasior, “High sensitivity tune measurement using direct diode detection”, Proc. of BIW’12, Virginia, U.S.A, 2012.

[62] P. Moritz, “Analogue Signal Processing for the Beam Position Measurement System at SIS18”, GSI Scientific Report, page 335, 1986.

[63] P Moritz, “RF-KO Extraktion”, Internal note, http://bel.gsi.de/mk/fg/ko extr.pdf, 2005.

[64] M. Kirk, P. Moritz, D. Ondreka, P. Spiller, “Status Report on RF Knock-Out Extraction”, GSI Scientific Report, 2011.

[65] Private communications with W. Kaufmann, GSI beam diagnostics group, 2011.

[66] S. Sorge et al., Phys. Rev. ST Accel. Beams, **14**, 052802, 2011.

[67] P. Forck, “Lecture notes on beam instrumentation”, JUAS, Archamps, France, 2010.

[68] P. Kowina et al., “Optimisation of shoe-box type beam position monitors using the finite element methods”, Proc. of DIPAC 2005, Lyon, France, 2005.

[69] R. Steinhagen et al., “Tune and chromaticity diagnostics”, CAS 2008, Darmstadt, Germany, 2008.

[70] O. Chorniy, “Measurement and interpretation of the bunched beam transfer function in SIS 18 with space charge”, PhD Thesis, TU Darmstadt, 2008.

[71] C.Y. Tan, “Novel tune diagnostics for the Tevatron”, Proc. of 2005 Particle Accelerator Conference, Knoxville, Tennessee, U.S.A, 2005.

[72] P. Cameron et al., “Progress in Tune, Coupling, and Chromaticity Measurement and Feedback During RHIC Run-7”, PAC’07, Albuquerque, NM, p. 886-888, 2007.

[73] Private communications with M. Gasior, CERN beam instrumentation group, 2012.

[74] Private communications with P. Kowina, GSI beam diagnostics group, 2012.

[75] J. Latzko, P. Kowina, “Simulations of the position sensitivity for the SIS18 capacitive BPM with a non-standard geometry”,GSI Scientific report 2012.

[76] H. Klingbeil et al., “Beam Experiment 4:2:1 Bunch Merging in SIS18”, GSI scientific report, PHN-ACC-RD-15, 2010.

[77] J. Belleman et al., “Trajectory measurement system at PS”, BPM Workshop CERN, Geneva, 2012.

[78] A. Galatis et al., “Beam Position Algorithms at GSI”, DIPAC 2005, Lyon, France, 2005.

[79] A. Galatis et al., “Digital beam position measurement at GSI SIS-18 and CERN-PS”, DIPAC 2005, Lyon, France, 2005.

[80] D. Liakin et al., “Advanced methods for digital beam position determination”, Proc. of DIPAC 2011, Hamburg, Germany, 2011.

[81] S. Oser, “Theory of Measurement”, Lecture notes, University of British Columbia, Canada, 2011.

[82] T. O'Haver, "Intro to Signal Processing - Deconvolution", University of Maryland at College Park, Retrieved October 2012.

[83] Larry Wasserman, "All of nonparametric statistics", Berlin: Springer-Verlag, 2006.

[84] R. E. Tavares, "Integration and low pass filtering", IEEE trans. signal processing, 1966.

[85] K. Lang et al., "Performance tests of digital signal processing for GSI Synchrotron BPMs", PCaPAC08, Ljubljana, Slovenia, 2008.

[86] Private communications with Kevin Lang, GSI Beam Diagnostics Group, 2012.

[87] M. Herbordt et al., "Achieving High Performance with FPGA-Based Computing", IEEE Computer society, 2007.

[88] I. Markovsky, S Van Huffel, "Overview of total least squares methods", Signal Processing, vol. 87, pp. 2283-2302, 2008.

[89] R. Bartolini et al., "Algorithms for precise tune detemination", presented at LHC95, Part. Accel. 55, 1996.

[90] R. Bartolini et al., "Algorithms for a precise determination of the betatron tune", Fifth European Accelerator Conference, edited by J. Pool and C. Petit, Institute of Physics UK, London, 1996.

[91] N. Biancacci et al., "Refined techniques for phase measurements", Optics Workshop, CERN, Geneva, Switzerland, 2011.

[92] John Stensby, "Class notes on Random signals and noise", EE385/603, University Alabama in Huntsville, 2012.

[93] A. Zoubir, "Lecture notes on Digital signal processing", TU Darmstadt, Germany, 2010.

[94] R. O. Schmidt,"A signal subspace approach to multiple emitter location and spectral estimation", Ph.D. thesis, Stanford University, Stanford, CA, USA, 1981.

[95] J. Capon, "Maximum-likelihood spectral estimation" in Nonlinear Methods of Spectral Analysis (S. Haykin, ed.), New York:Springer-Verlag, 1983.

[96] T. Ekman et al., "On the efficient implementation of the Capon spectral estimator", Uppsala University, 1998.

[97] Hongbin Li et al., "Performance Analysis of Forward-Backward Matched-Filterbank Spectral Estimators", IEEE Trans. signal processing, 2000.

[98] G. O. Gletis et al., "A Fast Algorithm for APES and Capon Spectral Estimation", IEEE Trans. signal processing, 2008.

[99] Erik G. Larsson, Jian Li and Petre Stoica, "High-resolution nonparametric spectral analysis: theory and applications", 2008.

[100] P. Stoica and R. Moses, "Introduction to Spectral Analysis", Upper Saddle River, NJ: Prentice Hall, 1997.

[101] A. Zoubir, "Seminars on advanced statistical signal processing", Lecture notes, TU Darmstadt, Germany, 2011.

[102] U. Schaaf, "Schottky-Diagnose und BTF- Messungen an gekuhlten Strahlen im Schwerionenspeichering ESR", PhD thesis, Univesität Frankfurt, 1991.

[103] Tektronix user manual, RSA3303A, RSA3308A 3 GHz to 8 GHz Real-Time Spectrum Analyzers. 071-1409-03.

[104] H. Reeg et al., "Current Transformers for GSI's KeV/u to GeV/u Ion Beams - An Overview", Proc. of DIPAC 2001, Grenoble, France, 2001.

[105] T. Giacomini et al., "Development of Residual Gas Profile Monitors at GSI", Proc. of BIW'04, Knoxville, U.S.A, 2004.

[106] F. Caspers, "Schottky Signals", CAS 2008, Dourdon, France, 2008.

[107] T.Mohite, "Beam loading effect and adiabatic capture in SIS-18 at GSI", PhD Thesis, TU Darmstadt, Germany, 2011.

[108] M. Kirk et al., “Phase space growth during RF capture in the GSI heavy ion synchrotron SIS-18”, Laser and Particle Beams, 21, 85089. Printed in the USA, 2003.

[109] Private communication with K. Ningel, GSI RF group, 2011.

[110] P. J. Bryant, “Linear betatron coupling”, Proc. of CAS 1992, University of Jyväskylä, Finland, ISBN 92-9083-057-3, 1994.

[111] W. Daqa et al., “Linear coupling with space charge in SIS18”, Proc. of IPAC 2010, Kyoto, Japan, 2010.

[112] G. Franchetti et al., Phys. Rev. ST Accel. Beams **13**, 114203, 2010.

Acknowledgement

This work is the result of numerous direct and indirect contributions from several individuals. Mentioning each name and contribution is out of scope but is remembered with deep gratitude. Dr. Peter Forck has shown immense trust and responsibility towards me and my work. Not to mention, his numerous scientific contributions, I thank him for the encouragement and intellectual freedom, he provided me during the past three years. Dr. Piotr Kowina contributed almost each time when it mattered. I thank him, for the numerous Friday evening discussions on a wide array of topics. I thank Prof. Dr. Thomas Weiland for accepting me as PhD student in his institute. All discussions with him brought in something novel for me. Prof. Dr. Harald Klingbeil provided insightful comments on various stages of this work and especially helped with his careful and detailed inputs in the writing phase of this dissertation. Prof. Dr. Oliver Boine-Frankenheim contributed by providing a theoretical beam physics perspective to the experimental results through his simulations. I thank him for his insistence on the publication of the experimental results which turned out to be a fruitful experience.

My colleagues at the Beam Instrumentation group accepted me warmly in the group. They shared their deep insights on various aspects of beam diagnostics. All of them, were always willing to take "the extra step" to ensure the timely completion of this work. My special thanks goes to my collaborators Dmitry, Kevin, Oleksandr, Rainer, Tobias, Tino and Wolfgang. I thank Andreas, Beata, Hannes, Frank, Rolf, Christiane, Febin for taking time to educate me on other dimensions of life, be it culture, music or language in addition to their technical contributions. Our group leader, Dr. Marcus Schwickert is gratefully acknowledged for his continuous efforts in the "background" for harmonious functioning of the group and thus my work. The operating crew of SIS-18 has been very helpful and efficient which ensured the success of the beam experiments despite the odd working times. I thank them a lot for their efforts. I also thank the administrative and technical organization of GSI for the good support they provided during my work. I also thank Rainer and Lea Wunderlich both of whom took serious efforts to read through this thesis and helped against the linguistic errors.

I must thank **DITANET FP7 Marie Curie Initial Training Network (ITN)** scheme for the funding of this work. The DITANET organization and colleagues made the PhD time lively due to numerous meetings and workshops. The network was personally a very successful venture primarily in terms of the scientific exposure it provided. Dr. Marek Gasior from CERN provided extra-ordinary support for BBQ system installation, and it was while working with him on a DITANET secondment, I was convinced of the utility of the system for SIS-18 installation. Further, HGS-Hire ensured continuous learning by forcing me to participate in several suitable lecture weeks and soft-skills workshop. I should also mention the high quality of masters education imparted by **"Erasmus Mundus Masters in Photonics (EMMP)"** which encouraged me to pursue a PhD at the first place. Finally the authors and contributors to PGFplots/Tikz are also warmly acknowledged for providing an excellent plotting tool which is used throughout this thesis.

Desire alone defines man - as is his desire, so is his will; as is his will, so will he act; as is his deed, so is his destiny.

– Brihadaranyaka Upanishad

My loved ones/friends are now spread all over the world had a major share in shaping my desires and thus this work. My family has played a major role in everything I have done till this point. My mother gave me the freedom and a sense of responsibility from a very early age and tried to teach me discipline and dedication. My sisters form a constant support structure I can fall back upon. Dr. V. Mohan introduced me to various beautiful mysteries of science with his inexhaustible enthusiasm, which has motivated me more than once, thus this section would have been incomplete without mentioning him. The wonderful emotional and technical support from Neha during this whole period is splashed all across the thesis. I must also mention Dr. Pushpendra P. Singh for his continuous encouragement and for several stimulating discussions on science and politics.

There were several constructive criticisms during the period of this work, they refined my thoughts and forced me to have a critical look at everything "one more time". I thank the critics for their contributions to this work.

Academic curriculum vitae

Rahul Singh

Born on 30.09.1984 in Jalesar, Uttar Pradesh, India

Academic education

2000-2002 – Intermediate school, CBSE Board, Govt. Higher Secondary School, Itanagar, Arunachal Pradesh, India. grade : A1 (84%).

2002-2006 – Bachelors in Electronics and Telecommuncations Engineering, SRTM University, SGGS College of Engineering and Technology, Nanded, Maharashtra, India; grade : First class with distinction.

2006-2008 – Erasmus Mundus Masters in Photonics, Consortium of Ghent University, Free University of Brussels and Royal Institute of Technology, Stockholm; grade : Very good.

2007-2008 – Masters thesis with Prof. A. Karlsson in Quantum Optics group at KTH Stockholm, Sweden, “Source of correlated photons pairs using 2D periodically poled KTP crystals”.

Professional experience

06/2007-08/2007 – Internship at VUB Cyclotron facility, “Simulation and lab tests of low bending loss holed optical fibers”, Brussels, Belgium.

05/2008-08/2009 – System Manager at AXE platform, Ericsson AB, Stockholm, Sweden.

10/2009-09/2012 – Early Stage Researcher in ITN-DITANET working at the beam diagnostics group at GSI Helmholtzzentrum für Schwerionenforschung GmbH, Darmstadt, Germany, on the topic “Tune measurements and applications”. It included a 6 week secondment at CERN (April-May 2011), where a prototype of Matlab based closed orbit DAQ system for LHC “Jaw BPMs” was developed.

University courses attended during thesis work

1. Joint University Accelerator School: Module 1, Archamps, France, January 2010. (With examination)
2. Digital Signal Processing by Prof. A. Zoubir, TU Darmstadt, winter semester 2009/2010. (With examination)
3. Analog Intergrated Circuit Design by Prof. A. Hofmann, TU Darmstadt, winter semester 2009/2010. (With examination)
4. Technical Electrodynamics for iCE masters by Prof. I. Munteanu, TU Darmstadt, winter semester 2010/2011. (With examination)
5. Acceleration of Charged Particles in Electromagnetic Fields by Prof. H. Klingbeil, TU Darmstadt, winter semester 2010/2011.

Other courses

1. DITANET Complimentary skills course, March 2010.
2. DITANET Advanced beam diagnostics school, March 2011.
3. HGS Hire Softskill course level 1, May 2011.
4. HGS-Hire Lecture week: Introduction to Accelerator Physics,October 2011.
5. HGS-Hire Lecture week: Introduction to Linear accelerators, September 2012.

6. HGS-Hire Softskill course level 3, March 2013.

Relevant Publications

1. R. Singh, O. Boine-Frankenheim, O. Chorniy, P. Forck, R. Haseitl, W. Kaufmann, P. Kowina, K. Lang, T. Weiland, “Interpretation of transverse tune spectra in a heavy-ion synchrotron at high intensities”, Phys. Rev. ST Accel. Beams 16, 034201 (2013).
2. R. Singh, O. Boine-Frankenheim, P. Forck, P. Kowina, T. Weiland„ “Chromaticity measurements using head-tail modes at SIS-18”, GSI Scientific report 2012.
3. R. Singh, P. Forck, P. Kowina, O. Boine-Frankenheim, O. Chorniy, R. Haseitl, W. Kaufmann, K. Lang, T. Weiland, “Coherent and incoherent tune shifts for bunched beams at SIS-18”, GSI Scientific report 2012.
4. R. Singh, O. Boine-Frankenheim, O. Chorniy, P. Forck, R. Haseitl, W. Kaufmann, P. Kowina, K. Lang, T. Weiland, “Measurements and interpretation of the betatron tune spectra of high intensity bunched beam at SIS-18”, HB2012, China, September 2012.
5. P. Kowina, P. Forck, R. Singh, F. Caspers, “Momentum spread determination of Linac beams using incoherent components of the bunch signals”, HB2012, Bejing, China, September 2012.
6. R. Singh, P. Forck, P. Kowina, W. Kaufmann, K. Lang, T. Weiland, “High intensity effect on Betatron tune at GSI SIS-18”, BIW 2012, Newport News, Virginia, U.S.A, April 2012.
7. R. Singh, P. Forck, P. Kowina, W. Kaufmann, K. Lang, T. Weiland, “High Intensity Effects on Betatron Tune at SIS-18”, GSI Scientific report 2011.
8. D. Liakin, P. Forck, K. Lang, R. Singh, “Advanced digital processing for effective beam position monitoring”, DIPAC 2011, Hamburg, Germany, May 2011.
9. R. Haseitl, H. Bräuning, T. Hoffmann, K. Lang, R. Singh, “Development of FESA-based Data Acquisition and Control for FAIR”, DIPAC 2011, Hamburg, Germany, May 2011.
10. R. Singh, P. Forck, W. Kaufmann, P. Kowina, “Tune measurements with high intensity ion beams at GSI SIS-18”, DIPAC 2011, Hamburg, Germany, May 2011.
11. R. Singh, P. Forck, P. Kowina, U. Springer, P. Moritz, T.Weiland, “Tune measurement with high intensity at SIS-18”, GSI Scientific report 2010.
12. R. Singh, P. Forck, P. Kowina, U. Springer, P. Moritz, T.Weiland, “Observation of space charge effects on tune using the new digital tune measurement system” HB 2010, Morschasch, Switzerland, October 2010.

Posters

1. Beam Diagnostics at GSI, HGS-hire graduate program, Mainz, Germany, October 2012
2. High intensity effects on Betatron tune at GSI SIS-18, BIW 2012, Newport News, Virginia, U.S.A, April 2012
3. Position calculation algorithms at GSI SIS-18, Seville, Spain, November 2011
4. Tune Measurements with High intensity ion beams at GSI SIS-18, KWT 2011, Kleinwalsertal, Austria, August 2011
5. Tune measurements with high intensity beams at GSI SIS-18, DIPAC 2011, Hamburg, Germany, May 2011
6. Observation of space charge effects on tune using the new digital tune measurement system: HB 2010, Morschasch, Switzerland, October 2010

External Talks

1. Understanding tune spectrum at high intensities, DPG spring meeting 2013, Dresden, Germany, March 2013

2. Measurements and interpretation of the betatron tune spectra of high intensity bunched beam in the SIS18, HB 2012, Bejing, China, September 2012 (Invited)
3. Betatron Tune measurements, Beam physics for FAIR, Odenwald, Germany, May 2012
4. High intensity effects on betatron tune at GSI SIS-18, University Maryland Electron Ring, Maryland, U.S.A, April 2012
5. Tune measurements with high intensity ion beams at GSI SIS-18: Methods and Results, DPG spring meeting 2012, Göttingen, Germany, February 2011
6. Numerical Methods for Beam Position Evaluation at GSI, BPM Workshop, CERN, Switzerland, January 2012 (Invited)
7. Tune measurements at GSI SIS-18: Methods and Results, RRCAT, Indore, India, January 2011
8. Tune measurements at GSI SIS-18: Methods and Results, Seminars on Accelerator Physics, TEMF, Germany, November 2011
9. Tune measurements at GSI SIS-18: Methods, Ditanet International Conference, Seville, Spain, November 2011
10. Tune measurements at GSI SIS-18, COSY, Jülich, Germany, July 2011
11. Observation of space charge effects on tune using the new digital tune measurement system, KWT Workshop 2010, Waren Müritz, Germany, August 2010